

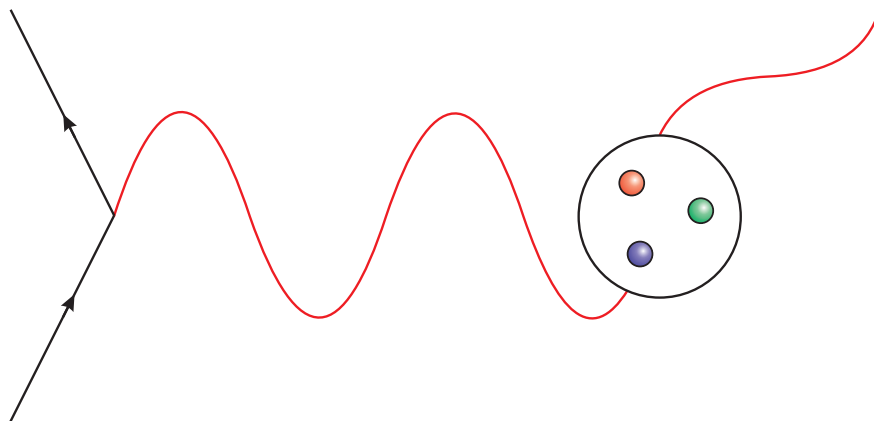


---

# Double-polarized virtual Compton scattering as a probe of the proton structure

---

Dubbelgepolarizeerde virtuele Compton verstrooiing  
als een probe van de protonstructuur



Peter Janssens

Promotor: Prof. Dr. Dirk Ryckbosch  
Co-promotor: Prof. Dr. Luc Van Hoorebeke

Proefschrift ingediend tot het verkrijgen van de graad van  
Doctor in de Wetenschappen: Natuurkunde



---

# Contents

---

<b>1</b>	<b>Introduction</b>	<b>1</b>
<b>2</b>	<b>Physics framework</b>	<b>5</b>
2.1	Form factors of the proton . . . . .	6
2.2	Polarizabilities . . . . .	9
2.3	Real Compton scattering . . . . .	11
2.4	Virtual Compton scattering below pion threshold . . . . .	14
2.4.1	Kinematics of VCS . . . . .	14
2.4.2	Decomposition of the photon electroproduction amplitudes . . . . .	16
2.4.3	Low energy theorem . . . . .	19
2.5	Generalized polarizabilities . . . . .	21
2.5.1	Multipole expansion of $H_{\text{NB}}$ . . . . .	21
2.5.2	Definition of the generalized polarizabilities . . . . .	22
2.5.3	Interpretation of the generalized polarizabilities . . . . .	25
2.6	Observables of VCS in threshold experiments . . . . .	26
2.6.1	Structure functions . . . . .	26
2.6.2	Unpolarized cross section . . . . .	27
2.6.3	Single-spin asymmetry . . . . .	29
2.6.4	Double-spin asymmetry . . . . .	30
<b>3</b>	<b>Model predictions and VCS experiments</b>	<b>33</b>
3.1	Theoretical models . . . . .	34
3.1.1	Heavy baryon chiral perturbation theory . . . . .	34
3.1.2	Linear sigma model . . . . .	37
3.1.3	Constituent quark model . . . . .	37
3.1.4	Effective Lagrangian model . . . . .	38
3.1.5	Dispersion relations . . . . .	39

3.2	Experiments . . . . .	40
3.2.1	First MAMI experiment . . . . .	41
3.2.2	JLab experiment . . . . .	44
3.2.3	MIT-Bates experiment . . . . .	45
3.2.4	MAMI beam single-spin asymmetry experiment . . . . .	47
3.3	Conclusion . . . . .	48
<b>4</b>	<b>Experimental setup</b>	<b>51</b>
4.1	MAMI accelerator . . . . .	52
4.2	Three-spectrometer setup . . . . .	52
4.2.1	Spectrometer magnets . . . . .	54
4.2.2	Focal plane detection system . . . . .	56
4.2.3	Spectrometer optics . . . . .	59
4.3	Target cell . . . . .	60
4.4	Förster probe . . . . .	61
4.5	Møller polarimeter . . . . .	62
4.5.1	Principle . . . . .	62
4.5.2	Detector system . . . . .	63
4.6	Focal plane polarimeter . . . . .	63
4.6.1	Principle . . . . .	64
4.6.2	Detector system . . . . .	66
<b>5</b>	<b>Monte Carlo simulation</b>	<b>69</b>
5.1	The simulation package . . . . .	70
5.1.1	VCS event generator . . . . .	70
5.1.2	Detector resolution effects . . . . .	71
5.1.3	Event reconstruction . . . . .	72
5.1.4	Cross section grid . . . . .	72
5.1.5	Effective solid angle . . . . .	73
5.2	Radiative effects . . . . .	75
5.2.1	External bremsstrahlung . . . . .	75
5.2.2	Internal bremsstrahlung . . . . .	76
5.2.3	Testing the radiative corrections in the simulation . . . . .	79
5.2.4	Effectively applied correction factor . . . . .	81
5.3	Implementation of the spectrometers resolution . . . . .	81
5.3.1	Resolution effects in the focal plane . . . . .	82
5.3.2	Additional resolution effects . . . . .	85
5.3.3	Adjustment of the detector resolution effects . . . . .	86
5.4	Comparison with data . . . . .	91
5.5	Possible improvements . . . . .	91

---

<b>6</b>	<b>Unpolarized cross section</b>	<b>95</b>
6.1	Data selection . . . . .	96
6.1.1	Momentum acceptance of the spectrometers . . . . .	97
6.1.2	Coincidence time . . . . .	97
6.1.3	Scintillators . . . . .	99
6.1.4	Cherenkov detector . . . . .	100
6.1.5	Reconstructed z-vertex . . . . .	103
6.1.6	Missing mass . . . . .	106
6.1.7	Kinematical cuts . . . . .	106
6.1.8	Additional acceptance cut . . . . .	107
6.2	Estimation of the background . . . . .	109
6.3	Calculation of the unpolarized cross section . . . . .	111
6.3.1	Calculation of the Bethe Heitler + Born cross section . . . . .	111
6.3.2	Solid angle . . . . .	112
6.3.3	Detector efficiency . . . . .	113
6.3.4	Cross section . . . . .	115
6.4	Determination of the structure functions . . . . .	115
6.4.1	Extraction method . . . . .	115
6.4.2	Iterations . . . . .	117
6.4.3	Systematic uncertainties . . . . .	119
6.4.4	Conclusion . . . . .	121
6.5	Interpretation of the result . . . . .	123
<b>7</b>	<b>Double-spin asymmetry</b>	<b>125</b>
7.1	Data selection . . . . .	126
7.1.1	VCS events . . . . .	126
7.1.2	Drift chambers . . . . .	126
7.1.3	Carbon analyzer . . . . .	127
7.1.4	Large-angle scattering events . . . . .	128
7.1.5	Resolution of the HDCs . . . . .	128
7.1.6	Analyzing power . . . . .	131
7.2	Beam polarization . . . . .	131
7.3	Measurement of the double-spin asymmetry . . . . .	131
7.3.1	Calculation of the Bethe-Heitler + Born polarizations . . . . .	131
7.3.2	Rotations of the spin . . . . .	133
7.3.3	Maximum-likelihood fit of the polarization . . . . .	139
7.3.4	Representation of the polarization results . . . . .	140
7.3.5	Constraints on the likelihood fit . . . . .	140
7.4	Extraction of the structure functions . . . . .	145
7.4.1	Effect of the GPs on the polarization . . . . .	145

---

7.4.2	Extraction method and analysis . . . . .	146
7.5	Outlook . . . . .	155
<b>8</b>	<b>Conclusion</b>	<b>157</b>
	<b>Nederlandstalige samenvatting</b>	<b>159</b>
	<b>Acknowledgments</b>	<b>167</b>
	<b>Bibliografie</b>	<b>169</b>
<b>A</b>	<b>Calibration of the spectrometers</b>	<b>i</b>
<b>B</b>	<b>Reference frames and coordinates</b>	<b>iii</b>
B.1	Hall laboratory reference frame . . . . .	iii
B.2	Spectrometer reference frame . . . . .	iii
B.3	Focal plane reference frame . . . . .	v
B.4	HDC reference frame . . . . .	v
B.5	Proton reference frame . . . . .	v
B.6	Center-of-mass reference frames . . . . .	v
B.7	Rotation from center-of-mass frame to the spectrometer frame . . . . .	ix
<b>C</b>	<b>Tables</b>	<b>xi</b>
C.1	Overview of the settings . . . . .	xi
C.2	Resolution effects in the simulation . . . . .	xii
C.3	Cross section . . . . .	xiii
C.4	Double-spin asymmetry . . . . .	xv

# CHAPTER 1

---

## Introduction

---

After the discovery of the electron in 1897 by Thomson, it became clear that there must be also positive charge centers within the atom to compensate for the negatively charged electrons, because an atom is overall electrically neutral. In 1911 Rutherford discovered that these positive charges are concentrated in a very small fraction of the volume, called the nucleus. While the size of the atom is of the order of  $10^{-10}$  m, the size of the nucleus is a factor of  $10^4$  to  $10^5$  smaller. It contains the main part of the mass of the atom: the nucleus is thus a very dense object.

In 1919 Rutherford published the results of an other experiment, where  $\alpha$ -particles scattered off nitrogen atoms. He noticed that hydrogen nuclei were knocked out of the nitrogen nuclei [1]:

*We must conclude that the nitrogen atom is disintegrated under the intense forces developed in a close collision with a swift alpha particle, and that the hydrogen atom which is liberated formed a constituent part of the nitrogen nucleus.*

This experiment showed that the hydrogen nucleus is a building block of nuclei. At that time it was believed to be an elementary particle, just like the electron, and Rutherford called it the proton. This experiment is considered as the discovery of the proton.

Later on, in 1932, the neutron, the second building block of nuclei, was discovered by Chadwick. Both proton and neutron are collectively called nucleons. To explain  $\beta$ -decay yet another particle was necessary: the neutrino  $\nu_e$ . Around 1940 nuclear phenomena like their decay and excitation spectra could be understood using these four *elementary* particles.

Scattering experiments around 1950 showed that nucleons were not pointlike particles, but that they had an extended shape and in the late 1960s nucleon excited states were discovered. This meant that nucleons can no longer be considered as elementary particles and their building blocks, the quarks, are the *new* elementary particles. Apart from an electric charge, the

quarks also carry a color charge: they are labeled as red, green and blue. A single free quark has not been observed and all particles built from quarks (called hadrons) are colorless. The hadrons can be divided in two classes: mesons and baryons. Mesons are built from a quark and an antiquark with e.g. color charge red and anti-red to make it colorless particles. In baryons all three quarks carry a different color charge.

The electron and neutrino are examples of a different type of particles, called the leptons. At the present moment six quarks flavors and six different leptons have been observed. Quarks and leptons are, as far as we know, elementary particles: no excited states of quarks or leptons have been observed, yet.

The world of these elementary particles is governed by four forces: gravity, electromagnetic interaction, weak interaction and strong interaction. However, on the level of elementary particles gravity plays no important role. The weak interaction is responsible for e.g. the  $\beta$ -decay of nuclei. The electromagnetic and weak interaction are unified at high energies into the electroweak interaction. The strong interaction governs the interaction between the quarks. Its coupling constant increases when the distance between the involved particles increases. This phenomenon is called confinement and it is thought to be responsible for the fact that no colored particles have been observed. The interactions between the particles are described by the exchange of vector bosons: photons for the electromagnetic, Z and W bosons for the weak and gluons for the strong interaction.

The experiment described in this thesis can be situated at the border between nuclear and particle physics. The object under study is the proton whose structure is, ninety years after its discovery, still not completely understood. The proton is at the same time the smallest nucleus and a building block of other nuclei. Also the energy range of this experiment lies in between the typical energies of nuclear and particle physics experiments. The goal is to measure the generalized polarizabilities (GPs), which are global properties of the proton. They are of course sensitive to the quark structure of the proton, but the individual quarks are not resolved in this experiment. Only the collective behavior of the components of the proton is studied. The reaction mechanism used for this research is virtual Compton scattering below the pion production threshold, where a real photon is produced by the interaction of a virtual photon with the proton. Apart from the real photon no other particles are created in this reaction.

Virtual Compton scattering, the definition of the generalized polarizabilities and the framework used for the extraction of the GPs are described in chapter 2. Special attention goes to the physics interpretation behind these GPs.

A lot of models are available for the description of the nucleon structure at a low energy scale and the GPs have been calculated in several of these models. Chapter 3 gives an overview of the various models. A confrontation of the model predictions with real Compton scattering experiments and the three unpolarized VCS experiments performed up to now teaches

already a lot about the interplay between the components of the nucleon.

Chapter 4 focuses on the experimental setup of the first double-polarized VCS experiment ever, performed at the MAMI accelerator.

In the next chapter the Monte Carlo simulation, developed at the Ghent University is described. This Monte Carlo was used in analyses of previous VCS experiments and has been improved by implementing a more realistic description of the resolution effects in the focal plane detectors. The simulation is used to calculate the solid angle of the detection apparatus. It is a very important tool in understanding the physical processes taking place in the experiment.

When the information of the polarimeters is not used the data can be used to obtain unpolarized cross sections. The determination of the cross section and the extraction of linear combinations of GPs is discussed in chapter 6.

The preliminary analysis of the double-spin asymmetry is presented in chapter 7. The analysis allows the determination of an additional structure function.

Finally, an overview of the conclusions of this thesis can be found in chapter 8.



---

# Physics framework

---

Protons and neutrons are the lightest baryons. Both contain only up ( $u$  with electric charge  $+2/3$ ) and down ( $d$  with electric charge  $-1/3$ ) quarks as valence quarks: two  $u$  and one  $d$  quark for the proton and in the neutron one finds one  $u$  and two  $d$  quarks. The proton has an electrical charge  $+1$  and the neutron is electrically neutral. Their total mass is approximately  $940 \text{ MeV}/c^2$ . However, the mass of the three valence quarks contributes less than 3% to this total mass. The major part of the nucleon mass originates from the gluons, the gauge bosons of the strong interaction, and the sea quarks, virtual quark-antiquark pairs continuously being created and annihilated inside the nucleon.

All these constituents are bound together into an object with a radius of about 1 fm. A first interesting question one could ask is how these components are distributed inside this small volume of a few  $\text{fm}^3$ . Since all quarks are electrically charged, one could have a look at the distribution of charges and currents to get an idea of the position and motion of the quarks inside the nucleon. These distributions are described by the electromagnetic form factors of the nucleon, obtained in elastic electron scattering experiments (see section 2.1).

The next question might be: “How rigid is the nucleon?”, which is related to: “How strong are the constituents bound together?” This can be answered by measuring the deformation of the shape of the nucleon induced by an external force. An external electromagnetic field will influence the distributions of charges and currents inside the nucleon. As will be explained in section 2.2 the nucleon becomes polarized and hence the deformation is described by polarizabilities. Section 2.3 explains how these polarizabilities can be determined in real Compton scattering (RCS) experiments.

In the same way as the electric form factor generalizes the total charge of the nucleon by expressing how the charge is distributed as a function of the transverse position, the idea of polarizabilities can also be generalized. These new observables are called generalized polarizabilities (GPs) and they are sensitive to the spatial distribution of the polarizability inside

the nucleon. The GPs are experimentally accessed via virtual Compton scattering (VCS). The VCS reaction and its kinematics are described in section 2.4, while section 2.5 is devoted to the definition and interpretation of the GPs. Finally, the framework in which the VCS experiments below pion production threshold are analyzed is defined.

This chapter is mainly focused on the proton, although the concepts of form factors, polarizabilities and generalized polarizabilities apply to all compound particles. Experiments to measure these properties for the proton are easier to perform since the proton is a stable particle.

## 2.1 Form factors of the proton

The geometry of a microscopic object can be obtained from the elastic scattering of particles off the object under study. Elastic scattering is a clean process where both particles stay in their ground state and no other particles are created. The observed cross section depends on the interaction between the scattered particle and the scatterer and on the structure of both objects.

According to the de Broglie relation a wave can be associated to each particle. The relation between the wave length  $\lambda$  and the momentum  $q$  is given by Planck's constant  $h$ :

$$\lambda = \frac{h}{q}. \quad (2.1)$$

The larger the momentum, the smaller the wavelength becomes. To investigate the structure of an object, the wavelength of the projectile should be of the order of the dimension of the object.

Using electrons as projectiles to study the proton structure has several advantages. In the first place the electron is a pointlike particle, which means that the cross section depends only on the geometry of the proton. Secondly, the interaction of the electron with the constituents of the nucleon is well understood: quantum electrodynamics (QED) describes this interaction by the exchange of a virtual photon. The momentum of the virtual photon is given by the four-vector  $\mathbf{q} = \mathbf{k} - \mathbf{k}'$ , with  $\mathbf{k}$  and  $\mathbf{k}'$  the four-momenta of the incoming and scattered electron. The diagram of the scattering of an electron off the proton is depicted in figure 2.1: the electron  $e$  scatters off the proton  $p$  via the exchange of a virtual photon  $\gamma^*$ .

Unfortunately electron scattering experiments have some important drawbacks. The cross sections in such experiments are low due to the small coupling constant  $\alpha$  of the electromagnetic interaction and electrons are very light charged particles, thus they easily undergo radiative processes. The experimental data have to be corrected for these radiative effects.

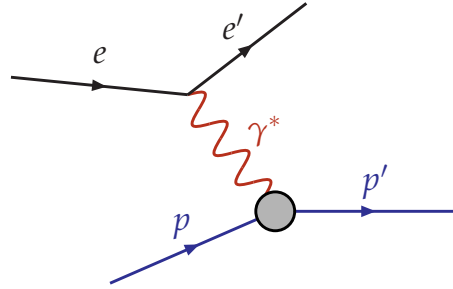


**Figure 2.1:** Diagram of the elastic scattering of an electron off a proton.

The interaction of an electron with a pointlike and spinless target is described by the Mott cross section, which includes the effects of the spin of the electron. The Mott cross section for the scattering of relativistic electrons ( $\beta = v/c \rightarrow 1$ , with  $v$  the velocity of the electron and  $c$  the speed of light in vacuum) on protons is given by (see eg. [2])

$$\left(\frac{d\sigma}{d\Omega}\right)_{\text{Mott}} = \left(\frac{2\alpha\hbar E'}{Q^2 c}\right)^2 \cdot \cos^2 \frac{\theta_e}{2} \cdot \frac{E'}{E}, \quad (2.2)$$

where  $Q^2 = -\mathbf{q}^2$ , the momentum transfer squared of the virtual photon.  $E$  ( $E'$ ) is the energy of the incoming (scattered) electron,  $\theta_e$  is the scattering angle of the electron in the laboratory system, and  $\hbar = h/2\pi$ . The scale of the observation is set by  $Q^2$  via the de Broglie relation. For sufficiently high  $Q^2$  the wavelength of the virtual photon  $\gamma^*$  is small enough to probe the internal structure of the proton.

The proton is a spin 1/2 particle with a substructure. The effect of the internal structure of the proton on the scattering cross section is described by the electric and magnetic form factors  $G_E^p(Q^2)$  and  $G_M^p(Q^2)$ :

$$\left(\frac{d\sigma}{d\Omega}\right) = \left(\frac{d\sigma}{d\Omega}\right)_{\text{Mott}} \left( \frac{G_E^{p2}(Q^2) + 2\tau G_M^{p2}(Q^2)}{1 + \tau} + 2\tau G_M^{p2}(Q^2) \tan^2 \frac{\theta_e}{2} \right), \quad (2.3)$$

where  $\tau = Q^2/4m_p^2 c^2$ , and  $m_p$  is the proton mass. This equation is known as the Rosenbluth formula [3].  $G_E^p(Q^2)$  and  $G_M^p(Q^2)$  can be obtained for a fixed value of  $Q^2$  by measuring the cross section at different scattering angles  $\theta_e$ . After dividing the obtained cross sections by the calculable Mott cross section a linear fit as a function of  $\tan^2 \theta_e/2$  yields  $G_E^p(Q^2)$  and  $G_M^p(Q^2)$ .

In the form factor the internal structure of the proton is encoded: the inverse Fourier transform of the form factors provides information about the radial distribution of charge and magnetic moments. These are accessible if the form factors are precisely measured over a sufficiently large range in momentum transfer.

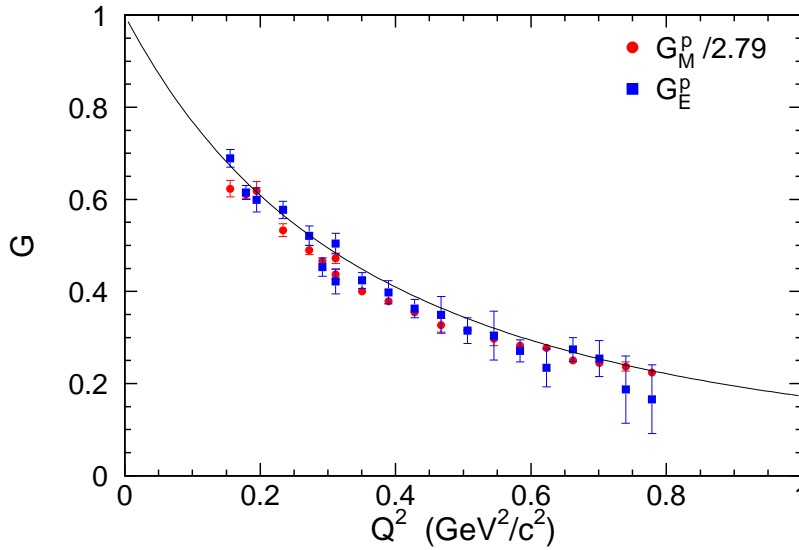


**Figure 2.2:** Electromagnetic form factors of the proton [4]. The full line represents  $G_D$ .

A special case is  $Q^2 = 0 \text{ MeV}^2/c^2$ :  $G_E^p$  becomes equal to 1, the charge of the proton and  $G_M^p$  reduces to the magnetic moment of the proton,  $\mu_p = 2.79$  in units of the nuclear magneton  $\mu_N = e\hbar/2m_p$ . The anomalous magnetic moment  $\kappa$  of the proton is defined as  $\mu_p - 1$ .

The behavior of the form factors  $G_E^p$  and  $G_M^p$  as a function of  $Q^2$  is very similar and can, in first approximation, be described by the dipole form factor  $G_D$  (see figure 2.2):

$$G_D(Q^2) = \left(1 + \frac{Q^2}{0.71(\text{GeV}/c)^2}\right)^{-2} = \frac{G_E^p(Q^2)}{1} = \frac{G_M^p(Q^2)}{2.79}. \quad (2.4)$$

This means that e.g. the charge distribution of the proton falls off exponentially: the proton is a sphere, but its surface is diffuse. To get an estimate of the size of the proton one can refer to the mean square radius. It can be found from the slope of  $G_E^p(Q^2)$  at  $Q^2 = 0 \text{ MeV}^2/c^2$ :  $\sqrt{\langle r_E^{p2} \rangle} = 0.847 \text{ fm}$  [5].

As of today the form factors have been measured over a wide range in  $Q^2$  and a lot of efforts have been made to find a good parameterization for the observed form factors. In the analysis of previous VCS experiments the form factors of Bosted *et al.* [6] and Höhler *et al.* [7] were used. In the current analysis more recent parameterizations are used: Mergell *et al.* [5] and Friedrich *et al.* [8]. The different parameterizations of  $G_E^p$  and  $G_M^p$  are shown in figure 2.3. The experimental uncertainties on the form factors have about the same magnitude as the differences between the different parameterizations.

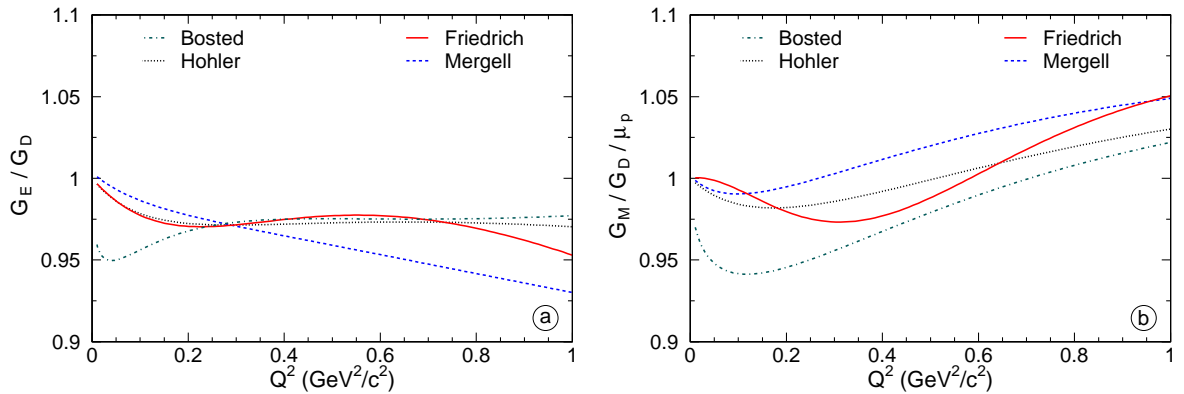


**Figure 2.3:** The parameterizations of the electric (a) and magnetic (b) form factor of the proton relative to the dipole form factor. The parameterizations have been taken from reference [6] (Bosted), [7] (Höhler), [5] (Mergell) and [8] (Friedrich).

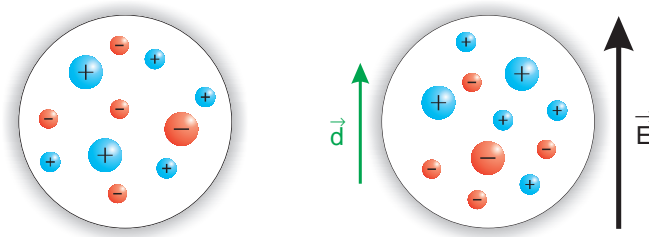


**Figure 2.4:** On the left the undistorted proton is shown: the large spheres represent the valence quarks; the small spheres represent the pions of the pion cloud. The external electric field  $\vec{E}$  pulls the charges inside the proton in opposite directions. The resulting electric dipole moment  $\vec{d}$  is proportional to the applied field. This is shown on the right.

## 2.2 Polarizabilities

The form factors parameterize the distribution of charges ( $G_E^p$ ) and currents ( $G_M^p$ ) inside the undistorted nucleon. In this section it is studied what happens if a nucleon is placed in an external electromagnetic field and the principle of polarizabilities is explained.

To this end, the following naïve model for the nucleon at a relatively large scale (small  $Q^2$ ) is considered: the nucleon consists of three valence quarks surrounded by a pion cloud. The valence quarks are charged and have an intrinsic magnetic moment, due to their spin. The pions are charged and they are treated as pointlike, spinless particles, which is a reasonable approximation at sufficiently low  $Q^2$ . On the left-hand side of figure 2.4 and 2.5 the proton is represented in this model.

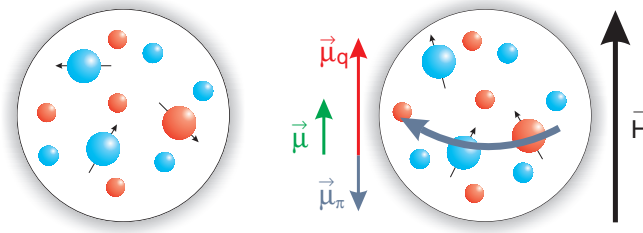


**Figure 2.5:** Similar as in figure 2.4, the undistorted proton is shown on the left. The intrinsic magnetic moments of the valence quarks are indicated by the arrows. On the right the proton is placed in an external magnetic field  $\vec{H}$ . The intrinsic magnetic moments of the valence quarks align with the applied field and a current is induced in the pion cloud, indicated by the arrow. Both effects give opposite contributions to the induced magnetic moment  $\vec{\mu}$ :  $\vec{\mu}_q$  and  $\vec{\mu}_\pi$ , respectively.

Due to an external electric field  $\vec{E}$  the charges inside the proton move in opposite directions: positive charges move in the direction of the electric field, whereas negative charges are pulled in the other direction. Initially, the centers of the distributions of positive and negative charges coincide, but placed in the field  $\vec{E}$  they become separated. This results in a electric dipole moment  $\vec{d}$ . The induced deformation of the charge distribution is proportional to the applied field. The proportionality factor between  $\vec{d}$  and  $\vec{E}$  is called the electric polarizability  $\alpha_E$ :

$$\vec{d} = \alpha_E \vec{E}. \quad (2.5)$$

The value of  $\alpha_E$  depends on the forces between the constituents of the nucleon: the stronger they are bound, the smaller the deformation for the same electric field, thus the smaller  $\alpha_E$ .

In the case of an applied magnetic field  $\vec{H}$  one must consider the contributions of the valence quarks and the pion cloud separately. The magnetic field will induce currents in the pion cloud, causing a diamagnetic magnetic moment  $\vec{\mu}_\pi$ , which weakens the magnetic field inside the nucleon. The intrinsic magnetic moments of the valence quarks, on the other hand, will become aligned with  $\vec{H}$ , yielding a paramagnetic contribution to the induced magnetic moment of the nucleon  $\vec{\mu}_q$ . For the total induced magnetic moment one can write a similar relation as for the induced electric moment, defining the magnetic polarizability of the nucleon  $\beta_M$ :

$$\vec{\mu} = \vec{\mu}_q + \vec{\mu}_\pi = (\beta_{\text{para}} + \beta_{\text{dia}}) \vec{H} = \beta_M \vec{H}. \quad (2.6)$$

More in general, one can describe the charge and current distributions inside the nucleon by the four-vector  $\mathbf{J} = (J^0/c, \vec{J})$ , where  $J^0(\mathbf{x})$  is the charge density and  $\vec{J}(\mathbf{x})$  the current vector at the space-time point  $\mathbf{x}$ . Due to the applied electromagnetic field  $\mathbf{A}^{\text{ext}}$  the charge and current

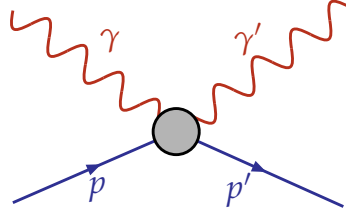


**Figure 2.6:** Schematic drawing of real Compton scattering. The incoming photon  $\gamma$  scatters off a proton  $p$ . After the reaction the scattered photon  $\gamma'$  and/or proton  $p'$  can be detected.

distributions will be modified:

$$\delta J^\mu(\mathbf{x}) = \int d^4\mathbf{y} P^{\mu\nu}(\mathbf{x}, \mathbf{y}) A_\nu^{\text{ext}}(\mathbf{y}). \quad (2.7)$$

The polarizability tensor  $P^{\mu\nu}$  generalizes the definitions of the polarizabilities defined above. It characterizes the capability of the constituents of the nucleon to rearrange themselves in response to a static or slowly varying external electromagnetic field.

### 2.3 Real Compton scattering

The polarizabilities  $\alpha_E$  and  $\beta_M$  of the proton can be measured via real Compton scattering (RCS). In RCS a real photon  $\gamma$  scatters off a proton  $p$  (see figure 2.6). The incident photon acts as an electromagnetic perturbation inducing a time dependence in  $\delta J^\mu$ . The latter causes an electromagnetic field, which is the final photon in the scattering process.

The three-momentum of the incident photon is denoted by  $\vec{q}$ ; the target proton is initially at rest and its three-vector is given by  $\vec{p} = \vec{0} \text{ MeV}/c$ . The three-vectors of the outgoing particles are defined by  $\vec{q}'$  and  $\vec{p}'$ , respectively. After the interaction the photon has scattered over an angle  $\theta_\gamma$  and  $\vec{p}' \neq \vec{0} \text{ MeV}/c$  due to the recoil of the proton. The kinematical variables are completely determined by the energy of the real photon<sup>1</sup>,  $q^0$ , and the scattering angle  $\theta_\gamma$ : the momenta and energies of  $\gamma'$  and  $p'$  can be expressed as a function of  $(q^0, \theta_\gamma)$ . For example for the energy of the outgoing photon,  $q'^0$  one finds (e.g. [2]):

$$q'^0 = \frac{q^0}{1 + \frac{q^0}{m_p}(1 - \cos \theta_\gamma)}. \quad (2.8)$$

<sup>1</sup> $q^0$  is the energy component of the four-vector  $\mathbf{q} = (q^0/c, \vec{q})$ .

Since the kinematics of the reaction are determined by  $(q^0, \theta_\gamma)$ , the cross section is a function of only these two kinematical variables, too. In figure 2.7 the cross section for RCS is shown as a function of  $q^0$  for  $\theta_\gamma = 135^\circ$ .

At low incident photon energies ( $q^0 \rightarrow 0$  MeV) the proton can be treated as a pointlike particle and the cross section can be described by the proton's static properties: its mass  $m_p$ , charge  $+e$  and anomalous magnetic moment  $\kappa$  [9]:

$$\begin{aligned} \frac{d\sigma^B}{d\Omega}(q^0, \theta_\gamma) = \frac{1}{2} \left( \frac{e^2}{m_p} \cdot \frac{q'^0}{q^0} \right)^2 \left\{ 1 + \cos^2 \theta_\gamma \right. \\ \left. + \frac{q^0 q'^0}{m_p^2} ([1 + \cos \theta_\gamma]^2 + a_0 + a_1 \cos \theta_\gamma + a_2 \cos^2 \theta_\gamma) \right\}, \end{aligned} \quad (2.9)$$

where

$$\begin{aligned} a_0 &= 2\kappa + \frac{9}{2}\kappa^2 + 3\kappa^3 + \frac{3}{4}\kappa^4, \\ a_1 &= -4\kappa - 5\kappa^2 - 2\kappa^3, \\ a_2 &= 2\kappa + \frac{1}{2}\kappa^2 - \kappa^3 - \frac{1}{4}\kappa^4. \end{aligned} \quad (2.10)$$

This formula is the so-called Born term to the cross section, also known as the Powell cross section. For  $\kappa = 0$  the Klein-Nishina formula [10] is obtained. This formula expresses the cross section for the scattering of photons on Dirac particles (pointlike, spin = 1/2), e.g. the electron or the proton at low  $q^0$ .

By increasing  $q^0$  the scale of the observation decreases and the process starts to be sensitive to the internal structure of the scatterer. The incoming photon deforms the proton, described by the polarizabilities  $\alpha_E$  and  $\beta_M$ . The induced deformation influences the scattering process and an extra term dependent on  $\alpha_E$  and  $\beta_M$  has to be included in the expression for the cross section<sup>2</sup>:

$$\begin{aligned} \frac{d\sigma}{d\Omega}(q^0, \theta_\gamma) = \frac{d\sigma^B}{d\Omega}(q^0, \theta_\gamma) \\ - q^0 q'^0 \left( \frac{q'^0}{q^0} \right)^2 \frac{e^2}{m_p} \left\{ \frac{\bar{\alpha}_E + \bar{\beta}_M}{2} (1 + \cos \theta_\gamma)^2 + \frac{\bar{\alpha}_E - \bar{\beta}_M}{2} (1 - \cos \theta_\gamma)^2 \right\} \end{aligned} \quad (2.11)$$

This formula, indicated by LEX in figure 2.7, is valid for  $q^0 \lesssim 80$  MeV. For higher energies the experimental cross section starts to deviate from equation (2.11) as can be observed in the figure. The approximation of the cross section up to the order  $q^0 q'^0$  in (2.11) is no longer valid and higher order terms have to be taken into account. In these higher order terms four further

---

<sup>2</sup>The polarizability  $\bar{\alpha}_E$  which is accessible in an experiment, contains the contribution from the electric polarizability plus retardation corrections and is therefore slightly different from  $\alpha_E$  (e.g. [11]).

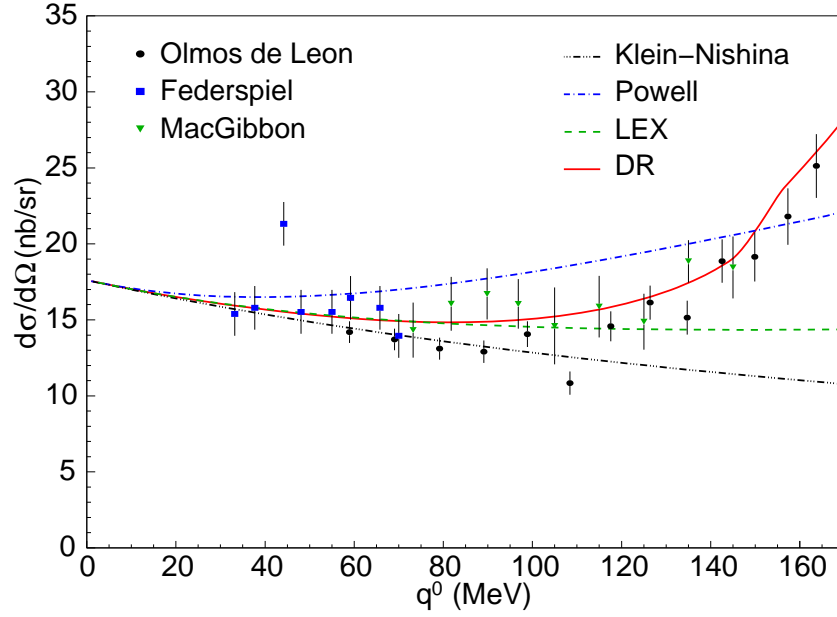


**Figure 2.7:** The differential cross section for real Compton scattering off the proton as a function of photon energy  $q^0$  at a fixed scattering angle  $\theta_\gamma = 135^\circ$ . The data points are taken from Olmos de Leon *et al.* [15], Federspiel *et al.* [16] and MacGibbon *et al.* [17]. The curves are explained in the text. (Taken from [18].)

polarizabilities  $\gamma_i$  ( $i = 1, 2, 3, 4$ ) appear [12]. One can also perform full calculations of the cross sections using dispersion relations (DR) [13] and [14] (see section 3.1.5).

A lot of effort has gone into measuring the cross section for real Compton scattering at low  $q^0$ , where equation (2.11) is valid. In figure 2.7 the results of relatively recent experiments [15], [16] and [17] are shown. The only unknown parameters in the cross section are  $\bar{\alpha}_E$  and  $\bar{\beta}_M$  and they appear as their sum and their difference. They can be determined by measuring the cross section at two different angles  $\theta_\gamma$ : the most interesting scattering angles are  $\theta_\gamma = 0^\circ$  and  $180^\circ$ , since then one of the two terms disappears due to the  $1 \pm \cos\theta_\gamma$ .

Baldin's sum rule [19] is very useful in the extraction of the polarizabilities from experimental data. This dispersion sum rule is an additional way of calculating  $\bar{\alpha}_E + \bar{\beta}_M$  and it reduces the uncertainty on the experimentally obtained values for  $\bar{\alpha}_E$  and  $\bar{\beta}_M$ . The sum rule is given by

$$\bar{\alpha}_E + \bar{\beta}_M = \frac{1}{2\pi} \int_{q_\pi^0}^{\infty} \frac{\sigma_\gamma(q^0)}{q^0{}^2} dq^0 = (13.8 \pm 0.4) \cdot 10^{-4} \text{ fm}^3, \quad (2.12)$$

where  $\sigma_\gamma(q^0)$  is the total photo-absorption cross section on the proton as a function of  $q^0$  and  $q_\pi^0$  is the threshold energy for  $\pi^0$  production. The value is taken from [15]. Other values for Baldin's sum rule have been reported in reference [20]:  $(13.69 \pm 0.14) \cdot 10^{-4} \text{ fm}^3$  and reference [21]:  $(14.0 \pm 0.3) \cdot 10^{-4} \text{ fm}^3$ .

The best global values for the polarizabilities are [15]:

$$\begin{aligned}\bar{\alpha}_E &= (12.1 \pm 0.3 \mp 0.4 \pm 0.3) \cdot 10^{-4} \text{ fm}^3, \\ \bar{\beta}_M &= (1.6 \pm 0.4 \pm 0.4 \pm 0.4) \cdot 10^{-4} \text{ fm}^3,\end{aligned}\tag{2.13}$$

where the error bars are the statistical, systematic and model dependent uncertainty of the analysis, respectively. The anti-correlated systematic error is caused by the uncertainty on the evaluation of Baldin's sum rule. This result is based on the low energy data of [15], [16], [17] and [22].  $\bar{\beta}_M$  is about 8 times smaller than  $\bar{\alpha}_E$ . This can be explained by the opposite sign of the para- and diamagnetic contributions,  $\bar{\beta}_{\text{para}}$  and  $\bar{\beta}_{\text{dia}}$ , to  $\bar{\beta}_M$ .

The (static) polarizabilities  $\bar{\alpha}_E$  and  $\bar{\beta}_M$  describe the nucleon's response to a static electromagnetic field, which corresponds to the limit  $q^0 \rightarrow 0$  MeV. Obviously, the RCS experiments are not performed at zero energy and therefore one needs to know the energy dependence of the nucleon structure parameters in order to extract the static properties of the nucleon. To this end dynamical polarizabilities were introduced, which are functions of the incident photon energy [23]. Using dispersion relation calculations these dynamical polarizabilities can be related to the static polarizabilities.

It is interesting to compare the electric and magnetic polarizabilities of the hydrogen atom with the polarizabilities of the nucleon. For hydrogen  $\alpha_E$  is of the order of the volume of the atom, but for the nucleon  $\alpha_E$  is  $4 \cdot 10^{-4}$  times its volume: the forces between the particles inside the nucleon, governed by the strong interaction, are much stronger than the electromagnetic interaction between the proton and the electron in hydrogen.

## 2.4 Virtual Compton scattering below pion threshold

### 2.4.1 Kinematics of VCS

In virtual Compton scattering (VCS) off the proton a virtual photon  $\gamma^*$  is absorbed by the proton  $p$  and a real photon  $\gamma$  is produced. This reaction can be accessed experimentally by the photon electroproduction reaction:  $e + p \rightarrow e' + p' + \gamma$  (see figure 2.8).

The incoming electron with three-momentum vector  $\vec{k}$  exchanges a virtual photon  $\gamma^*$  with momentum  $\vec{q}$  with the proton at rest.  $\vec{q}$  is given by  $\vec{k} - \vec{k}'$ , where  $\vec{k}'$  is the momentum vector of the outgoing electron. The electron scattering angle  $\theta_e$  is the angle between  $\vec{k}$  and  $\vec{k}'$ . Both vectors define the scattering plane.

The proton emits a real photon  $\gamma$  with momentum  $\vec{q}'$ . The momentum vector  $\vec{p}'$  of the recoiling proton and  $\vec{q}'$  define the reaction plane. Both planes contain the vector  $\vec{q}$ . The direction

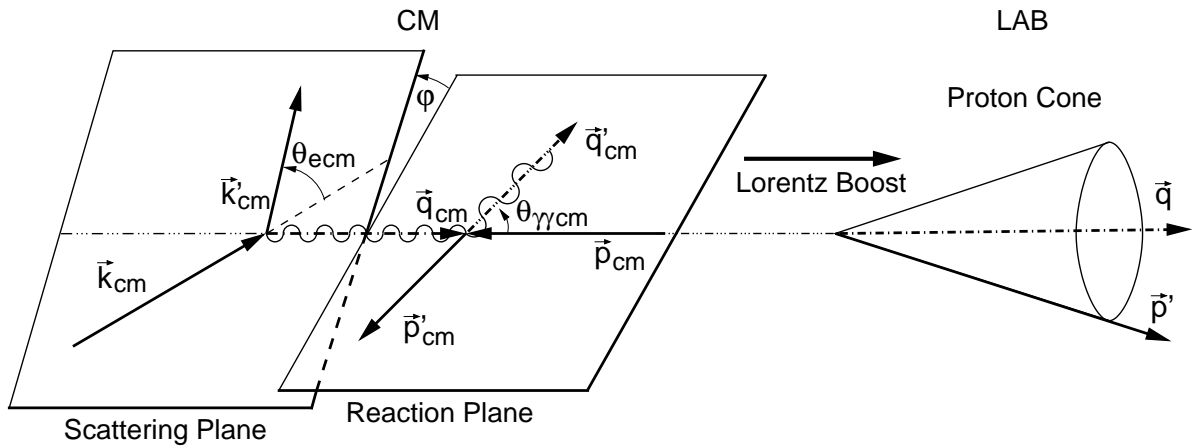


**Figure 2.8:** The VCS reaction: the electron scatters off the proton by exchange of a virtual photon. A real photon is produced in the interaction of the virtual photon and the incoming proton. On the left-hand side all variables are drawn in the center-of-mass of  $\gamma^*$  and  $p$ . In the laboratory system the proton is boosted on a cone around  $\vec{q}$  as shown on the right.

of the real photon in the center-of-mass (CM) system<sup>3</sup> of  $\gamma^*$  and  $p$  is determined by the angle between the two photons  $\theta_{\gamma\gamma\text{cm}}$  and the angle  $\varphi$  between the scattering plane and the reaction plane, as shown in figure 2.8.  $\varphi$  is defined equal to  $0^\circ$  when  $\vec{q}'$  lies in the scattering plane and points to the same side of  $\vec{q}$  as  $\vec{k}'$ . Its positive direction is indicated by the arrow in the figure. Note that this convention for  $\varphi$  is not in agreement with the usual convention in high-energy electron scattering experiments [24].

In the center-of-mass system,  $\gamma$  and  $p'$  move back-to-back. In the laboratory system (LAB) the recoiling proton is boosted in a (narrow) cone around  $\vec{q}$ , while  $\gamma$  can have any direction. This feature of the VCS kinematics makes it possible to cover a large range in  $\theta_{\gamma\gamma\text{cm}}$  by detecting the proton within the moderate solid angle of a high-resolution spectrometer.

In the context of this thesis, also the spin degrees of freedom are important. The helicities of the incoming and outgoing electrons are denoted by  $h$  and  $h'$  respectively.  $\lambda$  ( $\lambda'$ ) indicates the helicity of the virtual (real) photon and the spin projection of the initial (recoil) proton is  $\sigma$  ( $\sigma'$ ). Since the incoming electron is ultra-relativistic, its helicity does not change in the process:  $h = h'$  (see e.g. [25]).

The kinematics of the  $p(e, e' p')\gamma$  reaction is completely determined using the variables  $(k, k', \theta_e, \theta_{\gamma\gamma\text{cm}}, \varphi)$ , where  $k$  and  $k'$  are the moduli of  $\vec{k}$  and  $\vec{k}'$ . Based on the set  $(k, k', \theta_e, \theta_{\gamma\gamma\text{cm}}, \varphi)$  all

<sup>3</sup>Throughout this thesis all variables in the center-of-mass have an index cm; variables defined in the laboratory system have no index.

important parameters of the scattering process can be calculated, such as:

$$\begin{aligned}
 Q^2 &= 4kk' \sin^2\left(\frac{\theta_e}{2}\right), \\
 s &= -Q^2 + m_p^2 + 2m_p q^0, \\
 \varepsilon &= \left[1 + 2\frac{q^2}{Q^2} \tan^2\left(\frac{\theta_e}{2}\right)\right]^{-1},
 \end{aligned} \tag{2.14}$$

where  $\sqrt{s}$  is the total energy in the center-of-mass.  $\varepsilon$  is the linear polarization parameter for the virtual photon. Using  $s$  and  $Q^2$  the energies and the momenta of the particles in the center-of-mass are determined by:

$$\begin{aligned}
 q_{\text{cm}}^0 &= \frac{s - Q^2 - m_p^2}{2\sqrt{s}}, & q_{\text{cm}} &= \sqrt{Q^2 + q_{\text{cm}}^0{}^2}, \\
 q'_{\text{cm}}{}^0 &= \frac{s - m_p^2}{2\sqrt{s}}, & q'_{\text{cm}} &= q_{\text{cm}}^0, \\
 p_{\text{cm}}^0 &= \frac{s + Q^2 + m_p^2}{2\sqrt{s}}, & p_{\text{cm}} &= q_{\text{cm}}, \\
 p'_{\text{cm}}{}^0 &= \frac{s + m_p^2}{2\sqrt{s}}, & p'_{\text{cm}} &= q'_{\text{cm}}.
 \end{aligned} \tag{2.15}$$

Equations (2.14) and (2.15) show that there exists a one-to-one relation between  $(k, k', \theta_e)$  and  $(q_{\text{cm}}, q'_{\text{cm}}, \varepsilon)$ . Thus one can also use the variables  $(q_{\text{cm}}, q'_{\text{cm}}, \varepsilon, \theta_{\gamma\gamma\text{cm}}, \varphi)$  to define the kinematics of the VCS process. For the analysis of the data this last set of variables is used.

The reference frame of the center-of-mass  $\mathcal{R}_{\text{cm}}^r$  (shown in figure 2.9) is attached to the reaction plane [26]. The unit vectors  $(\hat{x}_{\text{cm}}^r, \hat{y}_{\text{cm}}^r, \hat{z}_{\text{cm}}^r)$  are defined in such a way that

$$\begin{aligned}
 \hat{z}_{\text{cm}}^r &= \frac{\vec{q}_{\text{cm}}}{q_{\text{cm}}}, \\
 \hat{y}_{\text{cm}}^r &= \frac{\vec{q}_{\text{cm}} \times \vec{q}'_{\text{cm}}}{q_{\text{cm}} q'_{\text{cm}} \sin \theta_{\gamma\gamma\text{cm}}}, \\
 \hat{x}_{\text{cm}}^r &= \hat{y}_{\text{cm}}^r \times \hat{z}_{\text{cm}}^r.
 \end{aligned} \tag{2.16}$$

## 2.4.2 Decomposition of the photon electroproduction amplitudes

The VCS process is characterized by an electron, a proton and a photon in the final state. In the Bethe-Heitler process a photon is emitted by the incident or outgoing electron and a final state is obtained with the same particles as in the case of VCS. Since both final states are identical, it is impossible to distinguish between these reactions in an experiment.

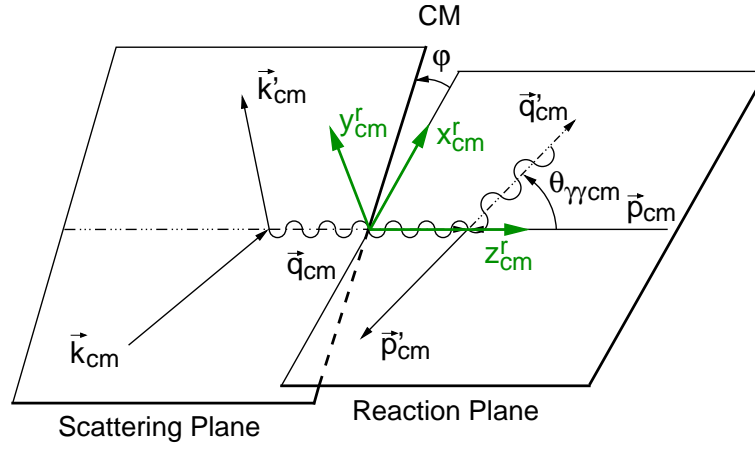


**Figure 2.9:** Definition of the center-of-mass reference frame  $\mathcal{R}_{\text{cm}}^r$  according to the definition of Guichon *et al.* [26].

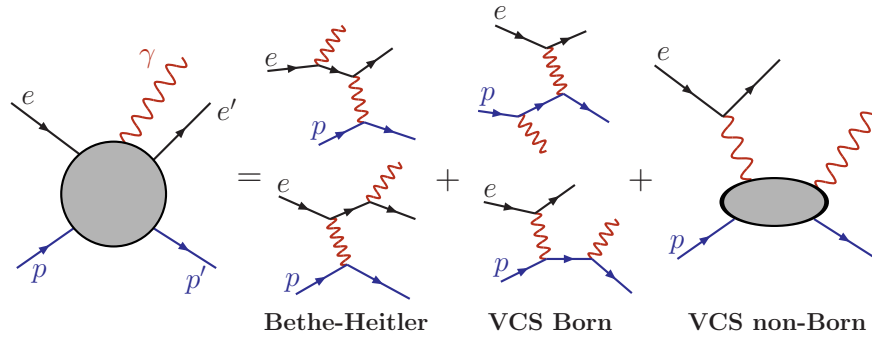


**Figure 2.10:** The  $ep \rightarrow e'p'\gamma$  reaction can be decomposed into three contributions: the Bethe-Heitler process and the full VCS process, which consists in its turn of two contributions: the Born and the non-Born term.

In quantum mechanics, the transition between the initial state and the final state of a scattering process is described by the scattering amplitudes. These amplitudes appear in the calculation of e.g. the cross section. The scattering amplitude for the photon electroproduction is denoted by  $T^{ee'\gamma}$ . Two different processes contribute to the  $p(e, e'p')\gamma$  reaction, and the matrix element  $T^{ee'\gamma}$  can be separated into two different terms:

$$T^{ee'\gamma} = T^{\text{FVCS}} + T^{\text{BH}}. \quad (2.17)$$

$T^{\text{FVCS}}$  corresponds to the (full) VCS process, where the photon is emitted by the proton, and  $T^{\text{BH}}$  is the amplitude of the Bethe-Heitler process. Figure 2.10 shows the diagrams contributing to the photon electroproduction reaction in the one-photon exchange approximation. The VCS process itself consists of two subprocesses, called VCS Born and VCS non-Born.

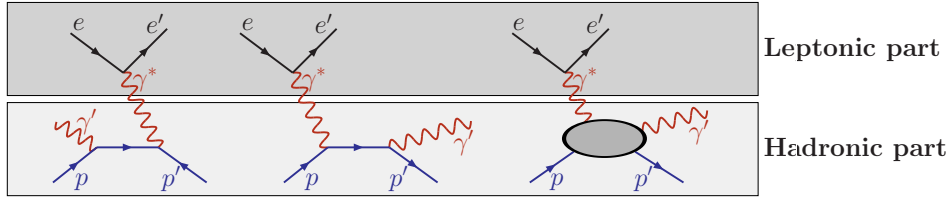


**Figure 2.11:** The full VCS reaction can be split in a leptonic and a hadronic part. The interaction of the virtual photon with the electron is the leptonic part and the scattering of the virtual photon on the proton is the hadronic part of the process.

The real photon in the Bethe-Heitler process appears due to bremsstrahlung of the incoming or outgoing electron: the reaction can be seen as elastic scattering off the proton, where the electron loses a part of its energy by bremsstrahlung before or after the scattering process. The emission of a photon by pointlike particles is well described in QED and the elastic scattering of electrons off the proton is known based on the form factors (see section 2.1). Since all ingredients of  $T^{\text{BH}}$  are known for a given parameterization of the proton form factors one can calculate this matrix element exactly.

The VCS Born term stands for the emission of a photon by the proton as if it was a rigid and non-deformable particle. Due to the momentum transfer of the virtual photon to the proton, the latter (which was initially at rest) is boosted and can emit a bremsstrahlung photon, since it is a charged particle. By this process the internal structure of the proton does not change; the photon is emitted due to the global motion of the proton. Just like the Bethe-Heitler process this VCS Born term contains  $G_E^p$  and  $G_M^p$ , and does not offer any new information about the structure of the proton.

The non-Born VCS term describes the absorption of the virtual photon by the proton and the real photon is emitted by the excited states of the proton. Below the pion production threshold there is not enough energy in the center-of-mass available for the production of such excited states, but they contribute virtually to the process as intermediate states. This non-Born term incorporates the unknown information about the proton.

The amplitude  $T^{\text{FVCS}}$  in formula (2.17) is unknown and contains the interesting part of the photon electroproduction process, but also the calculable VCS Born contribution. The interesting non-Born part can be separated from  $T^{\text{FVCS}}$  by remarking that the FVCS reaction consists of two sub processes: a leptonic and a hadronic interaction as indicated in figure 2.11. The emission of the virtual photon by the electron is described by a leptonic current (in this case an electron current), which produces the virtual photon. The second subprocess is the interaction of the virtual photon with the proton, producing a real photon. This is the pure VCS reaction ( $\gamma^* p \rightarrow \gamma p'$ ), which is described by the hadronic tensor,  $H^{\mu\nu}$ . The leptonic current is well-understood and therefore we focus on the hadronic part of the interaction.

The VCS tensor  $H^{\mu\nu}$  can be separated into a Born and a non-Born part:

$$H^{\mu\nu} = H_B^{\mu\nu} + H_{\text{NB}}^{\mu\nu}. \quad (2.18)$$

$H_B$  is the hadronic tensor of the VCS Born process and the tensor  $H_{\text{NB}}^{\mu\nu}$  describes the non-Born VCS process. Using the decomposition of the hadronic tensor, equation (2.17) becomes

$$T^{ee'\gamma} = T^{\text{BH}} + T^{\text{B}} + T^{\text{NB}}. \quad (2.19)$$

Here only the principle of splitting the scattering amplitude  $T^{ee'\gamma}$  into three contributions is explained. A detailed discussion can be found in [26]. There it is shown how gauge invariance is fulfilled for all three terms separately.

Observables like cross sections or asymmetries depend on the square of the matrix elements of the total photon electroproduction reaction, hence one should study the behavior of  $|T^{ee'\gamma}|^2$ :

$$\begin{aligned} |T^{ee'\gamma}|^2 &= |T^{\text{BH}}|^2 + |T^{\text{B}}|^2 + |T^{\text{NB}}|^2 \\ &+ (T^{\text{BH}*} T^{\text{B}} + T^{\text{BH}} T^{\text{B}*}) + (T^{\text{BH}*} T^{\text{NB}} + T^{\text{BH}} T^{\text{NB}*}) + (T^{\text{B}*} T^{\text{NB}} + T^{\text{B}} T^{\text{NB}*}). \end{aligned} \quad (2.20)$$

An electron emits photons much more easily than the proton does and therefore  $T^{\text{BH}}$  is the dominant term in expression (2.19). It is clear from formula (2.20) that the Bethe-Heitler process is responsible for the major contribution to  $|T^{ee'\gamma}|^2$  via the term  $|T^{\text{BH}}|^2$ , but also the interference of the Bethe-Heitler term with the VCS (Born and non-Born) terms is important: the Bethe-Heitler process interferes strongly with the VCS process. Actually, it is this interference that makes it possible to measure the VCS non-Born contribution to the photon electroproduction reaction.

### 2.4.3 Low energy theorem

In the previous section the scattering amplitude of the  $p(e, e' p')\gamma$  reaction was decomposed in three different components: Bethe-Heitler, VCS Born and VCS non-Born (see figure 2.10). According to the low energy theorem (LET), each of these contributions can be written as an expansion in powers of  $q'_{\text{cm}}$ . The aim of such an expansion is to reduce the complexity of the problem for low  $q'_{\text{cm}}$ : if  $q'_{\text{cm}}$  is small enough, then one can neglect the terms of the order  $q'_{\text{cm}}{}^2$ .

#### Bethe-Heitler amplitude

The scattering amplitude for the bremsstrahlung of low-energy photons by a pointlike spin 1/2 particle can be expanded in powers of  $q'_{\text{cm}}$ , starting from a term in  $q'_{\text{cm}}{}^{-1}$  [27]. The ampli-

tude for the Bethe-Heitler process can thus be written as

$$T^{\text{BH}} = \frac{a_{-1}^{\text{BH}}}{q'_{\text{cm}}} + a_0^{\text{BH}} + a_1^{\text{BH}} q'_{\text{cm}} + \mathcal{O}(q'_{\text{cm}}{}^2). \quad (2.21)$$

The matrix element of the Bethe-Heitler contribution can be calculated exactly, which means that all coefficients  $a_i^{\text{BH}}$  are known based on the parameterization of the form factors.

### VCS Born amplitude

In the VCS Born process the photon is emitted by the proton, due to its global motion: VCS Born is nothing more than bremsstrahlung by the proton. An expansion of the Born amplitude can be done in a similar way as for the Bethe-Heitler process:

$$T^{\text{B}} = \frac{a_{-1}^{\text{B}}}{q'_{\text{cm}}} + a_0^{\text{B}} + a_1^{\text{B}} q'_{\text{cm}} + \mathcal{O}(q'_{\text{cm}}{}^2). \quad (2.22)$$

The VCS Born amplitude does not contain any unknown information about the proton, which means that, just as for the Bethe-Heitler contribution, all the coefficients in equation (2.22) are known.

### VCS non-Born amplitude

According to a generalization of Low's theorem ([28] and [29]) for RCS to VCS [26] the VCS non-Born amplitude starts at a term in  $q'_{\text{cm}}$ :

$$T^{\text{NB}} = a_1^{\text{NB}} q'_{\text{cm}} + \mathcal{O}(q'_{\text{cm}}{}^2). \quad (2.23)$$

### Total photon electroproduction amplitude

Based on equation (2.19) and expressions (2.21), (2.22) and (2.23) one obtains the low energy expansion for the total photon electroproduction amplitude:

$$\begin{aligned} T^{e'e'\gamma} &= (a_{-1}^{\text{BH}} + a_{-1}^{\text{B}}) q'_{\text{cm}}{}^{-1} + (a_0^{\text{BH}} + a_0^{\text{B}}) + \left( (a_1^{\text{BH}} + a_1^{\text{B}}) + a_1^{\text{NB}} \right) q'_{\text{cm}} + \mathcal{O}(q'_{\text{cm}}{}^2) \\ &= a_{-1}^{\text{BH+B}} q'_{\text{cm}}{}^{-1} + a_0^{\text{BH+B}} + (a_1^{\text{BH+B}} + a_1^{\text{NB}}) q'_{\text{cm}} + \mathcal{O}(q'_{\text{cm}}{}^2). \end{aligned} \quad (2.24)$$

All coefficients in this equation are known, except  $a_1^{\text{NB}}$ , which appears in the term linear in  $q'_{\text{cm}}$ . In this way the low energy theorem gives a clear recipe to separate the trivial and non-trivial parts in the photon electroproduction amplitude. The trivial part consists of the well-

known Bethe-Heitler and Born processes, whereas the non-trivial part contains new information about the nucleon's internal structure.

## 2.5 Generalized polarizabilities

### 2.5.1 Multipole expansion of $H_{\text{NB}}$

In this section the unknown term  $H_{\text{NB}}^{\mu\nu}$  of equation (2.18) is studied.  $H_{\text{NB}}^{\mu\nu}$  depends on the variables  $(\vec{q}'_{\text{cm}}\sigma', \vec{q}_{\text{cm}}\sigma)$  and is responsible for the term  $a_1^{\text{NB}}q'_{\text{cm}}$  in equation (2.24). The goal is to develop a model-independent parameterization of  $H_{\text{NB}}^{\mu\nu}$  in which general laws like conservation of parity and angular momentum are embedded. For this reason the non-Born term is decomposed in multipoles in the center-of-mass frame.

The complete base of four-vectors,  $\mathbf{V}(\rho, L, M; \hat{k})$  ( $\rho = 0, \dots, 3$ ), for the decomposition is defined by

$$\begin{aligned}\mathbf{V}(0LM, \hat{k}) &= (Y_{LM}(\hat{k}), \vec{0}) , \\ \mathbf{V}(1LM, \hat{k}) &= (0, \vec{\mathcal{M}}_{LM}(\hat{k})) , \\ \mathbf{V}(2LM, \hat{k}) &= (0, \vec{\mathcal{E}}_{LM}(\hat{k})) , \\ \mathbf{V}(3LM, \hat{k}) &= (0, \vec{\mathcal{L}}_{LM}(\hat{k})) ,\end{aligned}\tag{2.25}$$

where

$$\begin{aligned}\vec{\mathcal{M}}_{LM}(\hat{k}) &= \vec{\mathcal{Y}}_{LM}^L(\hat{k}) , \\ \vec{\mathcal{E}}_{LM}(\hat{k}) &= \sqrt{\frac{L+1}{2L+1}} \vec{\mathcal{Y}}_{LM}^{L-1}(\hat{k}) + \sqrt{\frac{L}{2L+1}} \vec{\mathcal{Y}}_{LM}^{L+1}(\hat{k}) , \\ \vec{\mathcal{L}}_{LM}(\hat{k}) &= \sqrt{\frac{L}{2L+1}} \vec{\mathcal{Y}}_{LM}^{L-1}(\hat{k}) - \sqrt{\frac{L+1}{2L+1}} \vec{\mathcal{Y}}_{LM}^{L+1}(\hat{k})\end{aligned}\tag{2.26}$$

are the vector spherical harmonics. The vector functions  $\vec{\mathcal{Y}}_{LM}^L(\hat{k})$ , are defined using the spherical harmonics,  $Y_{lm}(\hat{k})$  (see e.g. [30]):

$$\vec{\mathcal{Y}}_{LM}^l(\hat{k}) = \sum_{\lambda\mu} \langle l\lambda, 1\mu | LM \rangle Y_{l\lambda}(\hat{k}) \vec{e}(\mu) .\tag{2.27}$$

Using the base four-vectors  $\mathbf{V}(\rho, L, M; \hat{k})$  the tensor  $H_{\text{NB}}^{\mu\nu}(\vec{q}'_{\text{cm}}\sigma', \vec{q}_{\text{cm}}\sigma)$  is decomposed in reduced multipoles,  $H_{\text{NB}}^{(\rho'L', \rho L)S}(q_{\text{cm}}, q'_{\text{cm}})$ .  $L$  and  $L'$  represent the angular momentum of the initial and final electromagnetic transition and  $S$  indicates whether there is a spin-flip transition of the nucleon ( $S = 1$ ) or not ( $S = 0$ ).  $\rho$  and  $\rho'$  parameterize the type of the multipole of the photons and they can take four values: ( $\rho = 0$ ) charge, ( $\rho = 1$ ) magnetic, ( $\rho = 2$ ) electric and

( $\rho = 3$ ) longitudinal. Due to gauge invariance the charge and longitudinal multipole type are not independent and one can eliminate the multipoles with  $\rho = 3$  and  $\rho' = 3$  [31].

The reduced multipoles are defined by

$$\begin{aligned}
& H_{\text{NB}}^{(\rho'L',\rho L)S}(q'_{\text{cm}}, q_{\text{cm}}) \\
&= \frac{1}{4\pi\mathcal{N}} \frac{1}{2S+1} \sum_{\sigma\sigma'M'M} (-1)^{\frac{1}{2}+\sigma'+L+M} \langle \frac{1}{2} - \sigma', \frac{1}{2}\sigma | S_S \rangle \langle L'M', L-M | S_S \rangle \\
& \int d\hat{q}'_{\text{cm}} d\hat{q}_{\text{cm}} V_{\mu}^*(\rho'L'M', \hat{q}'_{\text{cm}}) H_{\text{NB}}^{\mu\nu}(\vec{q}'_{\text{cm}}\sigma', \vec{q}_{\text{cm}}\sigma) V_{\nu}(\rho LM, \hat{q}_{\text{cm}}),
\end{aligned} \tag{2.28}$$

where the normalization factor  $\mathcal{N}$  is given by:

$$\mathcal{N} = 2\sqrt{p_{\text{cm}}^0 p'_{\text{cm}}{}^0}. \tag{2.29}$$

As can be seen in the definition of  $H_{\text{NB}}^{(\rho'L',\rho L)S}$  the dependence on the spin of the proton is removed by the summation over  $\sigma$  and  $\sigma'$  and reduced to a change in the proton spin between initial and final state given by  $S$ . In a similar way the angular dependence of the two photons is reduced via the integral over  $d\hat{q}'_{\text{cm}} d\hat{q}_{\text{cm}}$ .

The number of multipoles in the expansion can be reduced using general conservation laws of the electromagnetic interaction:

$$\begin{aligned}
& \text{Conservation of angular momentum: } |L' - S| \leq L \leq L' + S \quad (S = 0, 1), \\
& \text{Conservation of parity: } (-1)^{\rho'+L'} = (-1)^{\rho+L} \quad (\rho, \rho' = 0, 1, 2).
\end{aligned} \tag{2.30}$$

The total angular momentum of the intermediate state of the proton  $J$  equals  $(L \pm \frac{1}{2}) = (L' \pm \frac{1}{2})$ .  $L$  and  $L'$  can have any positive integer value. The multipoles vanish for  $L = L' = 0$ , and for  $L = 0$  only  $\rho = 0$  is possible.

For the real photon there exists an additional relation between the different types of each of the multipoles, which decreases the number of possible values of  $\rho'$ :  $\rho' = 1, 2$  [31]: a real photon can only be created via a transverse transition.

## 2.5.2 Definition of the generalized polarizabilities

For VCS below pion threshold only the low energy behavior of the multipoles is important. The lowest order in  $q'_{\text{cm}}$  and  $q_{\text{cm}}$  of the multipoles  $H_{\text{NB}}^{(\rho'L',\rho L)S}(q'_{\text{cm}}, q_{\text{cm}})$  is  $q'_{\text{cm}}{}^{L'} q_{\text{cm}}{}^L$ : at small  $(q'_{\text{cm}}, q_{\text{cm}})$  the multipoles behave like  $q'_{\text{cm}}{}^{L'} q_{\text{cm}}{}^L$  [31]. The most interesting part of  $H_{\text{NB}}^{\mu\nu}$  is the linear term in its expansion, which gives rise to  $a_1^{\text{NB}} q'_{\text{cm}}$  in equation (2.24). Clearly this part must come from the lowest order multipoles  $L' = 1$ . One can find 10 multipoles with  $L' = 1$ ,

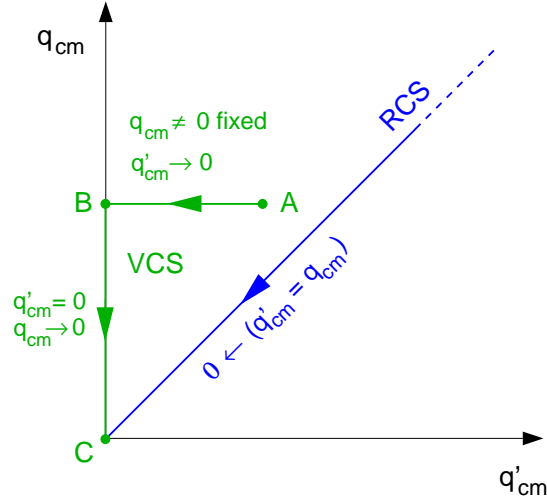


**Figure 2.12:** In RCS the origin of the  $(q'_{\text{cm}}, q_{\text{cm}})$  plane is reached along the  $(q'_{\text{cm}} = q_{\text{cm}})$  line. For VCS a different path is taken. (Taken from [32].)

fulfilling the selection rules given in section 2.5.1:

$$\begin{aligned}
 3 \text{ scalar multipoles } (S = 0): & \quad H_{\text{NB}}^{(11,11)0}, H_{\text{NB}}^{(21,01)0}, H_{\text{NB}}^{(21,21)0}, \\
 7 \text{ spin-dependent multipoles } (S = 1): & \quad H_{\text{NB}}^{(11,00)1}, H_{\text{NB}}^{(11,02)1}, H_{\text{NB}}^{(11,22)1}, \\
 & \quad H_{\text{NB}}^{(11,11)1}, H_{\text{NB}}^{(21,01)1}, H_{\text{NB}}^{(21,21)1}, H_{\text{NB}}^{(21,12)1}.
 \end{aligned} \tag{2.31}$$

For each of the 10 multipoles in (2.31) one can define a generalized polarizability (GP) denoted by  $P^{(\rho'L',\rho L)S}(q_{\text{cm}})$ :

$$P^{(\rho'L',\rho L)S}(q_{\text{cm}}) = \lim_{q'_{\text{cm}} \rightarrow 0} \left( \frac{1}{q'_{\text{cm}}{}^{L'} q_{\text{cm}}{}^L} H_{\text{NB}}^{(\rho'L',\rho L)S}(q'_{\text{cm}}, q_{\text{cm}}) \right), \tag{2.32}$$

to describe the low  $q'_{\text{cm}}$  behavior of the non-Born VCS amplitude. The GPs are a function of  $q_{\text{cm}}$ , as is indicated in equation (2.32).

Unfortunately this definition causes problems for some of the multipoles if one wants to compare the GPs to the polarizabilities obtained in RCS for  $(q'_{\text{cm}}, q_{\text{cm}}) \rightarrow (0,0)$  MeV/c (see figure 2.12). The origin of the  $(q'_{\text{cm}}, q_{\text{cm}})$  plane is reached along the  $(q'_{\text{cm}} = q_{\text{cm}})$  line in RCS. For VCS first the limit  $q'_{\text{cm}} \rightarrow 0$  MeV/c is taken for fixed  $q_{\text{cm}}$ , by definition of the GPs. This is the line AB in the figure. Afterwards one can go to the origin by taking  $q_{\text{cm}} \rightarrow 0$  MeV/c (line BC). The path followed to approach the origin of the  $(q'_{\text{cm}}, q_{\text{cm}})$  plane is different for both processes. To compare the GPs to the polarizabilities it is important that the limit  $(q'_{\text{cm}}, q_{\text{cm}}) \rightarrow (0,0)$  MeV/c is independent of the followed path. It has been shown that for  $\rho(\rho') = 0$  or  $\rho(\rho') = 1$  both limits are the same [26]. For  $\rho(\rho') = 2$  this is not the case.

GP	Electromagnetic transition	Excited state of the proton	Polarizability (RCS)
$P^{(\rho'L',\rho L)S}(q_{\text{cm}})$	$(\gamma^* \rightarrow \gamma)$	$J^P$	$(Q^2 \rightarrow 0)$
$P^{(01,01)0}(q_{\text{cm}})$	E1 $\rightarrow$ E1	$\frac{1}{2}^-$ or $\frac{3}{2}^-$	$-\frac{4\pi}{e^2} \sqrt{\frac{2}{3}} \bar{\alpha}_E$
$P^{(11,11)0}(q_{\text{cm}})$	M1 $\rightarrow$ M1	$\frac{1}{2}^+$ or $\frac{3}{2}^+$	$-\frac{4\pi}{e^2} \sqrt{\frac{8}{3}} \bar{\rho}_M$
$P^{(01,01)1}(q_{\text{cm}})$	E1 $\rightarrow$ E1	$\frac{1}{2}^-$ or $\frac{3}{2}^-$	0
$P^{(11,11)1}(q_{\text{cm}})$	M1 $\rightarrow$ M1	$\frac{1}{2}^+$ or $\frac{3}{2}^+$	0
$P^{(01,12)1}(q_{\text{cm}})$	M2 $\rightarrow$ E1	$\frac{3}{2}^-$	$-\frac{4\pi}{e^2} \frac{\sqrt{2}}{3} \gamma_3$
$P^{(11,02)1}(q_{\text{cm}})$	E2 $\rightarrow$ M1	$\frac{3}{2}^+$	$-\frac{4\pi}{e^2} \sqrt{\frac{8}{27}} (\gamma_2 + \gamma_4)$

**Table 2.1:** The six independent generalized polarizabilities and their properties.

One can overcome this problem by expressing the multipoles with  $\rho' = 2$  using the Siegert relation [33] applied to VCS:

$$H_{\text{NB}}^{(2L',\rho L)S}(q'_{\text{cm}}, q_{\text{cm}}) = -\sqrt{\frac{L'+1}{L'}} \frac{q'_{\text{cm}}}{q_{\text{cm}}} H_{\text{NB}}^{(0L',\rho L)S}(q'_{\text{cm}}, q_{\text{cm}}) + \mathcal{O}(q'_{\text{cm}}^{L'+1}). \quad (2.33)$$

This formula relates the low  $q'_{\text{cm}}$  behavior of the multipoles with  $\rho' = 2$  to that for the ones with  $\rho' = 0$  and in this way one can replace the multipoles ( $H_{\text{NB}}^{(21,01)0}$ ,  $H_{\text{NB}}^{(21,01)1}$ ,  $H_{\text{NB}}^{(21,12)1}$ ) by ( $H_{\text{NB}}^{(01,01)0}$ ,  $H_{\text{NB}}^{(01,01)1}$ ,  $H_{\text{NB}}^{(01,12)1}$ ) in the definition (2.32) of the GPs.

Then one still has to deal with  $H_{\text{NB}}^{(21,21)0}$ ,  $H_{\text{NB}}^{(11,22)1}$  and  $H_{\text{NB}}^{(21,21)1}$ . Due to charge conjugation in combination with nucleon crossing symmetry the low energy behavior of only two of the scalar multipoles is independent [34]. One has to define only 2 GPs based on the three scalar multipoles and one can avoid the definition of  $P^{(21,21)0}$ . In this way the problem with the corresponding multipole does not occur. Similarly the difficulties with  $H_{\text{NB}}^{(11,22)1}$  and  $H_{\text{NB}}^{(21,21)1}$  can be avoided, since there are only 4 independent GPs with  $S = 1$  [35]. The six remaining GPs and their properties are listed in table 2.1 and they are defined by applying equation (2.32) to:

$$\begin{aligned} & 2 \text{ scalar multipoles: } H_{\text{NB}}^{(01,01)0}, H_{\text{NB}}^{(11,11)0}, \\ & 4 \text{ spin-dependent multipoles: } H_{\text{NB}}^{(01,01)1}, H_{\text{NB}}^{(11,11)1}, H_{\text{NB}}^{(01,12)1}, H_{\text{NB}}^{(11,02)1}. \end{aligned} \quad (2.34)$$

In the limit ( $q_{\text{cm}} \rightarrow 0 \text{ MeV}/c$ ) one finds (linear combinations of) the polarizabilities, obtained by RCS, for 4 of the GPs as is indicated in table 2.1.

### 2.5.3 Interpretation of the generalized polarizabilities

The relation between the wavelength of a photon and its momentum is given by the de Broglie relation (see equation (2.1)): the lower the momentum of a photon, the larger its wavelength. If the momentum is low enough, the wavelength can be larger than the dimensions of the nucleon. On the scale of the nucleon the photon can then be seen as an electromagnetic field constant in time and space.

One can interpret virtual Compton scattering below pion threshold as electron scattering off the nucleon, placed in the field of the outgoing photon [31]: the real photon of the VCS reaction plays the role of the external applied field and VCS can be considered as elastic electron scattering on a target placed between the plates of a capacitor or between the poles of a magnet. The size of the perturbation is set by the momentum of the real photon: the stronger the external field, the larger the deformation of the proton.

This equivalence can be used to interpret the two contributions to the full VCS scattering amplitude (see section 2.4.2). A proton, placed in an electromagnetic field, will not only undergo a modification of its internal structure, described by  $\delta J^\mu$  in equation (2.7). The electromagnetic field will also cause a global motion of the proton, without changing its internal structure. This global motion of the proton is described by the Born term. The modification of  $J^\mu$  is contained in the non-Born.

The GPs parameterize the scattering amplitude of the non-Born VCS term, thus they quantify the deformation of the nucleon due to the external field, which is in lowest order linear to the applied field. The GPs are in this sense similar to the polarizabilities obtained in real Compton scattering. However, in RCS the incident photon is real and it fulfills  $\mathbf{q}^2 = 0$  (MeV/c)<sup>2</sup> or  $q^0 = q$ , since the photon is a massless particle. For the virtual photon  $\mathbf{q}^2 = -Q^2 \neq 0$  (MeV/c)<sup>2</sup>.  $q^0$  and  $q$  are independent and a virtual photon can be longitudinally polarized, too. There is an additional degree of freedom, which appears as the dependence of the GPs on  $Q^2$ : the GPs are a generalization of the polarizabilities obtained in real Compton scattering. By taking the real-photon limit  $Q^2 \rightarrow 0$  MeV<sup>2</sup>/c<sup>2</sup>, one obtains the polarizabilities of RCS.

Using electron scattering one can measure the Fourier transform of the charge and current distributions inside the nucleon. These form factors are functions of  $Q^2$ , where  $Q^2$  sets the distance scale of the observation. In the case of VCS these distributions are deformed by the external field of the outgoing photon and the process is sensitive to the form factors of the polarized nucleon: the GPs measure the spatial distribution of the polarizability inside the nucleon with a distance scale set by  $Q^2$  [36].

## 2.6 Observables of VCS in threshold experiments

The physical observables of the  $p(e, e' p')\gamma$  reaction are cross sections and asymmetries. The advantage of asymmetries is that they are measured via ratios of count rates, thus they are less sensitive to normalization effects. The GPs enter in these observables in specific linear combinations: the structure functions of VCS.

### 2.6.1 Structure functions

Based on the six independent GPs, six independent structure functions can be defined. They are given by [31]

$$\begin{aligned}
P_{LL}(q_{\text{cm}}) &= -2\sqrt{6}m_p G_E^p(\tilde{Q}^2) P^{(01,01)0}(q_{\text{cm}}) , \\
P_{TT}(q_{\text{cm}}) &= -3G_M^p(\tilde{Q}^2) \frac{q_{\text{cm}}^2}{\tilde{q}_{\text{cm}}^0} \left( P^{(11,11)1}(q_{\text{cm}}) - \sqrt{2}\tilde{q}_{\text{cm}}^0 P^{(01,12)1}(q_{\text{cm}}) \right) , \\
P_{LT}(q_{\text{cm}}) &= \sqrt{\frac{3}{2}} \frac{m_p q_{\text{cm}}}{\tilde{Q}} G_E^p(\tilde{Q}^2) P^{(11,11)0}(q_{\text{cm}}) + \frac{3}{2} \frac{q_{\text{cm}} \tilde{Q}}{\tilde{q}_{\text{cm}}^0} G_M^p(\tilde{Q}^2) P^{(01,01)1}(q_{\text{cm}}) , \\
P_{LT}^z(q_{\text{cm}}) &= \frac{3}{2} \frac{q_{\text{cm}} \tilde{Q}}{\tilde{q}_{\text{cm}}^0} G_M^p(\tilde{Q}^2) P^{(01,01)1}(q_{\text{cm}}) - 3 \frac{m_p q_{\text{cm}}}{\tilde{Q}} G_E^p(\tilde{Q}^2) P^{(11,11)1}(q_{\text{cm}}) , \\
P_{LT}'^z(q_{\text{cm}}) &= -\frac{3}{2} \tilde{Q} G_M^p(\tilde{Q}^2) P^{(01,01)1}(q_{\text{cm}}) + 3 \frac{m_p q_{\text{cm}}^2}{\tilde{Q} \tilde{q}_{\text{cm}}^0} G_E^p(\tilde{Q}^2) P^{(11,11)1}(q_{\text{cm}}) , \\
P_{LT}'^\perp(q_{\text{cm}}) &= \frac{3}{2} \frac{q_{\text{cm}} \tilde{Q}}{\tilde{q}_{\text{cm}}^0} G_M^p(\tilde{Q}^2) \left( P^{(01,01)1}(q_{\text{cm}}) - \sqrt{\frac{3}{2}} \tilde{q}_{\text{cm}}^0 P^{(11,02)1}(q_{\text{cm}}) \right) .
\end{aligned} \tag{2.35}$$

In some of the VCS matrix elements combinations of structure functions appear. To simplify the mathematical expressions of these matrix elements, three additional structure functions dependent on the structure functions in equations (2.35) are defined (with  $R = 2m_p/\tilde{Q}$ ):

$$\begin{aligned}
P_{LT}'^\perp(q_{\text{cm}}) &= \frac{R G_E^p(\tilde{Q}^2)}{2 G_M^p(\tilde{Q}^2)} P_{TT}(q_{\text{cm}}) - \frac{G_M^p(\tilde{Q}^2)}{2 R G_E^p(\tilde{Q}^2)} P_{LL}(q_{\text{cm}}) , \\
P_{TT}'^\perp(q_{\text{cm}}) &= \frac{G_M^p(\tilde{Q}^2)}{R G_E^p(\tilde{Q}^2)} (P_{LT}'^z(q_{\text{cm}}) - P_{LT}(q_{\text{cm}})) , \\
P_{TT}'^\perp(q_{\text{cm}}) &= \frac{G_M^p(\tilde{Q}^2)}{R G_E^p(\tilde{Q}^2)} (P_{LT}'^z(q_{\text{cm}}) + \frac{\tilde{q}_{\text{cm}}^0}{q_{\text{cm}}} P_{LT}(q_{\text{cm}})) .
\end{aligned} \tag{2.36}$$

The quantities with a tilde are the values of the variables in the limit  $q'_{\text{cm}} \rightarrow 0$  MeV/c. The equations (2.15) imply:

$$\begin{aligned}\tilde{q}_{\text{cm}}^0 &= m_p - \sqrt{m_p^2 + q_{\text{cm}}^2}, \\ \tilde{Q}^2 &= -2m_p \tilde{q}_{\text{cm}}^0.\end{aligned}\tag{2.37}$$

## 2.6.2 Unpolarized cross section

The unpolarized five-fold differential cross section for the photon electroproduction process is differential in  $k'$ ,  $\hat{k}'$  and  $q'_{\text{cm}}$ . As stated above, the cross section below the pion threshold is dominated by the BH+B cross section. The goal of the experiment is to determine the deviation of the measured cross section from the BH+B cross section.

The unpolarized cross section for the photon electroproduction process can be written as

$$\frac{d^5\sigma}{dk'd\Omega_{k'}d\Omega_{q'_{\text{cm}}}} = \frac{(2\pi)^5 k'}{64m_p k} \frac{2q'_{\text{cm}}}{\sqrt{s}} \mathcal{M} = \phi q'_{\text{cm}} \mathcal{M},\tag{2.38}$$

where the phase space factor,  $\phi$ , is given by

$$\phi = \frac{(2\pi)^5 k'}{32m_p k} \frac{1}{\sqrt{s}}.\tag{2.39}$$

$\mathcal{M}$  is the probability of the interaction. For the unpolarized cross section one has to average the scattering amplitude  $T^{ee'\gamma}$  over all possible initial spin states of the incoming particles and sum over the spin states of the final particles:

$$\mathcal{M} = \frac{1}{4} \sum_{\sigma\sigma'h\lambda'} |T^{ee'\gamma}|^2.\tag{2.40}$$

Using equation (2.24) one can formally rewrite equation (2.38) for low  $q'_{\text{cm}}$  as

$$\begin{aligned}d^5\sigma &= \phi q'_{\text{cm}} \left| (a_{-1}^{\text{BH+B}} q'_{\text{cm}}{}^{-1} + a_0^{\text{BH+B}} + a_1^{\text{BH+B}} q'_{\text{cm}}) + a_1^{\text{NB}} q'_{\text{cm}} \right|^2 + \mathcal{O}(q'_{\text{cm}}{}^2) \\ &= \phi q'_{\text{cm}} \underbrace{\left| (a_{-1}^{\text{BH+B}} q'_{\text{cm}}{}^{-1} + a_0^{\text{BH+B}} + a_1^{\text{BH+B}} q'_{\text{cm}}) \right|^2}_{\mathcal{M}^{\text{BH+B}}} \\ &\quad + \phi q'_{\text{cm}} \underbrace{(a_{-1}^{\text{BH+B}} a_1^{\text{NB}*} + a_{-1}^{\text{BH+B}*} a_1^{\text{NB}})}_{\mathcal{M}_0^{\text{NB}}} + \mathcal{O}(q'_{\text{cm}}{}^2),\end{aligned}\tag{2.41}$$

where  $d^5\sigma$  is a short-hand notation for  $\frac{d^5\sigma}{dk'd\Omega_{k'}d\Omega_{q'_{\text{cm}}}}$ . In this expression the assumption is made that  $T^{ee'\gamma}$  is independent of the spin states of the involved particles. This does not influence

the general result: the non-Born term appears as a term linear in  $q'_{\text{cm}}$  in the expression of the cross section.

The five-fold differential photon electroproduction cross section, which includes the effect of the GPs, can be written in the LET approximation as

$$d^5\sigma = d^5\sigma^{\text{BH+B}} + \phi q'_{\text{cm}} \mathcal{M}_0^{\text{NB}} + \mathcal{O}(q'^2_{\text{cm}}), \quad (2.42)$$

where

$$d^5\sigma^{\text{BH+B}} = \phi q'_{\text{cm}} \mathcal{M}^{\text{BH+B}}. \quad (2.43)$$

Since the differential cross section for the Bethe-Heitler + Born process can be calculated exactly, it is possible to determine  $\mathcal{M}_0^{\text{NB}}$  by measuring the unpolarized cross section of the photon electroproduction reaction.  $\mathcal{M}_0^{\text{NB}}$  contains the GPs and it is the lowest order interference term of the Bethe-Heitler + Born and the non-Born contributions to the reaction. The term can be written as a function of 3 structure functions [26]<sup>4</sup>:  $P_{\text{LL}}$ ,  $P_{\text{TT}}$  and  $P_{\text{LT}}$ .

$$\begin{aligned} \mathcal{M}_0^{\text{NB}} = 2K_2 \left\{ v_1 [\varepsilon P_{\text{LL}}(q_{\text{cm}}) - P_{\text{TT}}(q_{\text{cm}})] \right. \\ \left. + (v_2 - \frac{\tilde{q}_{\text{cm}}^0}{q_{\text{cm}}} v_3) \sqrt{2\varepsilon(1+\varepsilon)} P_{\text{LT}}(q_{\text{cm}}) \right\}, \end{aligned} \quad (2.44)$$

where  $K_2$  is defined by

$$K_2 = e^6 \frac{q_{\text{cm}}}{\tilde{Q}^2} \frac{2m_p}{1-\varepsilon} \sqrt{\frac{2E_q}{E_q + m_p}}, \quad \text{with} \quad E_q = \sqrt{m_p^2 + q_{\text{cm}}^2}. \quad (2.45)$$

The angle dependent kinematical coefficients in expression (2.44) are defined by

$$\begin{aligned} v_1 &= \sin \theta_{\gamma\gamma\text{cm}} (\omega'' \sin \theta_{\gamma\gamma\text{cm}} - k_{\text{T}} \omega' \cos \theta_{\gamma\gamma\text{cm}} \cos \varphi), \\ v_2 &= -(\omega'' \sin \theta_{\gamma\gamma\text{cm}} \cos \varphi - k_{\text{T}} \omega' \cos \theta_{\gamma\gamma\text{cm}}), \\ v_3 &= -(\omega'' \sin \theta_{\gamma\gamma\text{cm}} \cos \theta_{\gamma\gamma\text{cm}} \cos \varphi - k_{\text{T}} \omega' (1 - \sin^2 \theta_{\gamma\gamma\text{cm}} \cos^2 \varphi)) \end{aligned} \quad (2.46)$$

<sup>4</sup>In [26] and [37] another definition of the structure functions was used. The structure functions used in this work are taken from [31].

and

$$\begin{aligned}
\omega &= \lim_{q'_{\text{cm}} \rightarrow 0} \left[ -q'_{\text{cm}} \left( \frac{1}{p_{\text{cm}} q'_{\text{cm}}} + \frac{1}{k_{\text{cm}} q'_{\text{cm}}} \right) \right], \\
\omega' &= \lim_{q'_{\text{cm}} \rightarrow 0} \left[ -q'_{\text{cm}} \left( \frac{1}{k'_{\text{cm}} q'_{\text{cm}}} - \frac{1}{k_{\text{cm}} q'_{\text{cm}}} \right) \right], \\
\omega'' &= \lim_{q'_{\text{cm}} \rightarrow 0} \left[ \omega q_{\text{cm}} - \omega' \sqrt{k'_{\text{cm}}{}^2 - k_{\text{T}}^2} \right], \\
k_{\text{T}} &= \tilde{Q} \sqrt{\frac{\varepsilon}{2(1-\varepsilon)}}.
\end{aligned} \tag{2.47}$$

In the remainder of this thesis, a shorthand notation for equation (2.44) will be used:

$$\mathcal{M}_0^{\text{NB}} = v_{\text{LL}} (P_{\text{LL}}(q_{\text{cm}}) - \frac{1}{\varepsilon} P_{\text{TT}}(q_{\text{cm}})) + v_{\text{LT}} P_{\text{LT}}(q_{\text{cm}}), \tag{2.48}$$

where

$$\begin{aligned}
v_{\text{LL}} &= 2K_2 v_1 \varepsilon, \\
v_{\text{LT}} &= 2K_2 (v_2 - \frac{\tilde{q}_{\text{cm}}^0}{q_{\text{cm}}} v_3) \sqrt{2\varepsilon(1+\varepsilon)}.
\end{aligned} \tag{2.49}$$

For the separation of  $P_{\text{TT}}$  and  $P_{\text{LL}}$  the unpolarized cross section has to be measured over a wide range in  $\varepsilon$  at a fixed  $Q^2$ . The range of  $\varepsilon$  at fixed  $Q^2$  is limited by the accelerator and the detector setup of the facility where the experiment is performed. Up to now it has not been possible to obtain a good separation of  $P_{\text{TT}}$  and  $P_{\text{LL}}$ . Therefore only two linear combinations of structure functions are obtained from the unpolarized cross section.

### 2.6.3 Single-spin asymmetry

More information about the GPs can come from the spin observables. One possibility is to study single-spin asymmetries (SSA). One example of such asymmetries is the beam single-spin asymmetry  $\mathcal{A}$  defined by

$$\mathcal{A} = \frac{d^5\sigma_{h=+\frac{1}{2}} - d^5\sigma_{h=-\frac{1}{2}}}{d^5\sigma_{h=+\frac{1}{2}} + d^5\sigma_{h=-\frac{1}{2}}}, \tag{2.50}$$

where  $d^5\sigma_{h=\pm\frac{1}{2}}$  is the photon electroproduction cross section for incoming electrons with helicity  $h = \pm\frac{1}{2}$ . Above the pion threshold it is an interesting observable, since it is sensitive to the imaginary part of the VCS amplitude and it allows to study the relative phase between the Bethe-Heitler and VCS amplitudes [38].

Below pion production, however, the VCS amplitude is purely real and all single-spin observables vanish and no additional information about the GPs can be obtained by studying single-spin asymmetries [31]. Therefore one has to investigate double-spin observables.

### 2.6.4 Double-spin asymmetry

One can define several double-spin asymmetries. This section focuses on the double-spin asymmetry measured in this work. For the present experiment a longitudinally polarized electron beam is used and the spin of the recoiling proton is measured by a polarimeter.

The double-spin asymmetry  $\mathcal{P}_i$  along the directions  $i = x, y, z$  in the center-of-mass is defined by:

$$\mathcal{P}_i = \frac{(\mathrm{d}^5\sigma_{h=+\frac{1}{2},s'_i\uparrow} - \mathrm{d}^5\sigma_{h=+\frac{1}{2},s'_i\downarrow}) - (\mathrm{d}^5\sigma_{h=-\frac{1}{2},s'_i\uparrow} - \mathrm{d}^5\sigma_{h=-\frac{1}{2},s'_i\downarrow})}{(\mathrm{d}^5\sigma_{h=+\frac{1}{2},s'_i\uparrow} + \mathrm{d}^5\sigma_{h=+\frac{1}{2},s'_i\downarrow}) + (\mathrm{d}^5\sigma_{h=-\frac{1}{2},s'_i\uparrow} + \mathrm{d}^5\sigma_{h=-\frac{1}{2},s'_i\downarrow})}. \quad (2.51)$$

$\mathrm{d}^5\sigma_{h=+\frac{1}{2},s'_i\uparrow}$  is the differential cross section of the ( $ep \rightarrow e'p'\gamma$ ) reaction, where the proton is polarized in the direction of the  $i$ -axis and the electron has helicity  $h = +\frac{1}{2}$ . The conventions for  $x, y$  and  $z$  are shown in figure 2.9.

One has  $\mathrm{d}^5\sigma_{h=+\frac{1}{2},s'_i\uparrow} = \mathrm{d}^5\sigma_{h=-\frac{1}{2},s'_i\downarrow}$  and  $\mathrm{d}^5\sigma_{h=+\frac{1}{2},s'_i\downarrow} = \mathrm{d}^5\sigma_{h=-\frac{1}{2},s'_i\uparrow}$  since below pion production threshold all single-spin asymmetries are 0. Using these relations, equation (2.51) can be simplified to

$$\mathcal{P}_i = \frac{\mathrm{d}^5\sigma_{h=+\frac{1}{2},s'_i\uparrow} - \mathrm{d}^5\sigma_{h=+\frac{1}{2},s'_i\downarrow}}{\mathrm{d}^5\sigma_{h=+\frac{1}{2},s'_i\uparrow} + \mathrm{d}^5\sigma_{h=+\frac{1}{2},s'_i\downarrow}} = \frac{\Delta\mathrm{d}^5\sigma_i}{2\mathrm{d}^5\sigma}, \quad (2.52)$$

where the denominator is twice the unpolarized cross section  $\mathrm{d}^5\sigma$ , which can be calculated using the low energy theorem as explained in section 2.6.2 and the numerator is given by

$$\Delta\mathrm{d}^5\sigma_i = \mathrm{d}^5\sigma_{h=+\frac{1}{2},s'_i\uparrow} - \mathrm{d}^5\sigma_{h=+\frac{1}{2},s'_i\downarrow}. \quad (2.53)$$

The low energy theorem is applied to  $\Delta\mathrm{d}^5\sigma_i$  and yields a similar relation as for the unpolarized cross section:

$$\Delta\mathrm{d}^5\sigma_i = \Delta\mathrm{d}^5\sigma_i^{\mathrm{BH+B}} + \phi q'_{cm} \Delta\mathcal{M}_{0,i}^{\mathrm{NB}} + \mathcal{O}(q'^2_{cm}) \quad (i = x, y, z). \quad (2.54)$$

The matrix elements  $\Delta\mathcal{M}_0^{\text{NB}}(h, i)$  introduce the effect of the GPs in formula (2.54) and they can be expressed as a function of the structure functions of equations (2.35) and (2.36) [26]:

$$\Delta\mathcal{M}_{0,x}^{\text{NB}} = 4K_2 \left\{ v_1^x \sqrt{2\varepsilon(1-\varepsilon)} P_{\text{LT}}^\perp(q_{\text{cm}}) + v_2^x \sqrt{1-\varepsilon^2} P_{\text{TT}}^\perp(q_{\text{cm}}) + v_3^x \sqrt{1-\varepsilon^2} P_{\text{TT}}^{\prime\perp}(q_{\text{cm}}) + v_4^x \sqrt{2\varepsilon(1-\varepsilon)} P_{\text{LT}}^{\prime\perp}(q_{\text{cm}}) \right\}, \quad (2.55)$$

$$\Delta\mathcal{M}_{0,y}^{\text{NB}} = 4K_2 \left\{ v_1^y \sqrt{2\varepsilon(1-\varepsilon)} P_{\text{LT}}^\perp(q_{\text{cm}}) + v_2^y \sqrt{1-\varepsilon^2} P_{\text{TT}}^\perp(q_{\text{cm}}) + v_3^y \sqrt{1-\varepsilon^2} P_{\text{TT}}^{\prime\perp}(q_{\text{cm}}) + v_4^y \sqrt{2\varepsilon(1-\varepsilon)} P_{\text{LT}}^{\prime\perp}(q_{\text{cm}}) \right\}, \quad (2.56)$$

$$\Delta\mathcal{M}_{0,z}^{\text{NB}} = 4K_2 \left\{ -v_1 \sqrt{1-\varepsilon^2} P_{\text{TT}}(q_{\text{cm}}) + v_2 \sqrt{2\varepsilon(1-\varepsilon)} P_{\text{LT}}^z(q_{\text{cm}}) + v_3 \sqrt{2\varepsilon(1-\varepsilon)} P_{\text{LT}}^{\prime z}(q_{\text{cm}}) \right\}. \quad (2.57)$$

The kinematical coefficients  $v_j$  for the z-component are the same as in equation (2.46). For  $x$  and  $y$  one has to define new angle dependent functions:

$$\begin{aligned} v_1^x &= \sin \theta_{\gamma\gamma\text{cm}} \cos \varphi (\omega'' \sin \theta_{\gamma\gamma\text{cm}} - k_{\text{T}} \omega' \cos \theta_{\gamma\gamma\text{cm}} \cos \varphi), \\ v_2^x &= -\omega'' \sin \theta_{\gamma\gamma\text{cm}} + k_{\text{T}} \omega' \cos \theta_{\gamma\gamma\text{cm}} \cos \varphi, \\ v_3^x &= -\cos \theta_{\gamma\gamma\text{cm}} (\omega'' \sin \theta_{\gamma\gamma\text{cm}} - k_{\text{T}} \omega' \cos \theta_{\gamma\gamma\text{cm}} \cos \varphi), \\ v_4^x &= k_{\text{T}} \omega' \sin \theta_{\gamma\gamma\text{cm}} \sin^2 \varphi, \end{aligned} \quad (2.58)$$

and

$$\begin{aligned} v_1^y &= \sin \theta_{\gamma\gamma\text{cm}} \sin \varphi (\omega'' \sin \theta_{\gamma\gamma\text{cm}} - k_{\text{T}} \omega' \cos \theta_{\gamma\gamma\text{cm}} \cos \varphi), \\ v_2^y &= k_{\text{T}} \omega' \cos \theta_{\gamma\gamma\text{cm}} \sin \varphi, \\ v_3^y &= k_{\text{T}} \omega' \sin \varphi, \\ v_4^y &= -k_{\text{T}} \omega' \sin \theta_{\gamma\gamma\text{cm}} \sin \varphi \cos \varphi. \end{aligned} \quad (2.59)$$

In the expressions (2.55) to (2.57) all GPs appear via the structure functions. Measuring the double-spin asymmetry over a sufficiently wide kinematical range (also out-of-plane) should allow the determination of the six GPs.



---

# Model predictions and VCS experiments

---

The generalized polarizabilities are fundamental properties of the nucleon. They offer a tool to acquire more knowledge about the interaction of the constituents of the nucleon at a low energy scale. The determination of the GPs is a challenge for both theory and experiment. The values of the GPs can be measured in experiments. However the experiment does not explain the underlying physics of the GPs. Only the combination of theory and experiment allows one to obtain a better understanding of the phenomena that govern the physics of the nucleon at low energy.

In this chapter an overview is given of some of the models used to calculate the GPs (see section 3.1). Section 3.2 describes the results of previous VCS experiments, and a summary of what can be learned from these theories and experiments is given in section 3.3.

### 3.1 Theoretical models

Quantum chromodynamics (QCD) is accepted as the fundamental gauge theory for the description of the strong interaction between pointlike quarks and gluons. At sufficiently large energy the coupling constant of QCD is small enough to allow perturbative calculations: the contributions containing higher powers in the coupling constant can be neglected with respect to the lower powers.

However, the QCD coupling constant increases for decreasing energy. In particular, to calculate the low-energy properties of nucleons the coupling constant is too large for a perturbative treatment and another approach is needed to perform the calculations. A wide range of theories has been developed to describe the low-energy behavior of the nucleon: some are based on phenomenological principles, others start from known symmetries of QCD. The GPs have been calculated in the framework of the heavy baryon chiral perturbation theory (HB $\chi$ PT), the linear sigma model (LSM), the non-relativistic constituent quark model (CQM), the effective Lagrangian model (ELM) and the dispersion relation model (DRM). These models are described in the next subsections.

Although all models describe the same object, the results of the calculations for the GPs are quite different: not only the magnitude, but also the  $Q^2$  dependence of the GPs vary from one model to another. A first and quick test to verify the theoretical models is to check how well they reproduce the real-photon limit of the scalar generalized polarizabilities, which should agree with the experimental values for the scalar polarizabilities  $\bar{\alpha}_E$  and  $\bar{\beta}_M$  obtained in RCS.

#### 3.1.1 Heavy baryon chiral perturbation theory

Chiral symmetry means that for massless fermions chirality is a constant of motion. A fermion mass breaks this symmetry by mixing the left- and right-handed components in the expression of the Lagrangian. In the standard model there are six different quark types: three of them are labeled as light quarks ( $u, d, s$ ) and the other three are the heavy quarks ( $c, b$  and  $t$ ). The masses of the light quarks are  $m_u = 5 \pm 2 \text{ MeV}/c^2$ ,  $m_d = 9 \pm 3 \text{ MeV}/c^2$  and  $m_s = 175 \pm 55 \text{ MeV}/c^2$ . Thus, chiral symmetry is explicitly broken by the masses of the quarks. However, for energy scales large compared to  $m_s$  chiral symmetry is approximately fulfilled for the system of the three lightest quarks. From the approximate flavor SU(3) symmetry for ( $u, d, s$ ) of the hadron spectrum one can conclude that chiral symmetry is spontaneously broken and 8 pseudo-scalar mesons appear as Goldstone bosons: 3 pions, 4 kaons and the eta. These Goldstone bosons obtain their masses due to the explicit symmetry breaking by the quark masses.

In chiral perturbation theory, an effective field theory, the calculation of the observables is done via a perturbative expansion in terms of small quantities, like the momentum of the

particles and the quark masses. The order of the expansion is indicated by  $\mathcal{O}(p^n)$ , which means that the calculation has been performed up to the  $n^{\text{th}}$  order in the small quantities. The general effective Lagrangian describes the interactions between the involved particles and is constructed in such a way that all relevant symmetries are fulfilled. The renormalization of chiral perturbation theory is done by identifying the infinities arising from loop diagrams order by order and absorbing them in coefficients in the effective Lagrangian. In this way the calculation is finite at any order in the perturbation.

Chiral perturbation theory was proven to be successful in calculating meson properties. To allow calculations for nucleons the theory has been extended by including the interactions of the Goldstone bosons with baryons. This extended chiral perturbation theory is called heavy baryon chiral perturbation theory and the calculations are not only expanded in powers of the quark masses and external momenta, but also in powers of the inverse nucleon masses.

For the study of the low energy behavior of the nucleon the mass of the  $s$ -quark can not be neglected and the SU(3) symmetry is reduced to a SU(2) symmetry of the  $u$  and  $d$  quarks. Only the pions remain as Goldstone bosons. At low energy the effective degrees of freedom of the system are not the quarks and gluons, but the pions and the nucleon itself. The chiral results are highly constrained, since all parameters used in the effective Lagrangian are accurately known: the pion mass  $m_\pi$ , the axial coupling constant  $g_A$ , and the pion decay constant  $F_\pi$ .

Real Compton scattering and the polarizabilities of the nucleon were among the first calculations to be performed in the nucleon sector of chiral perturbation theory. The theoretical predictions up to  $\mathcal{O}(p^4)$  for the polarizabilities are [39]:

$$\begin{aligned}\alpha_E &= 10.5 \cdot 10^{-4} \text{ fm}^3, \\ \beta_M &= 3.5 \cdot 10^{-4} \text{ fm}^3,\end{aligned}\tag{3.1}$$

close to the observed values given in equation (2.13). The reproduction of these values is an indication of the validity of the calculation.

HB $\chi$ PT of order  $\mathcal{O}(p^3)$  has been applied to virtual Compton scattering and the generalized polarizabilities by Hemmert *et al.* [40], [41] and [42]. Apart from the Born diagrams,  $N\pi$ -loop diagrams are important in this calculation. These diagrams are shown in figure 3.1 and they model the interaction of the photons with the pion cloud of the nucleon. Analytical expressions for the GPs were obtained in this framework. For example, for the electric and

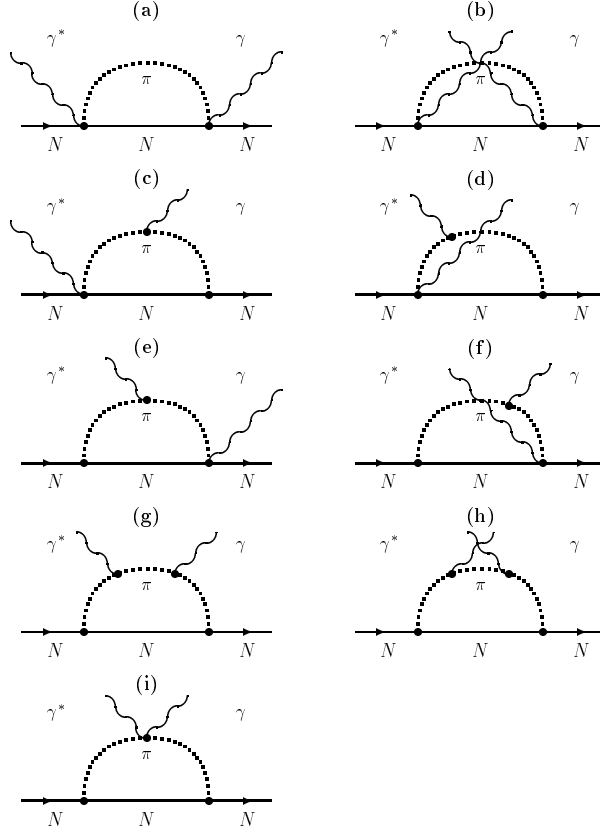


**Figure 3.1:**  $\mathcal{O}(p^3)$   $N\pi$ -loop diagrams for VCS representing the interactions with the pion cloud of the nucleon. (Taken from [42].)

magnetic polarizability one finds [42]:

$$\alpha_E(q_{\text{cm}}) = \frac{e^2 g_A^2 m_\pi}{64\pi^2 F_\pi^2} \cdot \frac{4 + 2\frac{q_{\text{cm}}^2}{m_\pi^2} - (8 - 2\frac{q_{\text{cm}}^2}{m_\pi^2} - \frac{q_{\text{cm}}^4}{m_\pi^4}) \frac{m_\pi}{q_{\text{cm}}} \text{atan} \frac{q_{\text{cm}}}{2m_\pi}}{q_{\text{cm}}^2 (4 + \frac{q_{\text{cm}}^2}{m_\pi^2})}, \quad (3.2)$$

$$\beta_M(q_{\text{cm}}) = \frac{e^2 g_A^2 m_\pi}{128\pi^2 F_\pi^2} \cdot \frac{-(4 + 2\frac{q_{\text{cm}}^2}{m_\pi^2}) + (8 + 6\frac{q_{\text{cm}}^2}{m_\pi^2} + \frac{q_{\text{cm}}^4}{m_\pi^4}) \frac{m_\pi}{q_{\text{cm}}} \text{atan} \frac{q_{\text{cm}}}{2m_\pi}}{q_{\text{cm}}^2 (4 + \frac{q_{\text{cm}}^2}{m_\pi^2})}.$$

The real Compton scattering limit of these expressions are even in better agreement with experimental data than the  $\mathcal{O}(p^4)$  predictions:

$$\alpha_E = 12.5 \cdot 10^{-4} \text{ fm}^3, \quad (3.3)$$

$$\beta_M = 1.25 \cdot 10^{-4} \text{ fm}^3.$$

In standard  $SU(2)$  HB $\chi$ PT, nucleon resonances like the  $\Delta(1232)$  are considered to be much heavier than the nucleon ground state and the contributions of these resonances is taken into account via counter terms. This approach is valid for low-energy processes, where the

contributions of the resonances are expected to be small. For processes at higher energies the  $\Delta(1232)$  resonance becomes more important and therefore a small-scale expansion [42] was developed including the  $\Delta(1232)$  resonance as an explicit degree of freedom in the Lagrangian, just like the pion and the nucleon. The agreement between RCS experiments and this small-scale expansion is less good than the 3<sup>rd</sup> order HB $\chi$ PT.

A 4<sup>th</sup> order calculation of the spin-dependent GPs has been performed by Kao *et al.* [43] and [44] showing a large correction with respect to  $\mathcal{O}(p^3)$  chiral perturbation theory. This causes a different behavior of the GPs as a function of  $Q^2$ . Even the sign of the GPs changes from  $\mathcal{O}(p^3)$  to  $\mathcal{O}(p^4)$  as shown in figure 3.9 at the end of this chapter.

A detailed description of chiral symmetry and chiral perturbation theory can be found in [45] and [46], which were the guiding texts for this section.

### 3.1.2 Linear sigma model

Another model that fulfills chiral symmetry is the linear sigma model (see e.g. [47]). In addition Lorentz and gauge invariance are embedded in the model. The structure of the proton is described by the interaction of the proton, treated as a pointlike particle, with pions and sigmas. The sigma is a fictitious meson, whose mass is a free parameter in the model. The  $\sigma$  meson originates from a spontaneously broken symmetry of the QCD Lagrangian.

The scalar generalized polarizabilities of the proton and neutron have been determined using the linear sigma model by evaluating the spin-independent VCS amplitude in the one-loop approximation for an infinite sigma mass [48], and later also the spin-dependent GPs were calculated in this framework [49]. The obtained polarizabilities  $\alpha_E$  and  $\beta_M$  are lower than the observed ones:

$$\begin{aligned}\alpha_E &= 7.5 \cdot 10^{-4} \text{ fm}^3, \\ \beta_M &= -2.0 \cdot 10^{-4} \text{ fm}^3.\end{aligned}\tag{3.4}$$

In the case of  $\beta_M$  this can be understood by the paramagnetic contribution of the  $\Delta(1232)$  resonance, which is not taken into account in this model.

### 3.1.3 Constituent quark model

The constituent quark model assumes the nucleon to be built out of three constituent quarks. The mass of each of these constituents is 1/3 of the total nucleon mass and they move in a harmonic potential, including additional spin-dependent hyperfine interactions [50]. In this model the GPs are calculated as the sum over the contributions of the different nucleon resonances.

The first calculation of the GPs in this framework was done by Guichon *et al.* [26]. All recoil effects were neglected by assuming a very heavy nucleon. In this calculation some of the GPs were found to be equal to 0. Later on this model was refined by Liu *et al.* [51] by including the recoil effects. In this newer calculation all GPs differ from 0. A similar model was developed by Pasquini *et al.* [52] using another procedure to order the contributing excited states.

This model is a strong simplification of reality, since it is non-relativistic and not gauge invariant and it has no relation to chiral symmetry. The results provide only an order-of-magnitude estimate for the contributions of the nucleon resonances to the GPs. In the real photon limit the polarizabilities are given by [52]:

$$\begin{aligned}\alpha_E &= 5.5 \cdot 10^{-4} \text{ fm}^3, \\ \beta_M &= 4.7 \cdot 10^{-4} \text{ fm}^3.\end{aligned}\tag{3.5}$$

### 3.1.4 Effective Lagrangian model

The scalar generalized polarizabilities  $\alpha_E(q_{\text{cm}})$  and  $\beta_M(q_{\text{cm}})$  have also been calculated using a relativistic effective Lagrangian model. The contributions of all relevant nucleon resonances to the non-Born term of the VCS scattering amplitude are taken into account by explicitly adding the corresponding Feynman diagrams. Also the contribution of  $\pi$ - and correlated  $\pi\pi$ -exchange between the proton and the two photons is incorporated in the calculation.

The parameters of the model have been adjusted to experimental data: e.g. the  $\pi\gamma\gamma$  coupling constant is calculated from the  $\pi^0 \rightarrow \gamma\gamma$  decay width. The main disadvantage of this approach is that only on-shell properties are taken into account, since only the on-shell effects of the resonance couplings can be fixed by experimental resonance photo-decay amplitudes.

This calculation [53] agrees well with  $\bar{\beta}_M$  obtained in real Compton scattering, but the electric polarizability is underestimated in this model:

$$\begin{aligned}\alpha_E &= 7.3 \cdot 10^{-4} \text{ fm}^3, \\ \beta_M &= 1.6 \cdot 10^{-4} \text{ fm}^3.\end{aligned}\tag{3.6}$$

Similar calculations have been performed to calculate the spin-dependent GPs [54]. In this newer calculation a more general treatment of the  $\Delta(1232)$  contribution was implemented by adding off-shell degrees of freedom to the model, but this did not cure the poor result for  $\alpha_E$ .

### 3.1.5 Dispersion relations

Dispersion relation (DR) theory offers a phenomenological description of the nucleon relying on a few basic principles. The theory is relativistic covariant and fulfills the requirements of causality and unitarity. The starting point is the construction of a complete set of invariant amplitudes in agreement with relativity without kinematical singularities. Causality requires specific analytic properties of these amplitudes in such a way that the amplitudes can be continued into the complex plane, where the relation between the real and imaginary parts is expressed by a dispersion relation. At the end, the imaginary part is evaluated via absorption cross sections and the real part can then be calculated by an integral over the imaginary part.

In this approach the VCS process is described using the variables  $Q^2$ ,  $\nu$  and  $t$ , where  $t$  is one of the Mandelstam invariants

$$s = (\mathbf{q} + \mathbf{p})^2, \quad t = (\mathbf{q} - \mathbf{q}')^2, \quad u = (\mathbf{q} - \mathbf{p}')^2 \quad (3.7)$$

and  $\nu$  is defined by

$$\nu = \frac{s - u}{4m_p}. \quad (3.8)$$

The VCS tensor  $T^{\text{FVCS}}$  of equation (2.17) can be separated in 12 invariant amplitudes [55] by defining an appropriate tensor basis in order to obtain non-Born invariant amplitudes free of kinematical singularities and constraints [35]. It has been shown that these amplitudes are related to the GPs [56]. Using this parameterization the VCS tensor  $H^{\kappa\lambda}$  (equation (2.18)) becomes:

$$H^{\kappa\lambda} = H_{\text{B}}^{\kappa\lambda} + H_{\text{NB}}^{\kappa\lambda} = \sum_{i=1}^{12} F_i(Q^2, \nu, t) v^\ell \rho_i^{\kappa\lambda}, \quad (3.9)$$

where  $\ell = 0$ , except for  $i = 3, 4, 8, 10$  for which  $\ell = 1$ .  $\rho_i^{\kappa\lambda}$  are independent tensors [57]. The GPs are defined in the limit  $q'_{\text{cm}} \rightarrow 0 \text{ MeV}/c$ , which corresponds to the limit  $\nu \rightarrow 0 \text{ MeV}$  and  $t \rightarrow -Q^2$ .

The contributions of ten of the invariant amplitudes to the VCS process are calculated through unsubtracted dispersion relations [57]:

$$\bar{F}_i(Q^2) = \text{Re } F_i^{\text{NB}}(Q^2, 0, t = -Q^2) = \frac{2}{\pi} \int_{\nu_0}^{+\infty} d\nu' \frac{\text{Im } F_i(Q^2, \nu', t = -Q^2)}{\nu'}. \quad (3.10)$$

The integral is calculated based on the absorption of the photon to  $\pi N$  intermediate states using the MAID analysis [58] and  $\nu_0$  is the pion production threshold. However, for two of

these amplitudes ( $\bar{F}_1$  and  $\bar{F}_5$ ) this is not possible, since the integrand of equation (3.10) has not the desired convergence behavior.

These two invariant amplitudes are separated in an integral and an asymptotic part. The integral in equation (3.10) is limited to the range  $\nu' \in [-\nu_{\max}, \nu_{\max}]$  and is finite for an appropriate choice of  $\nu_{\max}$ . The asymptotic contribution to  $\bar{F}_5$  mainly comes from  $\pi^0$ -exchange in the  $t$ -channel, which can be estimated based on the known properties of this process.  $\bar{F}_1$  depends on the generalized magnetic polarizability  $P^{(11,11)0}$  and the asymptotic part is parameterized by a dipole with mass scale  $\Lambda_\beta$ :

$$\beta_M(Q^2) - \beta_M^{\pi N}(Q^2) = \frac{[\beta_M(Q^2) - \beta_M^{\pi N}(Q^2)]_{Q^2 \rightarrow 0}}{(1 + Q^2/\Lambda_\beta^2)^2}, \quad (3.11)$$

where  $\beta_M^{\pi N}(Q^2)$  is the contribution to  $\beta_M(Q^2)$  from  $\pi N$  intermediate states.

To incorporate the contributions of the integrals beyond the  $\pi N$  intermediate states also the asymptotic behavior of the generalized electric polarizability  $\alpha_E(Q^2)$  is parameterized by a dipole with a mass scale  $\Lambda_\alpha$ :

$$\alpha_E(Q^2) - \alpha_E^{\pi N}(Q^2) = \frac{[\alpha_E(Q^2) - \alpha_E^{\pi N}(Q^2)]_{Q^2 \rightarrow 0}}{(1 + Q^2/\Lambda_\alpha^2)^2}. \quad (3.12)$$

$\Lambda_\alpha$  and  $\Lambda_\beta$  are the only free parameters of the model and they have to be adjusted to the data. The real-photon limit is used as a constraint in the parameterization of  $\alpha_E(Q^2)$  and  $\beta_M(Q^2)$ . Once the values  $\Lambda_\alpha$  and  $\Lambda_\beta$  are fixed, all VCS invariant amplitudes, and by consequence all GPs, are known for energies up to the  $\Delta(1232)$  resonance.

## 3.2 Experiments

The last decade a lot of effort has been made at the experimental side to measure the generalized polarizabilities, or linear combinations of them. Shortly after the publication of the paper defining the GPs by Guichon *et al.* [26] three VCS experiments were planned and performed in order to extract  $P_{LL} - P_{TT}/\varepsilon$  and  $P_{LT}$  from the unpolarized cross sections at different  $Q^2$ : at  $Q^2 = 0.06$  (GeV/c)<sup>2</sup> (MIT-Bates), at  $Q^2 = 0.33$  (GeV/c)<sup>2</sup> (MAMI) and at  $Q^2 = 0.92$  and  $1.76$  (GeV/c)<sup>2</sup> (JLab). The analyses of these experiments turned out to be very difficult.

After these unpolarized experiments a new ‘generation’ of experiments has been performed to measure polarization observables of the photon electroproduction reaction. The first polarized experiment was the measurement of the beam single-spin asymmetry for VCS above the pion production threshold. The interest of this measurement is that it allows to check the

description of the VCS amplitudes in the DR model. The second polarized experiment [59] is the measurement of the double spin asymmetry, described in this thesis.

### 3.2.1 First MAMI experiment

The experiment at MAMI [60] was the first attempt to measure the GPs via the  $p(e, e' p')\gamma$  reaction below the pion production threshold. It is similar to the present experiment since the same detectors and accelerator were used (see chapter 4).

The goal was the extraction of two linear combinations of structure functions:  $P_{LL} - P_{TT}/\varepsilon$  and  $P_{LT}$  via the determination of the unpolarized VCS cross section at different real photon momenta  $q'_{cm}$ : 33.6, 45, 67.5, 90 and 111.5 MeV/ $c$ . The observed cross sections are displayed in figure 3.2. The effect of the GPs changes the shape of the cross section and their influence increases with increasing  $q'_{cm}$ .

Measuring the cross section over a relatively wide range in  $q'_{cm}$  has several advantages. The measurement of absolute cross sections is very sensitive to systematic errors like the uncertainty on the experimental luminosity (beam current, target density, ...). In addition to the experimental sources of uncertainties, the extraction of the structure functions is strongly dependent on the parameterization of the form factors of the proton. In this analysis the form factors of Höhler *et al.* [7] were used. At  $q'_{cm} = 33.6$  MeV/ $c$  the effect of the GPs on the cross section is negligible and at such low real photon energies one measures only the Bethe-Heitler cross section. This can be used to perform an absolute normalization of the cross sections and it removes a large part of the systematic uncertainty induced by the choice of the form factors and the determination of the luminosity.

The GPs are defined in the limit  $q'_{cm} \rightarrow 0$  MeV/ $c$ . Using the range in  $q'_{cm}$  an extrapolation from the measured values of  $q'_{cm}$  to 0 MeV/ $c$  can be done. This extrapolation is model dependent. Figure 3.3 shows the extrapolation to  $q'_{cm} = 0$  MeV/ $c$  of  $\mathcal{M}_0^{NB}$ , defined in equation (2.42), for the LEX and DR analyses. In the LEX analysis  $\mathcal{M}_0^{NB}$  is supposed to be independent of  $q'_{cm}$  and the mean value for  $\mathcal{M}_0^{NB}$  is calculated over the 5 different settings. The width of the colored zone indicates the experimental uncertainty on this mean value. In the DR analysis the two parameters  $\Lambda_\alpha$  and  $\Lambda_\beta$  are adjusted to the cross section data and in this approach the evolution of  $\mathcal{M}_0^{NB}$  with  $q'_{cm}$  is predicted by the model. Only for  $\theta_{\gamma\gamma cm} \approx 0^\circ$  this  $q'_{cm}$  dependency is significantly different from the LEX analysis, which gives confidence in the LEX approach [18].

In the LEX approximation  $\mathcal{M}_0^{NB}/v_{LT}$  varies linearly with  $v_{LL}/v_{LT}$  as derived in equation (2.48). Figure 3.4 shows that this is valid in the kinematic range of the experiment. The extracted

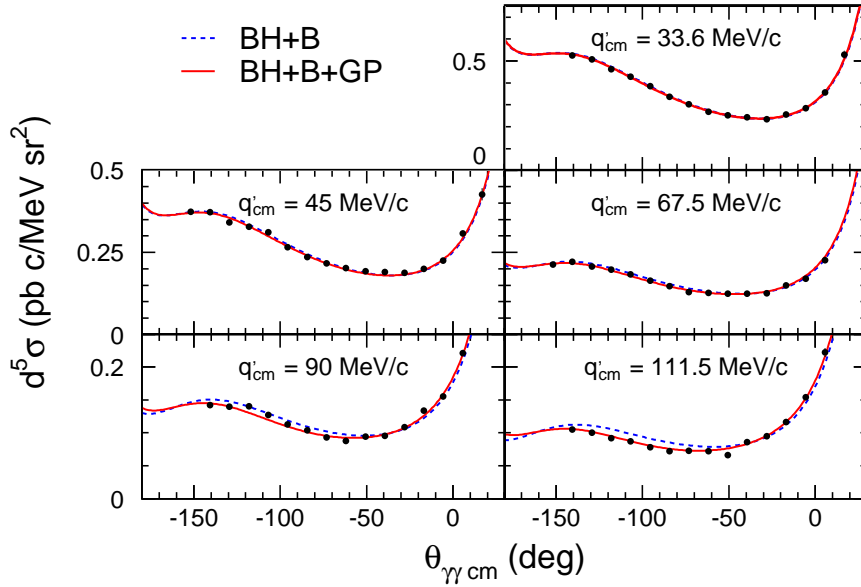


**Figure 3.2:** Photon electroproduction cross sections obtained in the first VCS experiment at MAMI for  $Q^2 = 0.33 \text{ (GeV}/c)^2$ ,  $\varepsilon = 0.62$ ,  $\varphi = 0^\circ$  and  $\varphi = 180^\circ$  (negative  $\theta_{\gamma\text{cm}}$  corresponds to  $\varphi = 180^\circ$ ) and different  $q'_{\text{cm}}$ . (The data are taken from [60].)

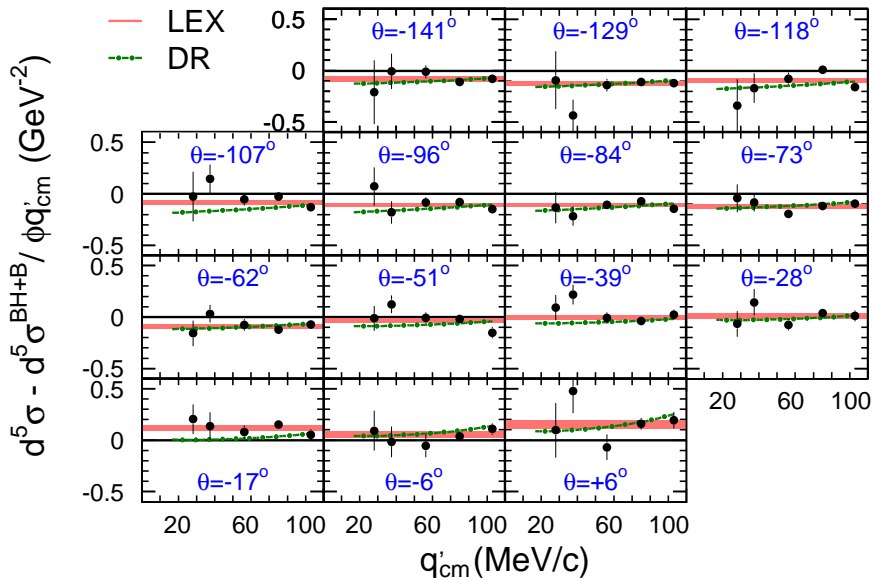


**Figure 3.3:**  $d^5\sigma - d^5\sigma^{\text{BH+B}}/\phi q'_{\text{cm}}$  for all values of  $\theta_{\gamma\text{cm}}$  as a function of  $q'_{\text{cm}}$  as obtained in the first MAMI experiment. The extrapolation to  $q'_{\text{cm}} = 0 \text{ MeV}/c$  is shown for the LEX and DR analysis. (The data are taken from [60].)

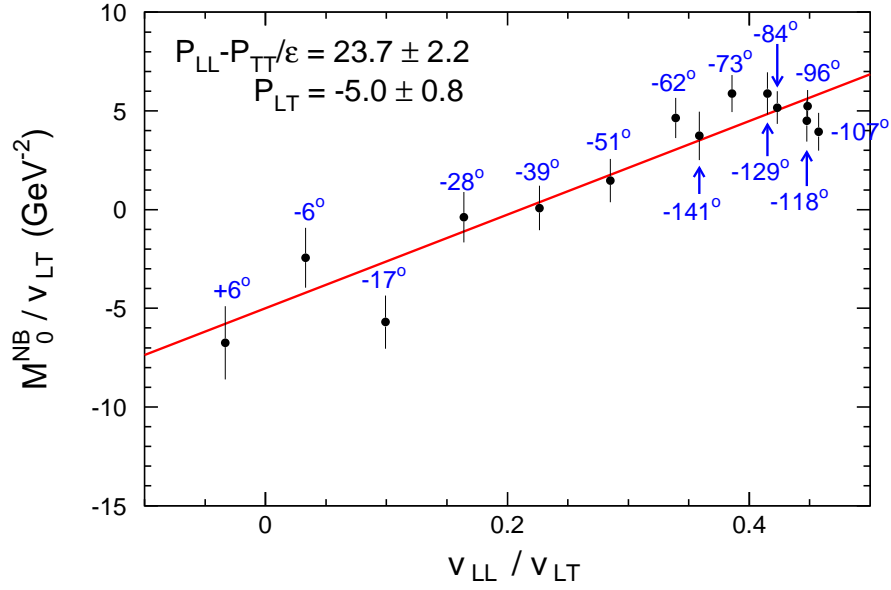


**Figure 3.4:** Extraction of two linear combinations of structure functions:  $P_{LL} - P_{TT}/\varepsilon$  and  $P_{LT}$ . The values of  $\theta_{\gamma\gamma\text{cm}}$  for each data point are indicated on the figure. (The data are taken from [60].)

structure functions are [60]

$$\begin{aligned} P_{LL} - P_{TT}/\varepsilon &= 23.7 \pm 2.2 \pm 0.6 \pm 4.3 \text{ GeV}^{-2}, \\ P_{LT} &= -5.0 \pm 0.8 \pm 1.1 \pm 1.4 \text{ GeV}^{-2}. \end{aligned} \quad (3.13)$$

The first error is the statistical uncertainty, the two other errors are the systematic uncertainties due to the normalization and the distortion, respectively, of the angular distributions of the photon.

The DR analysis yields consistent results [61]

$$\begin{aligned} P_{LL} - P_{TT}/\varepsilon &= 23.2 \pm 3.0 \text{ GeV}^{-2}, \\ P_{LT} &= -3.2 \pm 2.0 \text{ GeV}^{-2}, \end{aligned} \quad (3.14)$$

with  $\Lambda_\alpha = 1.6 \pm 0.2 \text{ GeV}$  and  $\Lambda_\beta = 0.5 \pm 0.2 \text{ GeV}$ .

More information about this experiment and the analysis can be found in references [60], [61] and in the Ph.D. theses of D. Lhuillier [62], J. Roche [63] and J.M. Friedrich [64].

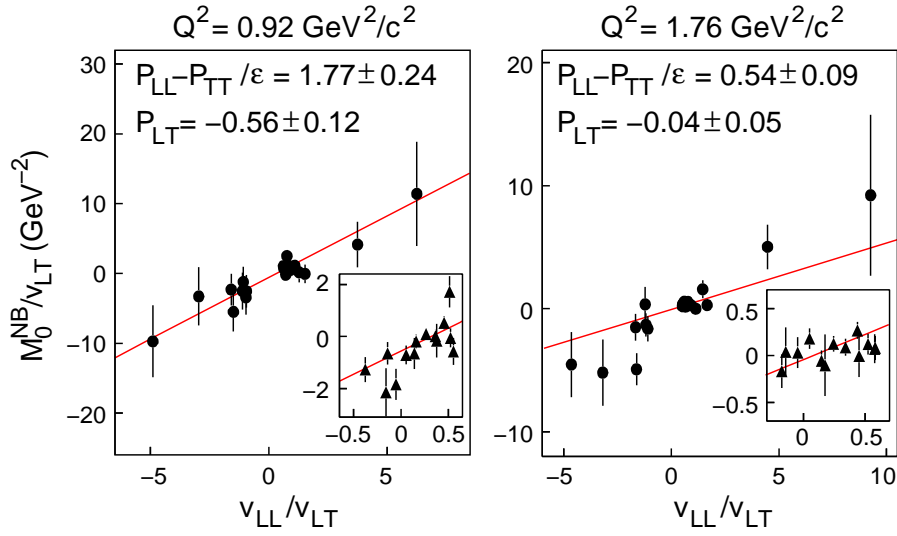


**Figure 3.5:** Extraction of two linear combinations of structure functions (JLab):  $P_{LL} - P_{TT}/\epsilon$  and  $P_{LT}$ . Circles correspond to out-of-plane data, and the inner plot is a zoom on the lepton plane data represented by the triangles. (Taken from [65].)

### 3.2.2 JLab experiment

At the Thomas Jefferson National Accelerator Facility (JLab) an unpolarized VCS experiment (E93-050) [65] has been performed at higher values of  $Q^2$ :  $0.92 \text{ (GeV}/c)^2$  and  $1.76 \text{ (GeV}/c)^2$ . Also this experiment aimed to extract  $P_{LL} - P_{TT}/\epsilon$  and  $P_{LT}$ .

The experiment made use of the continuous electron beam, with an energy of 4.03 GeV impinging on a 15 cm long liquid hydrogen target and the standard setup of hall A. The electron and the proton were detected in coincidence in two high-resolution magnetic spectrometers and the photon electroproduction events were tagged via missing mass reconstruction.

For both values of  $Q^2$  unpolarized cross sections were obtained and analyzed using a LEX and a DR analysis. The BH+B contribution was calculated using the parameterization of the form factors by Brash *et al.* [66]. The effect of the GPs reached at maximum 15% of the cross section below the pion threshold. The extraction of the structure functions using the LEX analysis is shown in figure 3.5. For the DR analysis the free parameters  $\Lambda_\alpha$  and  $\Lambda_\beta$  were fitted to the cross section data (see table 3.1), which fixes the DR predictions for all GPs. The advantage of the dispersion relation analysis is that also events above the pion production up to the  $\Delta(1232)$  resonance could be used. The results for both settings should, according to the dipole approximation in the DR model, result in the same parameters  $\Lambda_\alpha$  and  $\Lambda_\beta$ . This is fulfilled within the experimental uncertainties. Table 3.2 presents the obtained structure functions. Both analyses yield consistent results for the structure functions.

$Q^2$ (GeV/c) <sup>2</sup>	$\varepsilon$	$\Lambda_\alpha$ (GeV)	$\Lambda_\beta$ (GeV)
0.92	0.95	$0.741 \pm 0.040 \pm 0.175$	$0.788 \pm 0.041 \pm 0.114$
1.76	0.88	$0.774 \pm 0.050 \pm 0.149$	$0.698 \pm 0.042 \pm 0.077$

**Table 3.1:** Result of the DR analysis for  $\Lambda_\alpha$  and  $\Lambda_\beta$ , the only free parameters in the DR approach. (Taken from [65].)

$Q^2$ (GeV/c) <sup>2</sup>	$\varepsilon$	$P_{LL} - P_{TT}/\varepsilon$ (GeV <sup>-2</sup> )	$P_{LT}$ (GeV <sup>-2</sup> )	Analysis
0.92	0.95	$1.77 \pm 0.24 \pm 0.70$	$-0.56 \pm 0.12 \pm 0.17$	LEX
1.76	0.88	$0.54 \pm 0.09 \pm 0.20$	$-0.04 \pm 0.05 \pm 0.06$	LEX
0.92	0.95	$1.70 \pm 0.21 \pm 0.89$	$-0.36 \pm 0.10 \pm 0.27$	DR
1.76	0.88	$0.40 \pm 0.05 \pm 0.16$	$-0.09 \pm 0.02 \pm 0.03$	DR

**Table 3.2:** The extracted structure functions  $P_{LL} - P_{TT}/\varepsilon$  and  $P_{LT}$  based on LEX and DR analysis. (Taken from [65].)

The JLab experiment is described in the Ph.D. theses of N. Degrande [32], G. Lavessière [67], S. Jaminion [68] and C. Jutier [69] and the results have been published in [65].

### 3.2.3 MIT-Bates experiment

At the MIT-Bates linear accelerator a third unpolarized VCS experiment was performed at low  $Q^2 = 0.06$  (GeV/c)<sup>2</sup> using a beam energy between 570 to 670 MeV [70]. Like in the other two experiments a liquid hydrogen target (of 1.6 cm) was used and the scattered electron and recoiling proton were detected in spectrometers. The final state photon was identified by missing mass and time-of-flight techniques.

To extract  $P_{LL} - P_{TT}/\varepsilon$  and  $P_{LT}$  at  $q_{cm} = 240$  MeV/c and  $\varepsilon = 0.9$  the unpolarized cross section of the  $p(e, e' p')\gamma$  reaction was measured at fixed  $\theta_{\gamma\gamma_{cm}} = 90^\circ$  for  $\varphi = 90^\circ, 180^\circ$  and  $270^\circ$  and different real-photon energies ranging from 43 to 115 MeV. The two out-of-plane results ( $\varphi = 90^\circ$  and  $270^\circ$ ) are equal and the deviation from the BH+B cross section is proportional to  $P_{LL} - P_{TT}/\varepsilon$  and the in-plane cross section ( $\varphi = 180^\circ$ ) is proportional to the sum of  $P_{LL} - P_{TT}/\varepsilon$  and  $P_{LT}$ .

The resulting cross sections are shown in figure 3.6. For the analysis of the data the form factor parameterization of Höhler *et al.* [7] was used. At low  $q'_{cm}$  the agreement with the BH+B cross section is good, while at higher  $q'_{cm}$  the effect of the GPs results in a cross section, which is

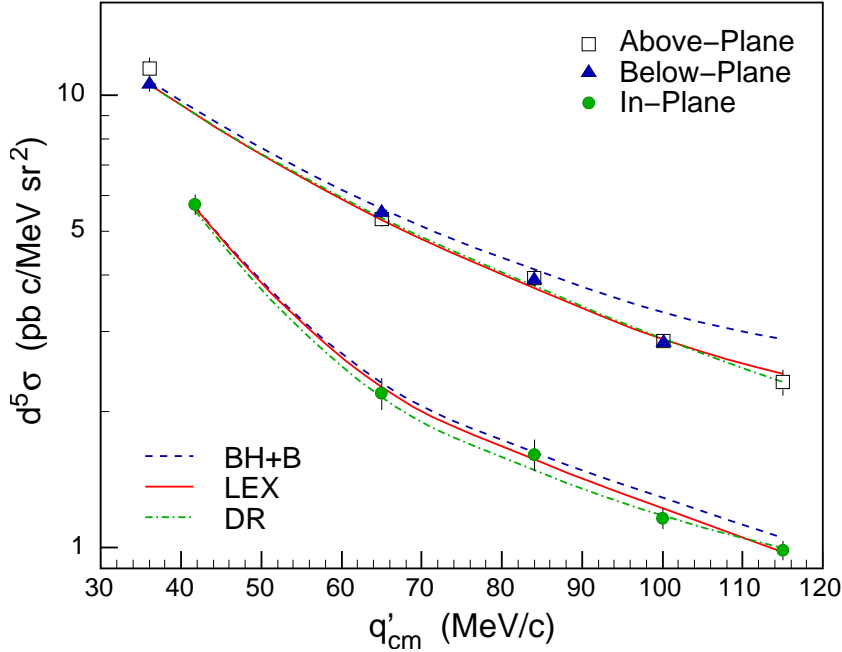


**Figure 3.6:** Unpolarized cross sections for the  $p(e, e' p')\gamma$  reaction at  $q_{\text{cm}} = 240 \text{ MeV}/c$  and  $\varepsilon = 0.9$  for  $\varphi = 90^\circ, 180^\circ$  and  $270^\circ$  obtained at MIT-Bates. (Taken from [70].)

systematically lower than the BH+B cross section. Using the LEX analysis one obtains:

$$\begin{aligned} P_{\text{LL}} - P_{\text{TT}}/\varepsilon &= 54.5 \pm 4.8 \pm 2.0 \text{ GeV}^{-2}, \\ P_{\text{LT}} &= -20.4 \pm 2.9 \pm 0.8 \text{ GeV}^{-2}. \end{aligned} \quad (3.15)$$

The errors are the statistic and systematic uncertainty, respectively.

Also a dispersion relation analysis was performed, yielding:

$$\begin{aligned} P_{\text{LL}} - P_{\text{TT}}/\varepsilon &= 46.7 \pm 4.9 \pm 2.0 \text{ GeV}^{-2}, \\ P_{\text{LT}} &= -8.9 \pm 4.2 \pm 0.8 \text{ GeV}^{-2}. \end{aligned} \quad (3.16)$$

The DR result for  $P_{\text{LL}} - P_{\text{TT}}/\varepsilon$  is in agreement with the LEX analysis, but the value of  $P_{\text{LT}}$  is significantly smaller. The cause of the discrepancy between the LEX and the DR analysis for  $P_{\text{LT}}$  is the cancellation of the electric and magnetic GPs at first order in  $q'_{\text{cm}}$  for in-plane kinematics and, by consequence, the effect of the GPs on the cross section is dominated by a term in  $q'_{\text{cm}}{}^2$  for that kinematics. This means that the LEX analysis is not valid at this particular kinematical point. The DR analysis does not suffer from this effect, since it takes into account all orders in  $q'_{\text{cm}}$ .

From a fit to the data on  $\alpha_{\text{E}}(Q^2)$  and  $\beta_{\text{M}}(Q^2)$  (based on this experiment and RCS data) the mean square electric and magnetic polarizability radius,  $\langle r_{\alpha}^2 \rangle$  and  $\langle r_{\beta}^2 \rangle$ , were ob-

tained [70]:

$$\begin{aligned} \langle r_\alpha^2 \rangle &= 1.95 \pm 0.33 \text{ fm}^2, \\ \langle r_\beta^2 \rangle &= -1.91 \pm 2.12 \text{ fm}^2. \end{aligned} \quad (3.17)$$

These values are in agreement with the  $\mathcal{O}(p^3)$  HB $\chi$ PT predictions [40]. Also the value for  $P_{\text{LL}} - P_{\text{TT}}/\varepsilon$  is in good agreement with the HB $\chi$ PT. The result for  $P_{\text{LT}}$  of the LEX analysis is much larger (in absolute value) than the HB $\chi$ PT calculations, while the agreement between theory and the result of the DR analysis is much better.

### 3.2.4 MAMI beam single-spin asymmetry experiment

Above the pion production threshold the VCS amplitudes becomes complex due to the contribution of the  $\pi N$  channel, causing non-vanishing single-spin observables like the beam single-spin asymmetry (SSA), defined in equation (2.50).

The experiment was performed using the standard detectors of hall A1 at MAMI (see chapter 4). The beam energy was 883.2 MeV and the beam polarization was 75 to 85%. Since the SSA vanishes for in-plane kinematics, spectrometer B was set to different out-of-plane settings (up to  $10^\circ$ ). The nominal kinematics are given by:  $Q^2 = 0.35 \text{ (GeV}/c)^2$ , a center-of-mass energy  $W = 1.19 \text{ GeV}$ ,  $\varepsilon = 0.48$  and  $\varphi = 220^\circ$ .

The SSA is proportional to the imaginary part of the non-Born VCS amplitude [38] and is mostly sensitive to the  $\pi N$  intermediate states. The measurement of the SSA in the  $\Delta(1232)$  region is a direct test for the description of this VCS amplitude in the DR model. Since the sensitivity of the SSA to the free parameters  $\Lambda_\alpha$  and  $\Lambda_\beta$  is small, this observable yields no information about the GPs. This information can be extracted from the unpolarized analysis. Such an analysis is in preparation [71].

Since in the experiment the  $(ep \rightarrow e'p'\pi^0)$  reaction was detected simultaneously, the SSA was also obtained for this channel at the same kinematics. The results are displayed in figure 3.7.

For the  $(\vec{e}p \rightarrow e'p'\gamma)$  reaction the result is compared to the dispersion relation (DR) formalism [57], which is the only model capable of predicting the SSA in this regime. The model uses the  $\pi N$  multipoles from the MAID parameterization [58]. The agreement with the DR-prediction is good.

Also for the SSA in the  $(\vec{e}p \rightarrow e'p'\pi^0)$  channel good agreement with theoretical predictions (MAID and DMT [73]) is observed. This experiment made the first simultaneous measurement in two de-excitation channels ( $\gamma N$  and  $\pi N$ ) of the  $\Delta(1232)$  resonance. Since these two channels are related by unitarity, this measurement provides stronger constraints for  $\pi N$  multipole adjustment.

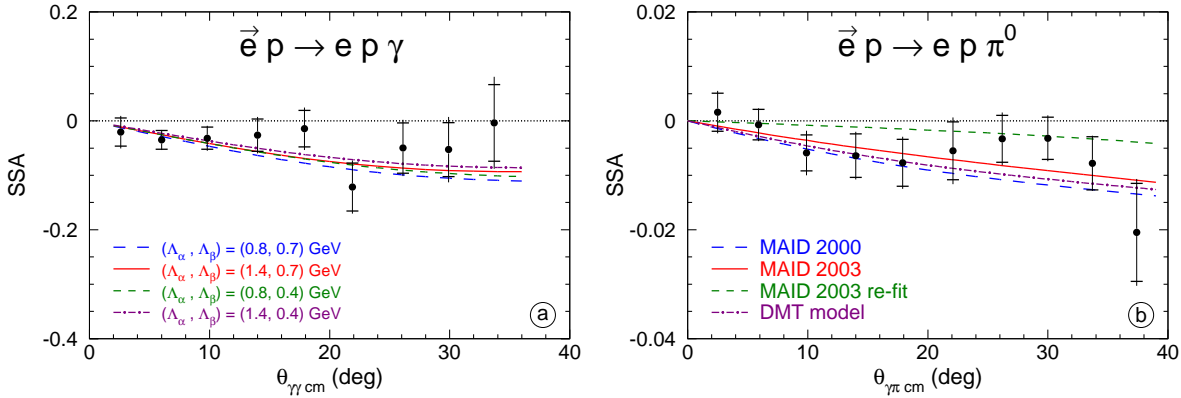


**Figure 3.7:** Beam SSA in photon electroproduction (a) and pion electroproduction (b) at  $Q^2 = 0.35$   $(\text{GeV}/c)^2$ ,  $W = 1.19$  GeV,  $\varepsilon = 0.48$  and  $\varphi = 220^\circ$ . The inner error bar is statistical, the outer is the quadratic sum of statistical and systematic errors. (The data are taken from [72].)

The results were published in [74] and an overview of the analysis can be found in the Ph.D. thesis of I. Bensafa [72] and in the analysis report [75].

### 3.3 Conclusion

By confronting the models described in this chapter with the polarizabilities obtained in RCS, one can conclude that only the heavy baryon chiral perturbation theory and the dispersion relation model are able to obtain values for  $\alpha_E$  and  $\beta_M$ , which are in agreement with the experiments. For the DR model this is no surprise since it is constrained to go through the experimental RCS point. All other models fail for several reasons. Some of them, like the linear sigma model, do not incorporate the  $\Delta(1232)$  resonance, which is expected to have an important contribution to  $\beta_M$ . In the case of the constituent quark model the pion cloud is not included in the calculations, while e.g. HB $\chi$ PT predicts a large contribution from the pion cloud to the scalar polarizabilities. This is confirmed by the experimentally obtained value for  $\langle r_\alpha^2 \rangle$  [70].

The VCS experiments performed up to now have put new constraints on the models. In table 3.3 an overview is given of the experimental results and the model predictions for  $P_{LL} - P_{TT}/\varepsilon$  and  $P_{LT}$  at  $Q^2 = 0.33$   $(\text{GeV}/c)^2$ . Just like in the real photon limit only two models describe the data rather well: the chiral perturbation theory and the dispersion relation model. For the DR model for VCS the two parameters  $(\Lambda_\alpha, \Lambda_\beta)$  were adjusted to the data to obtain the two experimental observables. In this sense the measurement of the unpolarized cross section at one value of  $Q^2$  is no real test for the DR model.

	$P_{LL} - P_{TT}/\varepsilon$ ( $\text{GeV}^{-2}$ )	$P_{LT}$ ( $\text{GeV}^{-2}$ )
MAMI (LEX) [60]	$23.7 \pm 2.2 \pm 4.3 \pm 0.6$	$-5.0 \pm 0.8 \pm 1.4 \pm 1.1$
HB $\chi$ PT [42]	26.3	-5.7
LSM [49]	10.9	0.2
ELM [53]	5.9	-1.9
CQM [52]	14.7	-4.5
DR [57]	23.2	-3.2

**Table 3.3:** Comparison of the MAMI results for  $P_{LL} - P_{TT}/\varepsilon$  and  $P_{LT}$  at  $Q^2 = 0.33$  ( $\text{GeV}/c$ )<sup>2</sup> with the models described in section 3.1.

The structure functions  $P_{LL} - P_{TT}/\varepsilon$  and  $P_{LT}$  have been measured at four different values of  $Q^2$ . In figure 3.8 the world VCS data is shown together with the results of the DR analyses of each of the experiments. From the figure one can conclude that there is no unique combination of values  $(\Lambda_\alpha, \Lambda_\beta)$  going through all data points. The difference is most striking for the electric generalized polarizability. This means that the dipole parameterizations in equations (3.11) and (3.12) are not valid over the complete  $Q^2$  range. It is important to note that the calculations of  $\alpha_E(q_{\text{cm}})$  and  $\beta_M(q_{\text{cm}})$  are not model independent: the predictions of the DR model for the spin-dependent GPs were used to calculate them based on  $P_{LL} - P_{TT}/\varepsilon$  and  $P_{LT}$  obtained by the LET analysis.

However, the general behavior of  $\beta_M(Q^2)$  is correctly predicted by the DR model and also by the HB $\chi$ PT. For low  $Q^2$  the magnetic GP first rises to reach a maximum and at larger  $Q^2$  it decreases. This indicates that there are local regions of paramagnetic (at small distances) and diamagnetic (at larger distances) magnetic polarizability densities in the nucleon.

For the spin-dependent GPs there are no experimental results at the moment. Figure 3.9 shows the predictions of HB $\chi$ PT  $\mathcal{O}(p^3)$  [42], HB $\chi$ PT  $\mathcal{O}(p^4)$  [44] and dispersion relations [57]. There is a large difference between the predictions of these three models. Very striking is the difference between 3<sup>rd</sup> and 4<sup>th</sup> order calculations in HB $\chi$ PT. One would expect that the 4<sup>th</sup> order only adds a little correction to the  $\mathcal{O}(p^3)$  HB $\chi$ PT, but this is not the case for the spin-dependent GPs: for some of them even the sign is different. In general the DR prediction lies in between the two HB $\chi$ PT results. The goal of the double-polarized VCS experiment at MAMI is to put experimental values on these figures.

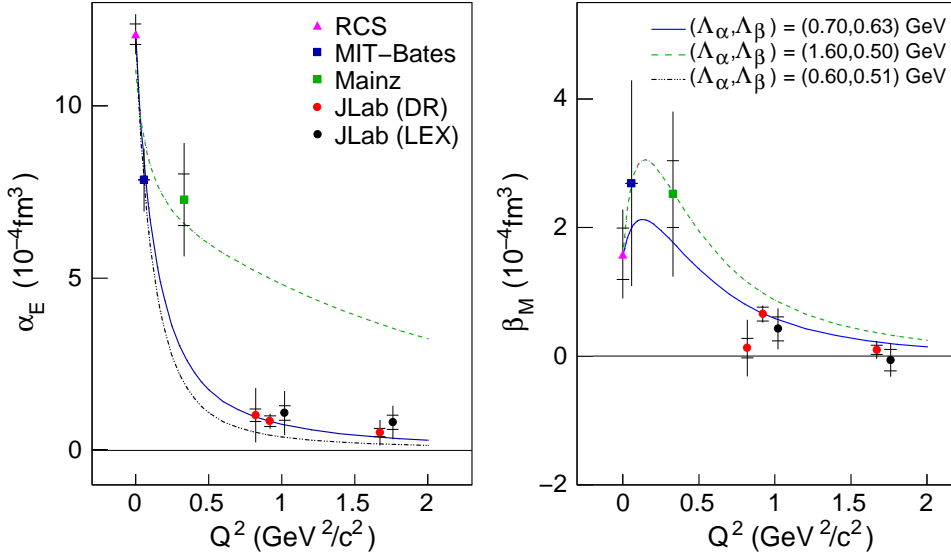


**Figure 3.8:** Compilation of the data on the electric  $\alpha_E(Q^2)$  and magnetic  $\beta_M(Q^2)$  GPs of the proton. The inner error bars are statistical; the outer ones are the total error. The RCS data is taken from [15]. The JLab points have been shifted in abscissa for better visibility. The DR curves correspond to the JLab (0.70,0.63), MAMI (1.60,0.50) and MIT-Bates (0.60,0.51) analysis. (Taken from [61].)

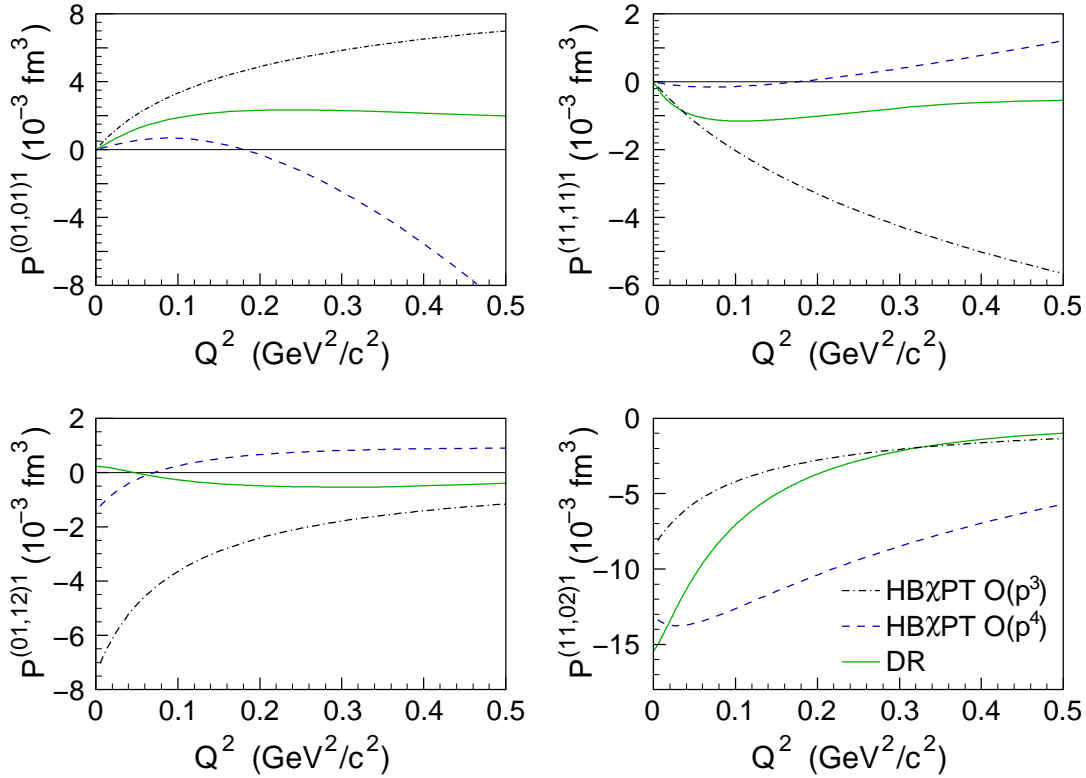


**Figure 3.9:** Predictions for the four spin-dependent GPs using HB $\chi$ PT  $\mathcal{O}(p^3)$  [42], HB $\chi$ PT  $\mathcal{O}(p^4)$  [44] and dispersion relations [57]. (Taken from [44].)

---

# Experimental setup

---

This measurement of the double-spin asymmetry for photon electroproduction reaction has been performed at the Mainzer Mikrotron (MAMI) accelerator using the high-resolution magnetic spectrometers of hall A1 at the Institut für Kernphysik of the Johannes Gutenberg Universität at Mainz. The experiment made use of the longitudinally polarized electron beam. The beam electrons scattered on a liquid hydrogen target and the scattered electron and recoil proton were detected in coincidence in the spectrometers. One of the spectrometers has been extended with a focal plane polarimeter (FPP) to measure the polarization of the recoiling proton.

In this chapter first the MAMI accelerator is described (section 4.1). Section 4.2 is devoted to the spectrometers of hall A1 and section 4.3 to the liquid hydrogen target cell. To monitor the beam current a Förster probe is used, which is described in section 4.4. On a regular basis the beam polarization is measured with the Møller polarimeter (section 4.5) and finally the focal plane polarimeter is described in section 4.6.

## 4.1 MAMI accelerator

The Mainzer Mikrotron (MAMI-B)<sup>1</sup> was originally designed to deliver a continuous electron beam with an energy between 180 and 855 MeV and a current up to 110  $\mu\text{A}$  [76]. A linear accelerator injects the electrons from the unpolarized electron source into the first of three race-track microtrons (RTM) at an energy of 3.5 MeV.

The principle of the race-track microtron is shown in figure 4.1. The electrons are accelerated in a linear accelerator and then they are bent by two recirculating magnets. After each turn the electrons enter the same accelerating section. Due to the increased momentum, the radius of the track in the magnets increases after each turn. After a certain number of turns the electrons have acquired the desired amount of energy and they are extracted from the microtron.

After being accelerated by the first microtron they are injected in the next one and at the end of the acceleration process the electrons are guided through the beam lines to one of the experimental halls.

Later on a polarized electron source was added [77]. The polarized electrons are emitted by a GaP semiconductor crystal by irradiation with circularly polarized laser light. The initial polarization is about 75% and the maximal current of the polarized beam is 25  $\mu\text{A}$ . The helicity of the beam is reversed every second to reduce the systematic uncertainty.

Finally, a fourth step has been built for the MAMI accelerator, called MAMI-C (e.g. [78]). It is a harmonic double sided microtron (HDSM) accelerator which increases the maximum beam energy up to 1.8 GeV. This fourth stage of the accelerator became operational at the beginning of 2007. Figure 4.2 shows the floor plan of the MAMI accelerator and the experimental halls.

## 4.2 Three-spectrometer setup

The main detectors of hall A1 are three high-resolution magnetic spectrometers (figure 4.3). The spectrometers can rotate around the same axis. At the central pivot point of these three spectrometers a fixed target is positioned.

The magnetic field of the spectrometers deflects the charged particles upwards to the focal plane, where the position and direction of the particles is measured using vertical drift chambers (VDCs). Apart from the VDCs there are also particle identification detectors (PID) in the focal plane detection apparatus. An overview of the parameters of the spectrometers can be found in table 4.1.

---

<sup>1</sup>The name MAMI-A is used for the first 2 stages of MAMI (RTM1 and RTM2). MAMI-A was used for experiments while the third step (RTM3) was still in development and delivered an electron beam of 183 MeV.

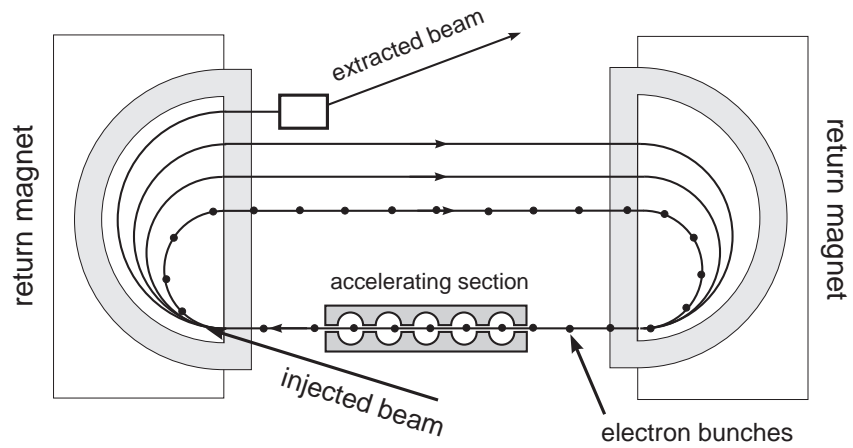


**Figure 4.1:** One of the three race-track microtrons of the MAMI-B accelerator. (Taken from [79].)

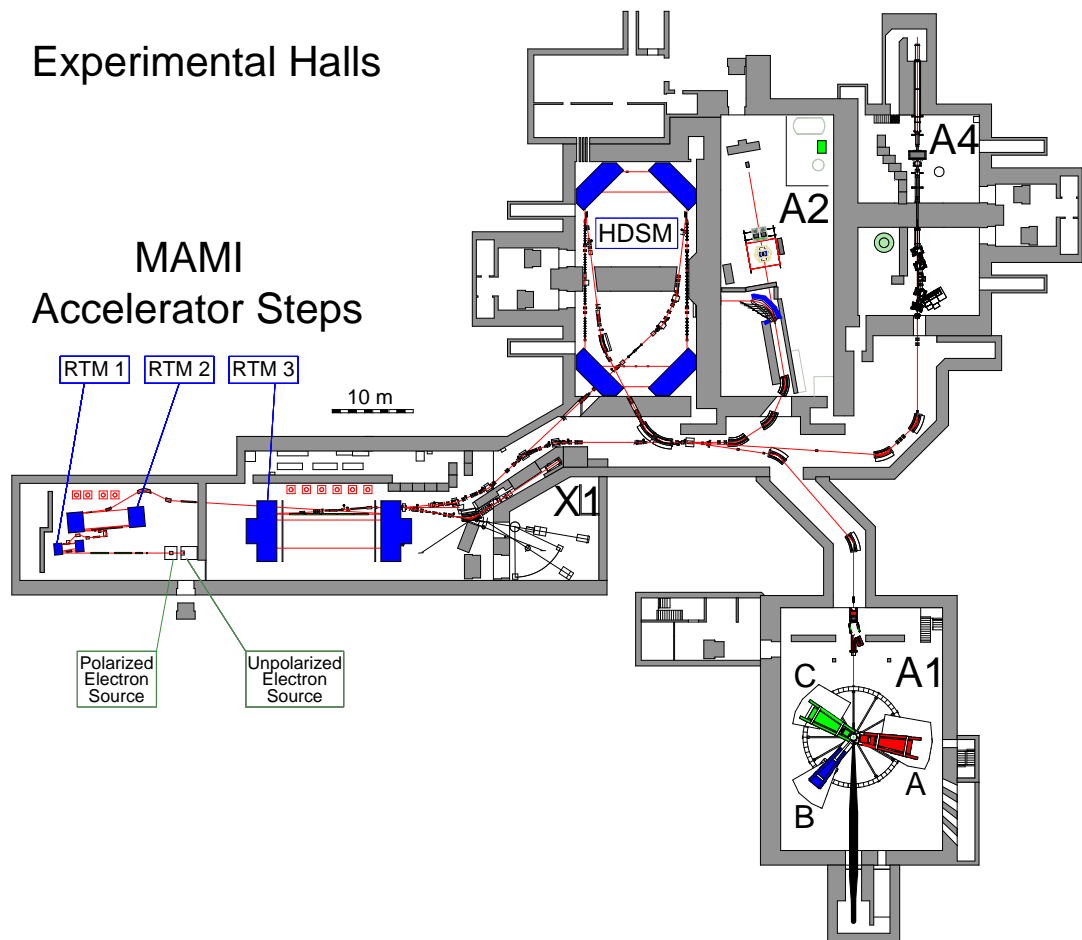


**Figure 4.2:** Floor plan of the MAMI accelerator and the experimental halls of the Institut für Kernphysik (Mainz). (Taken from [80].)

Spectrometer		A	B	C
Magnet configuration		QSDD	D	QSDD
Maximum momentum (central trajectory)	MeV/c	665	810	490
Maximum momentum	MeV/c	735	870	551
Momentum acceptance	%	20	15	25
Minimum scattering angle	deg	18	7	18
Maximum scattering angle	deg	160	62	160
Solid angle	msr	28	5.6	28
Horizontal angular acceptance	mrad	$\pm 95$	$\pm 20$	$\pm 95$
Vertical angular acceptance	mrad	$\pm 75$	$\pm 70$	$\pm 75$
Momentum resolution		$\leq 10^{-4}$	$\leq 10^{-4}$	$\leq 10^{-4}$
Angular resolution at target	mrad	$\leq 3$	$\leq 3$	$\leq 3$
Position resolution at target	mm	$3 \rightarrow 5$	$\leq 1$	$3 \rightarrow 5$

**Table 4.1:** Parameters of the three spectrometers [81]. Some of the current parameters differ from the design parameters. The new values are taken from [82].

Each spectrometer reconstructs 4 properties of the particles: the relative particle momentum  $\delta = (p - p_{\text{ref}})/p_{\text{ref}}$  (where  $p_{\text{ref}}$  is the reference momentum of the spectrometer), the vertical and horizontal angle  $\theta_0$  and  $\phi_0$ , respectively, and  $y_0$ , the  $y$ -coordinate of the intersection point of the particle track with the ( $z_{\text{tg}} = 0$ )-plane. An overview of the reference frames and the definitions of the coordinate systems is given in appendix B. These 4 parameters allow to reconstruct all necessary variables to determine the kinematics of the VCS process.

In the following subsections the spectrometers are only briefly discussed. For more information the reader is referred to reference [81].

### 4.2.1 Spectrometer magnets

#### Spectrometer A

Spectrometer A is a QSDD-type spectrometer: it consists of a quadrupole, sextupole and two dipole magnets (see figure 4.4). The magnets are designed in such a way that particles with a given momentum are focused on the same horizontal line in the focal plane. By measuring the intersection of the particle track and the focal plane, one can determine the momentum of the particle. In the dispersive direction there is a point to point relation between the target coordinates and the focal plane coordinates, which means that the dispersive angle  $\theta_0^A$ , and the relative momentum  $\delta^A$ , of the particle are reconstructed with a very good resolution.

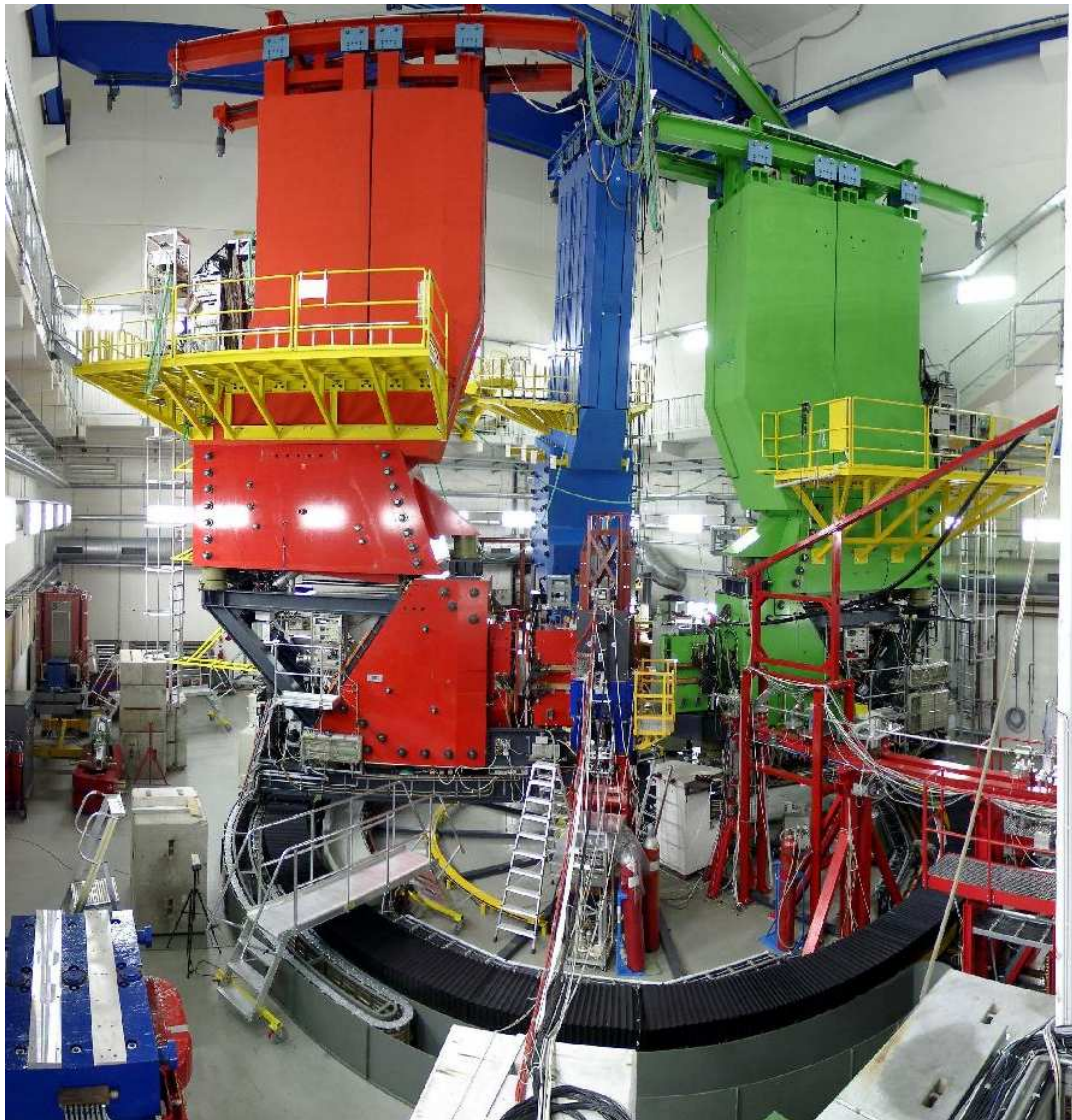


**Figure 4.3:** The three-spectrometer setup in hall A1. All three spectrometers can be rotated around the same axis. The target is placed at the intersection point of this axis and the horizontal plane through the centers of the acceptances of the spectrometers. (Taken from [80].)

Spectrometer A is designed to have a relatively large acceptance in the horizontal direction. The quadrupole and sextupole magnets of the spectrometer serve for focus corrections to the magnetic field to allow this wide angular acceptance. By consequence there is no point to point reconstruction, but a line to point reconstruction in the non-dispersive direction. This means that the reconstruction of  $y_0^A$  and thus the intersection of the particle track and the beam line is determined with a rather poor resolution (see table 4.1).

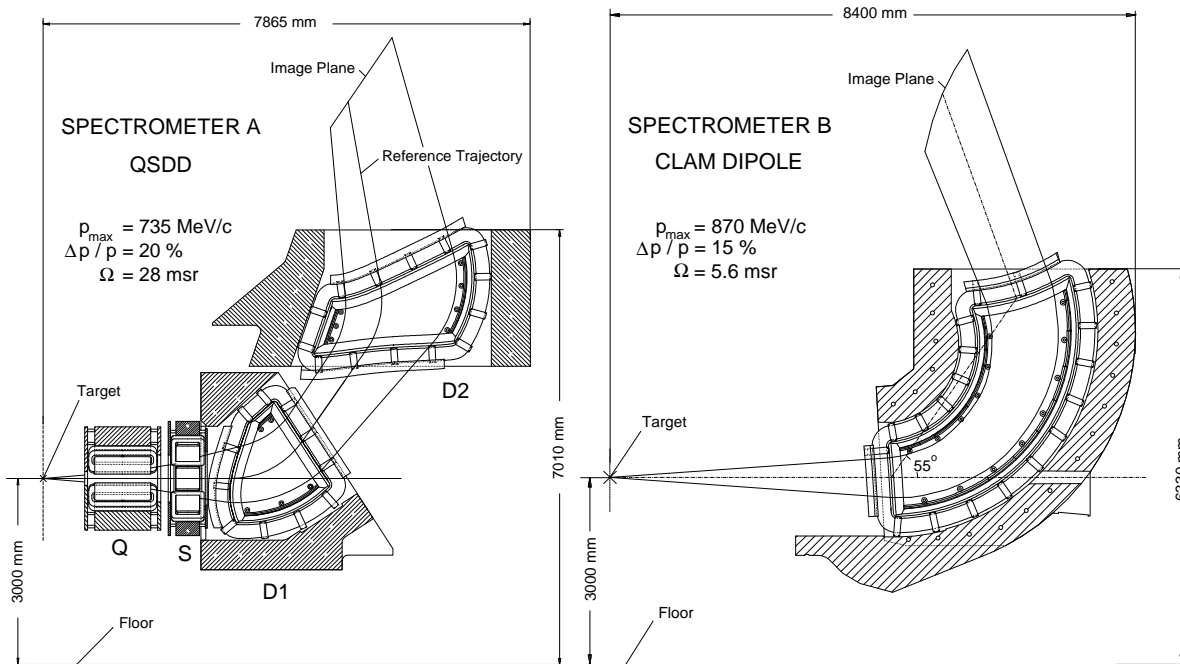


**Figure 4.4:** The magnets of spectrometer A and B. (Taken from [81].)

### Spectrometer B

Spectrometer B consists of one clamshell dipole magnet (see figure 4.4). It has a smaller acceptance in horizontal direction as compared to spectrometer A, but it is able to reconstruct the reaction vertex with a higher precision: in both directions (dispersive and non-dispersive) there is a point to point relation between the focal plane and target coordinates. For this reason spectrometer B is usually used for the reconstruction of the  $z$  coordinate of the interaction vertex. The construction of the spectrometer allows to move the spectrometer out of the horizontal plane to allow out-of-plane measurements, as was done for the measurement of the beam single-spin asymmetry (see section 3.2.4).

### Spectrometer C

Spectrometer C is of the same type as spectrometer A (QSDD), but it is smaller. For the measurement of the double-spin asymmetry this spectrometer was not used.

## 4.2.2 Focal plane detection system

The detectors in the focal plane of the spectrometers are designed to measure the particle track across the focal plane with an accuracy that permits a precise reconstruction of the target

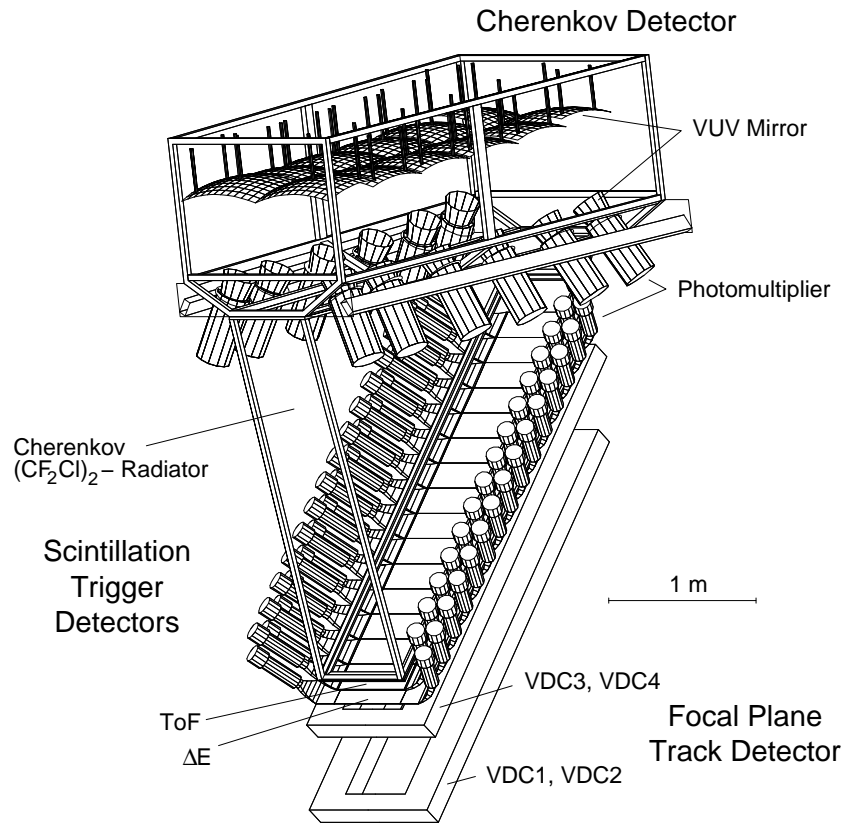


**Figure 4.5:** The detector setup in the focal plane: two double pair of VDCs measure the particle track, the trigger is generated by the scintillators and the nature of the particle is identified by the Cherenkov detector and the scintillators. (Taken from [81].)

coordinates and to identify the nature of the particle. Therefore several types of detectors are combined: vertical drift chambers (VDCs), two scintillator planes and a Cherenkov detector as displayed in figure 4.5.

### Vertical drift chambers

The desired precision for the reconstruction of the target variables in a wide kinematic range determines the specifications of the tracking detectors in the focal plane. To resolve the particle track with a very high accuracy four vertical drift chambers are used [83]. They consist of two cathode foils connected to a negative high voltage, and potential and signal wires in the middle of both foils (see figure 4.6). The wires are connected to ground potential.

When a charged particle passes through the VDC it ionizes the gas (an argon and isobutane mixture) and the created electrons drift towards the wires, where they are collected. The signal of each of the signal wires is read out. By measuring the drift time a two-dimensional projection of the particle track onto the plane perpendicular to the wires can be reconstructed.

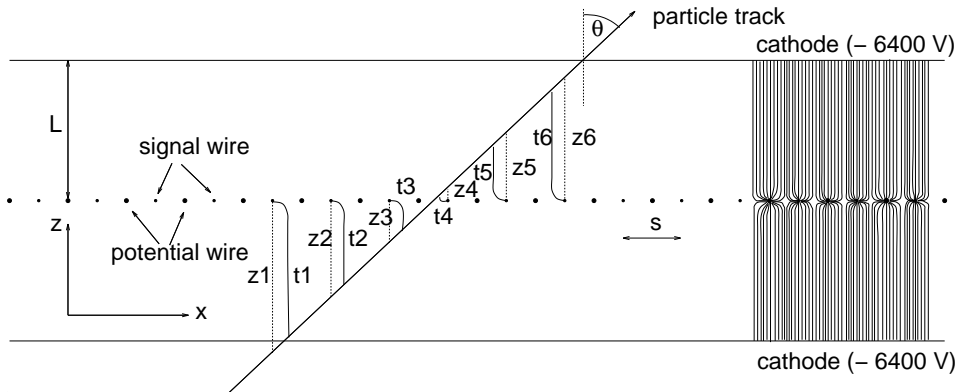


**Figure 4.6:** Working principle of a vertical drift chamber. The wires are placed between two cathode foils on negative high voltage. Based on the drift time  $t_i$  for each signal wire the vertical distance  $z_i$  is calculated. This allows a two-dimensional reconstruction of the particle track. (Taken from [81].)

This is only possible if enough wires are hit by the particles. In the spectrometers the VDCs are tilted over  $45^\circ$  with respect to the reference trajectory. In this way most particles hit 4 to 6 wires.

One VDC allows to measure one projection of the particle track and in combination with another VDC with the wires perpendicular to the first one, it is possible to reconstruct the particle track in three dimensions. In the case of the spectrometers at hall A1 the wires of the second plane (called the  $s$ -wires) are rotated over  $40^\circ$ , instead of  $90^\circ$ , with respect to the wires of the first plane ( $x$ -wires). This is done for practical reasons: the focal plane is about 2 m long. Since the angular resolution of one single pair of drift chambers is not good enough, two sets of double drift chambers are mounted in the spectrometers. With this setup a reconstruction of the focal plane coordinates with a precision of about ( $50 \mu\text{m}$ ,  $120 \mu\text{m}$ ,  $0.2 \text{ mrad}$ ,  $0.6 \text{ mrad}$ ) for  $(x, y, \theta, \phi)$  is reached.

### Scintillator detector

Two planes of scintillators are responsible for the trigger of the spectrometers. Each plane consists of 14 to 15 paddles (16 cm wide in the dispersive direction) and the segments are ordered in such a way that the gaps between the paddles are covered by one of the paddles of the other layer. When a particle passes through the scintillator, light is emitted by the material and a part of this light is detected by the photomultipliers (PMTs) attached at both sides of each paddle.

The bottom layer is 3 mm thick and is used to measure the energy loss,  $\Delta E$ , of the particles. Therefore it is called the  $\Delta E$ -plane. The second plane (time of flight scintillators - ToF) is

thicker (10 mm) and serves as the reference time point. Since scintillation is a fast process this detector generates the trigger of the spectrometer. Every time a charged particle is observed by one of the paddles, all focal plane detectors are read out by the electronics.

The scintillators are also used for particle identification: the energy loss of the detected pions and protons in the scintillator is different. The energy loss in the ToF scintillator is called  $E_{\text{ToF}}$  and by combining the  $E_{\text{ToF}}$  with the  $\Delta E$ -distributions a separation between pions and protons can be done. A separation between electrons and pions is not possible since they are both minimum ionizing particles in the momentum range of the spectrometers.

### Cherenkov detector

Charged particles moving faster than the speed of light in a medium emit Cherenkov radiation. This physical process can be used for particle identification e.g. to separate electrons and (negatively charged) pions. For the same momentum, pions are moving slower due to their higher mass. For the momentum range of the spectrometers this means that electrons emit Cherenkov light in the gas mixture, while pions do not.

After having passed through the VDCs and scintillators the particles enter a volume filled with  $(\text{CF}_2\text{Cl})_2$  as a radiator gas to produce the Cherenkov light. The light is collected by two rows of 6 mirrors (spectrometer A and C) or one single row of 5 mirrors (spectrometer B). These spherical mirrors reflect the light towards the PMTs (one for each mirror). When Cherenkov light is observed in one of these PMTs, the detected particle is tagged as an electron.

### 4.2.3 Spectrometer optics

The track of the particle after the deflection in the spectrometer magnets is represented by the focal plane coordinates  $(x, \theta, y, \phi)_{\text{fp}}$ .  $(x, y)$  is the intersection point of the track with the focal plane and  $(\theta, \phi)$  are the angles of the direction of the particle in dispersive and non-dispersive directions with respect to the focal plane reference frame. Based on the set  $(x, \theta, y, \phi)_{\text{fp}}$  the particle is traced back through the magnetic field of the spectrometer and the target coordinates  $(\delta, \theta_0, y_0, \phi_0)_{\text{tg}}$  are reconstructed. This calculation is performed by a fifth-order polynomial expansion in the focal plane coordinates:

$$\begin{aligned}
\delta &= \sum_{ijkl}^5 D_{ijkl} (x - x_{\text{ref}})^i (\theta - \theta_{\text{ref}})^j (y - y_{\text{ref}})^k (\phi - \phi_{\text{ref}})^l, \\
\theta_0 &= \sum_{ijkl}^5 T_{ijkl} (x - x_{\text{ref}})^i (\theta - \theta_{\text{ref}})^j (y - y_{\text{ref}})^k (\phi - \phi_{\text{ref}})^l, \\
y_0 &= \sum_{ijkl}^5 Y_{ijkl} (x - x_{\text{ref}})^i (\theta - \theta_{\text{ref}})^j (y - y_{\text{ref}})^k (\phi - \phi_{\text{ref}})^l, \\
\phi_0 &= \sum_{ijkl}^5 P_{ijkl} (x - x_{\text{ref}})^i (\theta - \theta_{\text{ref}})^j (y - y_{\text{ref}})^k (\phi - \phi_{\text{ref}})^l,
\end{aligned} \tag{4.1}$$

where  $(x_{\text{ref}}, \theta_{\text{ref}}, y_{\text{ref}}, \phi_{\text{ref}})$  are the focal plane coordinates of the reference track, which is the track followed by the particle that enters the spectrometer with  $(\delta = 0, \theta_0 = 0^\circ, y_0 = 0 \text{ mm}, \phi_0 = 0^\circ)$ .

The coefficients can be calculated from the magnet and detector geometry. However, in practice it is done via a  $\chi^2$ -fit to calibration measurements on specific targets and using special collimators [84]. The calibration of the spectrometer optics is valid over the complete angular acceptance of the spectrometers for all momenta within the nominal momentum acceptance.

### 4.3 Target cell

The liquid hydrogen target [85] is shown in figure 4.7. It is a 49.5 mm long, 11.5 mm wide and 10 mm high scattering cell with round end caps. It is constructed of 10  $\mu\text{m}$  thick Havar walls. The dimensions of the target cell are optimized to increase the luminosity and to reduce the energy loss of the scattered particles. The beam passes through the target along its longest direction.

The hydrogen is liquefied and cooled in a first step by a Philips-Sterling cooling machine and transported to the scattering chamber through the transfer pipe. A homogeneous temperature inside the target cell is obtained by pumping around the fluid continuously in a second loop, the Basel loop, which is cooled via the heat exchanger with the liquid hydrogen from the first cooling loop.

The temperature and pressure of the hydrogen inside the target (about 20.9 K and 1990 mbar, respectively) are continuously monitored for a precise determination of the luminosity. To prevent local heating of the target due to energy deposition of the incoming electron beam, the electron beam is deflected with an amplitude of a few mm and a frequency of a few kHz. This transverse beam position is known at any moment.

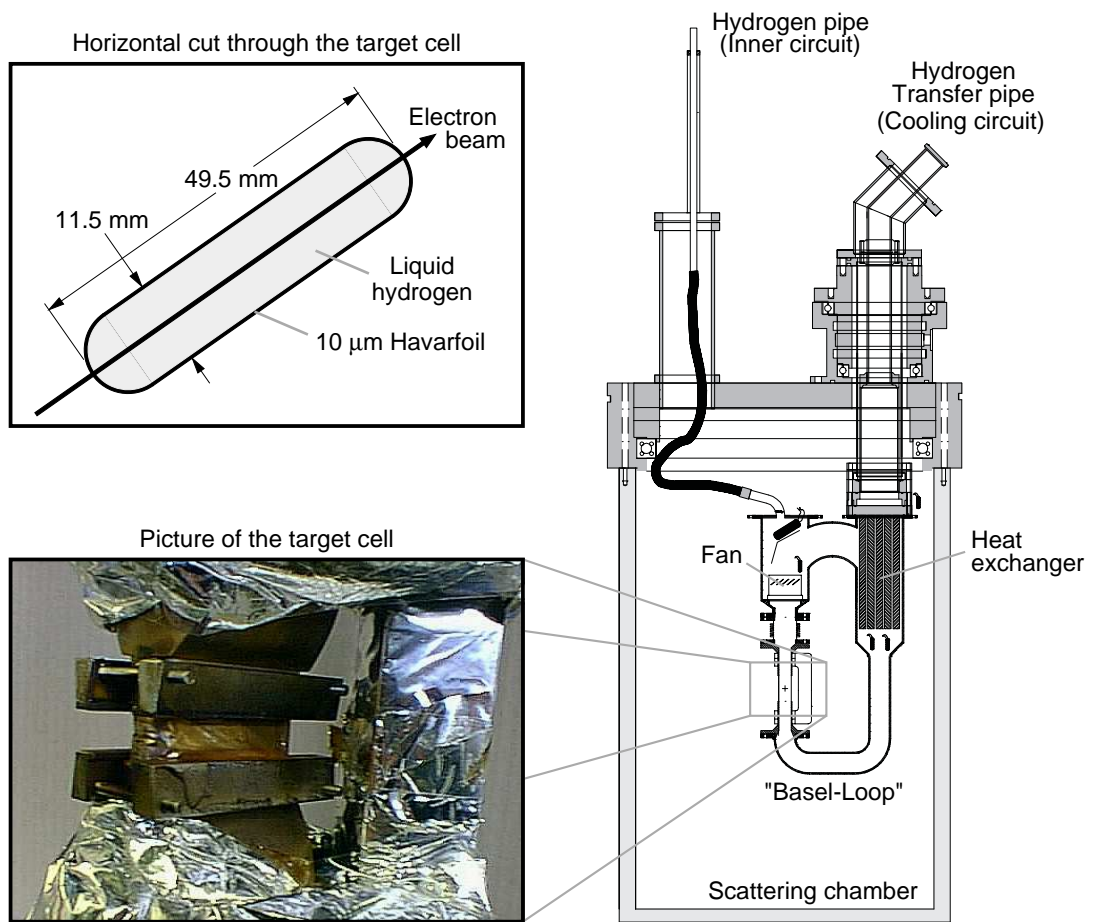


**Figure 4.7:** The liquid hydrogen target cell. On the left a top and a side view of the target cell are shown. The cooling system of the target is presented on the right. (Taken from [82].)

#### 4.4 Förster probe

The luminosity is defined by the product of the number of target nuclei per unit of surface and the number of electrons impinging on the target per unit of time. For the calculation of the luminosity, not only the target density, but also the beam current intensity must be monitored during the data taking. The measurement of the beam current is done by a Förster probe, placed at the axis of the accelerating section of the third microtron.

Two toroidal coils surround the beam. The magnetic field of the beam electrons induces currents in these toroidal coils proportional to the beam intensity. Due to the position of the Förster probe the electron bunches of all recirculations in the microtron traverse the coils and contribute to the signal. This is done to reduce the uncertainty on the obtained result.

## 4.5 Møller polarimeter

MAMI delivers a longitudinally polarized electron beam. The polarization of the beam is very important for the measurement of double-polarization observables and a polarimeter to measure the polarization of the electron beam is indispensable.

There are several types of polarimeters: Mott (e.g. [86]), Compton (e.g. [87]) and Møller (e.g. [88]) polarimeters, where the spin dependence of the cross section for the scattering of electrons on nuclei, real photons and electrons, respectively, is used to determine the polarization of the beam. In hall A1 at MAMI a Møller polarimeter is used to measure the longitudinal polarization of the beam. The main disadvantage of this type of polarimeters is that it can not be operated simultaneously with the experiment. Therefore the experiment is stopped once a day for the measurement of the beam polarization. This is justified by the fact that the beam polarization is a rather stable parameter of the MAMI accelerator.

A complete description of the Møller polarimeter can be found in the diploma and Ph.D. thesis of P. Bartsch ([89] and [90]). The subsections below give only a short summary about the working principle and the detector setup.

### 4.5.1 Principle

The scattering of electrons on electrons (both polarized) is called Møller scattering. The cross section of the process can be calculated precisely from QED and it can be separated in a spin-dependent and a spin-independent part:

$$\frac{d\sigma}{d\Omega} = \frac{d\sigma_0}{d\Omega} \left( 1 + A_e(\theta_{\text{cm}}) \mathcal{P}_b^z \mathcal{P}_t^z \right), \quad (4.2)$$

with  $\mathcal{P}_b^z$  and  $\mathcal{P}_t^z$  the polarization of the beam and the target electrons, respectively, and  $d\sigma_0/d\Omega$  is the spin-independent cross section. The analyzing power  $A_e(\theta_{\text{cm}})$  is a function of the scattering angle in the center-of-mass  $\theta_{\text{cm}}$ , and is well known from theoretical calculations [88].

By measuring the asymmetry

$$\frac{N^{\uparrow\uparrow} - N^{\uparrow\downarrow}}{N^{\uparrow\uparrow} + N^{\uparrow\downarrow}}, \quad (4.3)$$

where  $N^{\uparrow\uparrow}$  ( $N^{\uparrow\downarrow}$ ) is the event rate for parallel (anti-parallel) spin of the target and the beam electrons,  $\mathcal{P}_b^z$  can be determined, if  $\mathcal{P}_t^z$  is known.

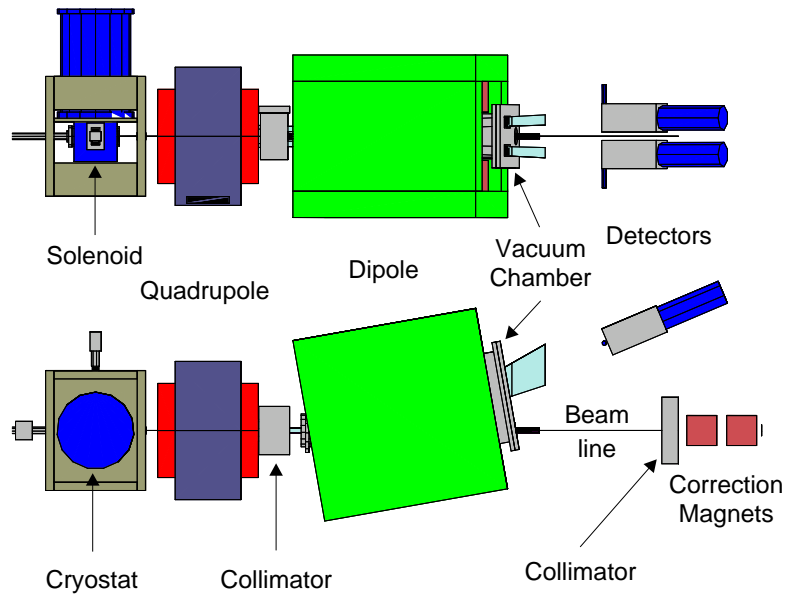


**Figure 4.8:** Side and top view of the Møller polarimeter. (Taken from [91].)

#### 4.5.2 Detector system

The Møller polarimeter is depicted in figure 4.8. The target is an iron foil, placed in the magnetic field of a He-cooled magnet. This magnetic field polarizes the target electrons in the plane of the foil. The angle between the incoming beam and the target foil is about  $20^\circ$ . The target polarization  $\mathcal{P}_t^z$  is calculated based on the strength of the magnetic field, that polarizes the target electrons to about 8%.

Both scattered and recoiling electrons are detected in coincidence using two identical detector systems mounted at one side of the beam on top of each other (symmetric with respect to the horizontal plane through the beam line). The detector system consists of a scintillator detector and a Pb-glass Cherenkov detector. The electrons are bent by a magnetic system (one quadrupole and one dipole magnet) before passing through a collimator to fix the scattering angle  $\theta_{\text{cm}}$ . The count rates for true and random coincidences, and of a luminosity detector, are monitored for the two helicity states of the incoming electrons. This allows to determine  $\mathcal{P}_b^z$  via the observed asymmetry.

### 4.6 Focal plane polarimeter

To measure the polarization of the recoiling proton another polarimeter is used. This polarimeter is mounted in the focal plane of spectrometer A. The space in the focal plane is

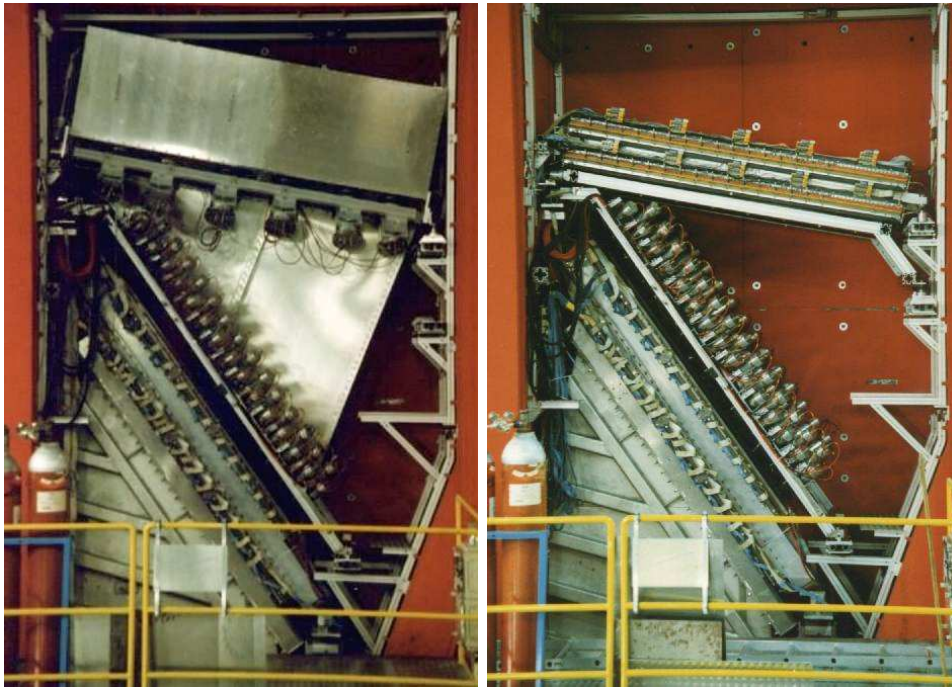


**Figure 4.9:** Pictures of the detectors in spectrometer A. In the picture on the right the Cherenkov detector has been replaced by the polarimeter. (Taken from [80].)

limited and therefore the Cherenkov detector had to be removed for the polarimeter (see figure 4.9).

The polarimeter measures the two components of the spin perpendicular to the proton momentum, while the longitudinal component is not accessible. The main advantage of using a polarimeter in the focal plane of a spectrometer is the precession of the spin in the magnetic field. This causes a mixing of the spin components, allowing to disentangle all components of the spin at the target by tracing back the spin in the magnet along the proton track. This procedure is only possible if the spin is rotated in such a way that the longitudinal component of the spin at the target contributes to the transverse component of the spin at the focal plane for a large fraction of the detected protons.

First, the working principle is explained (section 4.6.1), while section 4.6.2 describes the detector setup. For a more detailed overview the reader is referred to references [92] and [93] and the Ph.D. thesis of Th. Pospischil [82].

#### 4.6.1 Principle

The potential  $V$  of the scattering of a proton on a spinless target nucleus contains a part caused by the spin-orbit interaction: the relative orientation of the orbital angular momentum of the

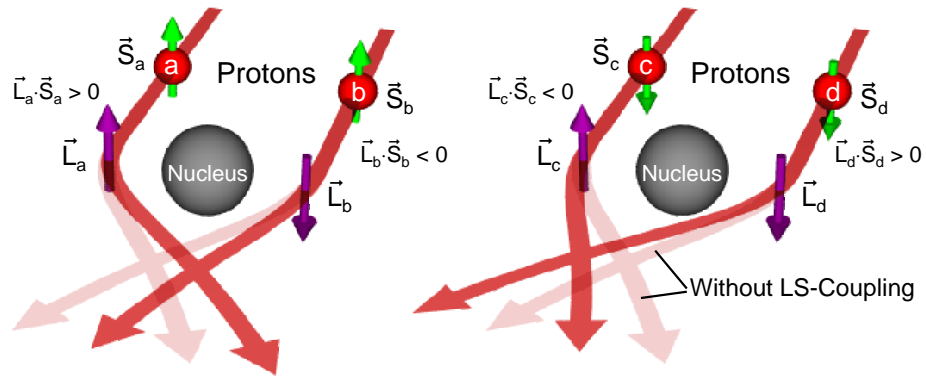


**Figure 4.10:** Scattering of a proton on a carbon nucleus. (Taken from [82].)

incident proton  $\vec{L}$  to its spin  $\vec{S}$  modifies the strength of  $V$ . The influence of the spin-orbit interaction for the electromagnetic interaction is much smaller than the dominating central potential  $V_r$ . This is not the case for the nuclear interaction, and the potential  $V$  can be split into a central part and the spin-orbit interaction  $V_{LS}$ :

$$V = V_r + V_{LS}(\vec{L} \cdot \vec{S}) . \quad (4.4)$$

Note that this equation is only valid if the spin of the target nuclei vanishes, which is the case for e.g.  $^{12}\text{C}$ . A proton for which  $\vec{L}$  is oriented in the same direction as its spin  $\vec{S}$  is deflected stronger than when  $\vec{L} \cdot \vec{S} < 0$ . This is indicated in figure 4.10: protons a and d are deflected over a larger angle than protons b and c. Suppose that all protons are polarized in the direction indicated by  $\vec{S}_a$ , then one would observe a left-right asymmetry in the scattering angles due to the strong interaction for protons that have scattered in the plane perpendicular to  $\vec{S}_a$ . By measuring this asymmetry one can calculate the polarization of the ensemble of protons. The orbital angular momentum for the scattering process is always perpendicular to the scattering plane, which means that only the polarization components perpendicular to the direction of the proton can be measured through this process.

The scattering of the proton on the carbon analyzer can be described by the polar and azimuthal angles  $(\theta_{fpp}, \phi_{fpp})$  in the proton reference frame (see appendix B.5). The spin-orbit coupling modifies the  $^{12}\text{C}(\vec{p}, p')$  cross section as compared to the polarization independent part  $\sigma_0(\theta_{fpp}, T_{CC})$  by adding a  $\phi_{fpp}$ -dependent part (e.g. [92]):

$$\sigma(\theta_{fpp}, \phi_{fpp}, T_{CC}) = \sigma_0(\theta_{fpp}, T_{CC}) \left( 1 + A_C(\theta_{fpp}, T_{CC}) (\mathcal{P}_y \cos \phi_{fpp} - \mathcal{P}_x \sin \phi_{fpp}) \right) , \quad (4.5)$$

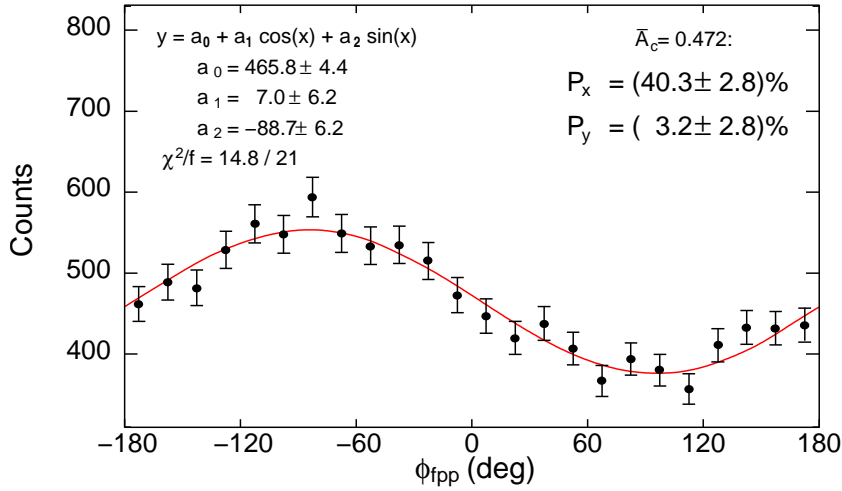


**Figure 4.11:**  $\mathcal{P}_x$  and  $\mathcal{P}_y$  are determined using a fit of  $a_0 + a_1 \cos \phi_{fpp} + a_2 \sin \phi_{fpp}$  to the observed  $\phi_{fpp}$ -distribution. (Taken from [82].)

where  $A_C(\theta_{fpp}, T_{CC})$  is the analyzing power of  $^{12}\text{C}$ . By fitting  $a_0 + a_1 \cos \phi_{fpp} + a_2 \sin \phi_{fpp}$  to the observed  $\phi_{fpp}$ -distribution the polarization components  $\mathcal{P}_x$  and  $\mathcal{P}_y$  can be calculated as shown in figure 4.11.

The analyzing power depends on  $\theta_{fpp}$  and on the kinetic energy of the proton at the center of the graphite analyzer  $T_{CC}$ . The analyzing power is well known: it has been measured by Pospischil *et al.* [92], Aprile-Giboni *et al.* [94] and McNaughton *et al.* [95]. In this analysis the parameterizations of McNaughton and Pospischil are used.

#### 4.6.2 Detector system

As analyzer material a 7 cm thick carbon slab is used. The reconstruction of the polar and azimuthal scattering angles requires proton tracking before and after the scattering process. The tracking before the analyzer is performed by the VDCs, and after the scattering on the graphite the proton track is measured by two double-planes of horizontal drift chambers (HDCs) [93].

Figure 4.12 shows a horizontal drift chamber. It consists of wires placed on different potentials: the signal wires are connected to a positive high voltage, and the potential wires are grounded. The wires are stretched across the chambers under  $45^\circ$  with respect to the frames and the wires of the two HDCs of one pair are perpendicular to each other. Above and below the wires grounded cathode foils are placed. The HDCs are filled with a gas mixture of 80% ethane and 20% argon.

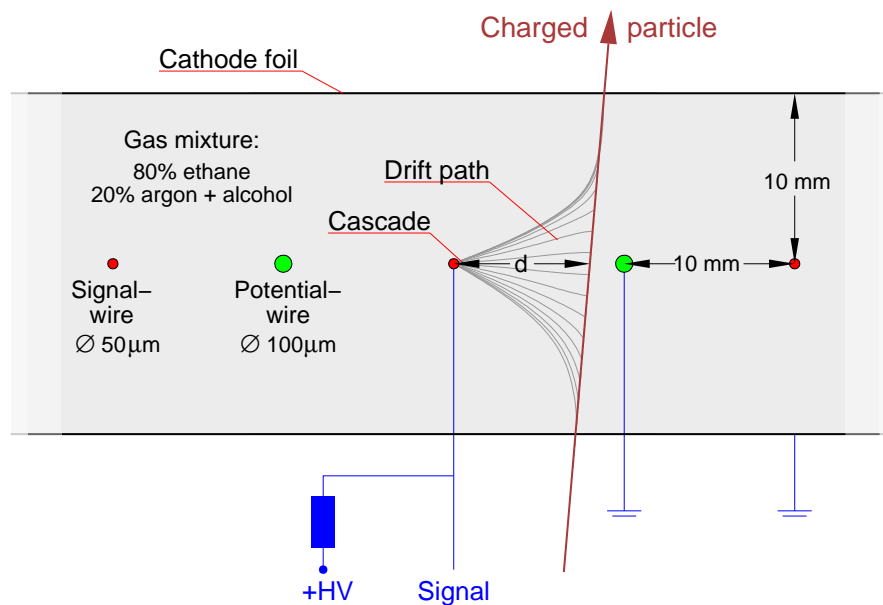


**Figure 4.12:** The horizontal drift chamber of the focal plane polarimeter. (Taken from [82].)

A charged particle passing through the gas mixture creates a number of charged particles. The electrons drift in horizontal direction to the signal wires of the HDC. The drift velocity of the electrons is known and a measurement of the drift time allows the reconstruction of the drift distance,  $d$ . For the precise reconstruction of the track the data acquisition electronics of the HDC is designed to determine whether the particle has passed on the left or on the right of the struck wire by measuring the signals induced on the neighboring potential wires. Using this technique the intersection point of the particle and the HDC is known and a spatial resolution of  $300\ \mu\text{m}$  is achieved.



---

# Monte Carlo simulation

---

For the analysis of the unpolarized VCS experiments at MAMI and JLab a Monte Carlo simulation was developed. The simulation generates photon electroproduction events according to a specified cross section (e.g. the Bethe-Heitler + Born cross section) and it takes into account all relevant resolution-deteriorating effects. Using the simulation the ‘effective’ solid angle for the various experimental settings can be calculated, which is necessary for the determination of the absolute cross section.

Apart from the determination of the effective solid angle, the simulation can be used to generate realistic spectra of the experimental variables. This gives important insights in the experiment and it allows to understand possible experimental problems.

The simulation is described extensively in [96]. This chapter focuses mainly on the new features in the simulation with respect to the version that was used for the analysis of the first experiment at MAMI-A1. After a short overview of the simulation (section 5.1) the implementation of the radiative corrections is discussed in section 5.2. In section 5.3 the treatment of the resolution effects in the focal plane detectors is explained. Finally, the results of the simulation are compared to the experimental data in section 5.4.

## 5.1 The simulation package

The simulation is divided into several programs, each of them dedicated to a specific part:

1. In the first step of the simulation, photon electroproduction events are generated according to the desired cross section behavior. All resolution-deteriorating effects taking place from the target up to the entrance windows of the spectrometers are implemented: energy losses by ionization and multiple scattering, external bremsstrahlung, and the part of the internal bremsstrahlung which influences the kinematics of the process.
2. The second program applies the resolution of the spectrometers to the simulated data. These resolution effects are implemented at the level of the vertical drift chambers of the spectrometers in order to reproduce the correlations in the errors.
3. Finally, the analysis program performs the full event reconstruction based on the output of the resolution program. The data file produced in this step of the simulation can be used to calculate the effective solid angle and it can be compared to the experimental data.

The simulation of the physical processes at the target, done by the first program, is the most time-consuming part of the simulation. The modular structure of the simulation allows to change e.g. the implementation of the resolution effects, without having to redo the generation of the VCS events.

Apart from these three main programs there are two more programs important for the simulation:

- The first one calculates the cross section grids used in the first step of the simulation. The use of cross section grids is necessary to increase the speed of the event generation.
- The last program uses the data files generated by the analysis program to calculate the effective solid angle. This effective solid angle is used for the determination of the unpolarized cross section.

### 5.1.1 VCS event generator

Before the generation of the VCS events, the simulation phase space in which the events have to be generated is determined. The cross section is differential in  $k'$ ,  $\hat{k}'$  and  $\hat{q}'_{\text{cm}}$ , and therefore the simulation phase space has to be a five-dimensional box  $\Delta k' \Delta \Omega_{e'}$   $\Delta \Omega_{\gamma\gamma_{\text{cm}}}$ . While being not too large, it should still cover the complete acceptance of the spectrometers. To be more precise: the simulation phase space should contain every event that possibly gets accepted

in the spectrometers. This means that it should be larger than the angular and momentum acceptances of the spectrometers: resolution effects taking place in the target and along the path towards the spectrometers' entrances affect the direction and momenta of the particles.

Once the simulation phase space has been defined, the generation of the events is started. First, the interaction point is sampled inside the liquid hydrogen target according to the beam position rastering. Energy losses, multiple scattering and external bremsstrahlung modify the momentum of the electron on its way to the interaction point.

At the interaction vertex the electron may undergo real internal bremsstrahlung (see section 5.2.2). Then, the four-vector of the VCS inducing electron is obtained and an  $ep \rightarrow e'p'\gamma$  event is constructed by sampling a scattered electron (direction and momentum) and a real outgoing photon direction in the simulation phase space using the acceptance-rejection method in five dimensions with a constant envelope. The cross section value is obtained by performing a logarithmic interpolation in the cross section grid. After the generation of the scattered particles, an energy loss by real internal bremsstrahlung is sampled for the outgoing electron.

Next, the outgoing particles are subjected to energy losses and multiple scattering. In addition to these resolution effects the outgoing electron can lose a part of its energy via external bremsstrahlung. Finally, the particles are tracked up to the entrances of the spectrometers and a check is made whether they are detected by the spectrometers or not.

During the simulation the simulated luminosity  $\mathcal{L}_{\text{sim}}$  is calculated.  $\mathcal{L}_{\text{sim}}$  is equivalent to the experimental one and it is used as a normalization factor for the solid angle and to compare simulated and experimental distributions on an absolute scale.  $\mathcal{L}_{\text{sim}}$  is calculated using

$$\mathcal{L}_{\text{sim}} = \frac{N_{\text{LPS}}}{\int_{\text{LPS}} \frac{d^5\sigma}{dk' d\Omega_{e'} d\Omega_{\gamma\text{cm}}} dk' d\Omega_{e'} d\Omega_{\gamma\text{cm}}}, \quad (5.1)$$

where  $N_{\text{LPS}}$  is the number of counts in the luminosity phase space (LPS), a sub-part of the simulation phase space and the denominator is the integral of the cross section over the luminosity phase space. The choice of the luminosity phase space is in principle arbitrary. However, some specific features of the Monte Carlo put strong restrictions on this choice [96].

### 5.1.2 Detector resolution effects

The second program of the simulation package introduces the resolution effects of the spectrometers. The program starts from the target variables, delivered by the event generator, and modifies them by adding the detectors' resolution.

In the experiment the particles are bent upwards to the focal plane, where their tracks are measured using vertical drift chambers (VDCs). In the analysis the track is traced back to the

target using the optical transport matrices to calculate the target variables (see section 4.2.3). The resolution of the VDCs will cause correlated errors on the reconstructed target variables due to this optical transport. The goal of the simulation is to reproduce these correlations.

This is done by applying the resolution effects in the focal plane of the spectrometers. The particles are transported to the focal plane where two types of errors are sampled: the multiple scattering in the materials of the focal plane detectors and the resolution of the wire chambers. In this scheme two tracks are considered: one with, and one without applying these resolution effects. Both particle tracks are used to reconstruct two sets of target variables and the difference between both sets quantifies the error. In this way correlations between the errors on the target variables are reconstructed. More details about this procedure are given in section 5.3.

### 5.1.3 Event reconstruction

The last part of the simulation package performs the event reconstruction in the same way as is done for the experimental data. First, the path lengths of the particles in the materials of the target are calculated to correct for energy losses. Afterwards, the kinematics of each event is reconstructed and all variables needed for the analysis of the data are calculated.

The output of the program is a data file which is used to calculate the effective solid angle (see section 5.1.5) and to compare the simulation to the data. The procedure to compare simulated and experimental data on an absolute scale is explained in section 5.4.

### 5.1.4 Cross section grid

To generate the events according to the desired cross section a fast algorithm for calculating this cross section is necessary. The cross section used in the simulation is the BH+B one. This cross section is known once the form factors of the proton are known and depends on the variables  $(q_{cm}, q'_{cm}, \varepsilon, \theta_{\gamma\gamma cm}, \varphi)$ .

An example of how the cross section behaves as a function of  $\theta_{\gamma\gamma cm}$  and  $\varphi$  for fixed  $q_{cm}$ ,  $q'_{cm}$  and  $\varepsilon$  is shown in figure 5.1. It is symmetric with respect to the scattering plane ( $\varphi = 0^\circ$ ), and therefore only a 'half-sphere' is shown. One clearly observes the two Bethe-Heitler peaks corresponding to real photon emission around the incoming and outgoing electron directions. Over the complete angular range the cross section varies by several orders of magnitude. However, if one moves away from the peak-regions, the cross section flattens substantially.

The theoretical code [53] to calculate the BH+B cross section on an event-by-event basis in the simulation is too slow. To solve this problem, the code is used to calculate the BH+B cross section at the nodes of a five-dimensional grid in the variables  $(q_{cm}, q'_{cm}, \varepsilon, \theta_{\gamma\gamma cm}, \varphi)$ . The

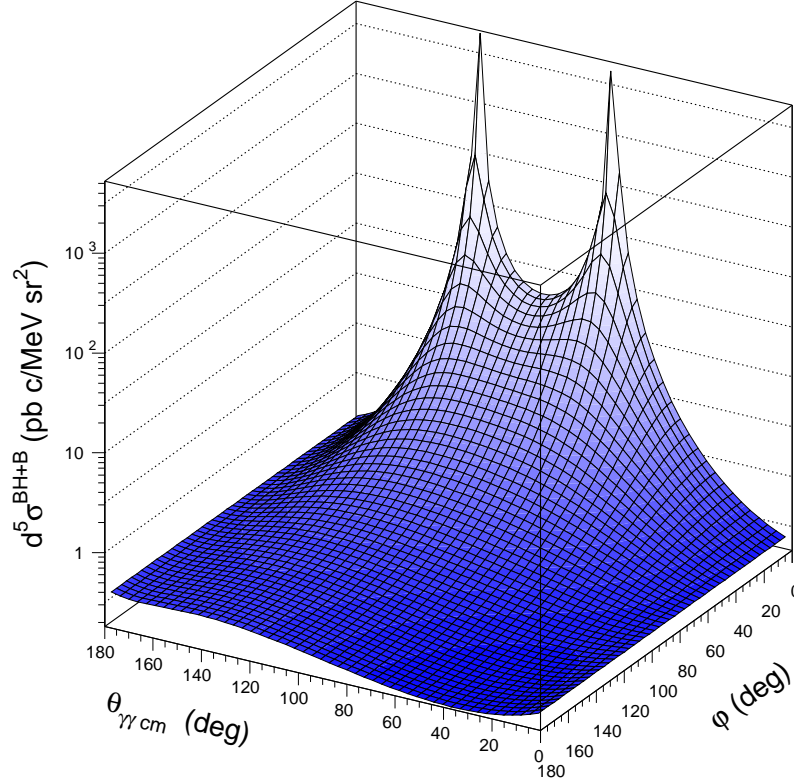


**Figure 5.1:** The five-fold differential cross section of the BH+B process  $d^5\sigma^{\text{BH+B}}$  as a function of  $\theta_{\gamma\gamma\text{cm}}$  and  $\varphi$  on a logarithmic scale for  $(q_{\text{cm}} = 600 \text{ MeV}/c, q'_{\text{cm}} = 45 \text{ MeV}/c$  and  $\varepsilon = 0.62$ ).

dimension of the grid in each of these variables is (12,33,6,45,31), which means that it contains  $3.3 \cdot 10^6$  cross section samples. In the simulation the cross section value is then obtained by interpolating in this grid, which makes the calculation faster by a factor of about 1000. In practice, a logarithmic interpolation is performed, reaching an accuracy of better than 1% over the complete simulation phase space.

### 5.1.5 Effective solid angle

For an ideal experiment the differential cross section  $d\sigma/d\Omega$ , is determined from the number of counts detected in a given phase space bin  $N_{\text{exp}}$ , the integrated luminosity  $\mathcal{L}_{\text{exp}}$ , and the solid angle of the acceptance of the detection apparatus  $\Delta\Omega$ , via

$$\frac{d\sigma}{d\Omega} = \frac{1}{\Delta\Omega} \cdot \frac{N_{\text{exp}}}{\mathcal{L}_{\text{exp}}}. \quad (5.2)$$

It is clear that in order to derive precise differential cross sections from the measured data,  $\Delta\Omega$  has to be accurately known.

However, the finite size of the bins in the experiment makes it more difficult to determine the cross section in a given point of the phase space. The number of counts in a given bin of finite dimensions is

$$N_{\text{exp}} = \mathcal{L}_{\text{exp}} \cdot \int \frac{d\sigma}{d\Omega} d\Omega = \mathcal{L}_{\text{exp}} \cdot \frac{\int \frac{d\sigma}{d\Omega} d\Omega}{\int d\Omega} \int d\Omega = \mathcal{L}_{\text{exp}} \cdot \left\langle \frac{d\sigma}{d\Omega} \right\rangle \cdot \Delta\Omega_1, \quad (5.3)$$

where  $d\Omega$  represents an infinitesimal bin in the phase space under study and  $\Delta\Omega_1$  the geometrical solid angle of the bin. Using equation (5.3) one determines  $\langle d\sigma/d\Omega \rangle$ , the cross section averaged over the solid angle  $\Delta\Omega_1$ .

When the cross section is not constant, ascribing the average cross section to the mean kinematics results in a bias. One can solve this bias by ascribing the measurement to an appropriate different kinematics (c.f. [97]). This is unpractical in the case of virtual Compton scattering because the cross section depends on five kinematical variables. In this case one can stick to the central kinematics (or choose any other kinematics in the bin) and apply an appropriate correction to the average cross section in order to obtain an unbiased result. The choice has been made to include this correction factor in the solid angle by defining another solid angle  $\Delta\Omega_2$ :

$$\begin{aligned} \frac{N_{\text{exp}}}{\mathcal{L}_{\text{exp}}} &= \left( \frac{d\sigma}{d\Omega} \right)_0 \int \left( 1 + \frac{\frac{d\sigma}{d\Omega} - \left( \frac{d\sigma}{d\Omega} \right)_0}{\left( \frac{d\sigma}{d\Omega} \right)_0} \right) d\Omega \\ &= \left( \frac{d\sigma}{d\Omega} \right)_0 \cdot (\Delta\Omega_1 + \omega) = \left( \frac{d\sigma}{d\Omega} \right)_0 \cdot \Delta\Omega_2, \end{aligned} \quad (5.4)$$

where  $(d\sigma/d\Omega)_0$  is the cross section at the chosen point. The solid angle  $\Delta\Omega_2$  deviates from  $\Delta\Omega_1$  by the amount  $\omega$ , which depends on the curvature of the cross section over the bin and the chosen point in the bin. To obtain  $\Delta\Omega_2$  one must know with sufficient accuracy the cross section behavior of the process under study in the phase space region under consideration. In principle, this must be the cross section which one is going to measure and which is therefore unknown at the moment of the simulation. A sufficiently good approximation is the BH+B cross section, since it is expected to deviate by less than 10% from the total  $ep \rightarrow e'p'\gamma$  cross section. In particular its curvature, which is the decisive feature in this context, is supposed to be a very good approximation to the real one.

The solid angles  $\Delta\Omega_1$  or  $\Delta\Omega_2$  must incorporate not only the actual detection geometry, but also the various resolution effects. This is why these solid angles are called 'effective', and why they can only be calculated by a Monte Carlo simulation. In addition, the resulting cross section has to be corrected for radiative effects. Part of the corrections are implemented directly in the simulation, whereas the other part is applied to the solid angle using a constant

factor  $f_{\text{cor}}$  over the whole phase space. The treatment of the radiative corrections is discussed in the next section.

## 5.2 Radiative effects

The radiative tail is a well-known feature of electron scattering experiments: after correction for the energy losses by ionization, the energy spectrum of the scattered electron shows a peak at the kinematically expected value, but this peak is accompanied by a radiation tail to lower energies [98] (see also figure 5.10.c and d). This tail is caused by energy loss of the incoming and outgoing electron via external bremsstrahlung in the materials of the target and up to the spectrometer's entrance and via internal real radiation in the scattering process itself. These effects are of course also present in VCS experiments and give rise to the radiative tail observed in the spectrum of the missing mass squared  $M_X^2$ , defined as  $(\mathbf{k} + \mathbf{p} - \mathbf{k}' - \mathbf{p}')^2$ . Such a distribution is shown in figure 5.2.

For the calculation of the effective solid angles, one needs a procedure to generate the radiation tail in the Monte Carlo simulation. Indeed, experimentally one applies a cut in the  $M_X^2$  spectrum around  $0 \text{ MeV}^2/c^4$  to select real-photon production events, and the same cut must be applied to the simulated events. The simulation reproduces the radiative tail well (see figure 5.2), which is very important because the final cross-section result has to be independent of the cut in  $M_X^2$ . In fact, the influence of the position of the cut in the missing mass squared on the resulting cross section was lower than 1% in this analysis. By reproducing the radiation tail in the simulation a part of the radiative corrections is taken into account and the simulated radiative tail is properly convoluted with the detector acceptance. Internal and external real radiation are incorporated in the simulation by only changing the electron energy, while its direction is assumed to be unaffected by the radiation effects (angular peaking approximation).

### 5.2.1 External bremsstrahlung

An electron passing through a slice of material of thickness  $t$  (in units of radiation length) emits photons due to bremsstrahlung. The energy loss  $\Delta E$  of the electron is equal to the sum of the energies of all produced photons. The distribution of  $\Delta E$  is given in very good approximation by [99] ( $t < 0.05$ )

$$I_{\text{ext}}(E_0, \Delta E, t) = \frac{bt}{1 - 0.5772bt} \left(\frac{\Delta E}{E_0}\right)^{bt} \left[ \frac{1}{\Delta E} \left(1 - \frac{\Delta E}{E_0} + \frac{3}{4} \left(\frac{\Delta E}{E_0}\right)^2\right) \right]. \quad (5.5)$$

$E_0$  is the kinetic energy of the electron before bremsstrahlung and  $b = \frac{4}{3}$ .

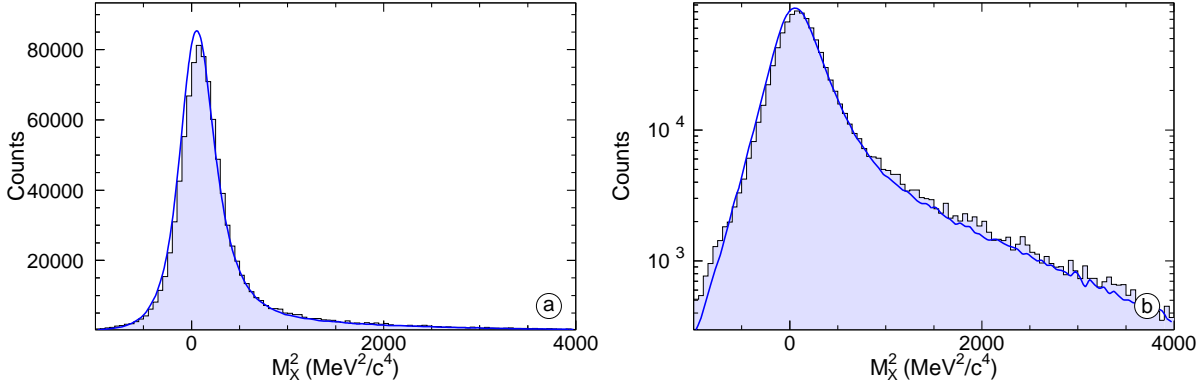


**Figure 5.2:** The experimental (histogram) and simulated (line) distributions of the missing mass squared  $M_X^2$  for the kinematics of the present experiment ( $q'_{\text{cm}} = 90$  MeV/c,  $\varepsilon = 0.645$ ,  $q_{\text{cm}} = 600$  MeV/c) for the events used for the calculation of the unpolarized cross section on a linear (a) and logarithmic (b) scale. For the simulation the BH+B cross section was used and the simulated distribution is normalized using the factor  $\mathcal{L}_{\text{exp}} / (\mathcal{L}_{\text{sim}} f_{\text{cor}})$ .

An energy loss is sampled according to the distribution (5.5) and the electron energy is decreased by the obtained value for  $\Delta E$ . Only the energy of the electron is changed, which is equivalent with photon emission along the electron-momentum direction (peaking approximation). This is a good approximation, since bremsstrahlung is very forwardly peaked. The smaller  $\Delta E$ , the better this approximation. Moreover, the scattering angle due to bremsstrahlung is small compared to that from multiple scattering.

## 5.2.2 Internal bremsstrahlung

### Virtual and real internal corrections

The cross section for the  $ep \rightarrow e'p'\gamma$  reaction  $\sigma_{\text{th}}$  i.e. for the process involving only one virtual photon and one real photon, cannot be measured directly, since in reality the pure  $p(e, e'p')\gamma$  process can be accompanied by additional photons, either real or virtual. These internal radiative effects give rise to a measured cross section  $\sigma_{\text{exp}}$ , which deviates from  $\sigma_{\text{th}}$ :

$$\sigma_{\text{exp}} = (1 + \delta_{\text{tot}})\sigma_{\text{th}}. \quad (5.6)$$

The correction term  $\delta_{\text{tot}}$  is negative and depends on the cut in the radiative tail accompanying the scattering process  $\Delta E_{\text{cm}}^c$ . The internal radiative corrections to VCS are discussed in detail

in [100]. Written in first order, one has

$$\delta_{\text{tot}}^{(1)} = \delta_{\text{vac}} + \delta_{\text{ver}} + \delta_{\text{rad}}. \quad (5.7)$$

where  $\delta_{\text{vac}}$  accounts for vacuum polarization diagrams,  $\delta_{\text{ver}}$  is the vertex correction and  $\delta_{\text{rad}}$  is the correction for radiation in the one-additional-photon-approximation. One can approximately take into account higher order radiative corrections by writing [100]:

$$\sigma_{\text{exp}} = \frac{e^{\delta_{\text{ver}} + \delta_{\text{rad}}}}{(1 - \frac{\delta_{\text{vac}}}{2})^2} \sigma_{\text{th}}. \quad (5.8)$$

For  $Q^2 \gg m_e^2$ , one has:

$$\delta_{\text{rad}} \approx \frac{\alpha}{\pi} \left\{ \ln \left( \frac{(\Delta E_{\text{cm}}^c)^2}{E_{\text{cm}} E'_{\text{cm}}} \right) \left[ \ln \left( \frac{Q^2}{m_e^2} \right) - 1 \right] - \frac{1}{2} \ln^2 \left( \frac{E_{\text{cm}}}{E'_{\text{cm}}} \right) + \frac{1}{2} \ln^2 \left( \frac{Q^2}{m_e^2} \right) - \frac{\pi^2}{3} + Sp \left( \cos^2 \frac{\theta_{e'_{\text{cm}}}}{2} \right) \right\}, \quad (5.9)$$

$$\delta_{\text{ver}} \approx \frac{\alpha}{\pi} \left\{ -\frac{3}{2} \ln \left( \frac{Q^2}{m_e^2} \right) - 2 - \frac{1}{2} \ln^2 \left( \frac{Q^2}{m_e^2} \right) + \frac{\pi^2}{6} \right\}, \quad (5.10)$$

$$\delta_{\text{vac}} \approx \frac{2\alpha}{3\pi} \left\{ -\frac{5}{3} + \ln \left( \frac{Q^2}{m_e^2} \right) \right\}, \quad (5.11)$$

where  $E_{\text{cm}}$  ( $E'_{\text{cm}}$ ) is the incoming (outgoing) electron energy at the reaction vertex,  $\alpha$  is the fine-structure constant and  $m_e$  is the electron mass.  $Sp$  is the Spence function, e.g. [100]. The virtual correction terms  $\delta_{\text{ver}}$  and  $\delta_{\text{vac}}$  are independent of  $\Delta E_{\text{cm}}^c$  and nearly constant over the phase space of interest. The correction for these effects will be applied by a constant correction factor  $f_{\text{cor}}$  to the measured cross section. Since only the first term of  $\delta_{\text{rad}}$ ,  $\delta_{\text{rad1}}$ , depends on  $\Delta E_{\text{cm}}^c$ , this term is related to the radiative tail:

$$\delta_{\text{rad1}} = \frac{\alpha}{\pi} \ln \left( \frac{(\Delta E_{\text{cm}}^c)^2}{E_{\text{cm}} E'_{\text{cm}}} \right) \left[ \ln \left( \frac{Q^2}{m_e^2} \right) - 1 \right], \quad (5.12)$$

$$\delta_{\text{rad2}} = \delta_{\text{rad}} - \delta_{\text{rad1}}.$$

The remaining terms of  $\delta_{\text{rad}}$ ,  $\delta_{\text{rad2}}$ , are independent of the cut position and they can be considered to be constant over the phase space of interest. Therefore, they will be treated in the same way as  $\delta_{\text{ver}}$  and  $\delta_{\text{vac}}$ . The global correction factor is given by

$$f_{\text{cor}} = \frac{e^{\delta_{\text{ver}} + \delta_{\text{rad2}}}}{(1 - \frac{\delta_{\text{vac}}}{2})^2}. \quad (5.13)$$

The radiative tail appears in the spectrum of  $M_X^2$ . The relation between  $\Delta E_{\text{cm}}^c$  and the corresponding cut in the missing mass squared,  $M_X^{c,2}$ , is given by [100]

$$\Delta E_{\text{cm}}^c = \frac{\sqrt{M_X^{c,2}}}{2}. \quad (5.14)$$

Given this relation the correction factor in (5.8) could be used to calculate  $\sigma_{\text{th}}$  based on the measured cross section  $\sigma_{\text{exp}}$ , without including the internal radiative effects in the simulation. However, this procedure is only valid if the acceptance of the detectors does not cut in some parts of the phase space more severely in  $M_X^2$  than the cut on the missing mass itself. Since this happens in the present experiment (see section 5.2.4) the simulation must generate the full radiative tail by implementing electron energy losses by radiation. In addition, this allows to reproduce realistic spectra of kinematical variables which can be compared to the experimental data.

### Generating a radiative tail due to internal real radiation

The  $\Delta E_{\text{cm}}^c$ -dependent part of the radiative correction,  $\mathcal{C}_{\text{rad}}$ , can be written as

$$\mathcal{C}_{\text{rad}} = \exp(\delta_{\text{rad}1}) = \left( \frac{(\Delta E_{\text{cm}}^c)^2}{E_{\text{cm}} E'_{\text{cm}}} \right)^a = \left( \frac{\Delta E_{\text{cm}}^c}{E_{\text{cm}}} \right)^a \left( \frac{\Delta E_{\text{cm}}^c}{E'_{\text{cm}}} \right)^a, \quad (5.15)$$

where  $a = \frac{\alpha}{\pi} [\ln(\frac{Q^2}{m_e^2}) - 1]$ .  $\mathcal{C}_{\text{rad}}$  is the part of the radiative correction incorporated in the simulation. Assuming angular peaking, we can write [100]

$$\left( \frac{\Delta E_{\text{cm}}^c}{E_{\text{cm}}} \right)^a \left( \frac{\Delta E_{\text{cm}}^c}{E'_{\text{cm}}} \right)^a = \left( \frac{\Delta E_e}{E_e} \right)^a \left( \frac{\Delta E'_e}{E'_e} \right)^a. \quad (5.16)$$

Following [100] we interpret the factors  $(\Delta E_e/E_e)^a$  and  $(\Delta E'_e/E'_e)^a$  as the fraction of incoming and outgoing electrons respectively, which have lost less than  $\Delta E_e$  due to internal real radiation. To sample  $\Delta E$  the distribution,  $I_{\text{int}}(E, \Delta E, a)$  is used:

$$I_{\text{int}}(E, \Delta E, a) = \frac{a}{\Delta E} \left( \frac{\Delta E}{E} \right)^a, \quad (5.17)$$

which is normalized to 1. Note the similarity between  $I_{\text{int}}(E, \Delta E, a)$  and the leading term of  $I_{\text{ext}}(E, \Delta E, t)$  (equation (5.5)).  $bt$  has been replaced by the quantity  $a$ , which is known in the literature as 'equivalent radiator' [101], i.e. an imaginary radiator placed before and after the scattering center to generate internal real radiation.

The procedure used to introduce the radiation tail due to internal radiation in the Monte Carlo simulation is then:

1. Sample an energy loss  $\Delta E_e$  according to the distribution (5.17) with  $E$  equal to the incoming electron energy  $E_e$ .
2. Generate the kinematics of a  $ep \rightarrow e'p'\gamma$  event at the vertex for the reduced energy  $E_e - \Delta E_e$  of the incoming electron. The events are sampled according to the cross section at this reduced energy. After the scattering process the outgoing electron has an energy  $E'_e$  at the vertex.
3. Sample an energy loss  $\Delta E'_e$  according to the distribution (5.17) with  $E = E'_e$ . The outgoing electron energy is now  $E'_e - \Delta E'_e$ .

Remark that the above procedure implies electron-energy losses both at the incoming and the outgoing electron sides. To calculate the equivalent-radiator thickness  $a$ , one needs the value of  $Q^2$  for the event, which one can only calculate after the complete process has taken place. However, due to the slow variation of  $\ln(\frac{Q^2}{m_e^2})$ , one obtains a very good approximation by using the value of  $Q^2$  given by elastic electron-proton scattering at the nominal beam momentum  $k_i$  and scattering angle  $\theta_e$ .

### 5.2.3 Testing the radiative corrections in the simulation

In the previous section a procedure was described to apply the factor  $\mathcal{C}_{\text{rad}}$  in the simulation. This paragraph describes a procedure used to compare the result of the simulation to the theoretically calculated correction factor. To this end a special version of the Monte Carlo simulation was developed. In this simulation only the internal real bremsstrahlung is incorporated. Up to now a similar procedure had only been tested for elastic scattering.

In section 2.4.1 it is explained that the kinematics of the VCS reaction is completely determined by 5 variables:  $(Q^2, \varepsilon, q'_{\text{cm}}, \varphi, \theta_{\gamma\gamma\text{cm}})$ , and that a bijection exists between  $(Q^2, \varepsilon, q'_{\text{cm}})$  and  $(k, k', \theta_e)$ : at any given point  $(Q^2, \varepsilon, q'_{\text{cm}}, \varphi)$  the energies of the two electrons ( $E$  and  $E'$ ) are fixed. These electron energies are needed at the vertex of the interaction to produce the event with the desired kinematical properties. Using the energies  $E$  and  $E'$ , one samples energy losses  $\Delta E$  and  $\Delta E'$  according to the distribution  $I_{\text{int}}(E, \Delta E, a)$  in equation (5.17). Note that to generate an energy loss for the incoming electron, its initial energy  $E_i$  is needed, which is not known until the energy loss is calculated. Therefore the energy  $E = E_i - \Delta E$  is used as an approximation for  $E_i$  in equation (5.17), which holds in case of the emission of low energy photons. After this step the incoming electron energy is given by  $E + \Delta E$  and the outgoing electron energy equals  $E' - \Delta E'$ .

By sampling  $\theta_{\gamma\gamma\text{cm}}$  uniformly between  $-\pi$  and  $\pi$  the kinematics of the event is fixed and the four-vectors of all particles are calculated. Then  $M_x^2$ , the square of the mass of the produced (hard) photon plus the additional photons from internal radiation, is calculated for each event.

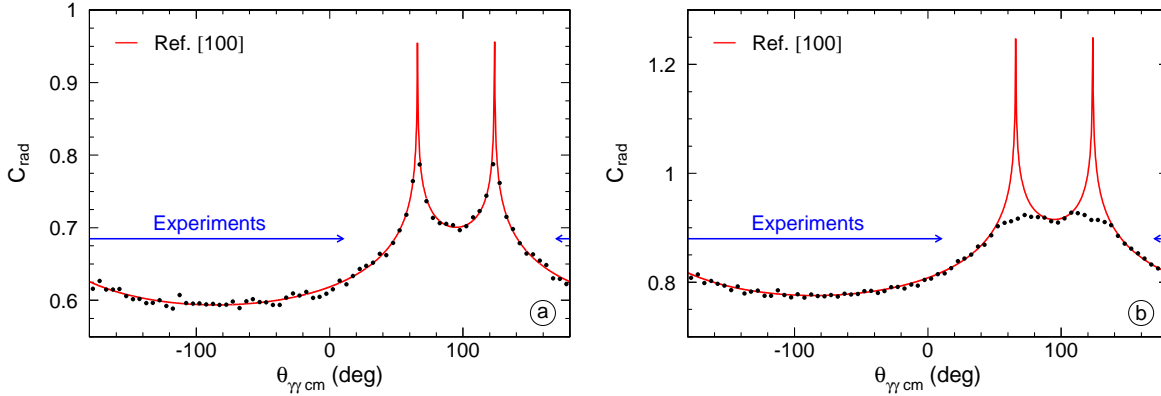


**Figure 5.3:**  $M_X^c$ -dependent part of the radiative corrections for real internal radiation in the  $p(e, e' p')\gamma$  reaction as a function of  $\theta_{\gamma\gamma\text{cm}}$  for  $M_X^{c^2} = 50 \text{ MeV}^2/c^4$  (a) and  $M_X^{c^2} = 4000 \text{ MeV}^2/c^4$  (b),  $Q^2 = 0.33 \text{ MeV}^2/c^4$ ,  $\epsilon = 0.62$ ,  $q'_{\text{cm}} = 111.5 \text{ MeV}/c$  and  $\varphi = 0^\circ$ . The full line represents the theoretical calculation [100]; the data points show the result of the simulation. The kinematic range of the experiments at MAMI-A1 is indicated by the arrows.

The simulated correction factor,  $C_{\text{rad}}$ , for each bin in  $\theta_{\gamma\gamma\text{cm}}$  is the number of generated events  $N_{<}$  with  $(|M_X^2| < M_X^{c^2})$ , divided by the total number of generated events  $N_{\text{tot}}$ :

$$C_{\text{rad}} = \frac{N_{<}}{N_{\text{tot}}} . \quad (5.18)$$

Figure 5.3.a shows the theoretical calculation and the result of the simulation for  $C_{\text{rad}}$  for  $M_X^{c^2} = 50 \text{ MeV}^2/c^4$ . The agreement between the theory and the simulation is very good over the complete phase space.

For  $M_X^{c^2} = 4000 \text{ MeV}^2/c^4$  (where the cut is placed in the analysis of the data in reference [60]) a similar plot is shown in figure 5.3.b. In some parts of the phase space the theoretically calculated  $C_{\text{rad}}$  is even bigger than 1. In the simulation it is impossible to reproduce a correction factor larger than 1, causing a cut-off on the two spikes in the correction factor: in the region of the Bethe-Heitler peaks ( $40^\circ < \theta_{\gamma\gamma\text{cm}} < 140^\circ$ ) the method applied in the simulation does not work. However, this causes no problem, since the peak region is outside the experimental phase space ( $-150^\circ < \theta_{\gamma\gamma\text{cm}} < 5^\circ$ ).

To develop the procedure to introduce the  $M_X^c$ -dependent radiative effects in the simulation one uses the peaking approximation, which is not present in the calculation of  $\delta_{\text{rad}1}$ . The agreement between the theoretical calculation and the simulation shows that this approximation is justified for the emission of soft photons.

### 5.2.4 Effectively applied correction factor

The correction factor in equation (5.15) is implemented in the simulation in order to convolute it with all other experimental parameters and physical processes taking place at the target and spectrometers: acceptance of the spectrometers, ionization energy losses, ... The effectively applied correction factor  $C_{\text{rad}}^{\text{eff}}$  can only be calculated via a Monte Carlo simulation. The simulation [96] was used for this purpose: physical processes can be ‘switched on and off’ and therefore it is very useful to study this effectively applied radiative correction.

$C_{\text{rad}}^{\text{eff}}$  is calculated by running the Monte Carlo simulation twice. First, one runs the complete simulation (Bethe-Heitler + Born cross section behavior and all resolution-deteriorating effects included) and one calculates the solid angle  $\Delta\Omega_r$  for each bin in  $\theta_{\gamma\text{cm}}$ . Then, one performs a similar simulation without taking into account the radiative correction for internal bremsstrahlung, and one obtains  $\Delta\Omega_{\text{nr}}$ . Then  $C_{\text{rad}}^{\text{eff}}$  is given by

$$C_{\text{rad}}^{\text{eff}} = \frac{\Delta\Omega_r}{\Delta\Omega_{\text{nr}}} . \quad (5.19)$$

$C_{\text{rad}}^{\text{eff}}$  is calculated for two different settings of the spectrometers at MAMI-A1 and it is shown in figure 5.4. The kinematics of both settings is determined by  $Q^2 = 0.33 \text{ MeV}^2/c^4$ ,  $\epsilon = 0.645$ ,  $q'_{\text{cm}} = 90 \text{ MeV}/c$  and  $\varphi = 0^\circ$ . The resulting correction factor is different from the theoretical calculation,  $\exp(\delta_{\text{rad}1})$ . The reason for the difference is the size of the experimental bins in five dimensions, the convolution of the internal radiation with the acceptance of the spectrometers and all other physical processes taking place at the target and the detectors. The figure shows that it is necessary to include the internal radiative effects in the simulation.

## 5.3 Implementation of the spectrometers resolution

The measurement of the particle track in the focal plane detectors is not without resolution-degrading effects: processes like multiple scattering in the materials of the detection system and the intrinsic resolution of the wire chambers determine the limits of the event reconstruction. Scattering in the focal plane detectors causes correlated errors on the focal plane coordinates, since the process modifies the particle track. Additional correlations in the errors on the target coordinates originate from the optical transport: an error on one of the focal plane variables will have an influence on several target coordinates. The goal of the second program of the VCS simulation is to reproduce these correlated resolution effects on the target variables of the particles.

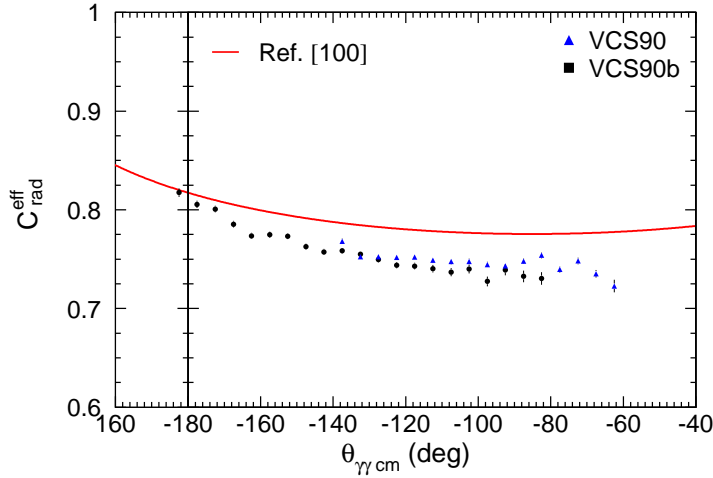


**Figure 5.4:** The effectively applied correction factor for real internal radiation in the  $p(e, e' p')\gamma$  reaction as a function of  $\theta_{\gamma\gamma_{\text{cm}}}$  for  $M_X^c = 4000 \text{ MeV}^2/c^4$ ,  $Q^2 = 0.33 \text{ MeV}^2/c^4$ ,  $\epsilon = 0.645$ ,  $q'_{\text{cm}} = 90 \text{ MeV}/c$  and  $\varphi = 0^\circ$ . The full line represents the theoretical calculation; the data points show the result of the simulation for two different settings of the spectrometers.

The intrinsic resolution of the wire chambers and the multiple scattering, mentioned above, cannot explain the resolution of the detectors. Some of them are due to imperfections of the magnetic fields of the spectrometers and all kind of other resolution-deteriorating effects (e.g. the stability of the beam position and energy, ...). This is implemented by adding an additional resolution effect at the level of the target variables.

### 5.3.1 Resolution effects in the focal plane

Figure 5.5 gives an overview of the implementation of the resolution effects in the focal plane [71]. The starting point of the procedure is a set of target variables  $(\delta, \theta_0, y_0, \phi_0)_{\text{tg}0}$  generated in the first step of the simulation. These coordinates are converted into the focal plane coordinates  $(x, \theta, y, \phi)_{\text{fp}1}$ . Since the inversion of the fifth-order optical transport polynomials is complicated, a first-order approximation is used:

$$\begin{pmatrix} x \\ \theta \\ y \\ \phi \end{pmatrix}_{\text{fp}} = \begin{pmatrix} A_{x\delta} & A_{x\theta} & 0 & 0 \\ A_{\theta\delta} & A_{\theta\theta} & 0 & 0 \\ 0 & 0 & A_{yy} & A_{y\phi} \\ 0 & 0 & A_{\phi y} & A_{\phi\phi} \end{pmatrix} \times \begin{pmatrix} \delta \\ \theta_0 \\ y_0 \\ \phi_0 \end{pmatrix}_{\text{tg}}. \quad (5.20)$$

The values of the matrix elements were obtained by an inversion of the optical transport matrices (up to first order) used in the experiment (see section 4.2.3). Only half of these matrix elements differ from 0.

Once  $(x, \theta, y, \phi)_{\text{fp1}}$  are known the particle track through the complete detection system in the focal plane can be generated. Multiple scattering modifies the direction of the particle. The deflection caused by multiple scattering is treated as explained in [102]. Energy losses of the particle are neglected, since they are small and the effect of multiple scattering is only weakly dependent on the energy of the particle.

In figure 5.6 a simplified picture of the double VDC is drawn. In total there are two of these mounted in the focal plane. The composition of the VDCs is important for the simulation of multiple scattering in the focal plane detectors. All materials are taken into account except for the aluminum layer on the high voltage foils (the Al layer is  $0.04 \mu\text{m}$  thick) and the 1.5% of ethanol in the gas mixture.

Before calculating the intersection point with each of the VDCs multiple scattering is applied to the particle track based on the materials it has passed. For the first plane ( $x_1$ ) this is the exit window of the magnet, the air layer up to the VDC and the lower part of the first VDC (the polyamide and mylar foils and 12 mm of argon-isobutane mixture). The material contributing to the scattering of the particle on its way from the first to the second plane of wires is: 24 mm of gas mixture, 1 mylar foil of  $5 \mu\text{m}$  and the wires of the  $x_1$  plane.

All particles pass through the foils of the VDCs, but only a part of them hit a wire. The probability to hit wire  $i$ ,  $P_{wi}$ , ( $i = 1,2$ ) is

$$\begin{aligned} P_{w1} &= \frac{d_1}{\ell_{\text{cel}} \sin \alpha_{\text{VDC}}} , \\ P_{w2} &= \frac{d_2}{\ell_{\text{cel}} \sin \alpha_{\text{VDC}}} , \end{aligned} \quad (5.21)$$

where  $d_1$  and  $d_2$  are the diameters of the sense and potential wires,  $\ell_{\text{cel}} = 5 \text{ mm}$  the length of the unit cell of the VDC and  $\alpha_{\text{VDC}} = 45^\circ$  the angle of the VDC with respect to the plane perpendicular to the reference track<sup>1</sup>. A random intersection point of the track with the plane of the wires is sampled, and in case a wire is struck, the distance the particle has passed through the wire is calculated. This distance is used for the sampling of the scattering angle.

At the end of the track generation the VDC coordinates  $(x_1, s_1, x_2, s_2)_{\text{VDC}}$  are calculated based on the intersection points with the wire planes of the VDCs. At the level of the VDC coordinates the intrinsic resolution of the VDCs is applied. Processes like delta rays, ... cause large errors on the reconstructed VDC coordinates and therefore the resolution distribution has large tails. In the present version of the simulation this distribution is approximated by

<sup>1</sup>In fact the particles pass through the VDC with different angles. In this approach, the mean value  $\alpha_{\text{VDC}}$  is used.

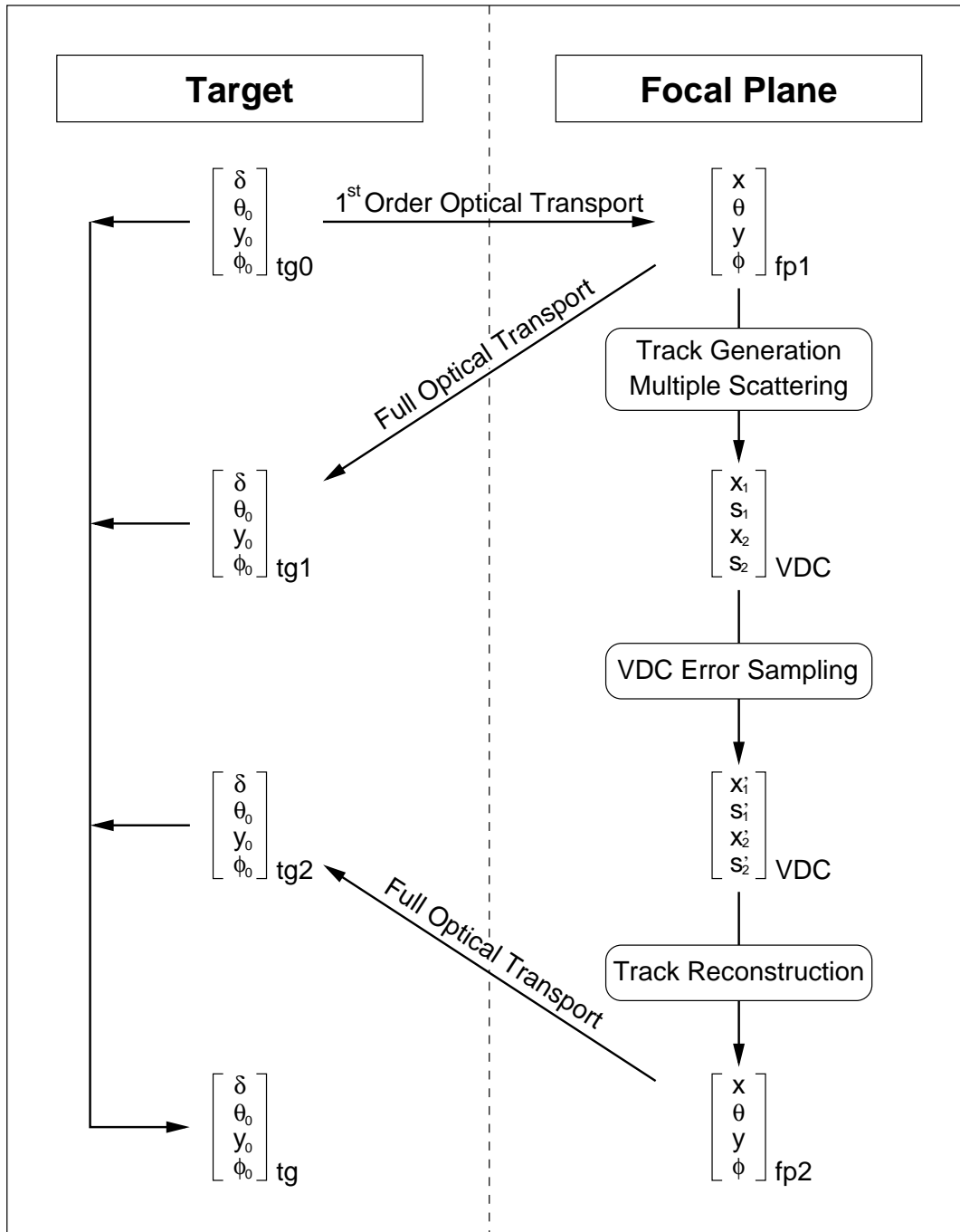


**Figure 5.5:** The simulation of the resolution effects in the focal plane. Based on the target variables,  $tg0$ , the focal plane coordinates,  $fp1$ , are calculated up to first order. After tracking the particle through the focal plane detectors (applying VDC resolution effects and multiple scattering) the modified focal plane variables,  $fp2$ , are obtained. Using the full optical transport matrix  $tg1$  and  $tg2$  are reconstructed. The resolution effects are quantified by  $tg2 - tg1$ .

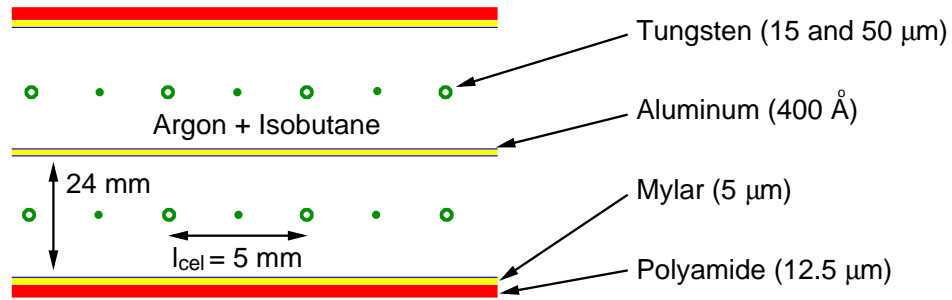


**Figure 5.6:** Model of the VDC in the simulation.

a combination of four Gaussians, each with different width and amplitude. Generally, five wires are struck by a particle in the  $x$  planes and four wires in the  $s$  planes. For the  $x$  planes an error is sampled five times, and four times for the  $s$  planes to reproduce this physical effect. Then the mean value for the error for each VDC coordinate is calculated and added to the value obtained by the track reconstruction. In this way a set of modified VDC coordinates  $(x'_1, s'_1, x'_2, s'_2)_{\text{VDC}}$  is created. These modified coordinates are used by the tracking algorithm in the simulation to construct new focal plane variables  $(x, \theta, y, \phi)_{\text{fp2}}$ .

At this point two sets of focal plane coordinates, labeled by fp1 and fp2, are obtained. The difference between both sets of variables is the effect of the resolution, which is only applied to the second set. For both sets the target coordinates are calculated using the experimental optical transport matrices as in equation (4.1). This transport is performed in exactly the same way as in the experiment to reproduce the experimental correlations between the resolution effects in the simulation.

The difference between both sets of target coordinates quantifies the resolution effects one wants to add to  $(\delta, \theta_0, y_0, \phi_0)_{\text{tg0}}$ :

$$\begin{pmatrix} \delta \\ \theta_0 \\ y_0 \\ \phi_0 \end{pmatrix}_{\text{tg}} = \begin{pmatrix} \delta \\ \theta_0 \\ y_0 \\ \phi_0 \end{pmatrix}_{\text{tg0}} + \underbrace{\begin{pmatrix} \delta \\ \theta_0 \\ y_0 \\ \phi_0 \end{pmatrix}_{\text{tg2}} - \begin{pmatrix} \delta \\ \theta_0 \\ y_0 \\ \phi_0 \end{pmatrix}_{\text{tg1}}}_{\text{Resolution effects}}. \quad (5.22)$$

### 5.3.2 Additional resolution effects

The difference in resolution between the experiment and the simulation at the end of the procedure described above is removed by sampling an additional error on the target coor-

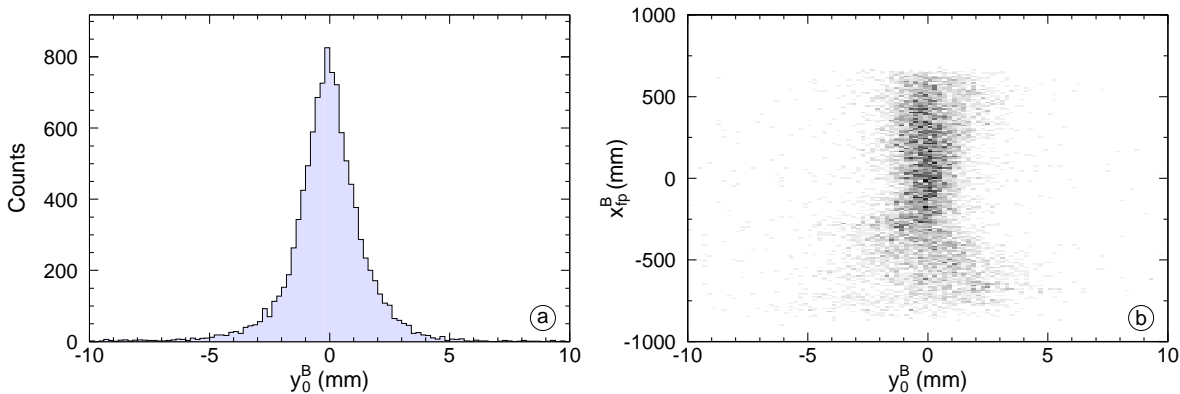


**Figure 5.7:** The reconstructed  $y_0^B$  for the quasi elastic scattering of electrons on a thin  $^{12}\text{C}$  foil (panel a) has wide tails due to the dependence of the reconstruction on the focal plane coordinates, as shown in panel b for  $x_{fp}^B$ .

dinates. Possible sources for these additional resolution effects are: instabilities in the beam energy and position, imperfections of the magnetic fields of the spectrometers, approximations in the optical transport calculation, . . . The fact that the optics of the spectrometers are not perfect is demonstrated for  $y_0^B$  in figure 5.7.

Most of these contributions cause correlations on the resolution effects, but at the moment of writing there is no model available to implement these correlations in the simulation. As a first approximation they are applied by sampling Gaussian distributed errors on the target variables.

### 5.3.3 Adjustment of the detector resolution effects

As explained above, there are different contributions to the resolution effects in the spectrometers. Here it is explained how these resolution effects were adjusted using experimental data.

#### Errors in the focal plane

In the experiment the variances of the focal plane coordinates  $(\Delta x, \Delta \theta, \Delta y, \Delta \phi)_{fp}$  are calculated based on how well the measured VDC coordinates agree with a straight particle track. In the simulation the same variables are reconstructed. This allows to compare simulation and data to adjust the error distribution in the simulation to the intrinsic resolution of the VDCs. This is done based on the data from elastic scattering of electrons on protons: the amplitudes and widths of the four Gaussians of the simulated error distribution were changed in order to reproduce the observed  $\Delta x$ -distribution for both spectrometers.

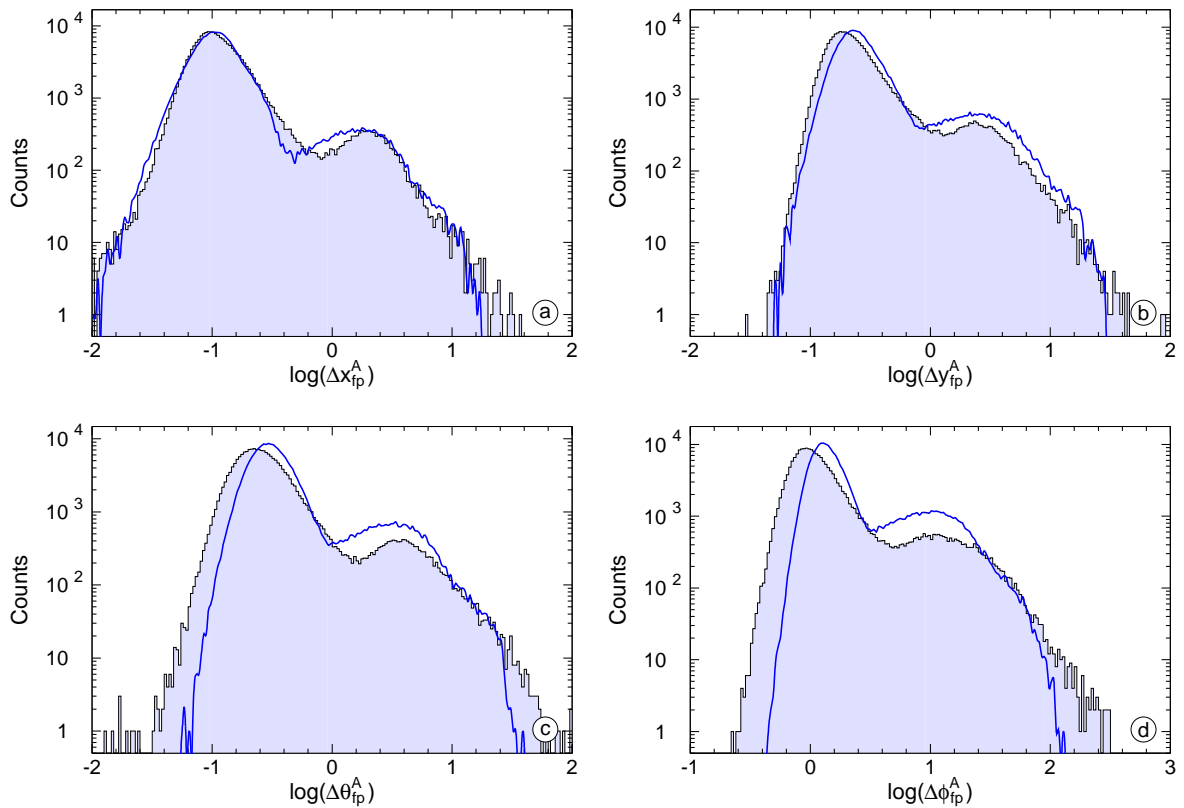


**Figure 5.8:** Errors on the focal plane coordinates in spectrometer A. Data: histogram; simulation: line.

The result is shown in figure 5.8, where the experimental data for the variances of the focal plane coordinates for spectrometer A (histograms) are compared to the simulation (line). The obtained agreement is good for  $\Delta x$  and  $\Delta y$ , but for  $\Delta\phi$  and  $\Delta\theta$  the procedure seems to work less well. The parameters of the four Gaussians are given in table C.2.

Although the distributions of the variances are not in full agreement with the experiment, the simulation reproduces the correlations quite well, as shown in figure 5.9.

### Additional resolution effects on the target coordinates

The additional resolution effects for the simulation are tuned to reproduce the experimental spectra for elastic scattering of electrons on protons and quasi-elastic electron scattering on  $^{12}\text{C}$ . The latter is only used to fix the resolution on  $y_0$ . For each of the target coordinates a Gaussian resolution effect is sampled on top of the resolution effects in the focal plane of the spectrometers. To define the correct width of the additional Gaussian on the target coordinates the following parameters are used:

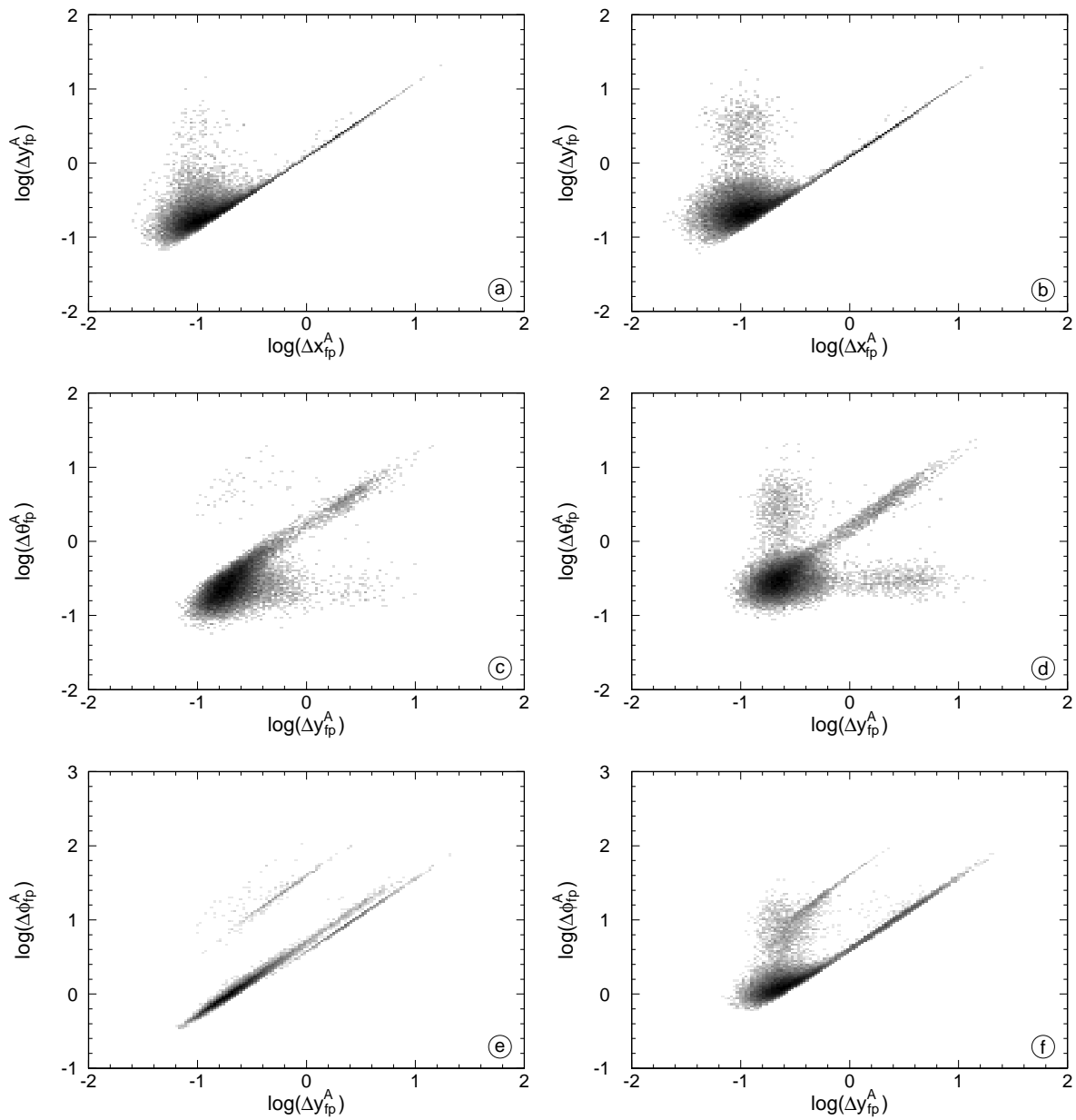


**Figure 5.9:** Correlations between the variances the focal plane coordinates in spectrometer A. Left: data; right: simulation.

- $E_{\text{miss}}$ : The missing energy in elastic  $p(e, e' p')$  scattering is defined by

$$E_{\text{miss}} = E_e - E_{e'} - E_{p'} , \quad (5.23)$$

where  $E_e$ ,  $E_{e'}$  and  $E_{p'}$  are the energies of incoming and outgoing electron and the recoiling proton, respectively. The width of the distribution of the missing energy is only sensitive to the energies of the detected particles. Thus it allows to set the resolution on the particle momenta.

- $\theta_{\text{dif}}$ : This variable is defined using conservation of momentum in the vertical direction. It is the difference between the measured value of the angle with respect to the horizontal plane for the proton ( $\theta_0^A$ ) and the one calculated using the momentum,  $k'$ , and  $\theta_0^B$  of the electron and the momentum of the proton,  $p'$ :

$$\theta_{\text{dif}} = \theta_0^A + \text{asin}\left(\frac{k'}{p'} \sin(\theta_0^B)\right) . \quad (5.24)$$

This formula is only valid for in-plane settings of spectrometer B. Once the resolution of the momenta is implemented in the correct way, this parameter is only sensitive to the resolution in  $\theta_0^A$  and  $\theta_0^B$ .

- $\phi_{\text{dif}}$ : This parameter is defined in a similar way as  $\theta_{\text{dif}}$ , but it is based on the horizontal conservation of momentum. In this variable the angular positions of the spectrometers,  $\theta_A$  and  $\theta_B$ , are important.

$$\phi_{\text{dif}} = \phi_0^A + \theta_A + \text{asin}\left(\frac{k'}{p'} \sin(\phi_0^B - \theta_B)\right) . \quad (5.25)$$

$\phi_{\text{dif}}$  allows to fix the resolution in  $\phi_0^A$  and  $\phi_0^B$ .

- $y_0^A$  and  $y_0^B$ : To adjust the resolution on  $y_0^B$  and  $y_0^A$  the experimental data on quasi-elastic scattering on a  $^{12}\text{C}$  foil, placed in the center of the laboratory frame are used: one should find  $y_0^B = y_0^A = 0$  mm.

Since in the method explained above the contribution of the resolution of spectrometer A and B can not be separated equal contributions are assumed from both spectrometers, except for  $y_0^A$  and  $y_0^B$ .

Figure 5.10 shows the distributions of the variables used for the adjustment of the resolution in the simulation and the resulting simulated histograms. Also the  $M_X^2$ -distribution is shown, because it gives a general idea of how well the experimental resolution effects are reproduced in the simulation. The FWHM of the additional Gaussians can be found in table C.3.

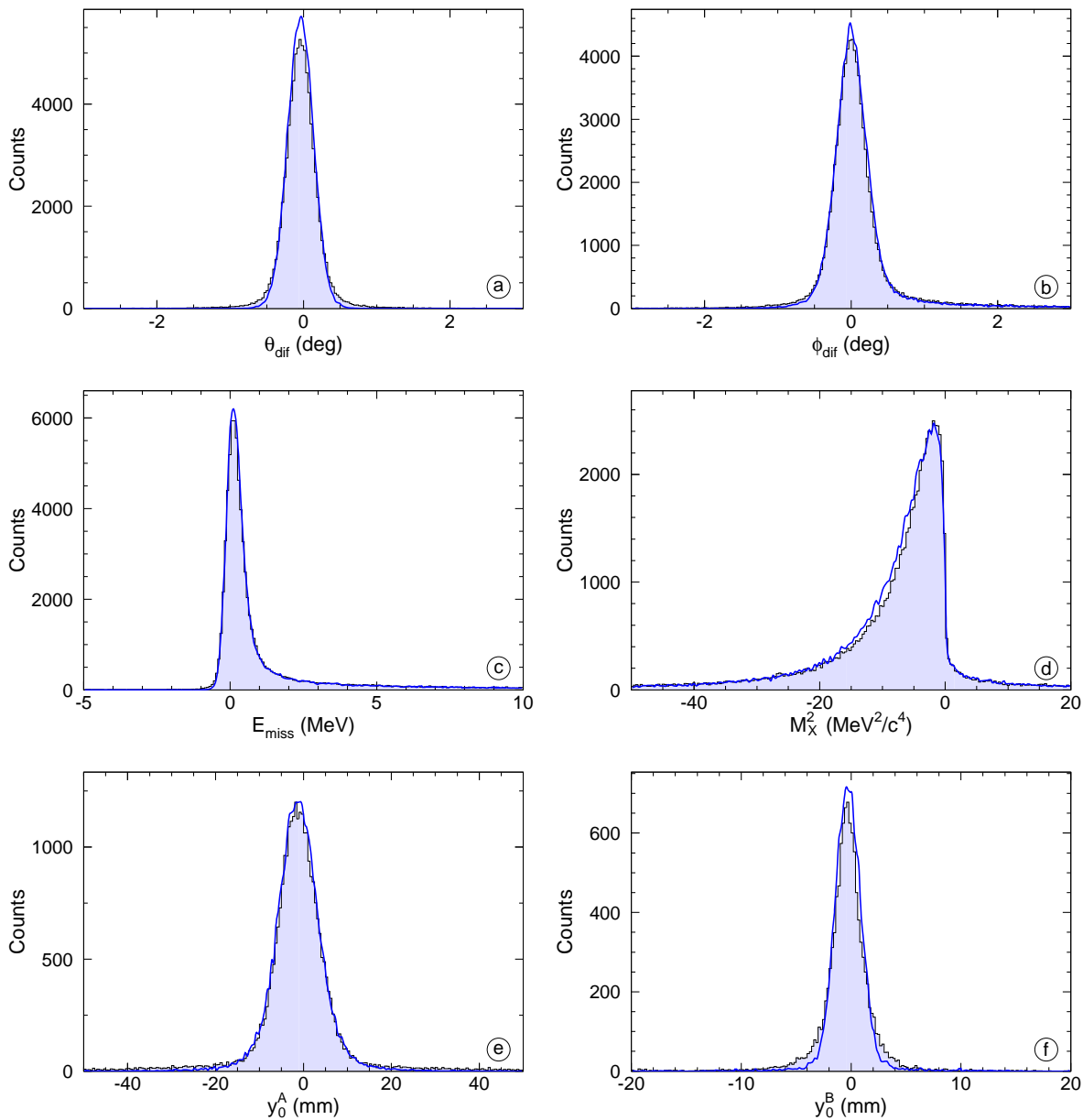


**Figure 5.10:** The resolution effects on the target coordinates in the simulation are adjusted using experimental data from elastic  $ep \rightarrow e'p'$  scattering (a to d) and quasi-elastic scattering of electrons on  $^{12}\text{C}$  (e and f). The procedure is explained in the text.

## 5.4 Comparison with data

The results of the simulation can be compared to the VCS data on an absolute scale. The same cuts used to select the photon electroproduction events in the experimental data are applied to the simulated data to produce the histograms. By normalizing these simulated histograms to the experimental luminosity one can predict the experimental number of counts in each bin. For this normalization the factor  $\mathcal{L}_{\text{exp}}/\mathcal{L}_{\text{sim}}$  could be used. However, this does not give the desired result. Also radiative corrections should be taken into account. This is done by applying the factor  $f_{\text{cor}}$  of equation (5.13). The correct normalization factor is:  $\mathcal{L}_{\text{exp}}/(\mathcal{L}_{\text{sim}}f_{\text{cor}})$ .

Figure 5.11 gives an overview of the distributions of some variables. The variables presented in the figure are the momentum  $p'$  of the recoil proton, the angular target variables  $\theta_0^A$  and  $\phi_0^A$  of the proton, the  $x$ -coordinate of the interaction point  $x_v$ ,  $\varepsilon$  and  $q_{\text{cm}}$ . The distribution of  $x_v$  shows the transverse modulation of the beam position to prevent the local boiling of the liquid hydrogen. Due to binning effects three spikes are present in the experimental  $x_v$ -histogram. As can be seen on the figure there is good agreement between simulation and data. In the simulation the BH+B cross section was used and differences between data and simulation are attributed to the effect of the GPs on the cross section.

## 5.5 Possible improvements

Several features in the simulation of the resolution of the spectrometers can still be improved.

- The agreement between simulation and data is good for  $\Delta x$  and  $\Delta y$ . The generation of the variances on the angles  $\theta$  and  $\phi$  in the focal plane is less good. This can be explained by the simplified tracking algorithm in the simulation. In the experiment, the VDCs offer more information than only the intersection point: also the angles of the particles are known by measuring the drift time. A more realistic tracking algorithm might improve the simulated variances on  $\theta$  and  $\phi$ .
- The multiplicity of the  $x$  and  $s$ -wire chambers is set to 5 and 4 respectively. One could implement the experimentally observed distribution of the multiplicities in the simulation.

Also the resolution effects which are sampled on the target coordinates can be improved:

- One could change the distribution used to sample the additional energy losses (now a Gaussian distribution is used) into a distribution with longer tails. In figure 5.10 one can observe that the experimental distribution for e.g.  $y_0^B$  has much wider tails than in the simulation.

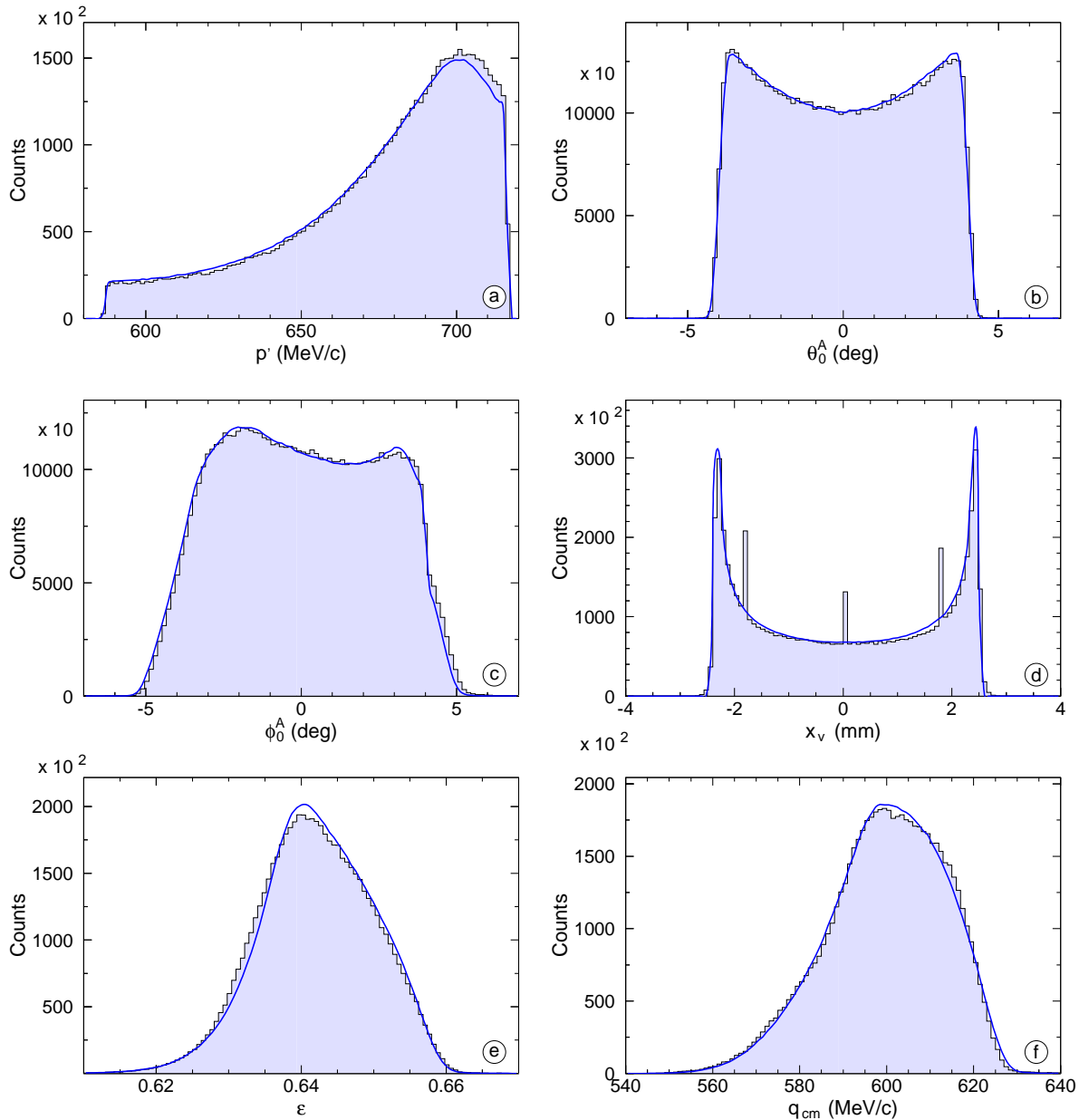


**Figure 5.11:** Comparison between simulation (line) and data (histogram) for the photon electroproduction reaction (setting VCS90b). The simulated events were generated according to the BH+B cross sections and deviations between simulation and data are due to the effect of the GPs on the cross section.

- More studies of the experimental setup are needed to improve the implementation of the 'additional' resolution effects. The resolution should be studied as a function of target and focal plane variables: figure 5.7 shows that the resolution in e.g.  $y_0^B$  is not constant over the complete acceptance. In some regions the resolution is better than in other parts. A complete simulation should also incorporate these effects.



---

# Unpolarized cross section

---

At low CM energies the unpolarized photon electroproduction cross section is dominated by the Bethe-Heitler and Born processes. The deviation of the experimental cross section from the exactly calculable BH+B contribution is about 10% for the kinematics considered here. The information about the GPs and VCS structure functions is embedded in this difference between the observed and the BH+B cross section.

This chapter describes the determination of the unpolarized five-fold differential photon electroproduction cross section using the data of the new VCS experiment at MAMI. Although the aim of the experiment is the measurement of double-polarized observables, unpolarized cross sections can be obtained by ignoring the helicity of the incoming electrons and the polarization of the recoil protons.

First the selection of the data used for the calculation is discussed (section 6.1). Then the amount of residual background in the selected events is estimated. The calculation of the solid angle and the cross section is treated in section 6.3. At the end of this chapter two linear combinations of structure functions are extracted from the measurement by subtracting the BH+B contribution from the obtained cross section. Special attention goes to the iteration procedure in the extraction of the structure functions.

## 6.1 Data selection

The calculation of the unpolarized cross section in this work is based on the data taken in December 2005 using the VCS90b setting (see table 6.1, table 6.2 and appendix C.1). The anti-correlation in the uncertainty on the central momenta is due to the calibration method (see appendix A). There are several reasons why this data set was used.

First of all the VCS90b settings covers the region around  $\varphi = 0^\circ$  and  $\theta_{\gamma\gamma\text{cm}} = 180^\circ$ , which increases the range in  $v_{\text{LL}}/v_{\text{LT}}$  with respect to the VCS90 setting. This allows a higher precision in the extraction of the linear combinations of structure functions.

The calibration of the spectrometers is the second reason for this choice. Before the measurement in December 2005, the HV foils of the VDCs in spectrometer A were replaced and dedicated calibration data were obtained, allowing a precise calibration of both spectrometers [103]. This is essential for the extraction of the linear combinations of GPs. The accuracy on the calibration of the spectrometers is of major importance to keep systematic errors as low as possible.

During the runs in December 2005 the beam quality and the conditions of the target were very good. The vacuum inside the scattering chamber was excellent, which means there was no deposition of ice on the target cell. This ice would be an additional source of uncertainty, because its thickness and composition are not monitored. After the replacement of the HV foils in spectrometer A the leakage current in the VDCs of spectrometer A was very low, resulting in a very good resolution in the reconstruction of the particle tracks.

Apart from the calibration of the detectors, a well-considered data selection is indispensable: one has to preserve as much as possible the photon electroproduction events while at the same time the contribution of the background processes has to be suppressed.

To remove the unwanted events from background sources one could make use of the particle identification detectors (PID) like the scintillators in both spectrometers and the Cherenkov detector in spectrometer B. A Cherenkov detector in spectrometer A was not available, since it had been replaced by the focal plane polarimeter. Due to imperfections in these PID detectors, to be discussed below, they are not used in the final analysis of the unpolarized data.

Even without using any PID detector a very clean extraction of photon electroproduction events from the data was obtained. The main part of the random coincidences is cut away by defining a window in the coincidence time and the remaining contribution is subtracted. The contribution of the target walls is suppressed by a cut in the reconstructed  $z$ -coordinate of the reaction vertex, and finally the photon electroproduction reaction is selected by requiring the mass of the missing particle to be close to zero. The way the data selection is done is explained in detail below.

Parameter	Spectrometer A	Spectrometer B	Unit
$p_{\text{ref}}$	$645.38 \mp 0.18$	$539.41 \pm 0.14$	MeV/c
$\theta$	38.0	50.6	deg
$\phi_{\text{oop}}$	0.0	0.0	deg

**Table 6.1:** Parameters of the spectrometer setup for the VCS90b-setting.

Beam energy	854.57 MeV
Mean beam current	21.805 $\mu\text{A}$
Mean density liquid H <sub>2</sub>	0.0688 g cm <sup>-3</sup>
Effective measuring time	232 h 16 min 49 s
Effective luminosity	$2.02 \cdot 10^7 \text{ pb}^{-1}$
Number of events	$4.3 \cdot 10^7$

**Table 6.2:** Overview of the VCS90b-setting.

### 6.1.1 Momentum acceptance of the spectrometers

The calibration of the spectrometers is only valid in the region where the transport matrices are determined (see section 4.2.3). This calibration is done for the complete geometrical acceptance of the collimator: for  $\theta_0$ ,  $\phi_0$  and  $y_0$  no additional cuts are necessary. For the momentum the calibration is only valid in the region given by table 4.1: 20% and 15% around the central momentum of spectrometer A and B, respectively. Therefore, a software cut on the momentum acceptance is necessary:

$$\text{MomentumCut} : \left( \left| (100 + \delta^A) \frac{630}{655} - 100 \right| < 10 \right) \&\& \left( |\delta^B| < 7.5 \right), \quad (6.1)$$

where the relative momenta  $\delta^A$  and  $\delta^B$  are expressed in percent.  $\delta^A$  is defined with respect to the reference momentum and not with respect to the central momentum. Therefore the expression is more complicated for spectrometer A than for spectrometer B.

### 6.1.2 Coincidence time

Using the scintillators the arrival times of the particles in the focal plane of the spectrometers are measured:  $T_A$  and  $T_B$ . To reconstruct the time of the interaction, this arrival time is corrected for the time the particle needs to travel from the interaction vertex up to the scintillators, called the time-of-flight  $T_{\text{TOF}}$ .  $T_{\text{TOF}}$  depends on the velocity of the particle and the path length of the particle in the magnets. The spectrometer measures the momentum of the

particle, thus the mass of the particle entering the spectrometer has to be specified to calculate the particle's velocity for the time-of-flight correction.

The difference between the departure times (at the interaction vertex) of the particles detected in spectrometer A and B is called the coincidence time  $T_{AB}$ . The coincidence time for a proton detected in spectrometer A and an electron in spectrometer B is given by

$$T_{AB} = (T_B - T_{\text{ToF},e}) - (T_A - T_{\text{ToF},p}) . \quad (6.2)$$

The histogram of  $T_{AB}$  is shown in figure 6.1.a. Particles coming from the same interaction start their travel to the focal plane at the same moment. They give rise to the central peak in the coincidence time at  $T_{AB} = 0$  ns. In figure 6.1.b the central peak of the  $T_{AB}$ -histogram is shown. The FWHM of the central peak is 0.85 ns, when a Gaussian fit is used.

A background extending from -50 to 50 ns is visible in the figure too. These random coincidences are due to the high rate of particles entering the spectrometer: the probability not negligible that a positively charged particle enters spectrometer A, within a time difference of  $\pm 50$  ns to the detection of a negatively charged particle in spectrometer B which does not come from the same interaction, and therefore these should be removed for the calculation of the cross section.

Except from the peak at  $T_{AB} = 0$  ns, a second contribution appears in the histogram at  $T_{AB} \approx 1.5$  ns. The events contributing to this peak are clearly not random coincidences, because they are focused around one value in the  $T_{AB}$ -spectrum. The two particles originate from the same interaction but the ToF calculation is wrong. The calculation of the time-of-flight fails, when particles, other than a proton (electron) enter spectrometer A (B), since their velocity is calculated using a wrong mass. It might be a negatively charged particle, heavier than the electron (e.g.  $\pi^-$ ,  $\mu^-$ ) detected in spectrometer B or a positively charged particle lighter than the proton (e.g.  $\pi^+$ ) in spectrometer A. The identification of these events can be done in the PID detectors of the spectrometers (see sections 6.1.3 and 6.1.4).

To select the good events the random coincidences have to be removed. In the analysis a cut in the coincidence time, `TimeCut`, is used:

$$\text{TimeCut} : |T_{AB}| < 3 \text{ ns} . \quad (6.3)$$

This value of 3 ns has been chosen to be much larger than the width of the coincidence time peak to keep all good events. On the other hand it is not too large, because otherwise too many random coincidences would contaminate the data.

These random coincidences are also present as a background in the central peak in the  $T_{AB}$ -histogram and they can not be removed by any cut. They have to be subtracted in the analysis,

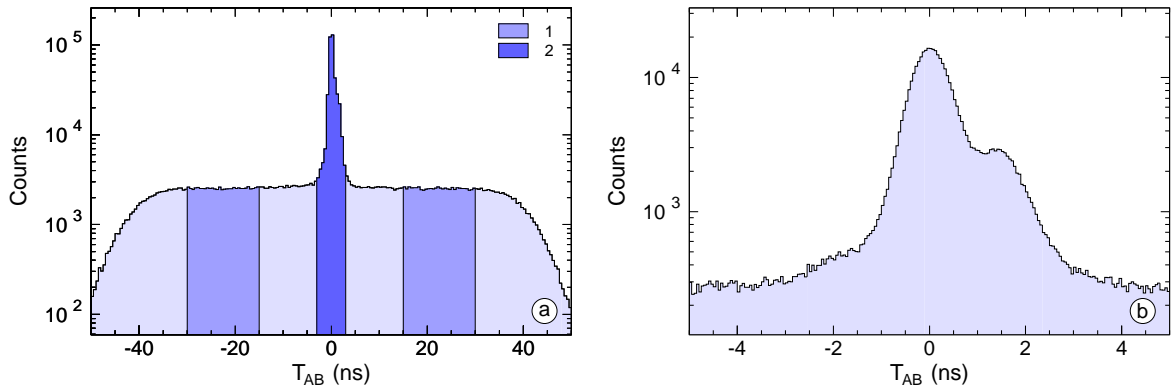


**Figure 6.1:** Histogram of the coincidence time  $T_{AB}$  on logarithmic scale. The central region (2) contains the events accepted for the calculation of the cross section and the events in the two windows left and right of the main peak (1) are used for the background subtraction. In the right panel a zoom on the central peak is shown.

which is done by selecting the random coincidences by a dedicated cut, `RandomCut`:

$$\text{RandomCut} : \left| T_{AB} - 22.5 \right| < 7.5 \text{ ns} . \quad (6.4)$$

This cut selects events in a time window of 15 ns around  $\pm 22.5$  ns. The time windows for both cuts are shown in figure 6.1: the darkest area (2) shows the window of the coincident events; the two other zones (1) are used for the subtraction of random coincidences.

To correct a certain histogram for random events, one creates two histograms:  $\mathcal{H}_t$  for the events within `TimeCut` and  $\mathcal{H}_r$  for the events selected by `RandomCut`. After rescaling  $\mathcal{H}_r$  to the width of the central time window of the true coincidences (in the case of this analysis the scaling factor is  $\frac{1}{5}$ ) the random events can be removed by subtracting the rescaled  $\mathcal{H}_r$  from  $\mathcal{H}_t$ .

### 6.1.3 Scintillators

The two layers of scintillator paddles in spectrometer A can be used for particle identification. In figure 6.2.a the signal of the  $\Delta E$ -scintillator  $\Delta E$  versus the signal of the ToF-scintillator  $E_{\text{ToF}}$  is shown. Protons give a higher signal in both layers than pions, allowing a separation of both types of particles by selecting one of both dark areas in the figure. The positively charged pions can be removed from the data by cutting away the events around the origin of figure 6.2.a as indicated by the red line. This cut is given by:

$$\text{ScintAProton} : (\Delta E/450)^2 + (E_{\text{ToF}}/1250)^2 > 1 . \quad (6.5)$$

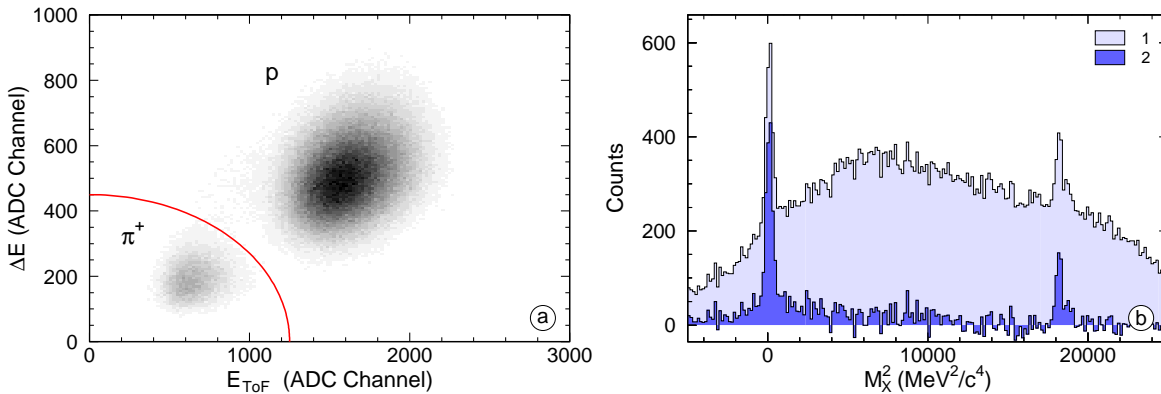


**Figure 6.2:** Panel a shows the ADCs signal of both scintillator planes ( $E_{\text{ToF}}$  and  $\Delta E$ ). The red line represents the cut on the scintillators to remove the  $\pi^+$  in the data. The  $M_\chi^2$ -distribution is shown in panel b for the events removed by ScintAProton without (1) and with (2) random subtraction.

Similarly the cut

$$\text{ScintAPion} : (\Delta E/450)^2 + (E_{\text{ToF}}/1250)^2 < 1 \quad (6.6)$$

selects the  $\pi^+$  events in figure 6.2.a.

However, the cut ScintAProton is not used in the analysis of the data, since it removes a fraction of the protons, too. In figure 6.2.b the missing mass distribution for all events cut away by ScintAProton is shown by histogram 1. A peak around  $M_\chi^2 = 0 \text{ MeV}^2/c^4$  is observed, which means that also good events are cut away. Moreover, most of the events which are removed by the cut defined in equation (6.5), are removed by the subtraction of the random coincidences, too. After random subtraction the  $M_\chi^2$ -spectrum of the events selected by the ScintAPion cut is nearly a clean  $M_\chi^2$ -distribution of photon electroproduction events (see histogram 2 in the same figure). Therefore the merit of this cut is negligible: it does not remove more background events than the random subtraction.

This does not mean one should ignore the  $\Delta E$ - $E_{\text{ToF}}$ -spectrum of the scintillators. It can be used to get an (over-)estimate of the contamination of  $\pi^+$  in the data. It is also useful to suppress background processes for studies where it is not important to keep all events or where subtraction of random coincidences is not possible.

#### 6.1.4 Cherenkov detector

The Cherenkov detector of spectrometer B can be used to separate electrons from muons and pions. For a same momentum, the electron has a higher velocity relative to a (heavier) muon

or pion. For the momentum region of spectrometer B (500 to 600 MeV/c) this means that electrons will emit Cherenkov light in the gas mixture of the detector, which is not the case for the heavier particles. For each of the 5 mirrors one can define a threshold in the Cherenkov signal. As soon as the signal in at least one of PMTs is above its threshold, the particle is identified as an electron.

The sum of the ADC signals of the different PMTs  $\Sigma$  Cher is displayed in figure 6.3.a<sup>1</sup>. The peak close to  $\Sigma$  Cher = 0 corresponds to  $\pi^-$  entering the spectrometer. Electrons contribute to the remaining part of the histogram.

The spectrum of all particles detected by PMT number 2 (B.mirror2) is shown in figure 6.3.b. To get a cleaner view of the histogram one can remove all events which are recognized as an electron by one of the other mirrors. The cleaned histogram gives a better separation between electrons and pions and is indicated by the distribution 2 + 3 in the figure. The threshold on B.mirror2 is set to the minimum of the histogram. All events above this line are tagged as electrons and indicated by distribution 3 in the figure.

To obtain the threshold for each mirror, histograms like figure 6.3.b were made for all mirrors and the following cut to select electrons in spectrometer B is obtained:

$$\begin{aligned} \text{CherElectron} : & (\text{B.mirror0} > 95) \parallel (\text{B.mirror1} > 107) \parallel (\text{B.mirror2} > 119) \\ & \parallel (\text{B.mirror3} > 105) \parallel (\text{B.mirror4} > 97) . \end{aligned} \quad (6.7)$$

The result of this cut on the  $T_{AB}$ -distribution is shown in figure 6.4.a. The CherElectron-cut removes the second peak in the coincidence time completely, which means that  $\pi^-$  production is responsible for this peak. The majority of these events originate from the havar end caps of the target. Figure 6.4.b shows the same spectrum for the rejected events. Apart from the maximum around  $T_{AB} = 1.5$  ns it is clear that also some of the coincident electron-proton events are rejected by the cut. The Cherenkov detector does not cover the focal plane of spectrometer B completely and the Cherenkov light emitted by electrons passing at the borders of the acceptance is not captured by any of the mirrors. This can be seen on figures 6.4.c and 6.4.d. They show  $x_{fp}^B$ , the  $x$ -coordinate of the intersection point of the particle track and the focal plane, versus the coincidence time for the events kept, respectively rejected, by the cut CherElectron. The cut works fine over a large region of  $x_{fp}^B$  (between the two lines), where only the second peak in the coincidence time is present. However, for low  $x_{fp}^B$  an important number of events around  $T_{AB} = 0$  ns is present. The zone between the two lines in figures 6.4.c and 6.4.d is covered by the Cherenkov detector.

The cut CherElectron removes good events and therefore it is not used in the final calculation of the cross section. CherElectron was only used to determine the nature of some of the

<sup>1</sup>The offsets in the individual mirrors, as visible in figure 6.3.b, have been removed to obtain figure 6.3.a.

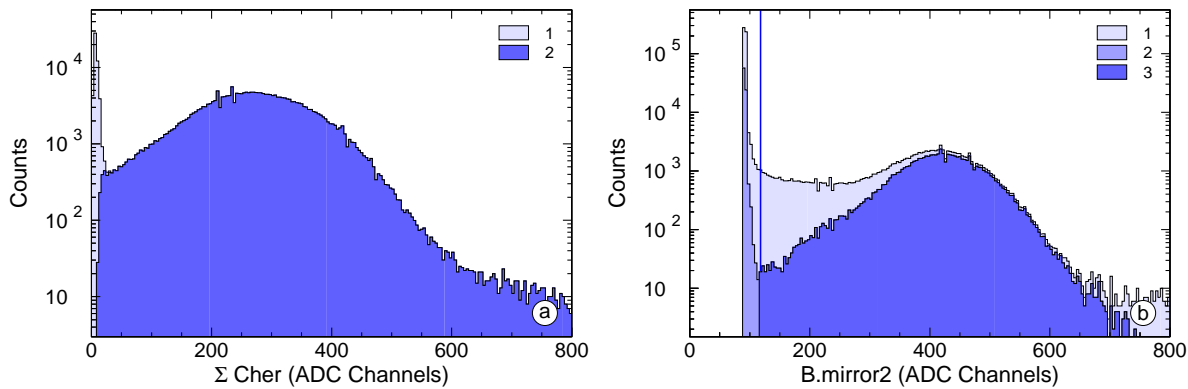


**Figure 6.3:** The histogram of  $\Sigma\text{Cher}$  for all events is shown in panel a by distribution 1. Distribution 2 only shows the events kept by the cut  $\text{CherElectron}$ . Panel b shows  $\text{B.mirror2}$ , the distribution of the ADC signals from PMT 2 of the Cherenkov detector (1). Events which are not tagged as an electron by other mirrors are shown by distributions (2 + 3). The threshold for  $\text{B.mirror2}$  is indicated by the line and the events indicated by distribution (2) are removed.

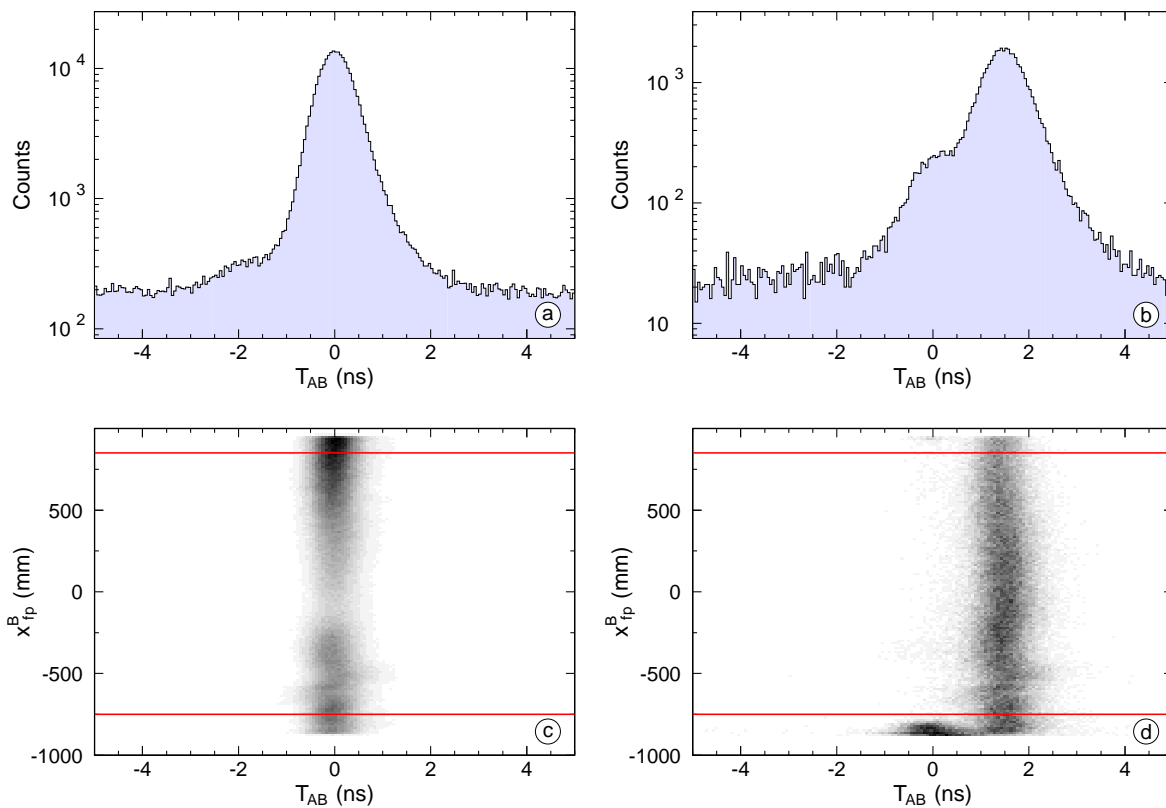


**Figure 6.4:** The plots on the left show  $T_{\text{AB}}$  and  $T_{\text{AB}}$  versus  $x_{\text{fp}}^{\text{B}}$  using the cut  $\text{CherElectron}$ ; the figures on the right are obtained for the rejected events. The Cherenkov detector covers only the central region of the focal plane of spectrometer B, indicated by the two lines in panel c and d.

background processes and to estimate the residual  $\pi^-$  contamination in the data. If one wants to apply a PID cut using the Cherenkov detector of spectrometer B, one should limit the region of the cut to  $-750 \text{ mm} < x_{\text{fp}}^{\text{B}} < 850 \text{ mm}$ :

$$\text{CherElectron2} : \text{CherElectron} \parallel (x_{\text{fp}}^{\text{B}} < -750) \parallel (x_{\text{fp}}^{\text{B}} > 850) . \quad (6.8)$$

### 6.1.5 Reconstructed $z$ -vertex

Using spectrometer B the  $z$ -coordinate  $z_v$  of the interaction vertex is reconstructed. The histograms of  $z_v$  for an empty target cell and the liquid hydrogen target are shown in figure 6.5. The target walls are made of havar and are much denser than the liquid hydrogen. This causes the peaks in the figure, since there are more interactions of the incident electrons with the material of the walls than in the hydrogen. The position of the first (second) target wall is denoted by  $z_{w1}$  ( $z_{w2}$ ).

It is important to know the position of the target walls to define an appropriate cut in  $z_v$ . To calculate the cross section of the photon electroproduction reaction, one does not want the data to be contaminated with events coming from the target walls, and to apply energy loss corrections, one needs to calculate the distances the particles have traveled through the liquid hydrogen and other materials of the target. Therefore the position of the target should be known with a precision comparable to the resolution of the  $z_v$ -reconstruction.

To estimate the influence of the walls of the target on the experimental spectra, some data runs have been taken on an empty target cell. The dimensions of this empty cell do not exactly agree with the normal target, but it is good enough to estimate the contamination due to interactions of the electrons with the target cell. Unfortunately, the statistics of these empty-target runs are not sufficient to draw very precise conclusions. Therefore, the VCS data are used to extract more information about the target walls. To this end a general function,  $f(z_v)$ , was developed fit to the experimental  $z_v$ -spectrum for the different runs.

This function consists of three parts:

1. To parameterize the peak of both target walls the functions  $G_i(z_v)$  ( $i = 1, 2$ ) are used, which are the sum of two Gaussians with same center given by  $z_{wi}$  (the  $z$ -coordinate of the target wall) but different widths  $\sigma_{i,1}$  and  $\sigma_{i,2}$  ( $\sigma_{i,2}$  corresponds to the widest of both Gaussians). The maximum of the contribution of the target wall is given by  $A_i$  and  $a_{fi}$  is the amplitude of the widest Gaussian with respect to the narrowest one.
2. The contribution of the interaction of the electrons with the liquid hydrogen is described by  $P(z_v)$ , a second order polynomial in  $z_v$  with coefficients  $a_j$ .
3. Finally a constant background term  $A_{\text{bg}}$  is taken into account.

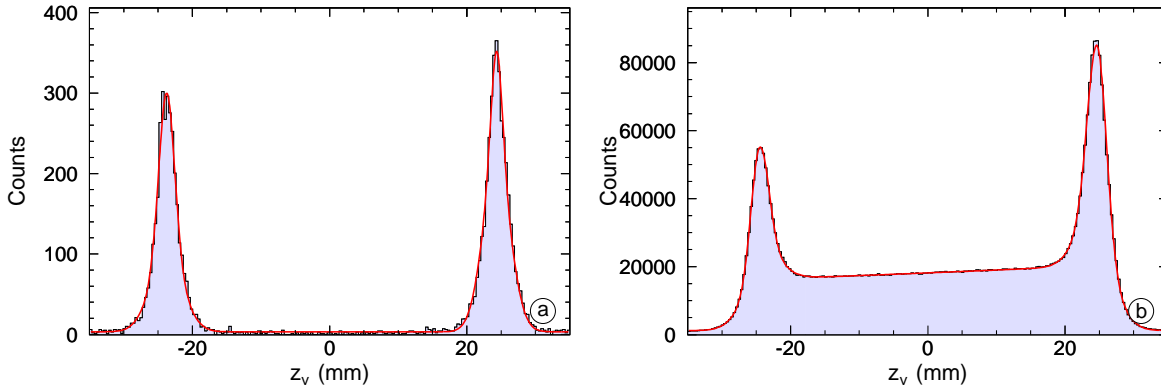


**Figure 6.5:** Histogram of  $z_v$  for the empty target cell and the hydrogen target. Random coincidences have been subtracted from the histograms. The full lines show the fits to the histograms using the function of equation (6.10).

The functions  $G_1(z_v)$ ,  $G_2(z_v)$  and  $P(z_v)$  are given in equation (6.9) and the complete function used for the fit in equation (6.10). The function has 14 free parameters in total.

$$\begin{aligned}
 G_1(z_v) &= (1 - a_{f1}) \exp\left(-\frac{(z_v - z_{w1})^2}{2\sigma_{1,1}^2}\right) + a_{f1} \exp\left(-\frac{(z_v - z_{w1})^2}{2\sigma_{1,2}^2}\right), \\
 G_2(z_v) &= (1 - a_{f2}) \exp\left(-\frac{(z_v - z_{w2})^2}{2\sigma_{2,1}^2}\right) + a_{f2} \exp\left(-\frac{(z_v - z_{w2})^2}{2\sigma_{2,2}^2}\right), \\
 P(z_v) &= a_0 + a_1 z_v + a_2 z_v^2.
 \end{aligned} \tag{6.9}$$

$$f(z_v) = \begin{cases} \left(P(z_{w1}) + A_1\right)G_1(z_v) + A_{bg} & (z_v < z_{w1}), \\ A_1 G_1(z_v) + A_2 G_2(z_v) + P(z_v) + A_{bg} & (z_{w1} < z < z_{w2}), \\ \left(P(z_{w2}) + A_2\right)G_2(z_v) + A_{bg} & (z > z_{w2}). \end{cases} \tag{6.10}$$

The resulting fits are shown in figure 6.5. Table 6.3 gives the parameters of the fit for the different targets.

Using the results of table 6.3 the relative contribution of the events from the target walls to the good events can be estimated. The cut in the target walls TargetCut is chosen at  $2.5 \times \sigma_{i,2}$ :

$$\text{TargetCut} : z_{c,\min} < z_v < z_{c,\max}. \tag{6.11}$$

Parameter	empty cell	hydrogen	hydrogen (VCS cuts)
$z_{w1}$	$-23.70 \pm 0.03$	$-24.43 \pm 0.01$	$-24.06 \pm 0.03$
$\sigma_{1,1}$	$1.09 \pm 0.14$	$1.29 \pm 0.02$	$1.45 \pm 0.05$
$\sigma_{1,2}$	$2.10 \pm 0.18$	$2.70 \pm 0.01$	$2.78 \pm 0.12$
$A_1$	$147 \pm 5$	$20660 \pm 63$	$501 \pm 12$
$a_{f1}$	$0.38 \pm 0.12$	$0.23 \pm 0.01$	$0.26 \pm 0.04$
$z_{w2}$	$24.40 \pm 0.03$	$24.61 \pm 0.01$	$24.51 \pm 0.01$
$\sigma_{2,1}$	$1.08 \pm 0.13$	$1.37 \pm 0.02$	$1.22 \pm 0.03$
$\sigma_{2,2}$	$2.11 \pm 0.13$	$2.64 \pm 0.01$	$2.53 \pm 0.12$
$A_2$	$166 \pm 5$	$33912 \pm 78$	$986 \pm 14$
$a_{f2}$	$0.44 \pm 0.10$	$0.25 \pm 0.01$	$0.13 \pm 0.02$
$a_0$	/	$9289 \pm 12$	$526 \pm 2$
$a_1$	/	$42.59 \pm 0.56$	$-1.29 \pm 0.13$
$a_2$	/	$0.12 \pm 0.06$	$-0.15 \pm 0.01$
$A_{bg}$	$1.81 \pm 0.21$	$627.46 \pm 5.58$	$2.67 \pm 0.36$
$z_{c,min}$	-18.44	-17.69	-17.11
$z_{c,max}$	19.14	18.00	18.20
$f_{wall}$	/	$(0.34 \pm 0.01)\%$	$(0.12 \pm 0.01)\%$

**Table 6.3:** The parameters of  $f(z_v)$  for the histograms in figures 6.5. The results in the right column are obtained by a fit to the  $z_v$ -histogram, when all cuts for the calculation of the cross section have been applied, except the cut on  $z_v$  (see figure 6.10.a).

In the table one can see, that for both peaks  $\sigma_{i,2}$  is about twice as large as  $\sigma_{i,1}$ . This means that the cut in  $z_v$  is approximatively at  $5 \times \sigma_{i,1}$  for the narrowest Gaussian: its contribution to the good events can be neglected.

Putting the cut at  $2.5 \times \sigma_{i,2}$  means that  $C = 98.76\%$  of the events in the widest Gaussian are removed. The resulting contamination of target wall events to the good events in terms of percentage  $f_{wall}$  can be estimated based on the fit. For the cut calculated based on the fit to the  $z_v$ -histogram using VCS cuts,  $f_{wall}$  is estimated to be  $(0.12 \pm 0.01)\%$ , which is well below the statistical error of the measurement. The cut used for the determination of the cross section is thus given by

$$\text{TargetCut} : -17.11 \text{ mm} < z_v < 18.20 \text{ mm} . \quad (6.12)$$

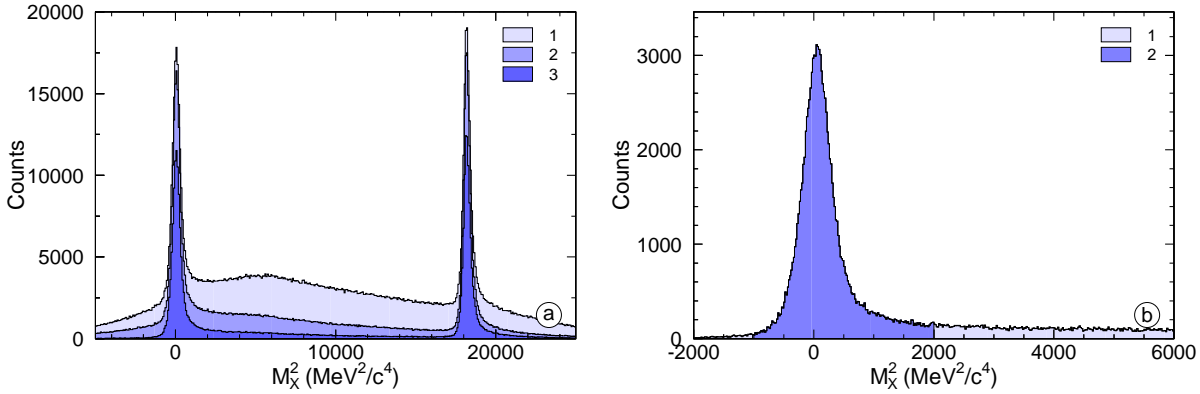


**Figure 6.6:** The left panel shows the influence of the different cuts on the  $M_X^2$ -distributions. 1: no cut, 2: TimeCut and 3: TimeCut + TargetCut. The window in  $M_X^2$  to select the photon electroproduction events ( $[-1000, 2000] \text{ MeV}^2/c^4$ ) is indicated by zone 2 in panel b (used cuts: TimeCut + TargetCut).

### 6.1.6 Missing mass

The reconstruction of the mass of the undetected particle allows to select the photon electroproduction events in the data. Figure 6.6 shows the influence of the different cuts on the distribution of  $M_X^2$ . A large background comes from random coincidences, removed by TimeCut. A second important background contribution to the  $M_X^2$ -distribution is due to the interactions of the electrons with the material of the target cell. These events are removed by TargetCut, but unfortunately a lot of good events are lost due to this cut, too.

After applying both cuts a clean  $M_X^2$ -histogram is obtained. The separation between the  $\gamma$  and  $\pi^0$  peaks is  $1.8 \cdot 10^4 \text{ MeV}^2/c^4$ , which is 30 times the FWHM of the photon peak. The window for the selection of the photon-production events is defined by

$$M_{\text{missCut}} : -1000 \text{ MeV}^2/c^4 < M_X^2 < 2000 \text{ MeV}^2/c^4 \quad (6.13)$$

and it is indicated in the right panel of figure 6.6. The background of remaining  $\pi^0$ -production can be neglected.

### 6.1.7 Kinematical cuts

In the sections above the selection of the photon electroproduction events was discussed. To extract the GPs, one needs to apply more cuts to select the appropriate kinematics of the reaction. The spectrometers are set to cover the interesting part of the phase space, but they also accept events which cannot be used for the determination of the GPs.

Five kinematical variables are important in the analysis of the VCS experiments below the pion production threshold:  $\theta_{\gamma\gamma_{\text{cm}}}$ ,  $\varphi$ ,  $\varepsilon$ ,  $q_{\text{cm}}$  and  $q'_{\text{cm}}$ . In this work the cross section is studied as a function of  $\theta_{\gamma\gamma_{\text{cm}}}$  and the central part of the acceptance is defined by  $\varphi = 180^\circ$  or  $0^\circ$  (in-plane events),  $\varepsilon = 0.645$ ,  $q_{\text{cm}} = 600 \text{ MeV}/c$  and  $q'_{\text{cm}} = 90 \text{ MeV}/c$ . The acceptances for these variables are shown in figure 6.7. The variables  $\theta_{\gamma\gamma_{\text{cm}}}$  and  $\varphi$  are transformed into  $\varphi'$  and  $\theta'$  (see figure 6.8). In-plane events are in this new convention characterized by  $\theta' = 90^\circ$  and  $\varphi' \in [-180^\circ, 180^\circ]$ . Using these new spherical coordinates in-plane events are selected using a cut  $|\theta' - 90^\circ| < 12^\circ$  and  $\varphi'$  corresponds to  $\theta_{\gamma\gamma_{\text{cm}}}$ . The advantage of this kind of cut is that the bin height on the sphere is independent of  $\varphi'$ .

The cuts to select the central kinematics are given by:

$$\begin{aligned}
 |\theta' - 90^\circ| &< 12^\circ, \\
 |\varepsilon - 0.645| &< 0.012, \\
 |q_{\text{cm}} - 600 \text{ MeV}/c| &< 12 \text{ MeV}/c, \\
 |q'_{\text{cm}} - 90 \text{ MeV}/c| &< 15 \text{ MeV}/c.
 \end{aligned} \tag{6.14}$$

### 6.1.8 Additional acceptance cut

After applying all the above cuts a discrepancy between simulation and data remains as can be observed in figure 6.9.a. For low  $z_v$  experiment and data agree very well, but for  $z_v > 10 \text{ mm}$  a deviation between the two appears.

In the simulation it is assumed that all particles passing through the collimator with a momentum within the acceptance of the spectrometer are properly detected. This is fulfilled for the major part of the events in the experiment. For high  $z_v$  and high  $\phi_0^A$  this is, however, not the case.

The discrepancy in figure 6.9.a is caused by the construction of the wire chambers in spectrometer A. A part of the protons with ( $z_v > 10 \text{ mm}$ ) && ( $\phi_0^A > 4^\circ$ ) hit the metal frame of the wire chambers and by consequence they are not properly detected. This frame is not incorporated in the simulation, causing the excess of events at high  $z_v$ . The problem can be solved by applying the additional cut on the acceptance of the spectrometers:

$$(z_v < 10 \text{ mm}) \parallel \phi_0^A < 4^\circ. \tag{6.15}$$

Simulation and data agree very well over the complete  $z_v$ -range after applying this cut, although the distribution of  $z_v$  is now deformed.

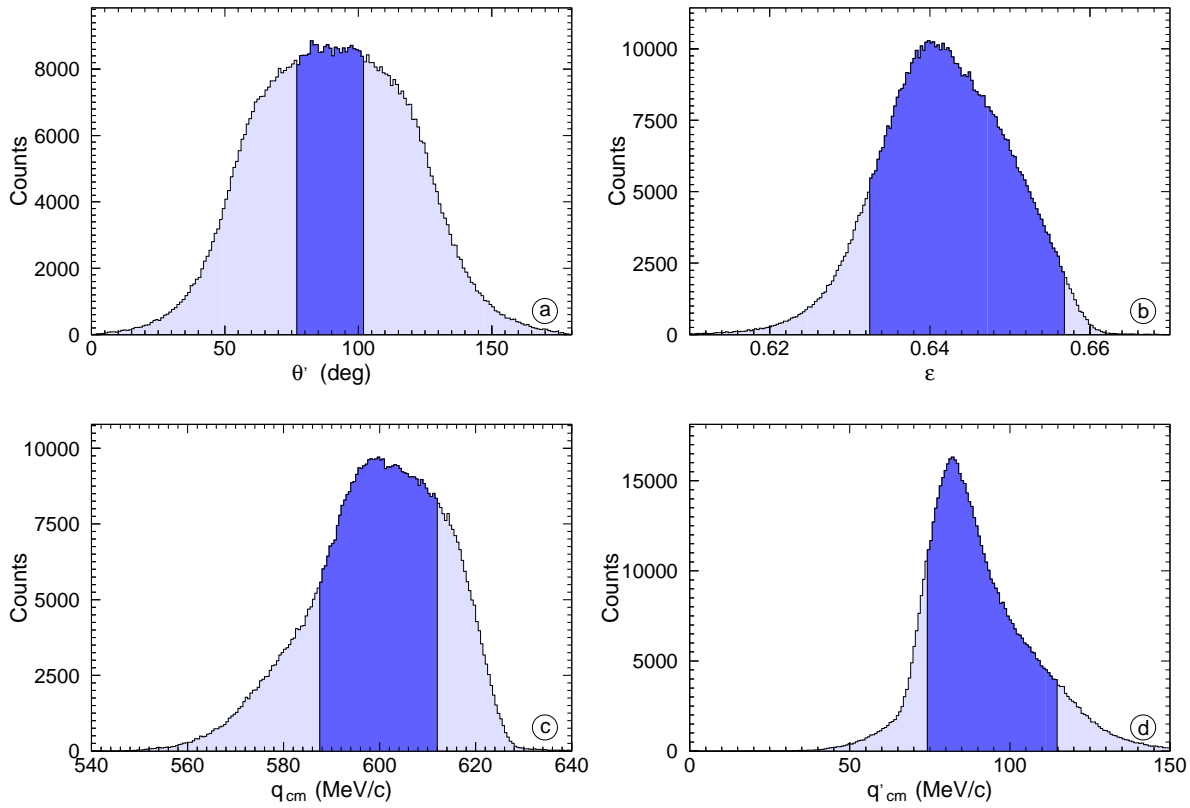


**Figure 6.7:** The distributions of the important kinematical variables for the five-fold differential photon electroproduction reaction for the VCS90b setting. The darker areas correspond to the accepted events.

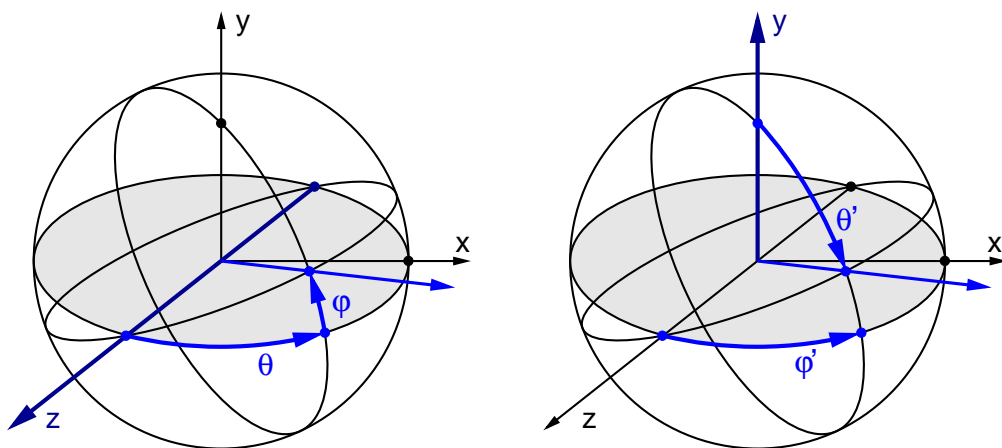


**Figure 6.8:** Transformation from  $(\theta, \varphi)$  to the new spherical coordinates  $(\theta', \varphi')$ . The two conventions use a different axis in the center-of-mass frame as polar axis:  $z$  for the  $(\theta, \varphi)$  and  $y$  for the  $(\theta', \varphi')$  convention. The grey zone shows the in-plane events.

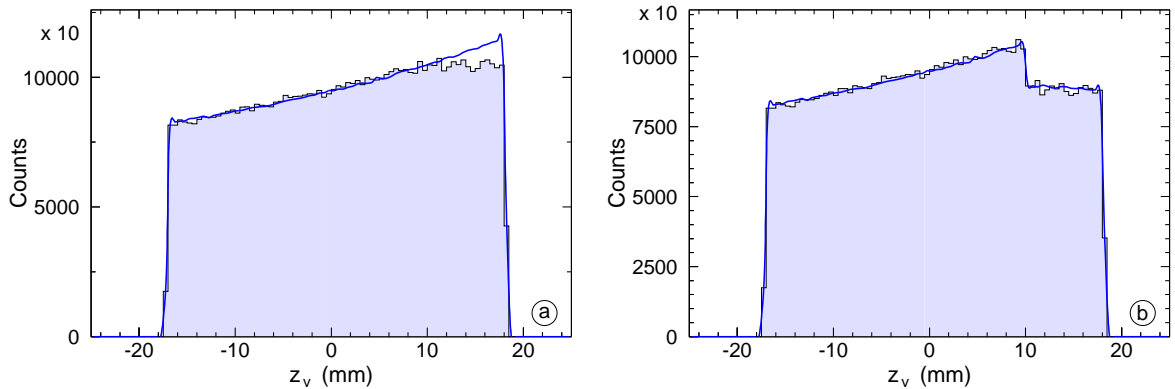


**Figure 6.9:** Comparison of the simulated and experimental  $z_v$ -spectra without (a) and with (b) the additional cut in the acceptance. The region of the target walls has been removed, because the interactions of the electrons with the havar walls are not incorporated in the simulation.

## 6.2 Estimation of the background

The main sources of background are pion production and interactions of the beam electrons with the end caps of the target cell. To estimate the contributions of these background processes surviving the VCS cuts the four histograms displayed in figure 6.10 are studied.

A first source of background events originates from the interaction of the beam electrons with the target cell. The contribution is estimated using a fit of the function defined in equations (6.10) and (6.9) to the observed  $z_v$ -distribution (figure 6.10.a). The result is given in table 6.3: the contribution of these events to the total number is estimated to be  $0.12 \pm 0.01\%$ .

Other sources of background are the  $\pi^-$ ,  $\pi^+$  and  $\pi^0$  production processes.  $\pi^-$  and  $\pi^+$  can be detected by the electron and proton spectrometer, respectively. The Cherenkov detector of spectrometer B is used to estimate the  $\pi^-$ -contribution to the data and a study of the signals of the scintillators of spectrometer A yields a value for the contamination of  $\pi^+$ . In section 6.1.6 it was shown that the contamination of  $\pi^0$ -production events to the VCS data can be neglected, since the separation between the two peaks in the  $M_X^2$ -distribution is much larger than their widths.

Figure 6.10.b shows  $\Sigma \text{ Cher}$ , the distribution of the sum of all Cherenkov mirrors for the events in the data (1). The Cherenkov detector can be used to obtain an upper limit of the contamination of  $\pi^-$  in a subset of the data ( $x_{fp}^B \in [-750, 800]$  mm). For the events inside  $x_{fp}^B \in [-750, 800]$  mm the events rejected and accepted by the Cherenkov cut are indicated by histogram 2 and 3, respectively, in figure 6.10.b. The fraction of the number of events in histogram 2 with respect to the events in histogram 3 is  $(0.29 \pm 0.05)\%$ . This is the best estimate one can get for the complete dataset. Most of the rejected events are indeed background

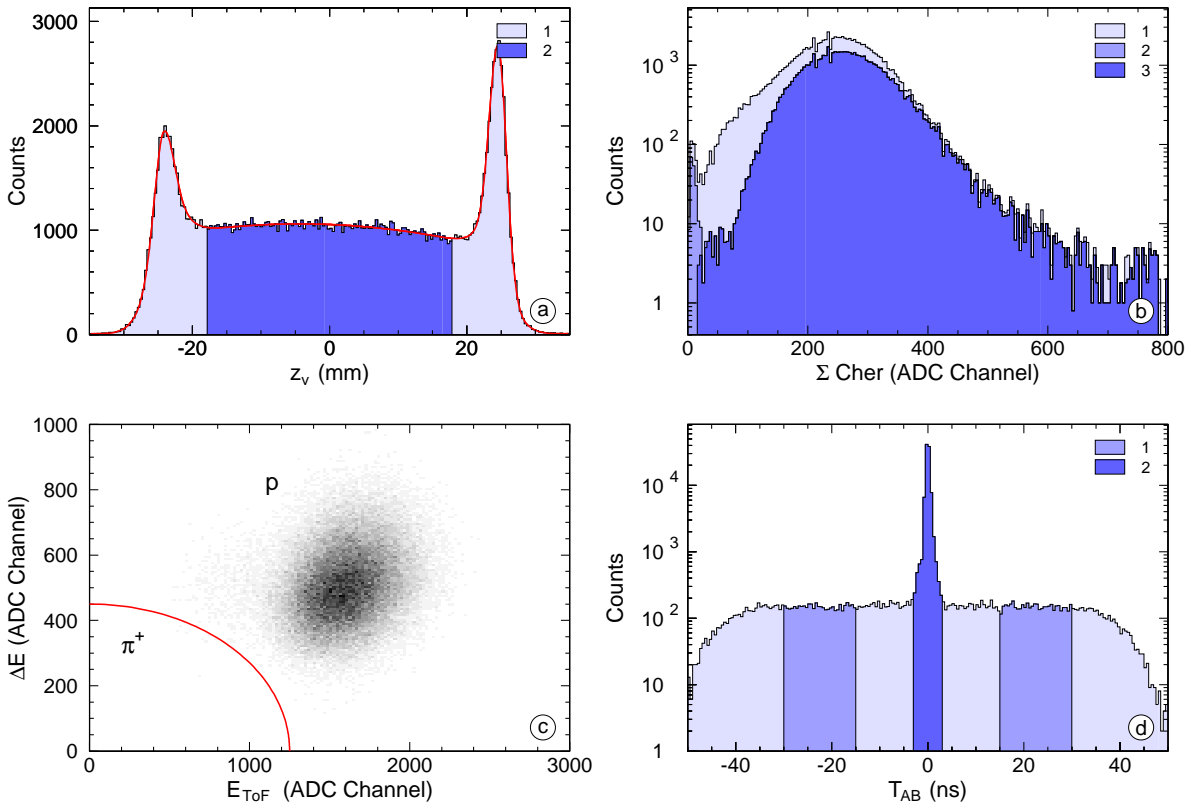


**Figure 6.10:** Histograms of different variables after applying all cuts for the unpolarized analysis (for the histograms of  $z_v$  and  $T_{AB}$  the cut on the variable itself was not used).

events, but a fraction of them (approximately 1/3) are in fact good events as it is shown by the  $M_X^2$ -distribution in figure 6.11. Therefore the stated value should be taken as an upper limit.

The signals of the  $\Delta E$ - versus the ToF-scintillators for the events inside the VCS cuts are shown in figure 6.10.c. Based on the number of events inside the ScintAPion-cut with respect to the total number of events in the dataset, an upper limit of the  $\pi^+$ -contamination is obtained:  $(0.25 \pm 0.03)\%$ . From figure 6.2 one can deduce that most of the events within this 0.25% are actually good photon electroproduction events, for which the particle identification in the scintillator has failed: the actual contribution of  $\pi^+$  to the data is much lower than the other uncertainties in the analysis.

Figure 6.10.d shows the distribution of  $T_{AB}$  for the VCS events. The total number of random coincidences inside  $[-3, 3]$  ns is calculated by the two side-windows in the coincidence time distribution:  $(1.80 \pm 0.04)\%$  of the events inside the peak region are due to random coinci-

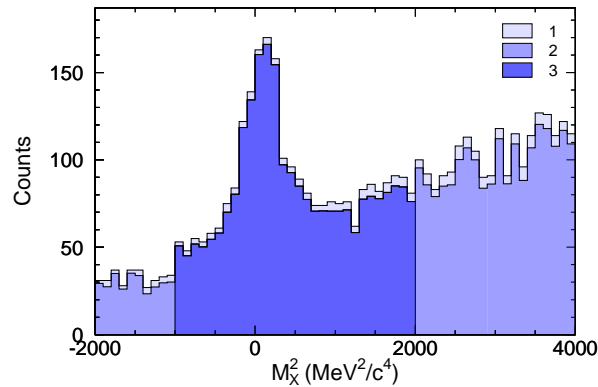


**Figure 6.11:**  $M_X^2$ -distribution of the events cut away by the CherElectron2-cut without (1) and with (2) subtraction of random coincidences. The window in  $M_X^2$  is indicated by (3).

dences. They have been subtracted to calculate the cross section and in this way they do not pollute the data.

## 6.3 Calculation of the unpolarized cross section

### 6.3.1 Calculation of the Bethe Heitler + Born cross section

As explained in chapter 2 the measured cross section deviates less than 10% from the Bethe-Heitler + Born cross section for the kinematics of this experiment. The BH+B contribution to the total cross section can be calculated using quantum electrodynamics based on the form factors of the proton. In section 2.1 it is described that the form factors are not known with infinite precision and several parameterizations are available. In this work two different sets of form factors are used. The first one is the parameterization of Friedrich *et al.* [8] and the other set of form factors is the one of Mergell *et al.* [5]. In the kinematical region of this work, both set of form factors differ by up to 3% (see figure 2.3). These different values for the form factors also yield a different Bethe-Heitler + Born cross section. Figure 6.12.a shows a comparison of the obtained BH+B cross section for both parameterizations. The main difference is the absolute normalization of the cross section, since the relative difference is approximately constant (about 4%) over the  $\theta_{\gamma\text{cm}}$ -range of the experiment (see figure 6.12.b).

The analysis is done for both set of form factors. Since the procedure of the analysis does not change when a different set of form factors is chosen, all figures and tables shown in this chapter are valid for the Friedrich parameterization of the form factors. When a figure or table is based on the Mergell parameterization it is explicitly mentioned in the caption.

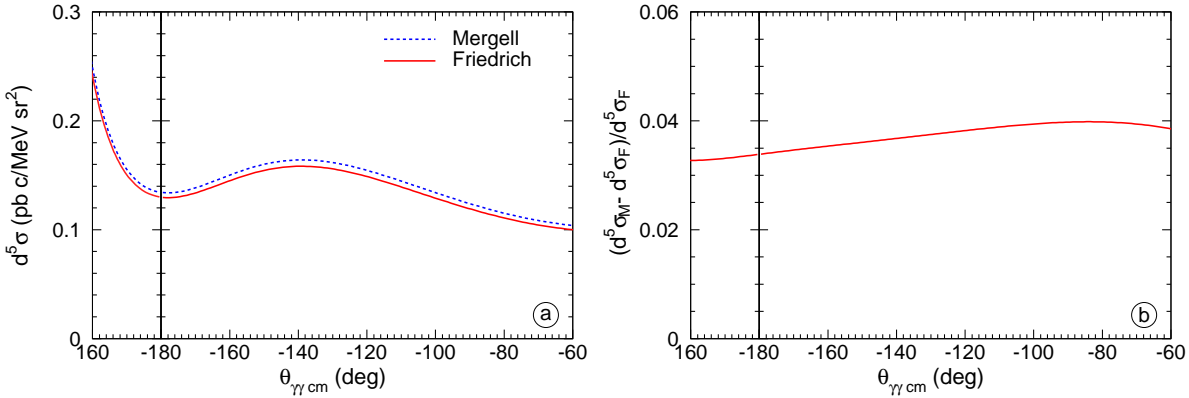


**Figure 6.12:** a: The Bethe-Heitler + Born cross section calculated with the form factors of Friedrich and Mergell. b: The relative difference between the cross sections calculated based on both parameterizations of the form factors.

### 6.3.2 Solid angle

The solid angle is calculated using the VCS Monte Carlo simulation described in chapter 5. The simulation generates a data file similar to the experimental data, which is analyzed in the same way as the experimental data: all cuts used to select the good events in the data<sup>2</sup> are applied to the simulated data and a histogram is created for the distribution of  $\theta_{\gamma\gamma\text{cm}}$ . The solid angle for each bin in  $\theta_{\gamma\gamma\text{cm}}$  is then calculated using:

$$\Delta\Omega = \frac{1}{f_{\text{cor}}} \frac{N_{\text{sim}}}{\mathcal{L}_{\text{sim}} \frac{d\sigma}{d\Omega}}, \quad (6.16)$$

where  $N_{\text{sim}}$  is the number of simulated events in each bin and  $d\sigma/d\Omega$  is the cross section used in the simulation in the given point in the bin.

The treatment of the radiative corrections is applied as described in section 5.2: a part of the internal radiative corrections ( $\delta_{\text{rad1}}$ ) is taken into account by implementing the real internal bremsstrahlung in the simulation. The remaining correction is a good approximation constant over the phase space under study and it is applied independent of the simulation in the calculation of the solid angle using the factor  $f_{\text{cor}}$  in formula (6.16). This factor is given in equation (5.13)

$$f_{\text{cor}} = \frac{\exp(\delta_{\text{rad2}} \delta_{\text{ver}})}{(1 - \delta_{\text{vac}})^2} \quad (6.17)$$

and equals 0.942 for the kinematical regime of the experiment. The theoretical uncertainty on this value is 2%.

<sup>2</sup>See equation (C.1) of appendix C for a summary.

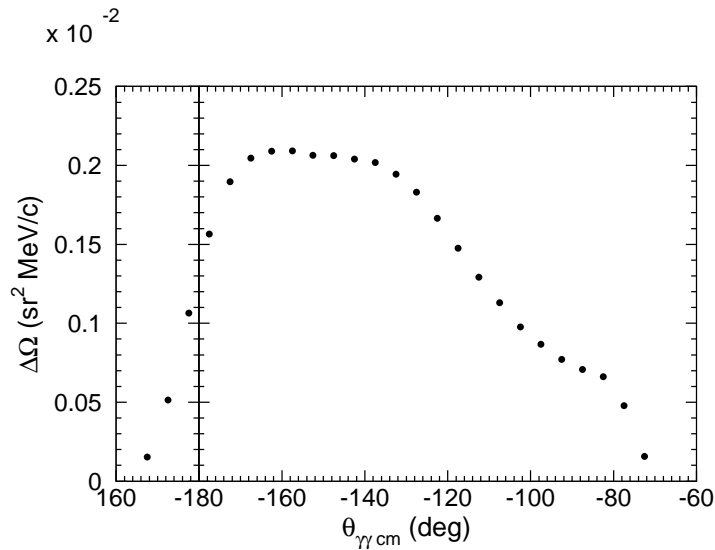


**Figure 6.13:** Effective solid angle as a function of  $\theta_{\gamma\gamma\text{cm}}$  for the VCS90b setting applying all cuts used in the analysis. The statistical error is smaller than the size of the symbols.

The effective solid angle  $\Delta\Omega$  for the VCS90b setting is displayed in figure 6.13. Due to the high amount of simulated events ( $3 \times 10^7$ ) the statistical uncertainty on the calculation of the solid angle is smaller than the size of the symbols in the figure.  $\mathcal{L}_{\text{sim}} = 3 \cdot 10^8 \text{ pb}^{-1}$ , which is 15 times the experimental luminosity to make sure that the statistical uncertainty on the cross section is only determined by the number of events in the data. The units of  $\Delta\Omega$  are  $\text{sr}^2 \text{MeV}/c$ . The unit of momentum inside the units of  $\Delta\Omega$  indicates the fact that the cross section is differential in the momentum of the scattered electron.

### 6.3.3 Detector efficiency

In order to derive the absolute cross section of the  $(ep \rightarrow e'p'\gamma)$  process the data have to be corrected for the detector efficiency. Only two detectors determine the efficiency of the spectrometer: the drift chambers and the scintillators. If a particle passes through one of the scintillator paddles a trigger is generated and all detectors of the spectrometer are read out.

The wire chambers are very sensitive: for each particle passing through the VDC several wires are hit. The chance that a particle has passed through the 4 VDCs without leaving any signal is negligible, even if one of the wires of the VDC is broken. Broken wires and VDC resolution effects have an influence on the quality of the reconstruction of the particle track, which is taken into account in the analysis via the Monte Carlo simulation.

The main inefficiency of the spectrometers is related to the trigger. When a particle is not detected in the scintillator, no trigger is generated and the signals of the VDCs are not registered. The inefficiency of each of the scintillator paddles in the spectrometers is negligible.

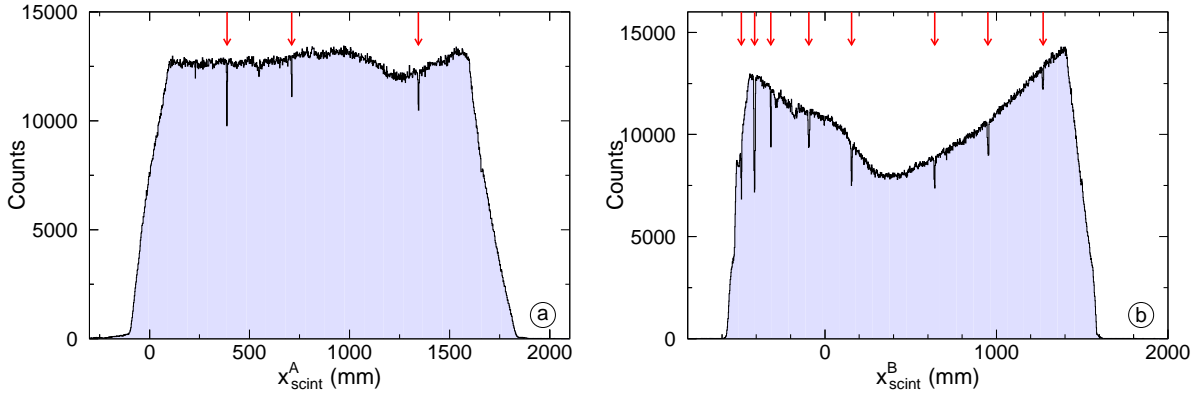


**Figure 6.14:** Histogram of  $x_{\text{scint}}$  for all particles entering spectrometer A (a) and B (b). The arrows indicate regions with lower trigger efficiency.

Spectrometer A			Spectrometer B		
$x_{\text{scint}}^{\text{A}}$ (mm)	Plane	Paddles	$x_{\text{scint}}^{\text{B}}$ (mm)	Plane	Paddles
1344	$\Delta\text{E}$	11 $\leftrightarrow$ 12	1272	$\Delta\text{E}$	12 $\leftrightarrow$ 13
710	$\Delta\text{E}$	7 $\leftrightarrow$ 8	950	$\Delta\text{E}$	10 $\leftrightarrow$ 11
388	$\Delta\text{E}$	5 $\leftrightarrow$ 6	640	$\Delta\text{E}$	8 $\leftrightarrow$ 9
			155	$\Delta\text{E}$	5 $\leftrightarrow$ 6
			-94	ToF	3 $\leftrightarrow$ 4
			-316	$\Delta\text{E}$	2 $\leftrightarrow$ 3
			-410	ToF	1 $\leftrightarrow$ 2
			-488	$\Delta\text{E}$	1 $\leftrightarrow$ 2

**Table 6.4:** Overview of the dead zones in the scintillators. All the dead zones are located in the gap between two paddles of one of the two scintillator planes.

However, if a particle passes through the small gap between two paddles, it might happen that no trigger is generated. To find these dead zones in the trigger detector one can examine the distribution of  $x_{\text{scint}}$ , the dispersive coordinate of the interaction point with the plane of the time-of-flight scintillators. These distributions for both spectrometers are shown in figure 6.14. The important dead zones in the scintillators are marked by the arrows. A list of these regions can be found in table 6.4.

By re-weighting the events inside or close to these dead zones a correction is applied for the loss of events. For the dead gaps in spectrometer B it is enough to apply a general correction factor to the data, since the angle  $\theta_{\gamma\gamma\text{cm}}$  is not directly correlated to  $x_{\text{scint}}^{\text{B}}$ . However, for spectrometer A this is not possible since  $\theta_{\gamma\gamma\text{cm}}$  is strongly correlated to the proton momen-

tum and the loss of events in the dead zones of the scintillator of spectrometer A has only an influence on a few bins in  $\theta_{\gamma\gamma\text{cm}}$ . Therefore a careful study has been done to make sure that the correction is only applied to the involved bins. The resulting correction is very small - for some of the bins it is of the order of 0.1% -, and it does not influence the values of the extracted structure functions.

### 6.3.4 Cross section

The experimental differential cross section is calculated using:

$$\frac{d^5\sigma}{dk'd\Omega_e'd\Omega_{\gamma\gamma\text{cm}}} = \frac{N_{\text{exp}}}{\mathcal{L}_{\text{exp}}} \cdot \frac{1}{\Delta\Omega}. \quad (6.18)$$

$N_{\text{exp}}$  is the number of counts in the experiment corrected for the random coincidences,  $\mathcal{L}_{\text{exp}}$  is the experimental luminosity, and  $\Delta\Omega$  is the effective solid angle of the acceptance, as calculated in equation (6.16).

The resulting differential cross section is shown in figure 6.15 as a function of  $\theta_{\gamma\gamma\text{cm}}$ . The indicated error bars show the statistical uncertainty on the result. The systematic uncertainties are discussed in section 6.4.3.

## 6.4 Determination of the structure functions

### 6.4.1 Extraction method

The measured differential cross section can be written according to the low energy theorem as the sum of the BH+B contribution and a term linear in  $q'_{\text{cm}}$  as in equation (2.48):

$$d^5\sigma = d^5\sigma^{\text{BH+B}} + \phi q'_{\text{cm}} \mathcal{M}_0^{\text{NB}} + \mathcal{O}(q'^2_{\text{cm}}), \quad (6.19)$$

where  $\mathcal{M}_0^{\text{NB}}$  is given by

$$\mathcal{M}_0^{\text{NB}} = v_{\text{LL}}(P_{\text{LL}}(q_{\text{cm}}) - \frac{1}{\varepsilon} P_{\text{TT}}(q_{\text{cm}})) + v_{\text{LT}} P_{\text{LT}}(q_{\text{cm}}). \quad (6.20)$$

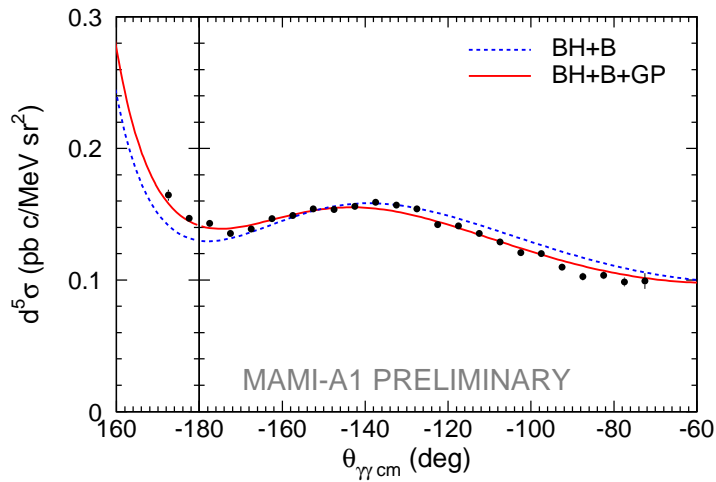


**Figure 6.15:** Experimental five-fold differential cross section of  $ep \rightarrow e'p'\gamma$  for in-plane kinematics with  $q_{cm} = 600 \text{ MeV}/c$ ,  $q'_{cm} = 90 \text{ MeV}/c$  and  $\varepsilon = 0.645$ . The dashed line shows the contribution of the Bethe-Heitler and Born contribution. The full line shows a fit to the data taking into account the effect of the GPs.

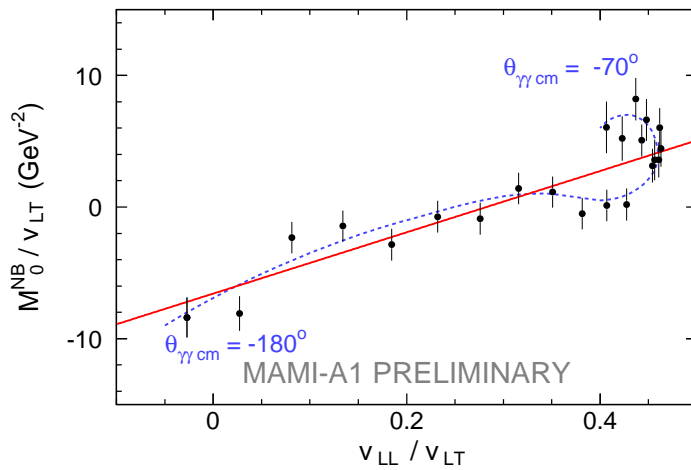


**Figure 6.16:** Extraction of 2 linear combinations of GPs. The reduced  $\chi^2$  of the linear fit is 2.37. The dashed line shows the evolution of the points with  $\theta_{\gamma\gamma cm}$ .

The term  $\mathcal{M}_0^{\text{NB}}$  contains two linear combinations of GPs:  $(P_{\text{LL}} - P_{\text{TT}}/\varepsilon)$  and  $P_{\text{LT}}$ . It is calculated based on the measured cross section  $d^5\sigma$  neglecting higher order terms (LET approximation):

$$\mathcal{M}_0^{\text{NB}} = \frac{d^5\sigma - d^5\sigma^{\text{BH+B}}}{\phi q'_{\text{cm}}} . \quad (6.21)$$

The two linear combinations of structure functions are determined by a linear fit of  $\mathcal{M}_0^{\text{NB}}/v_{\text{LT}}$  versus  $v_{\text{LL}}/v_{\text{LT}}$ .  $(P_{\text{LL}} - P_{\text{TT}}/\varepsilon)$  is the slope of the straight line and  $P_{\text{LT}}$  is the ordinate of the intersection point of the fit with  $v_{\text{LL}}/v_{\text{LT}} = 0$ . The fit is shown in figure 6.16. The reduced  $\chi^2$  of the fit is 2.37 and the resulting linear combinations are given by

$$\begin{aligned} P_{\text{LL}} - P_{\text{TT}}/\varepsilon &= 23.31 \pm 1.90 \text{ GeV}^{-2} , \\ P_{\text{LT}} &= -6.58 \pm 0.67 \text{ GeV}^{-2} , \end{aligned} \quad (6.22)$$

where the indicated error is the statistical uncertainty on the result of the fit. The relation between  $\theta_{\gamma\gamma_{\text{cm}}}$  and  $v_{\text{LL}}/v_{\text{LT}}$  is indicated by the dashed line:  $v_{\text{LL}}/v_{\text{LT}} = 0$  corresponds to  $\theta_{\gamma\gamma_{\text{cm}}} = -180^\circ$  and following the dashed line  $\theta_{\gamma\gamma_{\text{cm}}}$  increases up to  $-70^\circ$ . Note that the relation between  $\theta_{\gamma\gamma_{\text{cm}}}$  and  $v_{\text{LL}}/v_{\text{LT}}$  is not unique since  $v_{\text{LL}}/v_{\text{LT}}$  starts to decrease again when  $\theta_{\gamma\gamma_{\text{cm}}} > -100^\circ$ .

## 6.4.2 Iterations

### Procedure

For the calculation of the effective solid angle it is important that the simulation uses a cross section close to the real photon electroproduction cross section. This cross section is of course not known a priori and therefore the BH+B cross section was used initially to calculate the solid angle of the detector acceptance.

In section 6.4.1 new values for  $(P_{\text{LL}} - P_{\text{TT}}/\varepsilon)$  and  $P_{\text{LT}}$  were obtained. These values can now be used to include the effect of the GPs into the simulated data. This is done by reweighting each event by a factor  $d^5\sigma^{\text{BH+B+GP}}/d^5\sigma^{\text{BH+B}}$  in the calculation of the effective solid angle. The deviation from the initial solid angle is caused by the change in the behavior of the cross section, due to the effect of the GPs. Finally, new values for the structure functions are obtained.

The results of each iteration step are used to perform a next iteration. This procedure is applied until convergence is obtained in the values of the structure functions.

Iteration	$(P_{LL} - P_{TT}/\varepsilon)$ ( $\text{GeV}^{-2}$ )	$P_{LT}$ ( $\text{GeV}^{-2}$ )	reduced $\chi^2$
0	$23.31 \pm 1.90$	$-6.58 \pm 0.67$	2.37
1	$26.59 \pm 1.91$	$-7.79 \pm 0.67$	2.61
2	$27.00 \pm 1.91$	$-7.97 \pm 0.67$	2.63
3	$27.05 \pm 1.91$	$-7.99 \pm 0.67$	2.63
4	$27.06 \pm 1.91$	$-7.99 \pm 0.67$	2.63
5	$27.06 \pm 1.91$	$-7.99 \pm 0.67$	2.63

**Table 6.5:** Results of the iterations on the structure functions using the form factors of Friedrich *et al.* [8]. After 2 to 3 iterations the final result is obtained.

Iteration	$(P_{LL} - P_{TT}/\varepsilon)$ ( $\text{GeV}^{-2}$ )	$P_{LT}$ ( $\text{GeV}^{-2}$ )	reduced $\chi^2$
0	$24.33 \pm 1.90$	$-3.86 \pm 0.67$	2.02
1	$27.91 \pm 1.90$	$-4.96 \pm 0.67$	2.39
2	$28.40 \pm 1.91$	$-5.14 \pm 0.67$	2.41
3	$28.46 \pm 1.91$	$-5.17 \pm 0.67$	2.42
4	$28.47 \pm 1.91$	$-5.17 \pm 0.67$	2.42
5	$28.47 \pm 1.91$	$-5.17 \pm 0.67$	2.42

**Table 6.6:** Same as table 6.5 for the form factors of Mergell *et al.* [5].

### Effect of the iterations

In table 6.5 (and table 6.6 for the form factors of reference [5]) the resulting structure functions for the different iterations are given, showing a convergence to a stable result after two to three iterations. The effect of the iterations on the solid angle is shown in figure 6.17. As can be observed, the effect of the iterations is not negligible. In the analysis of the first VCS experiment at MAMI [60] the effect of the iterations was found to be smaller than the statistical errors (about 2%) and the iteration procedure was not applied.

Up to now, the starting point of the iteration procedure was  $(P_{LL} - P_{TT}/\varepsilon) = 0 \text{ GeV}^{-2}$  and  $P_{LT} = 0 \text{ GeV}^{-2}$ , which corresponds to the BH+B cross section. This initial point has been modified to test the method: the iterations have been performed for  $(P_{LL} - P_{TT}/\varepsilon) = 45 \text{ GeV}^{-2}$ , and  $P_{LT} = 10 \text{ GeV}^{-2}$  and  $(P_{LL} - P_{TT}/\varepsilon) = -10 \text{ GeV}^{-2}$  and  $P_{LT} = -15 \text{ GeV}^{-2}$  as initial values. Each time the structure functions converge to the same value as shown in figure 6.18.

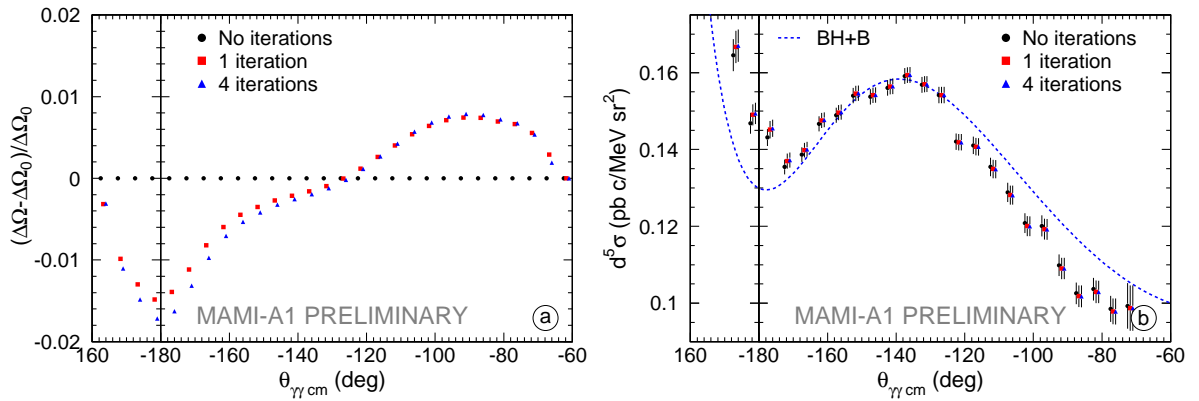


**Figure 6.17:** Relative change in the effective solid angle (a) and change in the cross section (b) as a function of  $\theta_{\gamma\gamma\text{cm}}$  during the iteration procedure. The data points for each successive iteration are shifted over  $0.75^\circ$  to the right for better visibility.

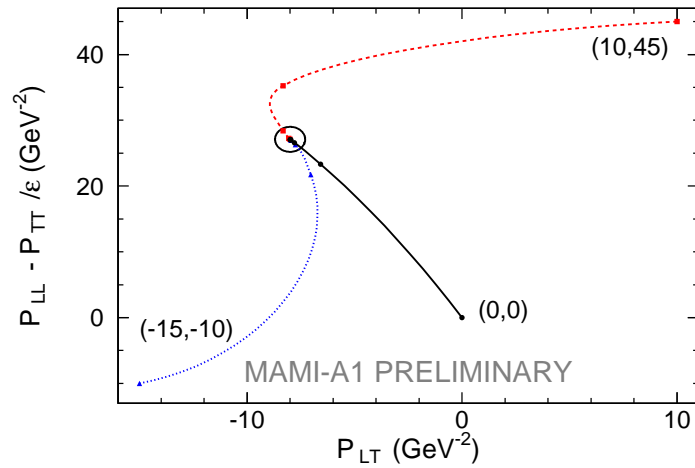


**Figure 6.18:** The convergence of the iteration procedure for different initial values of the structure functions. The ellipse represents the statistical error on the final values for  $(P_{LL} - P_{TT}/\varepsilon)$  and  $P_{LT}$ .

### 6.4.3 Systematic uncertainties

There are many sources of systematic errors: the absolute calibration of the spectrometers, the absolute normalization of the calculated cross section, the form factors of the proton used to calculate the BH+B contribution, ... The uncertainty on the absolute normalization of the cross section includes the uncertainty on the calculation of the luminosity and on the solid angle calculated by the simulation. Contributions of background sources can be neglected as shown above. The study of the effect of the different sources of systematic errors is performed on the first iteration.

$p_A$ (MeV/c)	$p_B$ (MeV/c)	$(P_{LL} - P_{TT}/\varepsilon)$ (GeV <sup>-2</sup> )	$P_{LT}$ (GeV <sup>-2</sup> )
645.38	539.41	$23.31 \pm 1.90$	$-6.58 \pm 0.67$
645.56	539.41	$24.28 \pm 1.90$	$-7.05 \pm 0.67$
645.20	539.41	$22.32 \pm 1.89$	$-6.12 \pm 0.67$
645.38	539.55	$21.70 \pm 1.89$	$-6.08 \pm 0.67$
645.38	539.27	$25.04 \pm 1.90$	$-7.11 \pm 0.67$
645.20	539.55	$20.84 \pm 1.89$	$-5.68 \pm 0.66$
645.56	539.27	$26.01 \pm 1.90$	$-7.59 \pm 0.67$

**Table 6.7:** Estimation of the systematic error due to the absolute calibration of the spectrometers.  $(P_{LL} - P_{TT}/\varepsilon)$  and  $P_{LT}$  were measured using the modified central momenta of the spectrometers (results after the first iteration).

The absolute calibration of the central momenta of the spectrometers is done using the peak position and width of the missing mass distribution (see appendix A). This results in a determination of the central momenta with an uncertainty of  $\mp 0.18$  MeV/c and  $\pm 0.14$  MeV/c for spectrometer A and B, respectively. To study the influence of these uncertainties, the spectrometer central momenta were changed within the precision of the calibration. Then the data were re-analyzed using the modified central momenta. The results are summarized in table 6.7. The first line shows the result for the first iteration (see section 6.4). The following 4 rows were obtained by modifying one of the central momenta by the size of the error bar and finally the effect of the correlation in the errors caused by the calibration procedure was estimated. The latter has the largest influence on the obtained result. The systematic error is estimated as the maximum deviation of the results in table 6.7 from the result in equation (6.22).

The uncertainty on the absolute normalization of the cross section and systematic error of the simulation is estimated as a constant factor over the complete phase space,  $f_{\text{abs}}$ . The accuracy of the luminosity calculation and the simulation with its embedded radiative corrections is estimated to be 2%. The systematic error due to the uncertainty on the absolute normalization for the cross section is determined in table 6.8 by applying the factor  $f_{\text{abs}}$  to the measured cross section.

From table 6.7 and 6.8 the systematic uncertainties are obtained. The final result of the calculation of the two structure functions is:

$$\begin{aligned}
 P_{LL} - P_{TT}/\varepsilon &= 27.1 \pm 1.9 \pm 2.7 \pm 0.6 \text{ GeV}^{-2} , \\
 P_{LT} &= -8.0 \pm 0.7 \pm 1.0 \pm 1.9 \text{ GeV}^{-2} .
 \end{aligned}
 \tag{6.23}$$

$f_{\text{abs}}$	$(P_{\text{LL}} - P_{\text{TT}}/\varepsilon) \text{ (GeV}^{-2}\text{)}$	$P_{\text{LT}} \text{ (GeV}^{-2}\text{)}$
1.02	$22.74 \pm 1.86$	$-4.78 \pm 0.65$
1.01	$23.02 \pm 1.88$	$-5.67 \pm 0.66$
1.00	$23.31 \pm 1.90$	$-6.58 \pm 0.67$
0.99	$23.60 \pm 1.92$	$-7.50 \pm 0.67$
0.98	$23.90 \pm 1.93$	$-8.45 \pm 0.68$

**Table 6.8:** Estimation of the systematic error due to the absolute normalization of the cross section. The two linear combinations of structure functions were obtained by applying the factor  $f_{\text{abs}}$  to the measured cross section (without iteration).

The first error is the purely statistical error of the measurement and the simulation. The two following errors are due to the uncertainty on the calibration of the spectrometers central momenta and the absolute normalization of the cross section, respectively.

#### 6.4.4 Conclusion

The final result for the cross section after the iterations is shown in figure 6.19.a. The linear fit for the extraction of the structure functions is displayed in figure 6.19.b. The linear combinations of structure functions were found to be (the systematic errors were added quadratically):

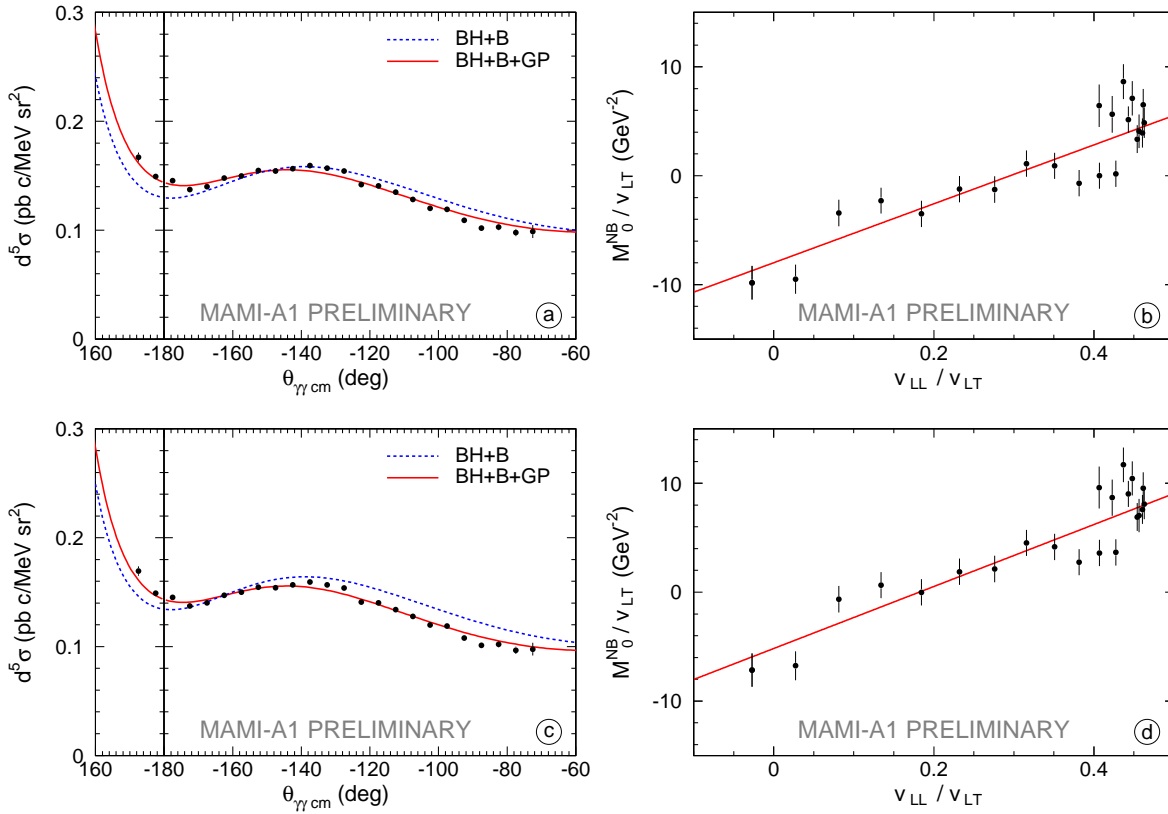
$$\begin{aligned} P_{\text{LL}} - P_{\text{TT}}/\varepsilon &= 27.1 \pm 1.9 \pm 2.8 \text{ GeV}^{-2}, \\ P_{\text{LT}} &= -8.0 \pm 0.7 \pm 2.1 \text{ GeV}^{-2}. \end{aligned} \quad (6.24)$$

When the form factors of Mergell *et al.* are used in the analysis, slightly different values for the structure functions are obtained:

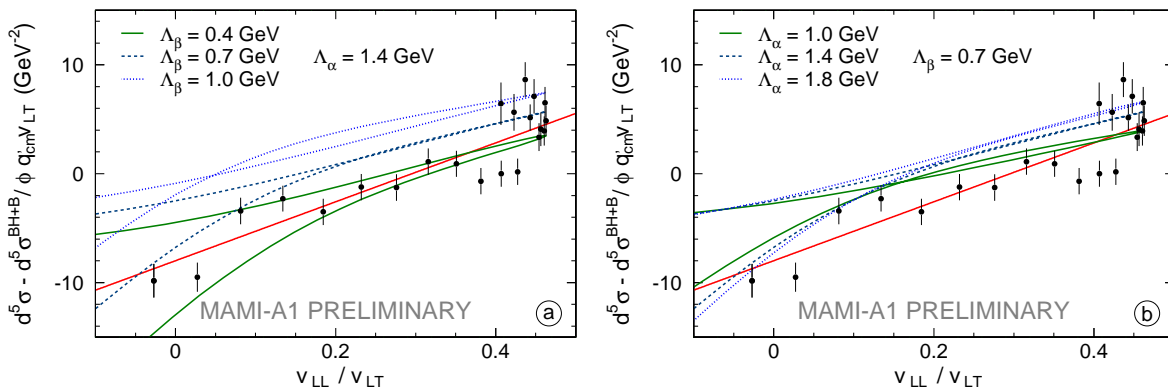
$$\begin{aligned} P_{\text{LL}} - P_{\text{TT}}/\varepsilon &= 28.5 \pm 1.9 \pm 2.8 \text{ GeV}^{-2}, \\ P_{\text{LT}} &= -5.2 \pm 0.7 \pm 2.1 \text{ GeV}^{-2}. \end{aligned} \quad (6.25)$$

Figure 6.19.c and d show the cross section and the extraction of the structure functions for these form factors.

$P_{\text{LT}}$  is more sensitive to the choice of the form factors than  $P_{\text{LL}} - P_{\text{TT}}/\varepsilon$ . This is explained by the fact that different form factors change mainly the absolute normalization and not the shape of the cross section. Since  $P_{\text{LL}} - P_{\text{TT}}/\varepsilon$  is determined by the slope of cross section, it is easy to understand that the variation in  $P_{\text{LL}} - P_{\text{TT}}/\varepsilon$  is smaller.



**Figure 6.19:** Final result for the unpolarized five-fold differential cross section and the extraction of the structure functions using the parameterization of Friedrich (a and b) and Mergell (c and d) for the form factors.



**Figure 6.20:** Comparison of the deviation of the experimental cross section from the BH+B cross section and the DR-model for different values of  $\Lambda_\alpha$  and  $\Lambda_\beta$ .

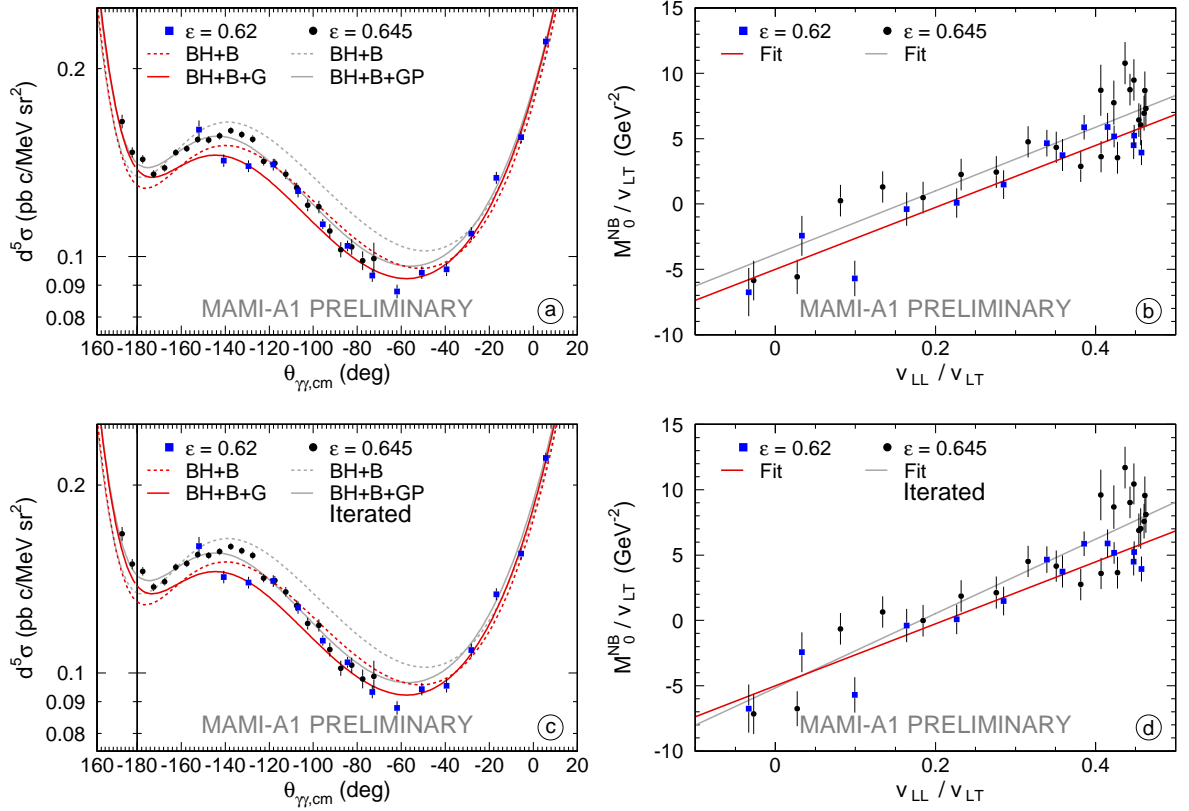


**Figure 6.21:** Comparison with the previous MAMI VCS experiment. For the new data the form factors of reference [5] were used.

## 6.5 Interpretation of the result

In figures 6.19.b and 6.19.d one can observe that, apart from the linear behavior of  $\mathcal{M}_0^{\text{NB}}$  versus  $v_{\text{LL}}/v_{\text{LT}}$ , there is also a higher order effect which makes the data points systematically deviate from a straight line. To estimate the size of this higher order effect one can use the dispersion relation (DR) model of reference [57]. This model includes all higher order effects. In figure 6.20 the deviation of the measured cross section is shown, together with the prediction of the DR-model for different values of the parameters  $\Lambda_\alpha$  and  $\Lambda_\beta$ . The DR model predicts deviations of the order of the observed ones, but there is no combination of parameters which agrees very well with the data.

The predictions of the heavy baryon chiral perturbation theory [42] (to  $\mathcal{O}(p^3)$ ) for  $P_{\text{LL}} - P_{\text{TT}}/\varepsilon$  and  $P_{\text{LT}}$  are re-evaluated using the Friedrich form factors for  $q_{\text{cm}} = 600 \text{ MeV}/c$  and  $\varepsilon = 0.645$ :

$$\begin{aligned} P_{\text{LL}} - P_{\text{TT}}/\varepsilon &= 25.98 \text{ GeV}^{-2} \\ P_{\text{LT}} &= -5.39 \text{ GeV}^{-2} . \end{aligned} \quad (6.26)$$

The predicted value for  $P_{LL} - P_{TT}/\varepsilon$  is compatible with the new result, but the prediction for  $P_{LT}$  is lower than observed in the experiment<sup>3</sup>.

The results of the present experiment can be compared to the results of the first VCS experiment at MAMI (see figure 6.21). That experiment was performed at similar kinematics as the present experiment. There the following values for the structure functions were obtained:

$$\begin{aligned} P_{LL} - P_{TT}/\varepsilon &= 23.7 \pm 2.2 \pm 4.3 \text{ GeV}^{-2}, \\ P_{LT} &= -5.0 \pm 0.8 \pm 1.8 \text{ GeV}^{-2}. \end{aligned} \quad (6.27)$$

These results were obtained using the Höhler parameterization of the form factors [7]. Without performing the iteration procedure the result for  $P_{LL} - P_{TT}/\varepsilon$  is in very good agreement with the new result. For  $P_{LT}$  a comparison is more complicated since this structure function is quite sensitive to the used form factors.

In the analysis of the old result no iterations were performed, since the effect of a first iteration had no significant influence on the determination of the solid angle. In the present analysis it has been shown that the influence of the iterations on the solid angle is indeed small (lower than 2%), but even this small effect has a significant influence on the extracted structure functions. After applying the iterations for the new experiment  $P_{LL} - P_{TT}/\varepsilon$  deviates more from the previous result. The agreement for  $P_{LT}$  depends on the chosen parameterization of the form factors, and is very good for the Mergell parameterization.

There is another important difference between the old and the new measurement. Previously the cross section was measured for  $\theta_{\gamma\gamma\text{cm}} \in [-150^\circ, 0^\circ]$ , whereas the new experiment is performed in the region from  $170^\circ \rightarrow -70^\circ$  in  $\theta_{\gamma\gamma\text{cm}}$ . From figure 6.20 one can deduce that the DR model predicts higher order effects, which result in different slopes for the two branches (branch 1:  $\theta_{\gamma\gamma\text{cm}} = 180^\circ \rightarrow -100^\circ$  and branch 2:  $\theta_{\gamma\gamma\text{cm}} = 0^\circ \rightarrow -100^\circ$ ). By combining the non-iterated cross sections of the old and the new experiment, these two branches are measured. The new measurement uses branch 1 to extract the structure functions and the old measurement used branch 2 for the same purpose. The DR model prediction that both branches should have different slopes is not supported by the experiments. Using the new data an improved measurement of the two linear combinations of VCS structure functions was possible. The main contribution to the systematic error on  $P_{LT}$  is due to the uncertainty on the parameterizations of the form factors.

<sup>3</sup>Note that the non-iterated result for  $P_{LT}$  agrees better with the  $\mathcal{O}(p^3)$  HB $\chi$ PT predictions.

---

# Double-spin asymmetry

---

In this chapter the determination of the double-spin asymmetry is discussed. The analysis is based on all beam times mentioned in appendix C.1. The nominal kinematics of the settings are given by  $q_{\text{cm}} = 600 \text{ MeV}/c$ ,  $q'_{\text{cm}} = 90 \text{ MeV}/c$ ,  $\varepsilon = 0.645$  and  $\varphi = 0^\circ$  or  $180^\circ$ . The spectrometers accept more events than only the ones with this particular kinematics and the complete data set covers a wide range in  $q_{\text{cm}}$ ,  $q'_{\text{cm}}$ ,  $\varepsilon$ ,  $\theta_{\gamma\gamma_{\text{cm}}}$  and  $\varphi$ . This wide acceptance is necessary for the extraction of the different structure functions.

Similar to chapter 6, the selection of the events used in the analysis is described first. The selection of the VCS events themselves is only briefly discussed, because it is very similar to the unpolarized analysis. However, the use of the polarimeter puts specific restrictions on the events and the focus of section 7.1 lies on the choice of the appropriate cuts to keep only these events which are useful for the determination of the double-spin asymmetry. Then, in section 7.2 the beam polarization is shown for the different data taking periods. Section 7.3 describes the calculation of the double-spin asymmetry. As will be shown in this section, the choice of good constraints to the fitting procedure is essential. Finally, a method is presented to extract more information on the structure functions and the results are discussed.

## 7.1 Data selection

### 7.1.1 VCS events

The selection of the photon electroproduction events is done in a similar way as for the unpolarized cross section. The main disadvantage of the use of a focal plane polarimeter is its efficiency. Only about 2% of the protons are useful for the reconstruction of the polarization; only this small fraction interacts via the nuclear interaction with the carbon foil. This low efficiency of the polarimeter and the low cross section of the VCS process make it impossible to select the events inside small bins around the the nominal kinematics as it was possible for the unpolarized analysis, discussed in chapter 6. Therefore the kinematical cuts defined in section 6.1.7 are not used.

The subtraction of the random coincidences is not possible in the polarized analysis, since it is not trivial to include them in the likelihood (see section 7.3.3). To suppress the random coincidences the window in the coincidence time is reduced: 3 ns instead of 6 ns (after applying all cuts the random coincidences contribute for less then 1%), and the cut on the scintillator in spectrometer A is used to suppress the  $\pi^+$  background. Additionally, the cut on the Cherenkov detector in spectrometer B is applied in the region where it covers the focal plane. This results in a better suppression of background events but, unfortunately, also a loss of good events. The number of good events removed by these cuts is rather low and since we are not interested in absolute count rates, it does not harm the analysis.

### 7.1.2 Drift chambers

After passing through the VDCs the protons scatter on the  $^{12}\text{C}$  analyzer of the polarimeter. Afterwards their track is measured by the HDCs and the scattering angles ( $\theta_{\text{fpp}}$ ,  $\phi_{\text{fpp}}$ ) are calculated. The histograms of the polar ( $\theta_{\text{fpp}}$ ) and azimuthal ( $\phi_{\text{fpp}}$ ) scattering angle are shown in figure 7.1.a and 7.1.b for the VCS events inside the validity domain of the spin transfer matrix, selected by the cut `SpinTraceCut` (see section 7.3.2). The distribution of  $\theta_{\text{fpp}}$  is dominated by small-angle scattering events. Scattering via the nuclear interaction dominates for larger scattering angles (approximately  $\theta_{\text{fpp}} > 10^\circ$ ). Four spikes dominate the  $\phi_{\text{fpp}}$ -distribution (at  $\phi_{\text{fpp}} = \pm 135^\circ$  and  $\pm 45^\circ$ ), which correspond to the directions of the wires of the HDCs. These spikes are instrumental features of the polarimeter and have nothing to do with the polarization of the recoil protons. The majority of these events is eliminated by requiring a good track reconstruction in the VDCs (cut 1,2 and 4) and in the HDCs (cut 1 and 3). For the definition of the cuts, see table 7.1. `VDCOK` and `HDCOK` are calculated based on the drift time and the number of wires hit by the particle, and they indicate the quality of the track reconstruction. The full explanation of these variables is given in reference [82].

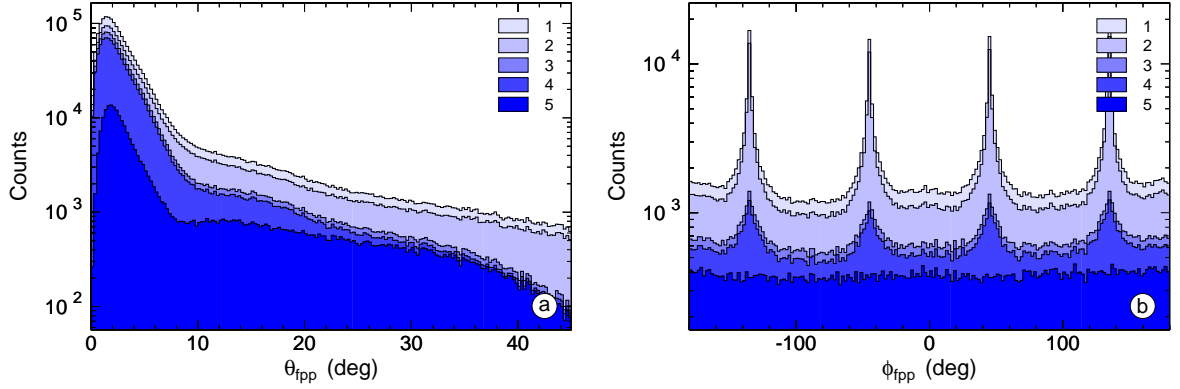


**Figure 7.1:** The polar ( $\theta_{fpp}$ ) and azimuthal ( $\phi_{fpp}$ ) angle are shown in histogram a and b, respectively. The definition of the cuts is given in table 7.1. To generate the histogram indicated by e.g. number 3, the cuts 1, 2 and 3 have all been applied. Histogram b shows the  $\phi_{fpp}$ -distribution for the large-angle scattering events only (selected by cut 6).

Cut	Definition
1	$(VDCOKA > 0) \&\& (HDCOK > 0) \&\& SpinTraceCut$
2	$(VDCOKA == 3)$
3	$(HDCOK > 0) \&\& (HDCOK < 7)$
4	$(\Delta\theta_{fp}^A < 0.4 \text{ mrad}) \&\& (\Delta\phi_{fp}^A < 2 \text{ mrad})$
5	$-185 \text{ mm} < z_s < -55 \text{ mm}$
6	$\theta_{fpp} > 12.66^\circ - 0.0238^\circ / \text{MeV } T_{CC}$

**Table 7.1:** The cuts to select the events in the focal plane polarimeter. Cuts 1 to 6 are similar to those in the analysis discussed in reference [82].

### 7.1.3 Carbon analyzer

The histograms 7.2.a and 7.2.b show the distribution of the scattering point ( $x_s, z_s$ ) in the focal plane. One can recognize the scintillators, the carbon analyzer and the two HDC planes (see also figure 7.11). By demanding good track reconstruction in the VDCs and HDCs the events scattered on the HDCs are suppressed. Scattering points in the empty space of the focal plane (e.g. between the scintillators and the carbon analyzer) are due to badly reconstructed tracks and they are also suppressed by the applied cuts. The scattering vertices inside the analyzer are selected by cut 5 in table 7.1:

$$\text{CarbonCut} : -185 \text{ mm} < z_s < -55 \text{ mm} . \quad (7.1)$$

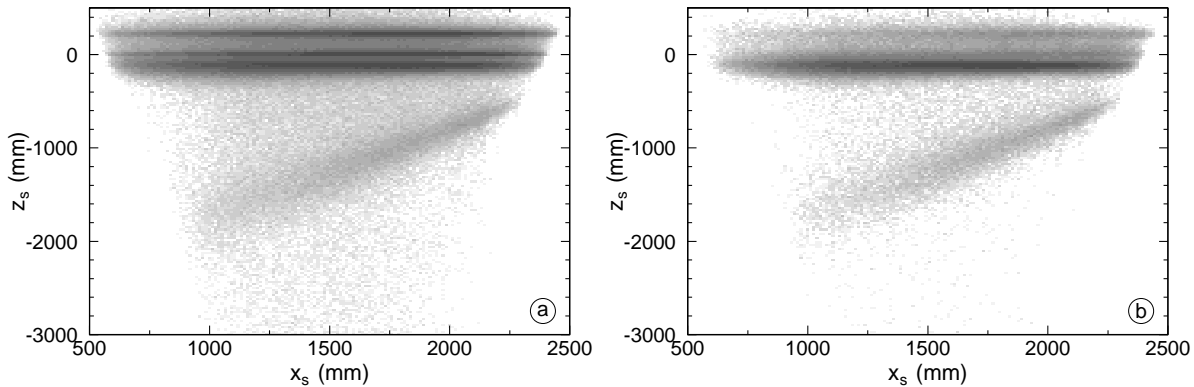


**Figure 7.2:** The position of the scattering point in the focal plane for all large-angle scattering events (cut 6) using a logarithmic grey-scale. For panel a no additional cut is applied, for histogram b cuts 1 to 4 of table 7.1 have been applied.

After applying this cut the distribution of  $\phi_{fpp}$  in figure 7.1.b is flat, which is expected since all single-spin asymmetries for VCS vanish. The effect of remaining single-spin asymmetries from false asymmetries and residual background sources have no influence on the double-polarized analysis [104].

#### 7.1.4 Large-angle scattering events

Now the large-angle scattering events have to be selected. As explained in section 4.6 only scattering via the nuclear interaction reveals information about the proton polarization. In distribution 5 in figure 7.1.a the dominance of the electromagnetic scattering can be observed in the region  $0^\circ < \theta_{fpp} < 9^\circ$  and around  $\theta_{fpp} = 9^\circ = \theta_{fpp}^c$  there is a local minimum. For angles larger than  $\theta_{fpp}^c$  the nuclear interaction dominates the scattering process. The angle  $\theta_{fpp}^c$  depends on the energy of the protons and therefore it is determined by searching the local minimum in the  $\theta_{fpp}$  distributions for bins in  $T_{CC}$ , the kinetic energy of the protons at the center of the carbon analyzer (see figure 7.3.a). Figure 7.3.b shows that the relation between  $T_{CC}$  and  $\theta_{fpp}^c$  is a straight line (cut 6 in table 7.1):

$$\text{ThetaCut} : \theta_{fpp} > (12.66^\circ - 0.0238^\circ/\text{MeV } T_{CC}) . \quad (7.2)$$

#### 7.1.5 Resolution of the HDCs

Although by applying the cuts of table 7.1 a clean  $\phi_{fpp}$ -distribution is obtained, there are some differences with a similar analysis of a  $\pi^0$ -production experiment [82], which was performed

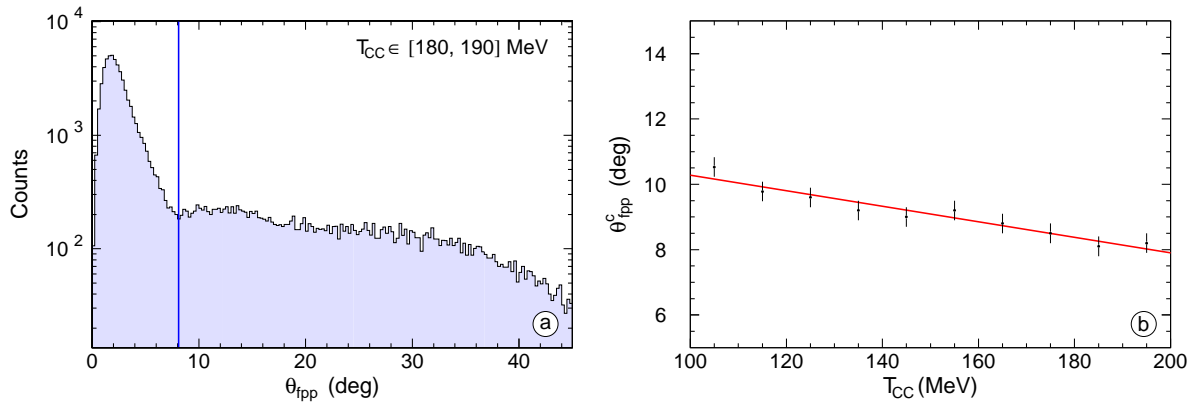


**Figure 7.3:** The local minimum in the  $\theta_{\text{fpp}}$  distribution is located for each bin in  $T_{\text{CC}}$  (a) and a linear fit yields the cut in the  $\theta_{\text{fpp}}$  versus  $T_{\text{CC}}$  distribution (b).

with the same detectors. In that analysis the effects of badly reconstructed tracks in the VDCs were more pronounced than in our data: in the distribution of  $\phi_{\text{fpp}}$  additional enhancements of count rates were present at  $\phi_{\text{fpp}} = 60^\circ, 120^\circ$  and  $\pm 90^\circ$ , which were removed by cut 4. The VDCs were also visible in the distribution of  $(x_s, z_s)$ . Apparently the reconstruction of the tracks by the VDCs is improved in the present data.

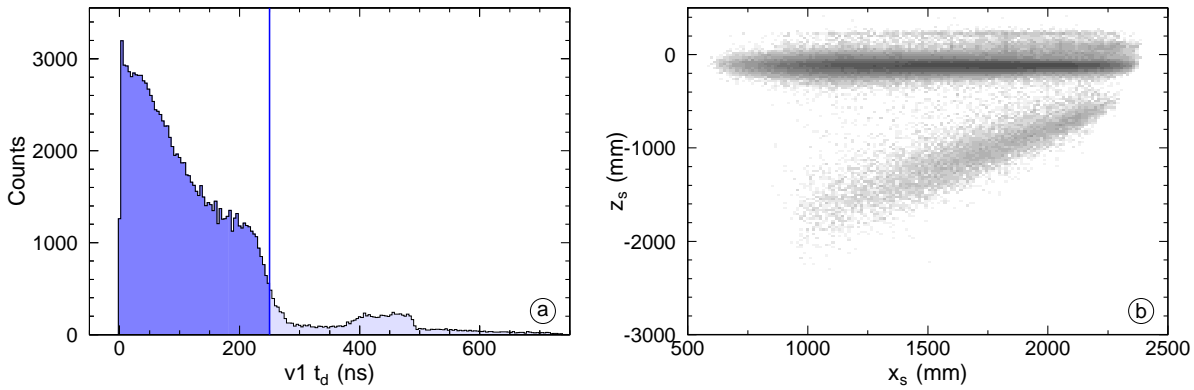
Unfortunately, not everything has improved as compared to the  $\pi^0$ -data. In the present data the scattering points inside the HDCs are not completely removed by the cuts 1 to 4. The suppression of these scattering points was much better in reference [82]. In addition, the local minimum in the  $\theta_{\text{fpp}}$ -distribution was located at  $7^\circ$  and now it is shifted to higher scattering angles ( $\approx 9.5^\circ$ ). This might indicate that the reconstruction of the tracks by the HDCs is less good.

The distribution of the drift times in the HDCs,  $t_d$ , for the V1 HDC is shown in figure 7.4.a. A drift time longer than 250 ns might indicate an error in the reconstruction of the HDC. The suppression of the scattering points outside the carbon analyzer in the  $(x_s, z_s)$ -plane can be improved by applying the cut:

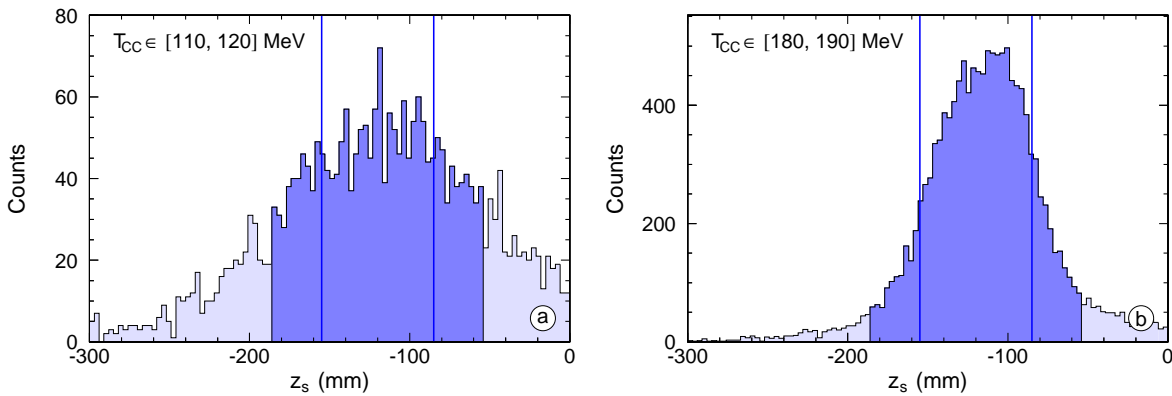
$$\text{TdCut} : t_d < 250 \text{ ns} . \quad (7.3)$$

Figure 7.4.b shows the resulting  $(x_s, z_s)$ -distribution. A cleaner distribution of the scattering points in the focal plane is obtained. Interactions with the scintillator of the spectrometer are not removed, because they correspond to real scattering events and not to reconstruction errors.

The resolution on the reconstruction of the scattering point in the focal plane can be studied via the distribution of  $z_s$  as a function of different variables. The main influence on the resolution comes from  $T_{\text{CC}}$  (see figure 7.5): the resolution in  $z_s$  becomes bad for low-energetic



**Figure 7.4:** The cut on the drift time in the HDCs (a) improves the suppression of scattering points outside the carbon analyzer (b). The line in the drift time spectrum indicates the position of the cut. Figure (b) has to be compared to figure 7.2.b.



**Figure 7.5:** Histogram of  $z_s$  for  $110 \text{ MeV} < T_{CC} < 120 \text{ MeV}$  (a) and for  $180 \text{ MeV} < T_{CC} < 190 \text{ MeV}$  (b). The lines indicate the position of the analyzer.

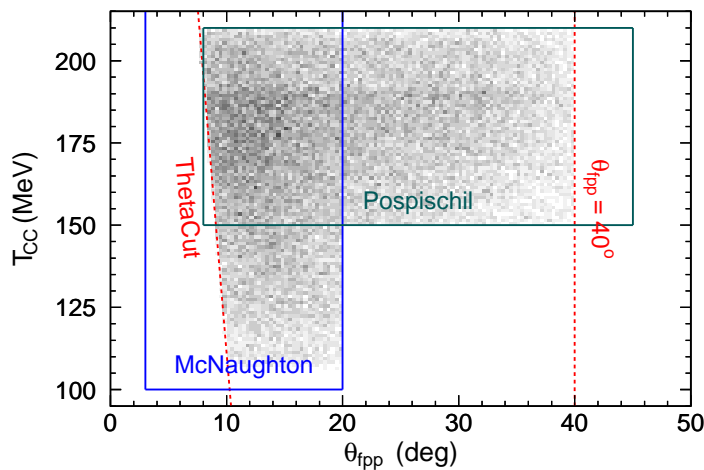


**Figure 7.6:** Validity domain of the parameterizations for  $A_C(\theta_{fpp}, T_{CC})$  of McNaughton *et al.* [95] and Pospischil *et al.* [92].

protons (approximately  $T_{CC} < 140$  MeV). This means that the track of low-energetic protons is not well reconstructed by the HDCs and the question arises if the scattering angles ( $\theta_{fpp}, \phi_{fpp}$ ) are calculated with sufficient precision to be used in the analysis. Therefore, the extraction of the structure functions is done with and without the cut

$$T_{ccCut} : T_{CC} > 140 \text{ MeV} . \quad (7.4)$$

### 7.1.6 Analyzing power

The analyzing power of the carbon slab has been measured by McNaughton *et al.* [95] and Pospischil *et al.* [92]. In both references a parameterization for  $A_C(\theta_{fpp}, T_{CC})$  can be found, which is only valid in a limited domain. The events for which the analyzing power is known, are shown in figure 7.6. The parameterization given in [92] is valid up to  $\theta_{fpp} = 45^\circ$ . However,  $A_C(\theta_{fpp}, T_{CC})$  is practically 0 above  $40^\circ$ .

$$\begin{aligned} \text{AnPowCut} : & (T_{CC} > 100 \text{ MeV}) \ \&\& \ (\theta_{fpp} > 3^\circ) \\ & \&\& \left( \left[ (\theta_{fpp} < 40^\circ) \ \&\& \ (T_{CC} > 150 \text{ MeV}) \right. \right. \\ & & \left. \left. \&\& \ (T_{CC} < 210 \text{ MeV}) \right] \ || \ (\theta_{fpp} < 20^\circ) \right) . \end{aligned} \quad (7.5)$$

## 7.2 Beam polarization

The polarization  $\mathcal{P}_b$  of the electron beam is measured once a day using the Møller polarimeter. The result of these measurements is shown in figure 7.7. The different beam times are indicated in the figure. An overview of the beam times is given in appendix C.1. The average polarization was about 80%, except for the measurement at the end of 2005.

## 7.3 Measurement of the double-spin asymmetry

The next subsections describe the calculation of  $\vec{\mathcal{P}}^{\text{BH+B}}$ , the contribution of the BH+B process to the polarization vector, the rotations of the spin, the likelihood method to fit  $\vec{\mathcal{P}}$  to the data of the polarimeter and the use of constraints to improve the reconstruction on  $\vec{\mathcal{P}}$ .

### 7.3.1 Calculation of the Bethe-Heitler + Born polarizations

In chapter 2 it was mentioned that the polarizations of the BH+B process can be calculated exactly based on the form factors of the proton. In principle one is free to choose any reference

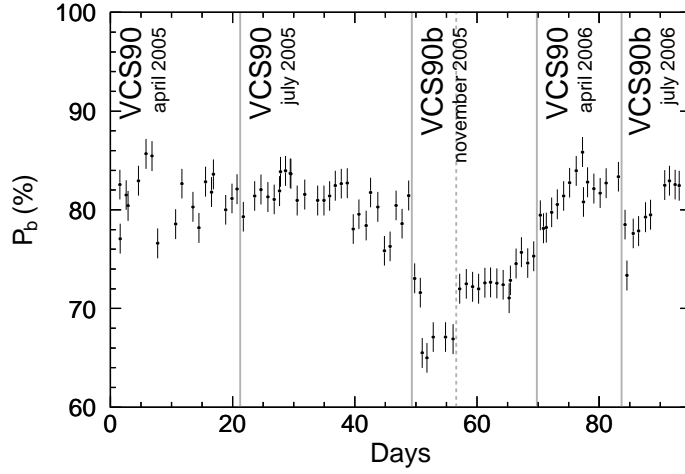


**Figure 7.7:** Polarization of the beam  $\mathcal{P}_b$  for the different beam times.

frame in the center-of-mass system to express the components of the polarization vector. Since the reference frame in the scattering plane  $\mathcal{R}_{\text{cm}}^s$  (see figure 7.8) is always defined in the case of a scattering process, this convention is used for presenting the results of the experiment in this work. The unit vectors of the center-of-mass reference frame  $\mathcal{R}_{\text{cm}}^s$  are defined by:

$$\begin{aligned}\hat{z}_{\text{cm}}^s &= \frac{\vec{q}_{\text{cm}}}{q_{\text{cm}}}, \\ \hat{y}_{\text{cm}}^s &= \frac{\vec{k}_{\text{cm}} \times \vec{k}'_{\text{cm}}}{k_{\text{cm}} k'_{\text{cm}} \sin \theta_{e \text{ cm}}}, \\ \hat{x}_{\text{cm}}^s &= \hat{y}_{\text{cm}}^s \times \hat{z}_{\text{cm}}^s,\end{aligned}\tag{7.6}$$

Another reason for this choice is the fact that the code of Vanderhaeghen [37] is used in the analysis. As it is shown in appendix B.6, this code calculates the polarizations in  $\mathcal{R}_{\text{cm}}^s$ <sup>1</sup>.

A similar remark as for the case of the unpolarized analysis should be made: in the present analysis both the form factors parameterizations of Mergell *et al.* [5] and Friedrich *et al.* [8] are used. Figure 7.9 represents  $\mathcal{P}_x^{\text{BH+B}}$  and  $\mathcal{P}_z^{\text{BH+B}}$  as a function of  $\theta_{\gamma\gamma_{\text{cm}}}$  for different choices of the form factors<sup>2</sup>. All figures and tables in this chapter are valid for the Friedrich form factors unless explicitly mentioned otherwise.

<sup>1</sup>However, internally in the calculations, the convention of Guichon (see figure 2.9) is used to be consistent with the formulas in reference [31] and chapter 2.

<sup>2</sup> $\mathcal{P}_y^{\text{BH+B}}$  is not shown in the figure, because it is 0 for in-plane kinematics.

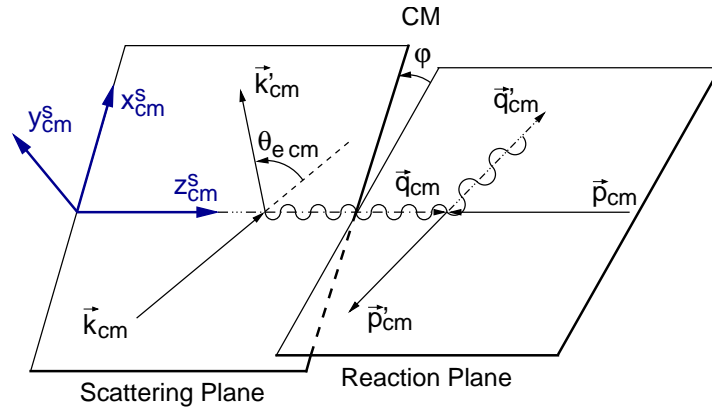


**Figure 7.8:** The polarization components in this analysis are expressed in  $\mathcal{R}_{\text{cm}}^s$ , the center-of-mass reference frame attached to the scattering plane.

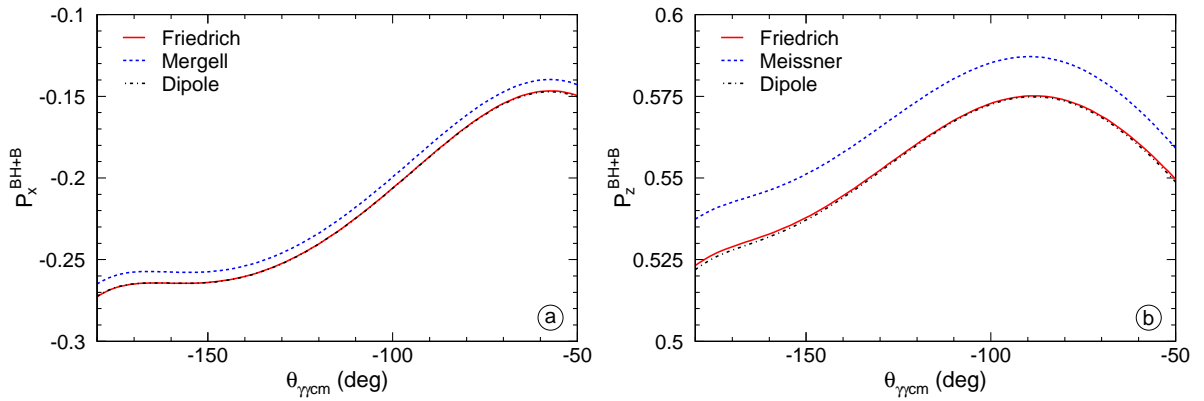


**Figure 7.9:** Effect of the form factors on  $\mathcal{P}_x$  and  $\mathcal{P}_z$  for in-plane kinematics with  $q'_{\text{cm}} = 90 \text{ MeV}/c$ ,  $q_{\text{cm}} = 600 \text{ MeV}/c$  and  $\varepsilon = 0.645$ .

### 7.3.2 Rotations of the spin

The polarization of the recoil proton in the  $\mathcal{R}_{\text{cm}}^s$ -frame can not be measured directly. It is measured using the polarimeter in the proton frame  $\mathcal{R}_p$ , after passing through the magnetic field of the spectrometer. To connect the measured polarization in the polarimeter with the center-of-mass polarization one has to take into account several rotations. There are two main contributions to the rotation of the spin (apart from rotations between reference frames): the Wigner-Thomas spin precession due to the Lorentz boost from the center-of-mass to the laboratory frame and the precession of the spin in the spectrometer magnet. The subsections below give a ‘chronological’ overview of the rotations to transform  $\vec{S}_{\text{cm}}^s$  (the spin in  $\mathcal{R}_{\text{cm}}^s$ ) to the spin measured at the polarimeter  $\vec{S}_p$ .

### Rotation to $\mathcal{R}_{\text{cm}}^r$

The components of the BH+B polarization are calculated in  $\mathcal{R}_{\text{cm}}^s$ , but the formulas to add the effect of the GPs are valid in  $\mathcal{R}_{\text{cm}}^r$  (see appendix B.6). Therefore the spin has to be rotated to  $\mathcal{R}_{\text{cm}}^r$ . This is done by a rotation over  $-\varphi$  around the  $z$ -axis:

$$\vec{\mathcal{S}}_{\text{cm}}^r = \mathbf{R}_z(-\varphi) \vec{\mathcal{S}}_{\text{cm}}^s . \quad (7.7)$$

where  $\mathbf{R}_i(\theta)$  represents a rotation of the reference frame about the  $i$ -axis over the angle  $\theta$ .

### Wigner-Thomas spin precession

To obtain the spin of the proton in the laboratory system one needs to define the reference frame  $\mathcal{R}^r$  which is in rest with respect to the hall. The unit vectors of  $\mathcal{R}^r$  have the same orientation as the unit vectors of  $\mathcal{R}_{\text{cm}}^r$ . The only difference between both frames is their velocity with respect to each other. The Lorentz boost from  $\mathcal{R}_{\text{cm}}^r$  to  $\mathcal{R}^r$  rotates the direction of the momentum three-vector of the proton over an angle  $\theta_p^r$ , given by

$$\theta_p^r = \theta_{\gamma p \text{cm}} - \theta_{\gamma p} , \quad (7.8)$$

where  $\theta_{\gamma p \text{cm}}$  and  $\theta_{\gamma p}$  are the angles between the virtual photon and the recoiling proton in the center-of-mass system and the laboratory system respectively. Due to the Lorentz boost the spin vector of the proton,  $\vec{\mathcal{S}}$ , will be rotated, too. This rotation is called the Wigner-Thomas precession and the angle of the precession is given by the Wigner angle  $\theta_W$  [105]:

$$\sin \theta_W = \frac{1 + \gamma}{\gamma_{p \text{cm}} + \gamma_p} \sin \theta_p^r . \quad (7.9)$$

In equation (7.9) the Lorentz factors  $\gamma$ ,  $\gamma_p$  and  $\gamma_{p \text{cm}}$  are related to the velocities of the center-of-mass frame against the laboratory frame, and of the proton in the center-of-mass and laboratory frames, respectively.  $\theta_W$  describes the precession of the spin with respect to the rotated direction of motion due to the Lorentz boost.

The difference between the rotation of the proton momentum and the Wigner angle

$$\omega = \theta_p^r - \theta_W \quad (7.10)$$

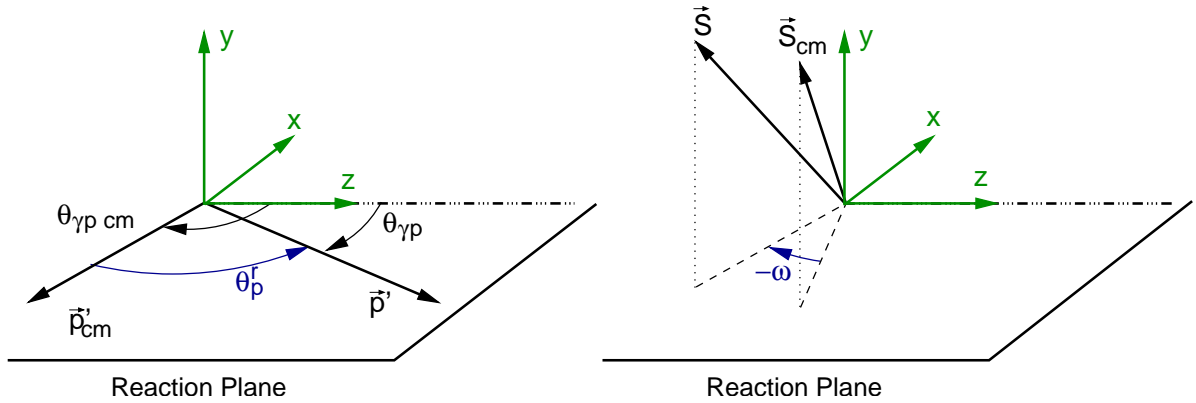


**Figure 7.10:** Left: The Lorentz boost in the direction of the  $z$ -axis rotates the momentum of the proton by an angle  $\theta_p^r$ . Right: The spin of the proton is rotated around the same axis by an angle  $-\omega$ . Only one reference frame (without labels) is shown since the axes of  $\mathcal{R}^r$  and  $\mathcal{R}_{cm}^r$  have the same orientation.

is rather small for the kinematics of this experiment (up to a few degrees) and can be calculated directly using [106]<sup>3</sup>:

$$\tan \frac{\omega}{2} = \frac{\gamma \beta \gamma_{p\text{cm}} \beta_{p\text{cm}} \sin \theta_{\gamma p\text{cm}}}{(1 + \gamma)(1 + \gamma_{p\text{cm}}) + \gamma \beta \gamma_{p\text{cm}} \beta_{p\text{cm}} \cos \theta_{\gamma p\text{cm}}}, \quad (7.11)$$

where  $\beta = \frac{|\mathbf{b}|}{b^0}$  for a particle with four-momentum  $\mathbf{b}$ . The advantage of equation (7.11) is that there is no ambiguity in the inversion of  $\tan \frac{\omega}{2}$ . The inversion of  $\sin \theta_W$  in equation (7.9) causes problems if  $\theta_p^r$  is close to  $90^\circ$ .

The method to apply the Wigner-Thomas precession to the spin of the recoiling proton is [108]:

- Rotate to a reference frame attached to the proton momentum via a rotation over  $180^\circ$  around the  $z$ -axis and a rotation over  $\theta_{\gamma p\text{cm}}$  around the new  $y$ -axis.
- Perform the Wigner-Thomas precession by rotating the spin over  $-\theta_W$  around the  $y$ -axis. This yields the spin in the reference frame attached to the proton momentum, which is rotated over  $\theta_p^r$  due to the Lorentz boost.
- Rotate over  $-\theta_{\gamma p}$  around the  $y$ -axis and over  $180^\circ$  around the  $z$ -axis to  $\mathcal{R}^r$ .

In the procedure described above there are three successive rotations around the  $y$ -axis, so they are combined in one rotation over  $\theta_{\gamma p\text{cm}} - \theta_W - \theta_{\gamma p} = +\omega$ . Taking into account the two rotations over  $180^\circ$  one can conclude that the Lorentz boost from the center-of-mass to the laboratory rotates the proton spin over  $-\omega$  around the  $y$  axis. This is shown in figure 7.10.

<sup>3</sup>See the erratum [107] for the correct application of the formulas in the paper.

The transformation  $\vec{\mathcal{S}}_{\text{cm}}^{\text{r}}$  and  $\vec{\mathcal{S}}^{\text{r}}$  is given by

$$\begin{pmatrix} \mathcal{S}_x^{\text{r}} \\ \mathcal{S}_y^{\text{r}} \\ \mathcal{S}_z^{\text{r}} \end{pmatrix} = \Lambda(-\omega) \begin{pmatrix} \mathcal{S}_{x,\text{cm}}^{\text{r}} \\ \mathcal{S}_{y,\text{cm}}^{\text{r}} \\ \mathcal{S}_{z,\text{cm}}^{\text{r}} \end{pmatrix} = \begin{pmatrix} \cos \omega & 0 & -\sin \omega \\ 0 & 1 & 0 \\ \sin \omega & 0 & \cos \omega \end{pmatrix} \begin{pmatrix} \mathcal{S}_{x,\text{cm}}^{\text{r}} \\ \mathcal{S}_{y,\text{cm}}^{\text{r}} \\ \mathcal{S}_{z,\text{cm}}^{\text{r}} \end{pmatrix}. \quad (7.12)$$

Formula (7.12) has been tested using the method described in [30] for which an axial four-vector  $\mathfrak{s}_{\text{cm}}^{\text{r}}$  is constructed based on the spin three-vector  $\vec{\mathcal{S}}_{\text{cm}}^{\text{r}}$ :

$$\begin{aligned} \mathfrak{s}_{\text{cm}}^{0\text{r}} &= \gamma \vec{\beta} \cdot \vec{\mathcal{S}}_{\text{cm}}^{\text{r}}, \\ \vec{\mathfrak{s}}_{\text{cm}}^{\text{r}} &= \vec{\mathcal{S}}_{\text{cm}}^{\text{r}} + \frac{\gamma^2}{\gamma + 1} (\vec{\beta} \cdot \vec{\mathcal{S}}_{\text{cm}}^{\text{r}}) \vec{\beta}. \end{aligned} \quad (7.13)$$

The transformation of the spin four-vector from the center-of-mass to the laboratory ( $\mathcal{R}_{\text{cm}}^{\text{r}} \rightarrow \mathcal{R}^{\text{r}}$ ) is described by the same Lorentz boost as for the proton momentum. After the transformation, the spin three-vector in the lab can be extracted from the boosted spin four-vector using:

$$\vec{\mathcal{S}}^{\text{r}} = \vec{\mathfrak{s}}^{\text{r}} - \frac{\gamma}{\gamma + 1} (\vec{\beta} \cdot \vec{\mathfrak{s}}^{\text{r}}) \vec{\beta}. \quad (7.14)$$

### Rotation to the spectrometer frame

The calculation of the spin precession in the magnet of spectrometer A starts from the spin in the spectrometer frame  $\vec{\mathcal{S}}_{\text{tg}}^{\text{A}}$ . The latter can be obtained by applying several rotations on  $\vec{\mathcal{S}}^{\text{r}}$ . This is explained in appendix B.7. As a result one finds:

$$\vec{\mathcal{S}}_{\text{tg}}^{\text{A}} = \mathbf{R}_x(-\theta_{\text{A}}) \mathbf{R}_z\left(\frac{\pi}{2}\right) \mathbf{R}_z(-\varphi_{\gamma}) \mathbf{R}_y(-\theta_{\gamma}) \mathbf{R}_z(\pi + \varphi) \vec{\mathcal{S}}^{\text{r}}. \quad (7.15)$$

$\theta_{\text{A}}$  is the horizontal angle of the spectrometer with respect to the beam line,  $\theta_{\gamma}$  and  $\varphi_{\gamma}$  are the polar and azimuthal angle of the virtual photon in the hall laboratory frame.

### Spin precession in the magnet of the spectrometer

The spin of the proton will precess in the magnets of spectrometer A depending on the magnetic field along the proton track. This causes the spin precession to vary from track to track, since the length of the track in the spectrometer is different and the magnetic field is not uniform. In this paragraph a brief overview is given about the spin precession in a magnetic field and how the precession is calculated for the magnetic field of spectrometer A. A more complete description of the spin precession in spectrometer A can be found in [82].

The equation of motion for the spin of a particle with velocity  $\vec{v}$ , charge  $e$ , mass  $m$  and Landé factor  $g$  in an electromagnetic field ( $\vec{E}$  and  $\vec{B}$ ) is given by the Thomas equation [109]:

$$\frac{d\vec{S}}{dt} = \frac{e}{m} \vec{S} \times \left\{ \left( \frac{g-2}{2} + \frac{1}{\gamma} \right) \vec{B} - \left( \frac{g-2}{2} \right) \frac{\gamma(\vec{v} \cdot \vec{B})\vec{v}}{c^2(\gamma+1)} - \left( \frac{g}{2} - \frac{\gamma}{\gamma+1} \right) \frac{\vec{v} \times \vec{E}}{c} \right\}. \quad (7.16)$$

For a magnetic spectrometer equation (7.16) can be simplified to

$$\frac{d\vec{S}}{dt} = \frac{e}{m\gamma} \vec{S} \times \left\{ \frac{g}{2} \vec{B}^{\parallel} + \left( 1 + \frac{g-2}{2} \gamma \right) \vec{B}^{\perp} \right\}, \quad (7.17)$$

where  $\vec{B}$  is decomposed in a component parallel ( $\vec{B}^{\parallel}$ ) and a component perpendicular ( $\vec{B}^{\perp}$ ) to the momentum of the particle.

Figure 7.11 illustrates the effect of the magnetic field on the spin of the proton for different tracks. All protons have initially the same momentum and spin. Only the direction of the momentum and  $y_0$  are different, causing important differences in the spin at the polarimeter. The polarimeter can only measure the polarization perpendicular to the direction of the particles, but due to the variation of the spin precession over the different trajectories in the magnetic field of the spectrometer, one can access the three components of the polarization at the target.

The spin transfer matrix  $\mathbf{M}$ , which has been developed by Th. Pospischil *et al.* ([82] and [92]), gives the relation between the spin of the proton in the proton reference frame  $\mathcal{R}_p$  (as shown in figure B.1) and the spin in the spectrometer frame  $\mathcal{R}_{\text{tg}}^A$ :

$$\vec{S}_p = \mathbf{M} \vec{S}_{\text{tg}}^A. \quad (7.18)$$

The matrix elements  $M_{\kappa\lambda}$  of  $\mathbf{M}$  are function of the target coordinates:

$$M_{\kappa\lambda} = \sum_{ijklm} C_{\kappa\lambda}^{ijklm} \delta^i \theta_0^j y_0^k \phi_0^l p_{\text{ref}}^m, \quad (7.19)$$

with  $\kappa, \lambda \in \{x, y, z\}$ . For different tracks the spin precession is calculated and a polynomial fit to these tracks yields the coefficients  $C_{\kappa\lambda}^{ijklm}$ . This fit is only valid in a part of the spectrometer acceptance:

$$\begin{aligned} \text{SpinTraceCut} : & (\delta^A < 16.2521) \ \&\& \ (\delta^A > -5.7794) \ \&\& \ (|\theta_0^A| < 75 \text{ mrad}) \\ & \ \&\& \ (|\phi_0^A| < 105 \text{ mrad}) \ \&\& \ (|y_0^A| < 30 \text{ mm}). \end{aligned} \quad (7.20)$$

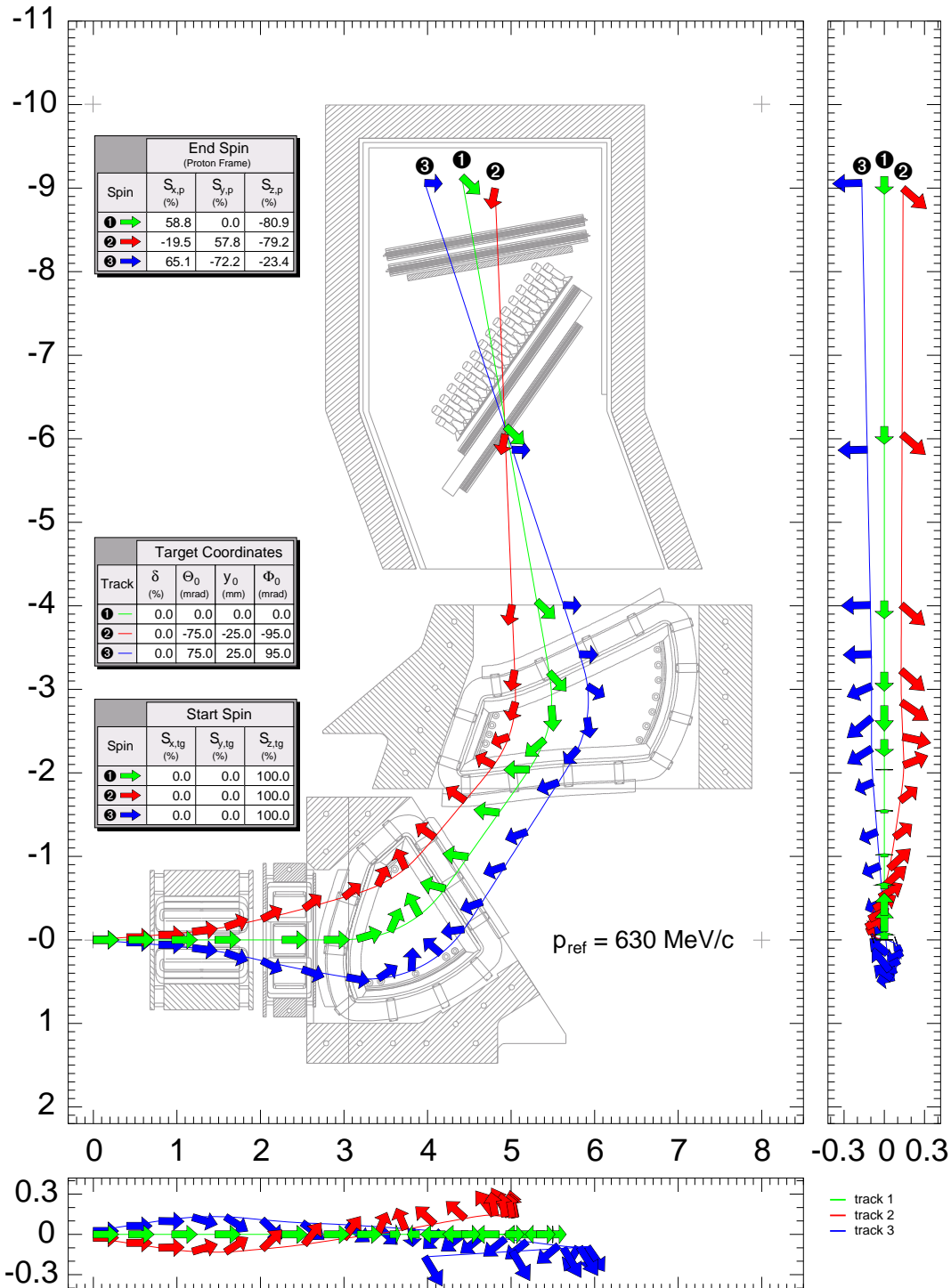


Figure 7.11: Precession of the spin in the magnets of spectrometer A for different tracks. All protons have initially the same momentum and spin. Only the direction and  $y_0$  of the 3 tracks are different. (Taken from [82].)

## Conclusion

Finally one has the complete transformation for the spin, starting from the reaction vertex in the center-of-mass to the proton frame at the polarimeter. It is given by:

$$\vec{\mathcal{S}}_p = \mathbf{M} \mathbf{T} \Lambda(-\omega) \mathbf{R}_z(-\varphi) \vec{\mathcal{S}}_{\text{cm}}^s, \quad (7.21)$$

where  $\mathbf{T}$  is a shorthand notation for  $\mathbf{R}_x(-\theta_A) \mathbf{R}_z(\frac{\pi}{2}) \mathbf{R}_z(-\varphi_\gamma) \mathbf{R}_y(-\theta_\gamma) \mathbf{R}_z(\pi + \varphi)$ .

### 7.3.3 Maximum-likelihood fit of the polarization

The polarimeter allows to measure the two components of the recoiling proton polarization perpendicular to the proton momentum. The goal is to fit  $\vec{\mathcal{P}}_{\text{cm}}^s$  to the observed  $(\theta_{\text{fpp}}, \phi_{\text{fpp}})$ -distribution. The polarization of the proton in the proton frame  $\vec{\mathcal{P}}_p$  is calculated starting from  $\vec{\mathcal{P}}_{\text{cm}}^s$  using equation (7.21):

$$\vec{\mathcal{P}}_p = \mathbf{M} \mathbf{T} \Lambda(-\omega) \mathbf{R}_z(-\varphi) \vec{\mathcal{P}}_{\text{cm}}^s, \quad (7.22)$$

Then the azimuthal angle  $\phi_{\mathcal{P}}$  of  $\vec{\mathcal{P}}_p$  is calculated:

$$\phi_{\mathcal{P}} = \text{atan} \left( \frac{\mathcal{P}_{p,y}}{\mathcal{P}_{p,x}} \right). \quad (7.23)$$

The angle  $\phi_{\mathcal{P}}$  is compared to the distribution of the azimuthal angle of the scattering of the proton on the analyzer by calculating the likelihood based on equation (4.5). The likelihood for the event is given by

$$1 - A_C(\theta_{\text{fpp}}, T_{\text{CC}}) \mathcal{P}_b \sqrt{\mathcal{P}_{p,x}^2 + \mathcal{P}_{p,y}^2} \sin(\phi_{\text{fpp}} - \phi_{\mathcal{P}}) \quad (7.24)$$

and expresses the probability that the scattering angles of a proton with a given  $\phi_{\mathcal{P}}$  are  $(\theta_{\text{fpp}}, \phi_{\text{fpp}})$ .

The likelihood  $\mathbb{L}$  for the complete data set is then given by

$$\mathbb{L} = \prod_{\text{all events}} \left( 1 - A_C(\theta_{\text{fpp}}, T_{\text{CC}}) \mathcal{P}_b \sqrt{\mathcal{P}_{p,x}^2 + \mathcal{P}_{p,y}^2} \sin(\phi_{\text{fpp}} - \phi_{\mathcal{P}}) \right), \quad (7.25)$$

which should be maximized by varying the components of  $\vec{\mathcal{P}}_{\text{cm}}^s$ . For practical reasons the logarithm of the likelihood is calculated and multiplied by  $-1$ :

$$-\ln \mathbb{L} = \sum_{\text{all events}} -\ln \left( 1 - A_C(\theta_{\text{fpp}}, T_{\text{CC}}) \mathcal{P}_b \sqrt{\mathcal{P}_{p,x}^2 + \mathcal{P}_{p,y}^2} \sin(\phi_{\text{fpp}} - \phi_{\mathcal{P}}) \right), \quad (7.26)$$

which now has to be minimized. This minimization is done by the simplex routine [110] independently in each bin in  $\theta_{\gamma\gamma\text{cm}}$ .

### 7.3.4 Representation of the polarization results

The result (without constraints) for  $\vec{\mathcal{P}}$  is shown in figure 7.12<sup>4</sup>. In the figures the results are compared to theoretical predictions<sup>5</sup>:

1. Measuring  $\vec{\mathcal{P}}$  in an experiment can only be done in a statistical manner. However, based on the kinematical variables one can calculate the theoretical BH+B and BH+B+GP prediction for the polarizations using third order HB $\chi$ PT predictions [42] and the LET truncations in equations (2.55)-(2.57), for each event in the (experimental) data set. These calculations are represented by the scatter plots of  $\mathcal{P}_i$  ( $i = x, y, z$ ) versus  $\theta_{\gamma\gamma\text{cm}}$ . In the left upper corner of the plot is indicated if the two-dimensional histogram represents the BH+B or the BH+B+GP polarizations.
2. The weight of each event in the determination of the polarization is  $A_C(\theta_{\text{fpp}}, T_{\text{CC}}) \mathcal{P}_b$ . Therefore  $A_C(\theta_{\text{fpp}}, T_{\text{CC}}) \mathcal{P}_b$  is used to calculate the weighted mean of  $\mathcal{P}_i$  for small bins in  $\theta_{\gamma\gamma\text{cm}}$  in each plot. The result is labeled by  $\langle \text{BH} + \text{B} \rangle$  or  $\langle \text{BH} + \text{B} + \text{GP} \rangle$  and shown as the black line.

Due to the extended acceptance of the spectrometers it is not possible to compare the obtained polarization directly to the theoretical predictions at the nominal kinematics of the experiment. The experimentally determined polarization is the average of the polarization over all events in the data set and therefore one should compare the results of the calculation to the black lines on the plots.

### 7.3.5 Constraints on the likelihood fit

Not all polarization components are properly reconstructed if no constraint is used. The effect of the GPs on  $\vec{\mathcal{P}}$  is expected to be small (less than 10% for the nominal kinematics) and it can not explain the systematic discrepancy between the observed and the predicted  $\mathcal{P}_z$ . Also the reconstruction of  $\mathcal{P}_y$  is not good. For  $\mathcal{P}_y$  one would expect to find a result within error bars compatible to 0. However,  $\mathcal{P}_y$  is systematically too low.

To solve this problem one can use the knowledge that  $\langle \mathcal{P}_y \rangle = 0$  by putting the constraint  $\mathcal{P}_y = 0$  (event per event) on the fit. The result is shown in figure 7.13. This constraint improves  $\mathcal{P}_z$ , however, the result is not satisfactory:  $\mathcal{P}_z$  is still systematically too low. Another important

<sup>4</sup> $\theta_{\gamma\gamma\text{cm}}$  displayed in the figures 7.12-7.14 and figure 7.20 is  $\varphi'$  from figure 6.8.

<sup>5</sup>In the remainder of this thesis  $\vec{\mathcal{P}}$  will be used as a short-hand notation for  $\vec{\mathcal{P}}_{\text{cm}}^{\text{s}}$ .

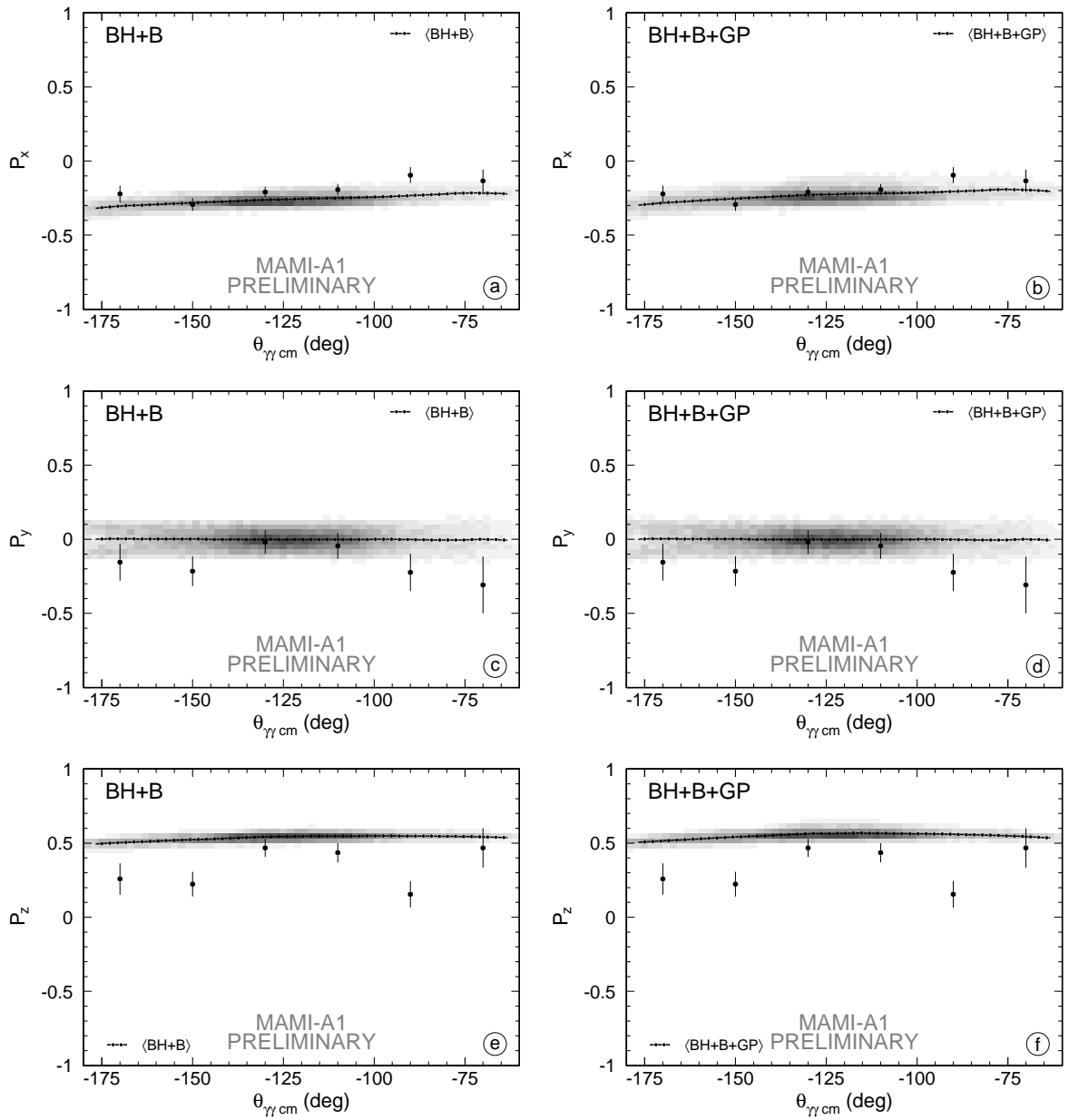


**Figure 7.12:** Calculation of the  $\mathcal{P}_x$ ,  $\mathcal{P}_y$ ,  $\mathcal{P}_z$  without constraints. The meaning of the line and the grey zone is explained in the text.

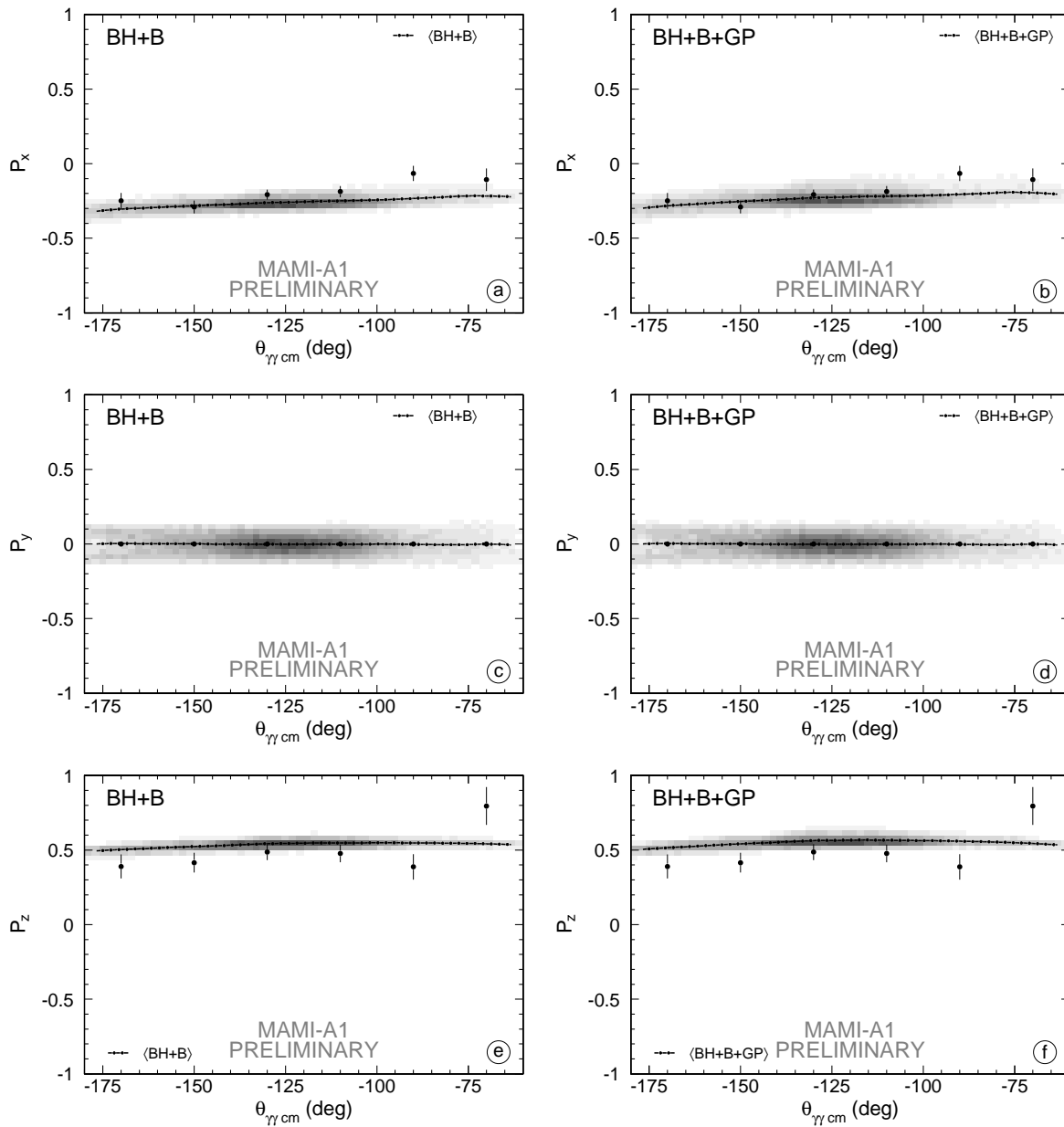


Figure 7.13: Same as figure 7.12 using the constraint  $\mathcal{P}_y = 0$ .

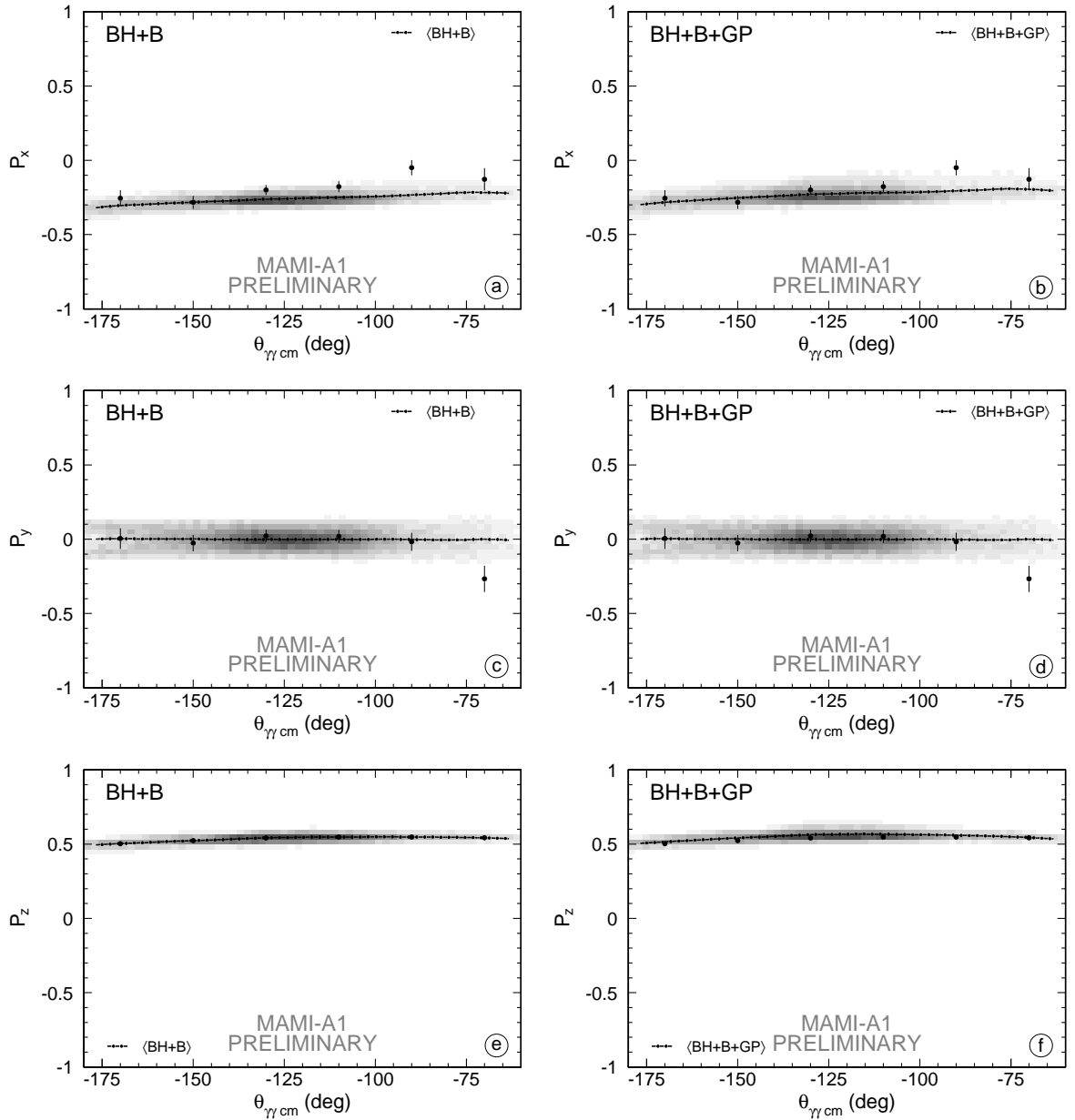


Figure 7.14: Same as figure 7.12 using the constraint  $\mathcal{P}_z = \mathcal{P}_z^{\text{BH+B}}$ .

observation is that  $\mathcal{P}_x$  is only weakly dependent on the constraint on  $\mathcal{P}_y$ . Another constraint on  $\mathcal{P}_y$  was tested too: for each event  $\mathcal{P}_y$  was set to the expected BH+B polarization along the  $y$ -axis. The result is comparable to the one obtained with constraint  $\mathcal{P}_y = 0$ .

Since the effect of the GPs on  $\mathcal{P}_y$  for in-plane kinematics is much smaller than their effect on  $\mathcal{P}_z$  it is tempting to put the constraint on  $\mathcal{P}_y$ . However, the reconstruction of  $\mathcal{P}_z$  is very difficult in the kinematical range of this experiment. Therefore it is better to use a constraint on  $\mathcal{P}_z$  instead of on  $\mathcal{P}_y$ . This was done by forcing  $\mathcal{P}_z = \mathcal{P}_z^{\text{BH+B}}$ . The result of this approach is presented in figure 7.14. The result yields small error bars on  $\mathcal{P}_y$  compared to figure 7.12 and, in addition, the reconstructed  $\mathcal{P}_y$  is in good agreement with theoretical predictions.

The improvement in the reconstruction of  $\mathcal{P}_y$  by using a constraint on  $\mathcal{P}_z$  is remarkable. To understand this one can treat the unit vectors of  $\mathcal{R}_{\text{cm}}^{\text{s}}$  as polarization vectors and apply the spin rotations on each of them, e.g.:

$$\hat{x}_{\text{sr}} = \mathbf{M} \mathbf{T} \mathbf{\Lambda}(-\omega) \mathbf{R}(-\varphi) \hat{x}_{\text{cm}}^{\text{s}} . \quad (7.27)$$

The sensitivity of the polarimeter  $S_i$  ( $i = x, y, z$ ) to each of the components is parameterized by the length of the projection of the unit vector after the spin rotations on the plane perpendicular to the proton momentum:

$$S_i = \sqrt{\hat{i}_{\text{sr},x}^2 + \hat{i}_{\text{sr},y}^2} . \quad (7.28)$$

The rotation of the spin is different for each proton, since all protons follow a different path in the magnet and the sensitivity is calculated for each event.

The interpretation of  $S_i$  is easy: if  $S_i \approx 1$  the  $i$ -component of  $\vec{\mathcal{P}}$  lies, after the spin rotations, in the plane perpendicular to the proton momentum and can therefore be measured accurately. When  $S_i < 1$  a (large) part of  $\mathcal{P}_i$  is parallel to the momentum of the proton in the focal plane and it is more difficult to measure  $\mathcal{P}_i$ . In figure 7.15 it is shown that  $S_x$  and  $S_y$  are close to 1 over the complete phase space of the experiment, but  $\langle S_z \rangle \approx 0.5$ , making it more difficult to measure  $\mathcal{P}_z$ . Also the correlations between the sensitivities are important:  $S_x$  and  $S_y$  are not correlated. The correlation between  $S_x$  and  $S_z$  is weak, but it is clear that  $S_y$  and  $S_z$  are strongly correlated, which explains why using a constraint on e.g.  $\mathcal{P}_z$  improves the reconstruction of  $\mathcal{P}_y$  without changing the  $x$ -component.

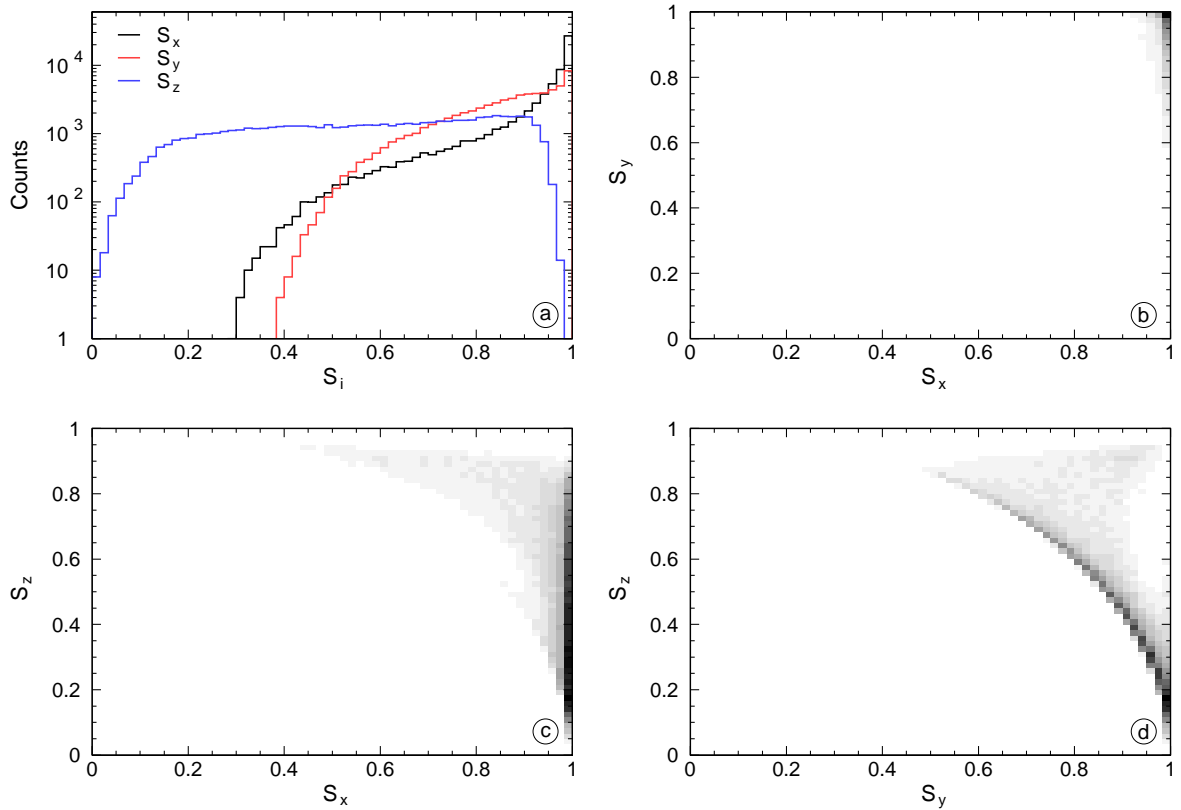


**Figure 7.15:** The sensitivity of the polarimeter to the components of the spin in the  $\mathcal{R}_{\text{cm}}^s$  over the kinematics of the experiment (a). In panels b, c and d the correlations between these sensitivities are shown.

## 7.4 Extraction of the structure functions

### 7.4.1 Effect of the GPs on the polarization

For the unpolarized analysis the effect of the GPs and structure functions on the cross section was known in advance, since it had been measured before. In this work the first double-polarized VCS experiment is reported and the effect of the GPs on these new observables is not known from previous measurements. Using the results of HB $\chi$ PT [42] one can get an estimate of the effect of each of the different GPs on  $\vec{\mathcal{P}}_{\text{cm}}^s$ . The results for in-plane ( $\varphi = 180^\circ$ ) and out-of-plane ( $\varphi = 210^\circ$ ) kinematics are shown in figures 7.16, 7.17 and 7.18.

The goal of the present experiment is to measure 5 of the 6 GPs with an in-plane measurement of  $\vec{\mathcal{P}}$ . Figures 7.16, 7.17 and 7.18 show that only five GPs should be taken into account in the analysis of the data.  $P^{(11,02)1}$  has only an influence on out-of-plane kinematics and even then its influence is negligible with respect to the other GPs.

The contributions of the structure functions  $P_{\text{LT}}^\perp$ ,  $P_{\text{TT}}^\perp$ ,  $P'_{\text{TT}}^\perp$  and  $P'_{\text{LT}}^\perp$  of reference [42] to  $\Delta\mathcal{M}_{0,x}^{\text{NB}}$  and  $\Delta\mathcal{M}_{0,y}^{\text{NB}}$  are shown in figure 7.19.a-d. One can conclude that:

- the contributions of  $P_{\text{TT}}^\perp$  and  $P'_{\text{TT}}^\perp$  tend to cancel each other at  $\theta_{\gamma\gamma\text{cm}} = 180^\circ$ , whereas at  $\theta_{\gamma\gamma\text{cm}} = 0^\circ$  they are equal.
- $P'_{\text{LT}}^\perp$  yields no contribution to the  $\Delta\mathcal{M}_{0,i}^{\text{NB}}$  for in-plane kinematics and for out-of-plane kinematics its influence is negligible.
- $P_{\text{LT}}^\perp$  has the largest contribution in the phase space of this experiment.

The effect of the GPs on  $\mathcal{P}_z$  is described via the structure functions  $P_{\text{TT}}^z$ ,  $P_{\text{LT}}^z$  and  $P'_{\text{LT}}^z$  as shown in figure 7.19.e and 7.19.f. The main contribution comes from  $P_{\text{TT}}^z$ , but none of the structure functions can be neglected.

For the kinematics of this experiment one can ignore the structure function  $P'_{\text{LT}}^\perp$ : its effect on  $\Delta\mathcal{M}_{0,i}^{\text{NB}}$  is less than 10% of the other structure functions and the relations (2.55) and (2.56) can thus be simplified to:

$$\Delta\mathcal{M}_{0,x}^{\text{NB}} \approx 4K_2 \left\{ v_1^x \sqrt{2\varepsilon(1-\varepsilon)} P_{\text{LT}}^\perp(q_{\text{cm}}) + v_2^x \sqrt{1-\varepsilon^2} P_{\text{TT}}^\perp(q_{\text{cm}}) + v_3^x \sqrt{1-\varepsilon^2} P'_{\text{TT}}^\perp(q_{\text{cm}}) \right\}, \quad (7.29)$$

$$\Delta\mathcal{M}_{0,y}^{\text{NB}} \approx 4K_2 \left\{ v_1^y \sqrt{2\varepsilon(1-\varepsilon)} P_{\text{LT}}^\perp(q_{\text{cm}}) + v_2^y \sqrt{1-\varepsilon^2} P_{\text{TT}}^\perp(q_{\text{cm}}) + v_3^y \sqrt{1-\varepsilon^2} P'_{\text{TT}}^\perp(q_{\text{cm}}) \right\}. \quad (7.30)$$

## 7.4.2 Extraction method and analysis

Since we can neglect the structure function  $P'_{\text{LT}}^\perp$  (and the GP  $P^{(11,02)1}$ ) only five free parameters are left. Based on the analysis of the unpolarized cross sections (see chapter 6) there are two constraints: 2 linear combinations of structure functions are already known, removing two degrees of freedom. Finally, only three free parameters ( $P_{\text{LT}}^\perp$ ,  $P_{\text{TT}}^\perp$ ,  $P'_{\text{TT}}^\perp$ ) have to be adjusted to the two polarization components  $\mathcal{P}_x$  and  $\mathcal{P}_y$ .

In section 7.3.5 it was shown that the constraint  $\mathcal{P}_z = \mathcal{P}_z^{\text{BH+B}}$  yields good results for the other components of the polarization. A fitting procedure has been built using this constraint, the equations (7.29) and (7.30) and the structure functions from the unpolarized analysis. For each event the BH+B polarization is calculated. Using equation (2.52) and (2.54) together with the simplified expressions for  $\Delta\mathcal{M}_{0,i}^{\text{NB}}$  ( $i = x, y$ ) the effect of the GPs on  $\mathcal{P}_x$  and  $\mathcal{P}_y$  is calculated for a set of the structure functions. The starting point of the fit is a combination of ( $P_{\text{LT}}^\perp$ ,  $P_{\text{TT}}^\perp$ ,  $P'_{\text{TT}}^\perp$ ),

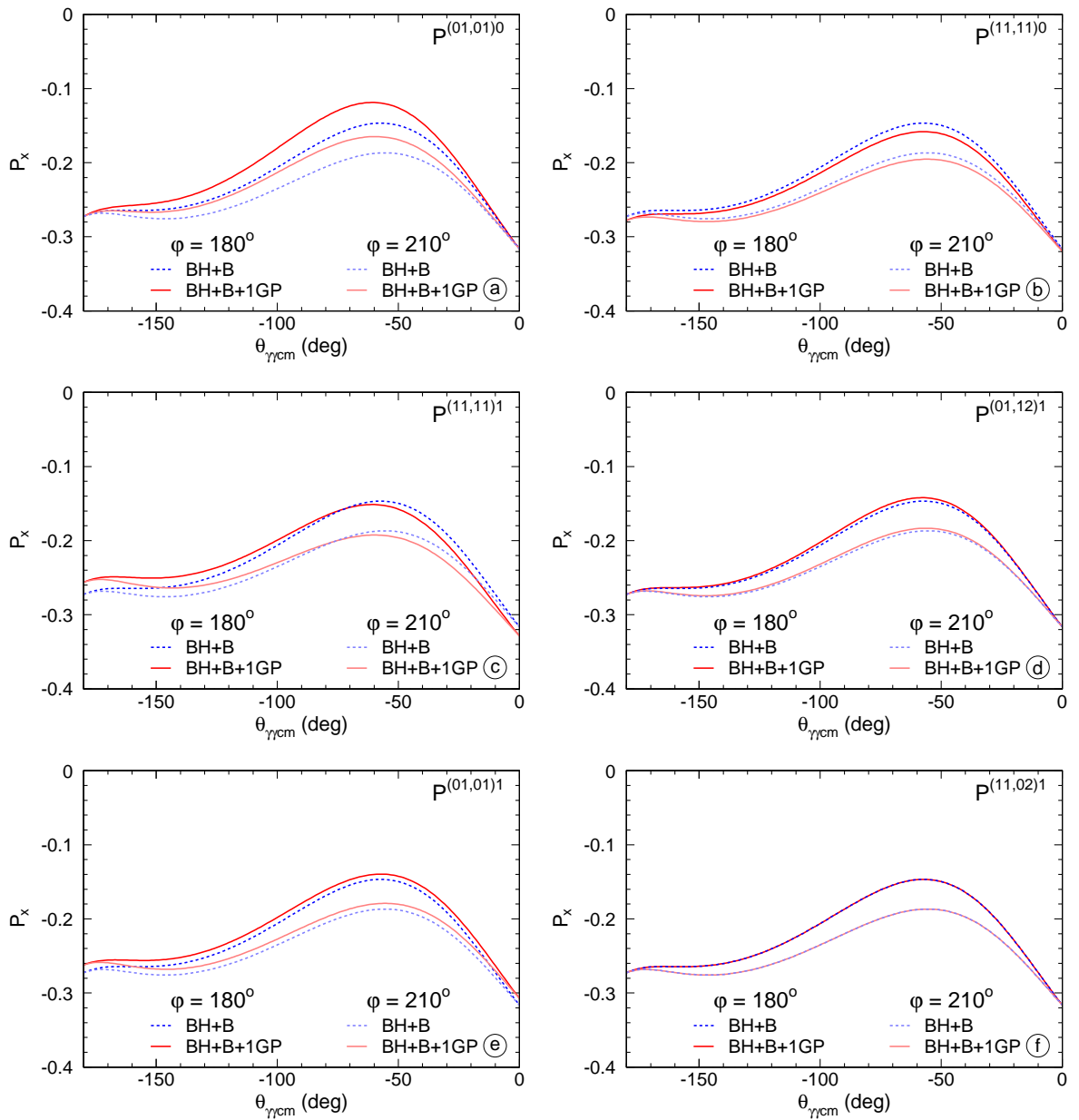


Figure 7.16: Effect of the GPs on  $\mathcal{P}_x^x$ .

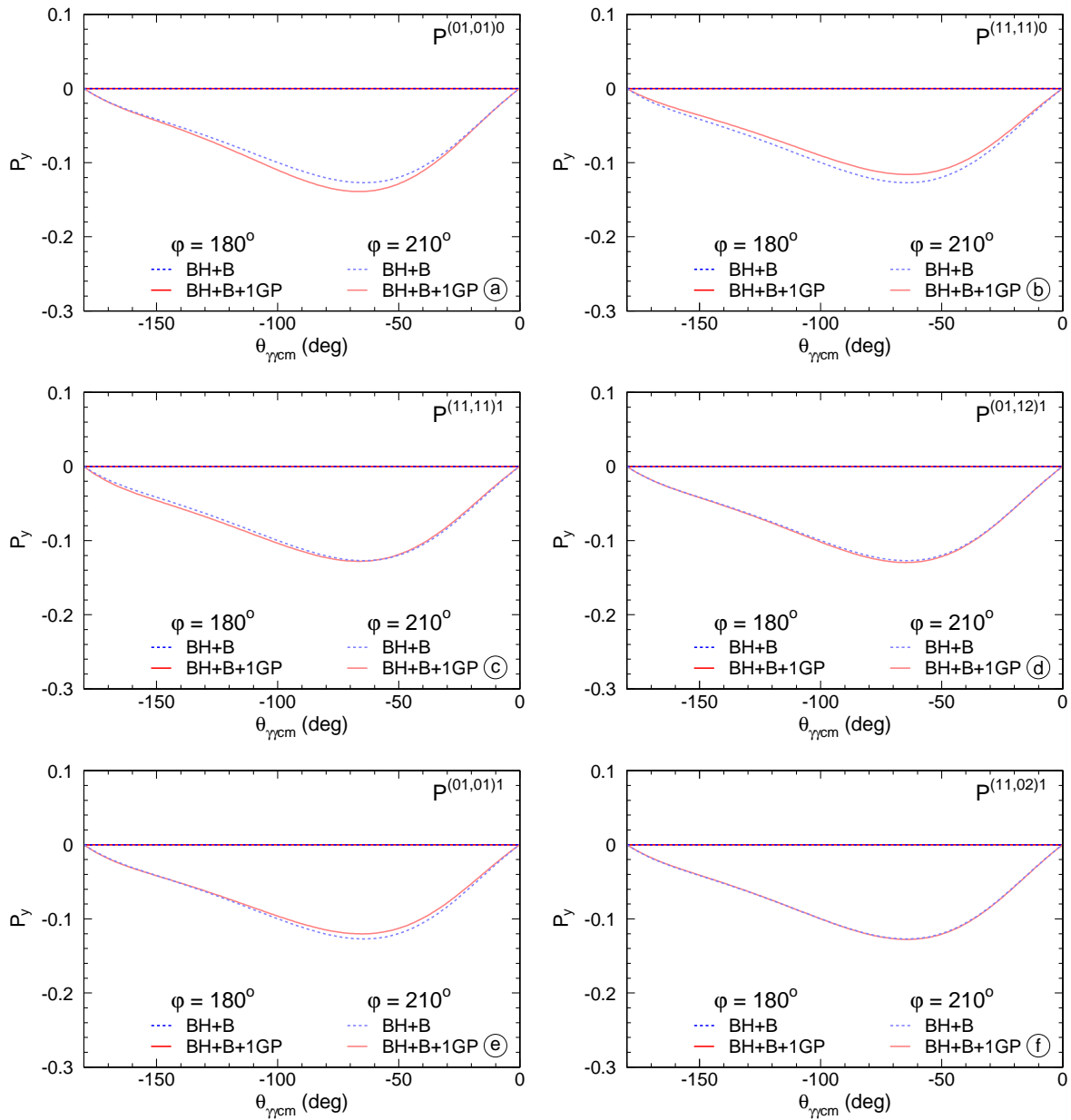


Figure 7.17: Effect of the GPs on  $\mathcal{P}_y$ .

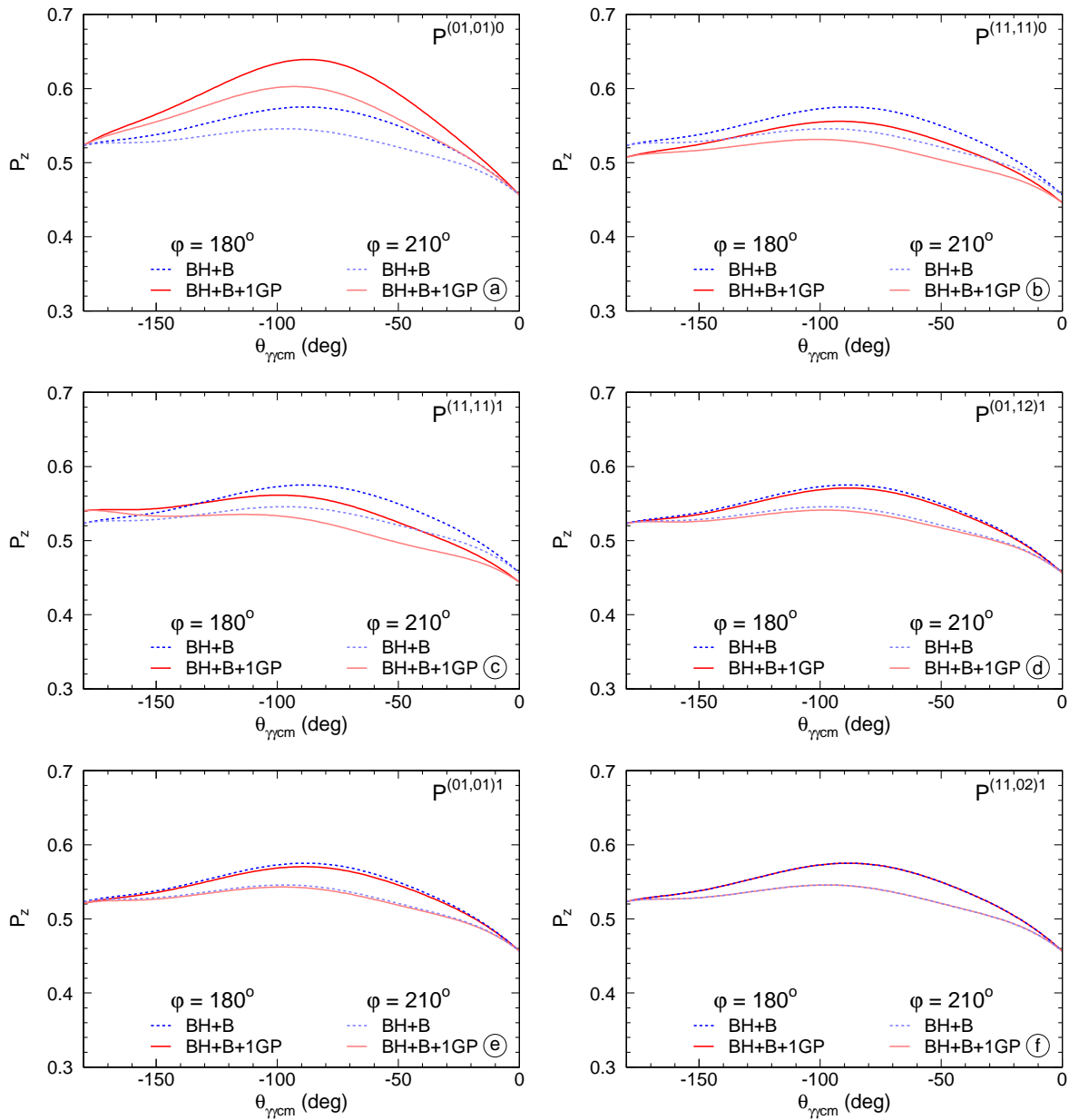
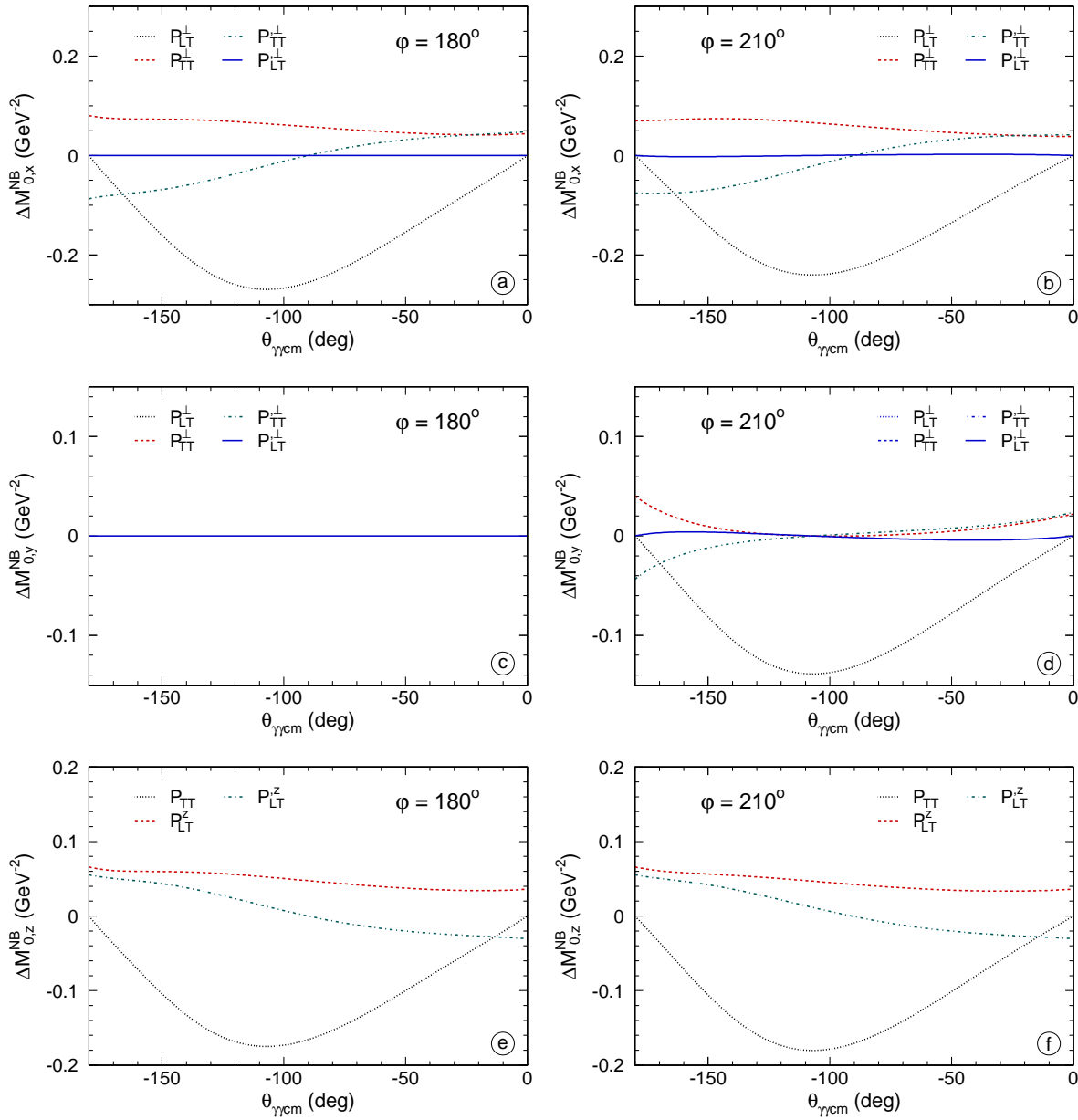


Figure 7.18: Effect of the GPs on  $\mathcal{P}_z$ .



**Figure 7.19:** Contributions of the structure functions to  $\Delta\mathcal{M}_{0,x}^{\text{NB}}$ ,  $\Delta\mathcal{M}_{0,y}^{\text{NB}}$  and  $\Delta\mathcal{M}_{0,z}^{\text{NB}}$  for in-plane ( $\varphi = 180^\circ$ ) and out-of-plane ( $\varphi = 210^\circ$ ) kinematics.

Initial values	$P_{LT}^\perp$ (GeV <sup>-2</sup> )	$P_{TT}^\perp$ (GeV <sup>-2</sup> )	$P'_{TT}^\perp$ (GeV <sup>-2</sup> )
-1 × HBχPT	-17.5 ± 2.8	-3.7 ± 0.6	-10.1 ± 9.1
0 × HBχPT	-20.2 ± 4.8	1.8 ± 2.0	-4.0 ± 2.6
1 × HBχPT	-22.3 ± 3.9	4.2 ± 2.0	-2.0 ± 2.1

**Table 7.2:** Extraction of the structure functions for different starting points of the fit using the cut TccCut.

Initial values	$P_{LT}^\perp$ (GeV <sup>-2</sup> )	$P_{TT}^\perp$ (GeV <sup>-2</sup> )	$P'_{TT}^\perp$ (GeV <sup>-2</sup> )
-1 × HBχPT	-20.9 ± 2.1	-0.1 ± 1.3	-6.8 ± 2.0
0 × HBχPT	-17.4 ± 1.9	-5.6 ± 1.7	-12.7 ± 1.7
1 × HBχPT	-23.5 ± 8.0	2.2 ± 6.9	-5.9 ± 2.4

**Table 7.3:** Extraction of the structure functions for different starting points of the fit without the cut TccCut.

where all structure functions are set to 0 GeV<sup>-2</sup>. The fit yields the following result:

$$\begin{aligned}
P_{LT}^\perp &= -20.2 \pm 4.8 \text{ GeV}^{-2}, \\
P_{TT}^\perp &= 1.8 \pm 2.0 \text{ GeV}^{-2}, \\
P'_{TT}^\perp &= -4.0 \pm 2.6 \text{ GeV}^{-2}.
\end{aligned} \tag{7.31}$$

The result becomes different, when the starting point is changed, e.g. when initially all GPs are set to their HBχPT predictions [42]:

$$\begin{aligned}
P_{LT}^\perp &= -10.6 \text{ GeV}^{-2}, \\
P_{TT}^\perp &= 2.7 \text{ GeV}^{-2}, \\
P'_{TT}^\perp &= 2.9 \text{ GeV}^{-2}.
\end{aligned} \tag{7.32}$$

An overview of the results for different initial values can be found in table 7.2.

From table 7.2 and 7.3 it becomes clear that the fitting procedure does not converge to fixed values for the structure functions, as it was the case for the analysis of the unpolarized data (see figure 6.18). However, one of the structure functions, namely  $P_{LT}^\perp$ , converges within the statistical uncertainty: the result for  $P_{LT}^\perp$  is weakly sensitive to the values of  $P_{TT}^\perp$  and  $P'_{TT}^\perp$ . This can be understood from figure 7.19, which shows that the influence of  $P_{LT}^\perp$  on  $\Delta\mathcal{M}_{0,x}^{\text{NB}}$  as a function of  $\theta_{\gamma\gamma\text{cm}}$  is completely different from that of the two other structure functions and, in addition, its effect is expected to be the main contribution. This has been tested further by

$P_{\text{TT}}^{\perp}$ and $P'_{\text{TT}}^{\perp}$ fixed	$P_{\text{LT}}^{\perp}$ (GeV $^{-2}$ )	
	TccCut	no TccCut
$-1 \times \text{HB}\chi\text{PT}$	$-14.3 \pm 3.1$	$-16.0 \pm 2.8$
$0 \times \text{HB}\chi\text{PT}$	$-15.5 \pm 3.8$	$-17.2 \pm 3.6$
$1 \times \text{HB}\chi\text{PT}$	$-16.8 \pm 5.8$	$-19.1 \pm 3.0$

**Table 7.4:** Determination of  $P_{\text{LT}}^{\perp}$  for fixed values of  $P_{\text{TT}}^{\perp}$  and  $P'_{\text{TT}}^{\perp}$ .

only adjusting the value for  $P_{\text{LT}}^{\perp}$  to the data for fixed values of  $P_{\text{TT}}^{\perp}$  and  $P'_{\text{TT}}^{\perp}$ . For example for  $(P_{\text{TT}}^{\perp}, P'_{\text{TT}}^{\perp}) = (0,0)$  GeV $^{-2}$  using the TccCut one finds:

$$P_{\text{LT}}^{\perp} = -15.5 \pm 3.8 \text{ GeV}^{-2}, \quad (7.33)$$

Table 7.2 shows that the sign and size of  $P_{\text{TT}}^{\perp}$  and  $P'_{\text{TT}}^{\perp}$  can not be determined via a fit of three parameters to the polarization data. Therefore the structure function  $P_{\text{LT}}^{\perp}$  is determined using the assumption that  $P_{\text{TT}}^{\perp} = P'_{\text{TT}}^{\perp} = 0$  GeV $^{-2}$ .

By neglecting the other two structure functions an uncertainty is induced on the obtained result. To estimate the effect of this systematic uncertainty the structure functions  $P_{\text{TT}}^{\perp}$  and  $P'_{\text{TT}}^{\perp}$  are fixed to the predictions of the HB $\chi$ PT and to the predictions for  $P_{\text{TT}}^{\perp}$  and  $P'_{\text{TT}}^{\perp}$  multiplied by  $-1$ . In table 7.4 an overview is given of the obtained values for  $P_{\text{LT}}^{\perp}$  for different assumptions for  $P_{\text{TT}}^{\perp}$  and  $P'_{\text{TT}}^{\perp}$ . From these observations and the central row of table 7.2 one can estimate the uncertainties on the obtained value for  $P_{\text{LT}}^{\perp}$ :

$$P_{\text{LT}}^{\perp} = -15.5 \pm 3.8 \pm 4.7 \text{ GeV}^{-2}, \quad (7.34)$$

The first error is the statistical uncertainty and the second one is the systematic uncertainty due to the procedure of the extraction. The effect of TccCut falls inside the systematic uncertainty mentioned here. There are of course more sources of systematic uncertainties: the systematic uncertainty on the polarization measured by the focal plane polarimeter, the uncertainty on the measurement of the beam polarization, the uncertainty on the unpolarized analysis, the influence of the radiative effects, ... These uncertainties have not been estimated in the present analysis.

The obtained value for  $P_{\text{LT}}^{\perp}$  is used to calculate the polarization including its effect on  $\Delta\mathcal{M}_{x,0}^{\text{NB}}$  and  $\Delta\mathcal{M}_{y,0}^{\text{NB}}$  for each event. Figure 7.20 displays the result, which is similar to figure 7.14: the polarizations are calculated using the constraint  $\mathcal{P}_z = \mathcal{P}_z^{\text{BH+B}}$ . The black line agrees much better with the data points, when the effect of  $P_{\text{LT}}^{\perp}$  is included.

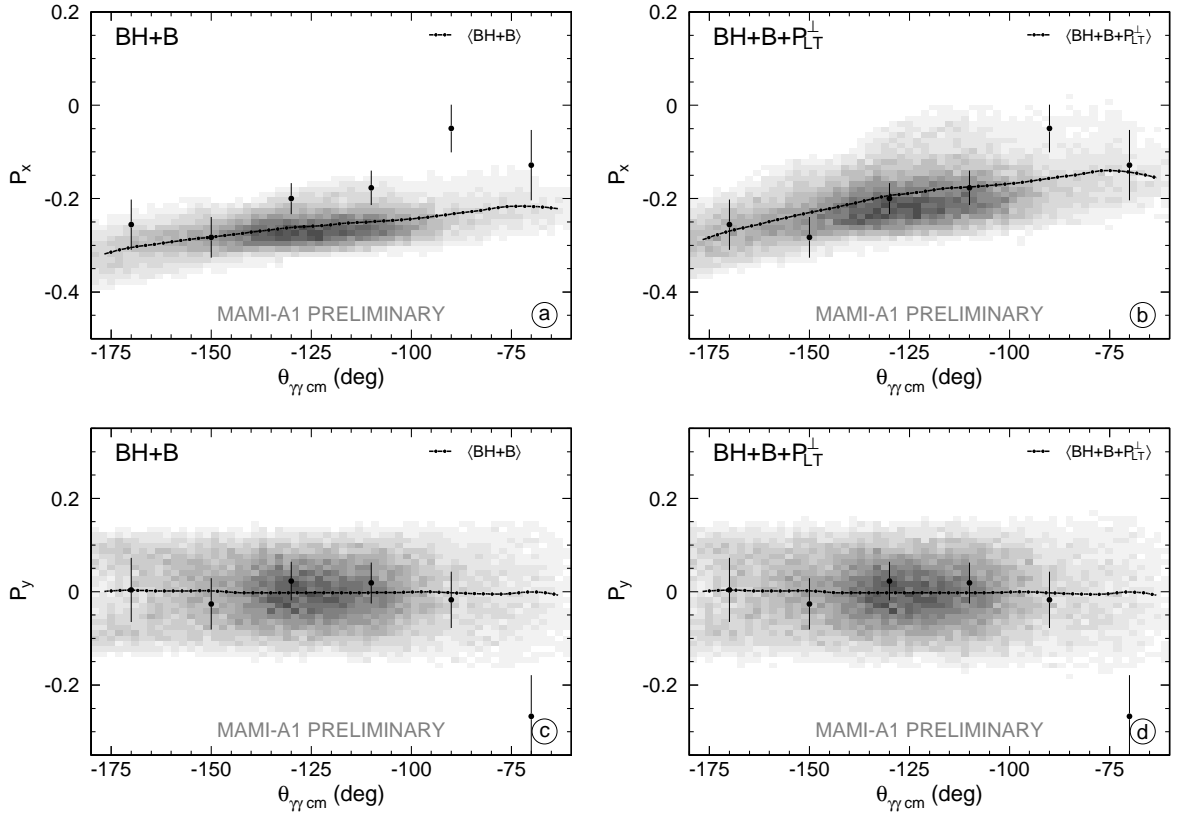


**Figure 7.20:** The measured  $x$  and  $y$  component of the polarization. On the left the result is compared to the BH+B polarization, whereas on the right the effect of  $P_{LT}^\perp$  determined in this analysis is included in the theoretically calculated polarizations. The reduced  $\chi^2$  improves from 3.8 to 1.2.

$P_{LT}^\perp$  is a linear combination of  $P_{LL}$  and  $P_{TT}$  and in the unpolarized analysis  $P_{LL} - P_{TT}/\varepsilon$  was determined. Both relations ( $P_{LT}^\perp = AP_{LL} + BP_{TT}$  and  $P_{LL} - P_{TT}/\varepsilon$ ) can now be used to extract  $P_{LL}$  and  $P_{TT}$  by solving the system of two linear equations. This yields:

$$\begin{aligned} P_{LL} &= 106. \pm 77. \pm 97. \text{ GeV}^{-2}, \\ P_{TT} &= 51. \pm 50. \pm 63. \text{ GeV}^{-2}, \end{aligned} \quad (7.35)$$

and  $\alpha_E$  can be obtained from  $P_{LL}$ :

$$\begin{aligned} P^{(01,01)0} &= \frac{-1}{2\sqrt{6}MG_E^p} P_{LL}, \\ \alpha_E &= (\hbar c)^3 \frac{-e^2}{4\pi} \sqrt{\frac{3}{2}} P^{(01,01)0} \\ &= (35. \pm 25. \pm 31.) \cdot 10^{-4} \text{ fm}^3. \end{aligned} \quad (7.36)$$

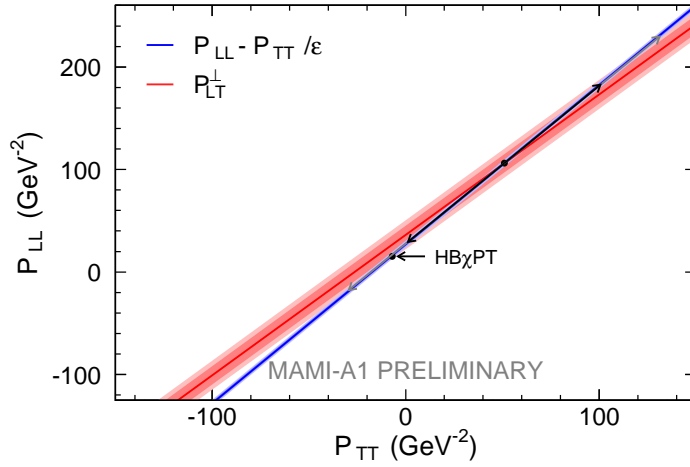


**Figure 7.21:** The two straight lines represent the two extracted relations between  $P_{LL}$  and  $P_{TT}$ . The colored band around the two lines indicate the statistical and total uncertainties. The extraction of  $P_{LT}^\perp$  yields a large statistical and total uncertainty represented by the black and grey arrows, respectively.

Using the Mergell form factors [5] one finds in a similar way:

$$\begin{aligned}
 P_{LT}^\perp &= -16.3 \pm 3.3 \pm 4.7 \text{ GeV}^{-2}, \\
 P_{LL} &= 74. \pm 42. \pm 61. \text{ GeV}^{-2}, \\
 P_{TT} &= 30. \pm 28. \pm 40. \text{ GeV}^{-2}, \\
 \alpha_E &= (24. \pm 14. \pm 20.) \cdot 10^{-4} \text{ fm}^3
 \end{aligned}
 \tag{7.37}$$

The large uncertainty on the values in equations (7.35) and (7.36) is explained by figure 7.21. Both relations can be represented by a straight line in the  $(P_{TT}, P_{LL})$ -plane. The intersection point of both lines is the solution for the system of equations. The slope of the straight line representing  $P_{LL} - P_{TT}/\varepsilon$  is determined by  $\varepsilon$ , whereas the slope of the line for  $P_{LT}^\perp$  is fixed by  $q_{cm}$  via the form factors of the proton in equation (2.36). For the kinematics of the present experiment both slopes are very close, causing a large region of overlap, if one takes into account the statistical and systematical uncertainty on the results.

The present kinematics are not optimized for the separation of  $P_{LL}$  and  $P_{TT}$ . If the  $z$  component of  $\vec{\mathcal{P}}$  would be accessible, there would be no problem, because the effect of the GPs on  $\mathcal{P}_z$  is dominated by  $P_{TT}$ . Once  $P_{TT}$  is known the result of the unpolarized analysis allows to determine  $P_{LL}$ . However, it seems not possible to reconstruct  $\mathcal{P}_z$ .

To perform a separation between  $P_{LL}$  and  $P_{TT}$  by a similar method as described above the kinematics of the experiment has to be changed to improve the separation of  $P_{LL}$  and  $P_{TT}$  based on  $P_{LT}^\perp$  and  $P_{LL} - P_{TT}/\varepsilon$ . To this end the angle,  $\psi$ , is studied.  $\psi$  is the angle between the

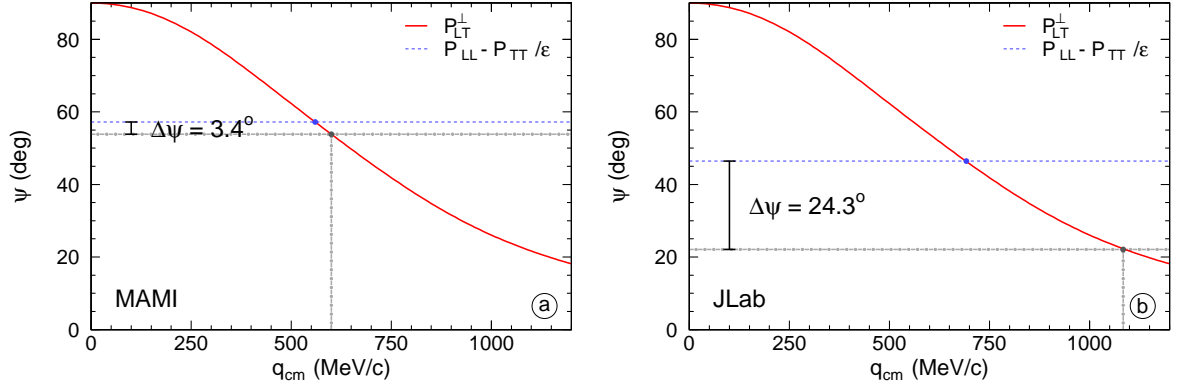


**Figure 7.22:**  $\psi$  for  $P_{LL} - P_{TT}/\varepsilon$  and  $P_{LT}^{\perp}$  as a function of  $q_{cm}$ . a: MAMI kinematics ( $q_{cm} = 600$  MeV/c,  $\varepsilon = 0.645$ ). b: JLab kinematics ( $q_{cm} = 1084$  MeV/c,  $\varepsilon = 0.952$ ).

straight line and the  $P_{TT}$ -axis in the  $(P_{TT}, P_{LL})$ -plane. For  $P_{LL} - P_{TT}/\varepsilon$ ,  $\psi$  is given by

$$\psi = \text{atan}\left(\frac{1}{\varepsilon}\right) = 57.18^{\circ}. \quad (7.38)$$

For the structure function  $P_{LT}^{\perp}$ ,  $\psi$  is calculated based on equation (2.36):

$$\psi = \text{atan}\left(\frac{RG_E^p(q_{cm})/2G_M^p(q_{cm})}{G_M^p(q_{cm})/2RG_E^p(q_{cm})}\right) = \text{atan}\left(\frac{R^2G_E^{p2}(q_{cm})}{G_M^{p2}(q_{cm})}\right). \quad (7.39)$$

$\psi$  depends on the form factors of the proton and its dependence with  $q_{cm}$  is shown by the full line in figure 7.22.a. The difference in slope,  $\Delta\psi$ , between both relations at  $q_{cm} = 600$  MeV/c is  $3.4^{\circ}$ . The only possibility to increase  $\Delta\psi$  is reducing  $\varepsilon$  and/or increasing  $q_{cm}$ . E.g. increasing  $q_{cm}$  to 700 MeV/c, without changing  $\varepsilon$  increases  $\Delta\psi$  to  $11.4^{\circ}$ . For comparison the same exercise is done in figure 7.22.b for one of the settings of the JLab experiment ( $q_{cm} = 1084$  MeV/c and  $\varepsilon = 0.952$ ), where a much better value for  $\Delta\psi = 24.3^{\circ}$  is obtained.

## 7.5 Outlook

The analysis presented in this chapter is preliminary and there are still many problems to be solved. One of the main problems is the estimation of the intrinsic uncertainty of the obtained double-spin asymmetry measured by the polarimeter. A lot of different variables and parameters enter this calculation: the measurement of the beam polarization, the analyzing power of the carbon, measurement of the scattering angles, ... The precision of the analyzing power and beam polarization is known, but the effect of the resolution of the HDCs, especially the dependence on the energy of the protons, is much harder to estimate. One way to study this

would be a complete Monte Carlo simulation of the scattering on the carbon analyzer and the track reconstruction in HDCs. At the moment of writing such a simulation is in preparation.

Another uncertainty in the analysis is the treatment of the radiative effects. In the presented analysis it is assumed that additional photon emission can be neglected for the events inside the  $M_X^2$ -cut. In reality this is not true and the radiative effects will cause errors in the reconstruction of the kinematics at the reaction vertex. The error induced by radiative effects on the obtained double-spin asymmetry should be evaluated via the Monte-Carlo simulation.

Apart from the systematic uncertainties it will also be important to collect more data to reduce the statistical error on the obtained polarizations. At the moment this uncertainty has about the same magnitude as the effect induced by the GPs. Having a smaller statistical uncertainty it should be possible to extract  $P_{TT}^\perp$  and  $P'_{TT}^\perp$  from the data. The present analysis yields an additional relation between the GPs. However, this relation could not be used to determine  $P_{LL}$  and  $P_{TT}$ , separately.

---

## Conclusion

---

In this work the analysis of the first double-polarized VCS experiment below the pion production threshold is discussed. The goal of the measurement is the determination of 5 of the 6 generalized polarizabilities by an in-plane experiment. Two different analyses are performed: the determination of the unpolarized cross section and the measurement of the double-spin asymmetry.

In the unpolarized analysis two linear combinations of structure functions,  $P_{LT}$  and  $P_{LL} - P_{TT}/\varepsilon$  are extracted from the cross section. This cross section is measured at  $q_{cm} = 600 \text{ MeV}/c$ ,  $q'_{cm} = 90 \text{ MeV}/c$  and  $\varepsilon = 0.645$  at in-plane kinematics ( $\varphi = 180^\circ$  or  $0^\circ$ ) over a wide range of photon scattering angles  $\theta_{\gamma\gamma_{cm}}$ . The kinematics was very similar to the first VCS experiment at the MAMI accelerator, performed at the same  $Q^2$  with a slightly different epsilon ( $\varepsilon = 0.62$  in the old measurement). The extraction of these structure functions, mainly  $P_{LT}$ , is very sensitive to the choice of the parameterization for the form factors. In this work the analysis was done using the parameterization of Mergell and Friedrich. Remarkable is the fact that the iteration procedure for the determination of the cross section has an important influence, which was not observed in the analysis of the old experiment at MAMI. Probably this is due to the relatively large statistical uncertainty on the calculated solid angles in the analysis of the previous experiment. Without performing any iterations, the result is in good agreement with results of the first measurement, but due to the iteration procedure the agreement becomes worse. Another interesting conclusion of the present analysis is the fact that the second order effects cause a systematic deviation of the cross section of the one predicted by the low energy expansion. The size of the second order effects is in agreement with the predictions of the DR model, however the dependency of these effects with  $\theta_{\gamma\gamma_{cm}}$  is not fully correctly predicted by the model. If one compares the obtained structure function with the predictions of the heavy baryon chiral perturbation theory, good agreement is observed for  $P_{LL} - P_{TT}/\varepsilon$ , but less good agreement is observed for  $P_{LT}$ .

The analysis of the double-spin asymmetry has shown that, for the present setting of spectrometer A, it was impossible to extract the three components of the polarization vector at the same time. In general a very low sensitivity to the z-component of  $\vec{\mathcal{P}}_{\text{cm}}$  was observed, which implied the necessity of a constraint on  $\vec{\mathcal{P}}_z$  to reconstruct the two other polarization components, but, unfortunately, it has put a strong restriction on the extraction of the GPs: the effect of the GPs on  $\mathcal{P}_z$  is much larger than on  $\mathcal{P}_y$  and the GPs appear in  $\mathcal{P}_z$  in different combinations than in  $\mathcal{P}_y$  and  $\mathcal{P}_x$ . The preliminary analysis in this thesis showed that it was impossible to access all GPs with the current number of events, but that one additional relation between the GPs could be extracted from the data via  $P_{\text{LT}}^\perp$ , which is dependent on  $P_{\text{LL}}$  and  $P_{\text{TT}}$ . Together with the result of the unpolarized analysis a separation of both structure functions was possible. However, this separation yielded very large and strongly correlated uncertainties due to the specific kinematics of the experiment. This experiment was performed to obtain the extraction of 5 linear combinations of GPs. To achieve that goal more data is needed over a wider range in the kinematical variables to improve the likelihood fit of the GPs.

	Friedrich [8] ( $\text{GeV}^{-2}$ )	Mergell [5] ( $\text{GeV}^{-2}$ )	HB $\chi$ PT ( $\text{GeV}^{-2}$ )	Observable
$P_{\text{LT}}$	$-8.0 \pm 0.7 \pm 2.1$	$-5.2 \pm 0.7 \pm 2.1$	-5.4	$d^5\sigma$
$P_{\text{LL}} - P_{\text{TT}}/\varepsilon$	$27.1 \pm 1.9 \pm 2.8$	$28.5 \pm 1.9 \pm 2.8$	26.0	$d^5\sigma$
$P_{\text{LT}}^\perp$	$-15.5 \pm 3.8 \pm 4.7$	$-16.3 \pm 3.3 \pm 4.7$	-10.6	$\vec{\mathcal{P}}$

**Table 8.1:** Overview of the (linear combinations of) structure functions obtained in this work for the two parameterizations of the form factors.

---

# Nederlandstalige samenvatting

---

## Inleiding

Bijna negentig jaar na Rutherford's ontdekking van het proton is de interne structuur van dit deeltje nog niet voldoende begrepen. Het onderzoek beschreven in dit doctoraat, is toegespitst op het meten van de veralgemeende polariseerbaarheden van het proton. Deze globale eigenschappen worden natuurlijk bepaald door de onderliggende quarkstructuur, maar de individuele quarks worden niet waargenomen in het experiment. Het gebruikte reactiemechanisme is virtuele Comptonverstrooiing onder de pionproductie drempel, waarbij een foton gevormd wordt bij de verstrooiing van een elektron aan een proton.

## Virtuele Comptonverstrooiing en veralgemeende polariseerbaarheden

Om de structuur van de protonen bij relatief lage energieën te bestuderen, wordt gebruik gemaakt van elektronenverstrooiingsexperimenten. Het voordeel hiervan is dat de interactie tussen de elektronen en de componenten van het proton goed gekend is. Bovendien zijn elektronen puntdeeltjes, zodat het verstrooiingsproces enkel beïnvloed wordt door de geometrie van het getroffen proton. De verstrooiing wordt beschreven door de uitwisseling van een virtueel foton, het ijkboson van de elektromagnetische wisselwerking, tussen het elektron en het proton. Dit virtueel foton is verantwoordelijk voor de overdracht van energie en impuls. Elektronenverstrooiingsexperimenten hebben echter ook belangrijke nadelen. Zo zijn de werkzame doorsneden doorgaans klein en is het elektron sterk onderhevig aan stralings-effecten. Deze stralingsprocessen bemoeilijken de analyse van de experimenten.

Bij elastische verstrooiing van elektronen aan protonen wordt de invloed van de structuur van het proton op de werkzame doorsnede geparametriseerd door de elektromagnetische vormfactoren  $G_E^p(Q^2)$  en  $G_M^p(Q^2)$ . Deze vormfactoren zijn functie van  $Q^2$ , wat een maat is voor de impuls-overdracht van het elektron op het proton. Deze vormfactoren kunnen geïnterpreteerd

worden als de Fouriergetransformeerde van de radiële ladings- en magnetische momenten distributies in het proton.

De interactie van een elektromagnetisch veld met het proton laat toe om de polariseerbaarheid van het proton te bepalen. Een elektrisch veld zal tegengestelde ladingen uit elkaar duwen, zodat het proton een dipoolmoment verkrijgt. Een magnetisch veld zal inspelen op de intrinsieke magnetische momenten van de valentiequarks en op de beweging van geladen deeltjes binnen het proton. Het verband tussen het geïnduceerde dipoolmoment en het aangelegde veld wordt uitgedrukt door de polariseerbaarheden. De belangrijkste zijn de elektrische en magnetische polariseerbaarheid ( $\alpha_E$  en  $\beta_M$ ), maar er bestaan ook spinpolariseerbaarheden  $\gamma_i$  ( $i = 1, \dots, 4$ ). De polariseerbaarheden laten toe om de krachten binnen het proton af te tasten. Hoe sterker de componenten aan elkaar gebonden zijn, hoe krachtiger het elektromagnetisch veld moet zijn om een bepaald dipoolmoment te induceren. De polariseerbaarheden werden opgemeten via reële Compton verstrooiing; de verstrooiing van fotonen op protonen.

Het concept polariseerbaarheid kan verruimd worden tot wat men veralgemeende polariseerbaarheden noemt (Engels: generalized polarizabilities - GPs). De GPs zijn, net als de vormfactoren, functies van  $Q^2$ . Zij beschrijven de radiële verdeling van de polariseerbaarheid in het proton. In totaal zijn er zes onafhankelijke GPs. Deze GPs kunnen bepaald worden aan de hand van virtuele Comptonverstrooiing (Engels: virtual Compton scattering - VCS) bij lage energie in het massacentrumstelsel. Dit is een reactie die toegankelijk is via de fotonelektroproductiereactie. Bij deze reactie worden elektronen verstrooid aan protonen en wordt er een (reëel) foton gevormd. Dit extra foton kan afgestraald worden door het inkomende of uitgaande elektron (het Bethe-Heitler proces), ofwel ontstaan door de interactie van het virtuele foton met het proton, wat de eigenlijke virtuele Comptonverstrooiing is. De VCS-reactie zelf kan op haar beurt worden opgesplitst in verschillende bijdragen. Gelijkaardig aan het Bethe-Heitler proces kan het foton ontstaan door bremsstrahlung van het proton, wat veroorzaakt wordt door een globale beweging van het proton. Deze bijdrage wordt het Born-proces genoemd. Het deel van de reactie dat overblijft is het interessantste. Het is de interactie van het virtueel foton met de interne structuur van het proton. Het is uit dit deel van het proces dat de GPs kunnen afgeleid worden.

In de experimentele observabelen van de fotonelektroproductiereactie komen de veralgemeende polariseerbaarheden voor in specifieke lineaire combinaties, de structuurfuncties genaamd. Aangezien er zes onafhankelijke GPs zijn, is het ook mogelijk om zes onafhankelijke structuurfuncties te definiëren. De observabelen die informatie verschaffen over de GPs zijn de niet-gepolariseerde werkzame doorsnede en de dubbelspin-asymmetrie. De niet-gepolariseerde werkzame doorsnede laat toe om in het beste geval drie van de zes structuurfuncties te bepalen. Om ze alle zes op te meten is een dubbelgepolariseerd experiment noodzakelijk.

### Theoretische modellen en eerdere VCS-experimenten

Kwantumchromodynamica is de ijktheorie die de interactie tussen quarks beschrijft door middel van de uitwisseling van gluonen. Bij hoge energieën is de koppelingsconstante voldoende klein om de fysische processen te beschrijven via een reeksontwikkeling in machten van de koppelingsconstante. Het grote probleem bij de beschrijving van de opbouw van protonen bij relatief lage energieën is dat deze koppelingsconstante te groot wordt. Hierdoor kunnen hogere-orde termen niet langer verwaarloosd worden.

Er zijn verschillende methoden om dit probleem te omzeilen. Zo kan men een beschrijving opbouwen door middel van een effectieve Lagrangiaan, die enkel de relevante vrijheidsgraden van het proton in rekening brengt of door middel van dispersierelaties, die uitgaan van een fenomenologische beschrijving. Heel wat modellen gaan uit van de opvatting dat het gedrag van het proton voornamelijk bepaald wordt door de pionenwolk die het proton omgeeft en voortkomt uit de spontane breking van de chirale symmetrie.

Tot nu toe, op basis van reële Comptonverstrooiing en de eerste virtuele Comptonverstrooiingsexperimenten, bleken de zware baryonen chirale storingstheorie (Engels: heavy baryon chiral perturbation theory - HB $\chi$ PT) die een effectieve veldentheorie is en het dispersie relatie model de beste resultaten op te leveren.

In het verleden werden reeds drie niet-gepolariseerde VCS-experimenten uitgevoerd bij verschillende waarden van  $Q^2$ . In elk van deze experimenten werd de werkzame doorsnede van de fotonelektroproductiereactie bepaald en op basis daarvan konden twee lineaire combinaties van structuurfuncties opgemeten worden, namelijk  $P_{LL} - P_{TT}/\epsilon$  en  $P_{LT}$ . Uit deze metingen blijkt dat de elektrische veralgemeende polariseerbaarheid afneemt met  $Q^2$  en de magnetische polariseerbaarheid eerst toeneemt om vervolgens af te nemen. Dit laatste fenomeen wijst op het bestaan van dia- en paramagnetische zones met verschillende afmetingen in het proton.

De voorspellingen van de verschillende modellen voor de spinafhankelijke GPs lopen ver uiteen. Daarom is een dubbelgepolariseerd VCS-experiment belangrijk om alle GPs afzonderlijk te kunnen bepalen en niet enkel in welbepaalde lineaire combinaties. Het experiment beschreven in deze thesis is de eerste dubbelgepolariseerde meting. Zij heeft als doel de extractie van vijf van de zes onafhankelijke GPs via het opmeten van de dubbelspin-asymmetrie (van het inkomende elektron en het verstrooide proton) bij de fotonelektroproductiereactie. De reden waarom niet alle GPs zullen kunnen bepaald worden is te wijten aan het feit dat deze laatste GP enkel een invloed heeft voor niet-coplanaire kinematica.

### Experimentele opstelling

Het experiment vond plaats aan de MAMI-versneller van het Institut für Kernphysik aan de Johannes Gutenberg Universität te Mainz. De longitudinaal gepolariseerde elektronenbundel viel in op een trefcel gevuld met vloeibaar waterstof. Door de interactie van het inkomende elektron met het getroffen proton, verlaten beide de trefcel en worden ze gedetecteerd met de magnetische spectrometers van de A1 hal.

De spectrometers kunnen met hoge precisie de impuls en de richting van het verstrooide elektron en het terugstootproton bepalen. De geladen deeltjes worden eerst afgebogen in het magnetisch veld van de spectrometer en daarna wordt hun baan opgemeten door middel van dradenkamers. De magneten van de spectrometers zijn zodanig ontworpen dat deeltjes met dezelfde impuls gefocuseerd worden op dezelfde plaats in het zogenaamde focaal vlak van de spectrometer. Dat laat toe om via de bepaling van het snijpunt van de baan van het deeltje met dat focaal vlak, de impuls van het deeltje op te meten.

Voor de bepaling van de polarisatie van de terugstootprotonen werd een polarimeter boven de dradenkamers van spectrometer A geplaatst. Het meetprincipe is gebaseerd op de spin-baan interactie van de sterke wisselwerking, die de verstrooiing van de protonen op een spinloze trefkern, zoals  $^{12}\text{C}$ , beïnvloedt. Daartoe bestaat de polarimeter uit een koolstofplaat, waarin de protonen verstrooien aan de individuele koolstofkernen, gevolgd door een set van dradenkamers. Door de baan van het proton op te meten na de verstrooiing aan de koolstofkern, kunnen de verstrooiingshoeken bepaald worden. Uit de distributie van de verstrooiingshoeken worden de componenten van de polarisatie van een ensemble protonen loodrecht op hun bewegingsrichting afgeleid.

### Monte Carlo simulatie

Om de werkzame doorsnede met voldoende precisie te kunnen bepalen, is een nauwkeurige berekening van de ruimtehoek van de spectrometers noodzakelijk. Daartoe werd een Monte Carlo simulatie ontwikkeld aan de Universiteit Gent. Deze simulatie werd reeds gebruikt voor de analyse van twee eerdere VCS-experimenten (MAMI en JLab). De simulatie genereert evenementen volgens de werkzame doorsnede van de BH+B reactie en houdt rekening met alle resolutiebepalende factoren, zoals energieverliezen van de deeltjes door ionisatie, bremsstrahlung, ... Bovendien is een deel van de stralingseffecten, met name dat deel dat een invloed heeft op de kinematica het proces, in de simulatie opgenomen. Hierdoor reproduceert de simulatie de experimenteel waargenomen stralingsstaarten.

Naast stralingscorrecties heeft ook de resolutie van de detectoren een belangrijke invloed op de metingen. Verstrooiing van het elektron of proton aan de materialen van de detectoren in het focaal vlak van de spectrometers zorgt ervoor dat de baan van het deeltje verandert

en daardoor niet correct wordt opgemeten. Bovendien hebben de dradenkamers een eindige nauwkeurigheid. Dit leidt tot gecorreleerde fouten in de bepaling van de baan van het deeltje, waardoor er na het optische transport ook gecorreleerde fouten ontstaan op de momenta (zowel de grootte als de richting). Daarom is het belangrijk dat deze correlaties zo goed mogelijk gereproduceerd worden in de simulatie. Dat doel wordt bereikt door de resolutie van de spectrometers te implementeren op het niveau van de dradenkamers en door de verstrooiing aan de materialen van de detectoren in het focaal vlak in de simulatie op te nemen.

### Niet-gepolariseerde werkzame doorsnede

In een eerste deel van de analyse werden de heliceit van het inkomende elektron en de polarisatie van de terugstootprotonen niet in rekening genomen. Op die manier kon de niet-gepolariseerde werkzame doorsnede van de fotonelektroproductiereactie gemeten worden. Hieruit werden, zoals bij eerdere VCS-experimenten, twee lineaire combinaties van GPs bepaald. De kinematica van de huidige meting ligt zeer dicht bij deze van het eerste VCS-experiment, dat ook plaatsvond aan de MAMI-versneller, waardoor een rechtstreekse vergelijking van beide experimenten mogelijk is.

De resolutie van de detectoren en de nauwkeurige tijdsbepaling maken het mogelijk de evenementen van de gewenste reactie te selecteren en gelijktijdig de achtergrondprocessen te onderdrukken. De voornaamste bronnen van achtergrond zijn de random coïncidenties en de interactie van de bundelelektronen met de wanden van de trefcel, die een veel hogere dichtheid hebben dan het waterstof. De random coïncidenties komen voort uit de hoge telkadansen in de detectoren.

De werkzame doorsnede als functie van  $\theta_{\gamma\gamma_{\text{cm}}}$  werd bepaald voor  $q_{\text{cm}} = 600 \text{ MeV}/c$ ,  $q'_{\text{cm}} = 90 \text{ MeV}/c$ ,  $\varepsilon = 0.645$  voor coplanaire kinematica ( $\varphi = 0^\circ$  of  $\varphi = 180^\circ$ ). Hierbij is  $q_{\text{cm}}$  het momentum van het virtueel foton,  $q'_{\text{cm}}$  het momentum van het uitgaande (reëel) foton en  $\varepsilon$  de lineaire polarisatieparameter van het virtueel foton. De polaire en azimutale hoeken van het reëel foton ten opzichte van het virtueel foton in het massacentrumstelsel worden voorgesteld door  $\theta_{\gamma\gamma_{\text{cm}}}$  en  $\varphi$ . De analyse, gebruik makend van het lage energietheorema, werd uitgevoerd voor twee verschillende parametrisaties van de vormfactoren van het proton (Mergell *et al.* [5] en Friedrich *et al.* [8]). Het verschil tussen beide parametrisaties veroorzaakt een verschil, dat nagenoeg constant is over het interval in  $\theta_{\gamma\gamma_{\text{cm}}}$ . Het verschil bedraagt 3 tot 4% van de Bethe-Heitler werkzame doorsnede. Aangezien de structuurfuncties bepaald worden uit het verschil van de gemeten werkzame doorsnede met de theoretisch berekende BH+B werkzame doorsnede, is het duidelijk dat de keuze van de vormfactoren een belangrijke invloed heeft op het uiteindelijke resultaat.

In principe moet de werkzame doorsnede, gebruikt in de simulatie, overeenstemmen met de werkelijke werkzame doorsnede. Omdat deze op voorhand niet gekend is, wordt in eerste in-

stantie de BH+B werkzame doorsnede gebruikt. Nadat hiermee de structuurfuncties bepaald werden, kan het effect van de GPs in de simulatie worden opgenomen om de ruimtehoek opnieuw te berekenen. Hiermee kunnen nieuwe waarden voor de structuurfuncties bekomen worden. Deze iteratieprocedure wordt uitgevoerd tot een stabiele oplossing voor de structuurfuncties bekomen wordt. Voor de lineaire combinatie van de structuurfuncties werden, na de iteraties, volgende waarden bekomen voor de Friedrich vormfactoren:

$$P_{LL} - P_{TT}/\varepsilon = 27.1 \pm 1.9 \pm 2.8 \text{ GeV}^{-2},$$

$$P_{LT} = -8.0 \pm 0.7 \pm 2.1 \text{ GeV}^{-2}$$

en

$$P_{LL} - P_{TT}/\varepsilon = 28.5 \pm 1.9 \pm 2.8 \text{ GeV}^{-2},$$

$$P_{LT} = -5.2 \pm 0.7 \pm 2.1 \text{ GeV}^{-2},$$

wanneer de Mergell parametrisatie werd gebruikt. In deze resultaten geeft de eerste fout de statistische en de tweede de systematische onzekerheid op het bekomen resultaat aan. Aan de twee sets van waarden kan men vaststellen dat de structuurfunctie  $P_{LT}$  het meest gevoelig is aan de keuze van de vormfactoren. Opvallend is dat het resultaat zonder de iteratieprocedure zeer goed overeenstemt met het eerder uitgevoerde VCS-experiment aan de MAMI-versneller, maar dat er een systematische afwijking optreedt bij het uitvoeren van de iteraties. In deze oude meting werd deze iteratieprocedure niet toegepast.

Twee belangrijke vaststellingen kunnen gedaan worden in deze analyse. Volgens het lage-energiethorema wordt het effect van de GPs op de werkzame doorsnede bepaald door een term lineair in  $q'_{\text{cm}}$ . Dit blijkt ook uit de data, maar hogere-orde effecten blijken een meetbaar effect te hebben. Een model dat alle hogere-orde termen in rekening brengt is het dispersiere-latiemodel. Berekeningen gebruik makende van dat model leveren hogere-orde effecten die qua grootte overeenstemmen met de waarnemingen. Echter wordt het verloop als functie van  $\theta_{\gamma\gamma_{\text{cm}}}$  niet correct gereproduceerd.

### Dubbelspin-Asymmetrie

In een tweede luik van de analyse werd de dubbelspin-asymmetrie van de fotonelektroproductiereactie bestudeerd. Dit heeft als doel de extractie van vijf van de zes structuurfuncties. Daartoe is het opmeten van de drie componenten van de polarisatie van het proton in het massacentrumstelsel noodzakelijk. De polarimeter, die geplaatst is in spectrometer A, moet toelaten om deze drie componenten op te meten. Normaal gezien kan een polarimeter enkel de twee componenten van de polarisatie loodrecht op de bewegingsrichting van de protonen bepalen. Dankzij de rotatie van de spin in de magneet van de spectrometer, die voor iedere proton anders is (afhankelijk van de gevolgde baan in de magneet) en bovendien gekend is,

is het in principe mogelijk om alle componenten te bepalen. De polarisatie van de inkomende elektronen werd opgemeten met de Møllerpolarimeter, die deel uitmaakt van de standaardtoestellen van de A1 hal.

Zoals reeds aangegeven zijn de rotaties van de spin van het proton zeer belangrijk voor de bepaling van de dubbelspin-asymmetrie. Naast de triviale rotatie van de spinvector bij veranderingen van referentiestelsel zijn er twee fysisch belangrijke oorzaken van het roteren van de spin. De eerste vindt plaats bij de overgang van het massacentrumstelsel naar het laboratoriumstelsel. Bij deze Lorentzboost treedt er een verdraaiing van de spin op. De hoek waarover de spin geroteerd wordt is de Wignerhoek. Een tweede rotatie is de reeds vermelde precessie van de spin in het magnetisch veld van de spectrometer. Deze rotatie wordt beschreven door de Thomasvergelijking. De sterkte van het magnetisch veld in de spectrometer is gekend en bijgevolg kan deze vergelijking opgelost worden voor een willekeurige baan van een proton in de spectrometermagneet.

Tijdens de analyse bleek al snel dat de  $z$ -component van de protonpolarisatie niet met voldoende nauwkeurigheid zou kunnen gereconstrueerd worden. Dat is te wijten aan het feit dat voor het grootste deel van de protonen deze component, na de rotatie in het magneetveld, hoofdzakelijk parallel met hun bewegingsrichting blijft. Bovendien werd een sterke correlatie waargenomen tussen de  $y$ - en de  $z$ -component. Door de voorwaarde op te leggen dat de  $\mathcal{P}_z$  gelijk is aan  $\mathcal{P}_z^{\text{BH+B}}$ , de theoretische voorspelling van de  $z$ -component van de polarisatie zonder de GPs, is de reconstructie van  $\mathcal{P}_y$  bruikbaar in de verdere analyse. De benadering  $\mathcal{P}_z = \mathcal{P}_z^{\text{BH+B}}$  is gerechtvaardigd omdat het effect van de GPs op  $\mathcal{P}_z$  klein is volgens de theoretische voorspellingen.

Eén van de structuurfuncties domineert voor  $\mathcal{P}_x$  en  $\mathcal{P}_y$ , namelijk  $P_{\text{LT}}^\perp$ . In de analyse van de data werd enkel deze structuurfunctie in rekening gebracht en de waarde ervan werd aangepast aan de gemeten waarden van  $\mathcal{P}_x$  en  $\mathcal{P}_y$ . De andere structuurfuncties die een invloed hebben op beide componenten werden verwaarloosd. De fout die hierdoor begaan wordt, is in de systematische onzekerheid op het bekomen resultaat opgenomen. Gebruik makende van de Friedrich vormfactoren werd

$$P_{\text{LT}}^\perp = -15.5 \pm 3.8 \pm 4.7 \text{ GeV}^{-2}$$

bekomen en

$$P_{\text{LT}}^\perp = -16.3 \pm 3.3 \pm 4.7 \text{ GeV}^{-2}$$

voor de Mergell parameterisatie. De structuurfunctie  $P_{\text{LT}}^\perp$  is een lineaire combinatie van  $P_{\text{LT}}^\perp$  en  $P_{\text{TT}}$  en in principe zou een scheiding van beide structuurfuncties mogelijk moeten zijn door het hier bekomen resultaat te combineren met de niet-gepolariseerde analyse. In de

praktijk blijkt dit niet zo evident te zijn en leidt deze methode tot een grote onzekerheid op het bekomen resultaat.

Vooraleer het mogelijk is een definitief resultaat van de gepolariseerde analyse te bekomen, moeten nog heel wat problemen opgelost worden. In de eerste plaats bevat de opgegeven systematische onzekerheid nog niet alle bronnen van systematische fouten: bijvoorbeeld de onzekerheid op de polarisatie van de elektronenbundel en ook het effect van stralingsverliezen werd niet in rekening genomen. Anderzijds zijn er nog een aantal experimentele zaken die nog niet voldoende begrepen en getest zijn. Zo is er bijvoorbeeld de energie-afhankelijkheid in de resolutie van de dradenkamers van de polarimeter. De Monte Carlo simulatie die momenteel ontwikkeld wordt binnen de A1 collaboratie zou veel van deze problemen moeten ophelderen.

## Besluit

Voor het eerst werd een dubbelgepolariseerd VCS-experiment beneden de pionenproductiedrempel uitgevoerd. De bekomen gegevens werden op twee manieren geanalyseerd.

In de niet-gepolariseerde analyse werden nieuwe waarden voor de reeds eerder bepaalde structuurfuncties  $P_{LL} - P_{LT}/\varepsilon$  en  $P_{LT}$  bekomen. Na het doorvoeren van een iteratieprocedure in de bepaling van de werkzame doorsnede, bleken beide groter (in absolute waarde) te zijn dan in de voorgaande meting.

Uit de analyse van de dubbelspin-asymmetrie werd een extra structuurfunctie bepaald, namelijk  $P_{LT}^\perp$ , zodat in totaal drie lineaire combinaties van GPs gekend zijn. Dat is minder dan in de oorspronkelijke doelstelling van het experiment. Om het vooropgestelde doel te bereiken is het noodzakelijk om meer gegevens te verzamelen, die bovendien gespreid moeten zijn over een groter kinematisch domein. Dit is niet zo eenvoudig te verwezenlijken aangezien de spectrometers en de protonpolarimeter de toegankelijke faseruimte sterk beperken. De ontwikkeling van een Monte Carlo simulatie van de processen in de polarimeter moet leiden tot een beter begrip van de systematische onzekerheden.

---

# Acknowledgments

---

In the first place I would like to thank my promoter Prof. Dirk Ryckbosch for giving me the opportunity to do a Ph.D. in his research group at the Department of Subatomic and Radiation Physics at the Ghent University and for offering me the freedom to choose my own direction for my Ph.D research.

I really appreciated the help of my co-promoter Prof. Luc Van Hoorebeke, who introduced me to virtual Compton scattering. He taught me a lot about the physics behind VCS, Monte Carlo techniques, the analysis of the experiment, ... Although he was very busy with his own research group, he always made time to answer my questions.

The analysis presented in this thesis is of course not only my own work. I'm very grateful to all the people who participated in the experiment: the members of the A1 collaboration, the shift personnel, the staff and operators of the MAMI accelerator. H el ene Fonvieille, Harald Merkel, Nicole d'Hose and Luca Doria should be mentioned in particular for all their help and suggestions for the analysis of the data and the development of the Monte Carlo simulation. Special thanks go to Luca and Sonia for their hospitality and the enjoyable dinners during the data-taking periods.

During the last four years I enjoyed working at the department of subatomic and radiation physics of the Ghent University. I would like to thank my friends at the institute for their company, for solving my computer problems, for reading parts of my thesis, for the coffee breaks [111], for being the victim of my jokes, ... I should not forget to mention the (former) members of our research group: Alejandro, Arne sr., Beni, Bino, Brecht, Charlotte, Freija, Michael, Uli, Yasser and Yves for the nice atmosphere at work. In particular I want to thank my office mates Tiko, Gunar and Arne jr.: I don't know if you enjoyed my presence in your office, but I appreciated your presence in my office.

A special 'thank you' is reserved for Rudi Verspille for his help in designing some of the figures and the cover of this thesis.

Here I would also like to thank the members of the reading committee (Prof. Dirk Ryckbosch, Prof. Luc Van Hoorebeke and H el ene Fonvieille) for their suggestions to improve this thesis, and the remaining members of the examination committee: Prof. Jan Ryckebusch, Prof. Kris Heyde, Prof. Dimitri Van Neck, Harald Merkel and Michael Tytgat.

Last but not least I would like to thank my family and friends for their friendship and support during the four years of my Ph.D. research.

---

# Bibliografie

---

- [1] E. Rutherford, Collision of Alpha Particles with Light Atoms; An Anomalous Effect in Nitrogen, *Phil. Mag.* 37 (1919) 538–587.
- [2] B. Povh, K. Rith, C. Scholz, F. Zetsche, *Particles and Nuclei: An Introduction to the Physical Concepts.*, Springer, 2002.
- [3] M. Rosenbluth, High Energy Elastic Scattering of Electrons on Protons, *Phys. Rev.* 79 (1950) 615–619.
- [4] T. Janssens, et al., Proton Form Factors from Elastic Electron-Proton Scattering, *Phys. Rev.* 142 (1966) 922–931.
- [5] P. Mergell, U. G. Meissner, D. Drechsel, Dispersion theoretical analysis of the nucleon electromagnetic form-factors, *Nucl. Phys.* A596 (1996) 367–396.
- [6] P. E. Bosted, Empirical fit to the nucleon electromagnetic form factors, *Phys. Rev.* C51 (1995) 409–411.
- [7] G. Höhler, et al., Analysis of Electromagnetic Nucleon Form Factors, *Nucl. Phys.* B114 (1976) 505–534.
- [8] J. Friedrich, T. Walcher, A coherent interpretation of the form factors of the nucleon in terms of a pion cloud and constituent quarks, *Eur. Phys. J.* A17 (2003) 607–623.
- [9] J. L. Powell, Note on the Bremsstrahlung Produced by Protons, *Phys. Rev.* 75 (1949) 32–34.
- [10] A. Klein, Y. Nishina, Über die Streuung von Strahlung durch freie Elektronen nach der neuen relativistischen Quantendynamik von Dirac, *Z. Phys.* 52 (1929) 853.
- [11] V. A. Petrun'kin, Scattering of Low-Energy Photons on a Zero-Spin Particle, *Nucl. Phys.* 55 (1964) 197–206.

- [12] S. Ragusa, Third order spin polarizabilities of the nucleon, *Phys. Rev. D* 47 (1993) 3757–3767.
- [13] A. I. L'vov, V. A. Petrun'kin, M. Schumacher, Dispersion theory of proton Compton scattering in the first and second resonance regions, *Phys. Rev. C* 55 (1997) 359–377.
- [14] D. Drechsel, M. Gorchtein, B. Pasquini, M. Vanderhaeghen, Fixed- $t$  subtracted dispersion relations for Compton scattering off the nucleon, *Phys. Rev. C* 61 (2000) 015204.
- [15] V. Olmos de Leon, et al., Low-energy Compton scattering and the polarizabilities of the proton, *Eur. Phys. J. A* 10 (2001) 207–215.
- [16] F. J. Federspiel, et al., The proton Compton Effect: A Measurement of the electric and magnetic polarizabilities of the proton, *Phys. Rev. Lett.* 67 (1991) 1511–1514.
- [17] B. E. MacGibbon, et al., Measurement of the Electric and Magnetic Polarizabilities of the Proton, *Phys. Rev. C* 52 (1995) 2097–2109.
- [18] D. Drechsel, B. Pasquini, M. Vanderhaeghen, Dispersion relations in real and virtual Compton scattering, *Phys. Rept.* 378 (2003) 99–205.
- [19] A. M. Baldin, et al., Polarizability of Nucleons, *Nucl. Phys.* 18 (1960) 310–317.
- [20] D. Babusci, G. Giordano, G. Matone, A new evaluation of the Baldin sum rule, *Phys. Rev. C* 57 (1998) 291–294.
- [21] M. I. Levchuk, A. I. L'vov, Deuteron Compton scattering below pion photoproduction threshold, *Nucl. Phys. A* 674 (2000) 449–492.
- [22] A. Zieger, et al., 180-degrees Compton scattering by the proton below the pion threshold, *Phys. Lett. B* 278 (1992) 34–38.
- [23] H. W. Griesshammer, T. R. Hemmert, Dispersion effects in nucleon polarisabilities, *Phys. Rev. C* 65 (2002) 045207.
- [24] A. Bacchetta, U. D'Alesio, M. Diehl, C. A. Miller, Single-spin asymmetries: The Trento conventions, *Phys. Rev. D* 70 (2004) 117504.
- [25] D. H. Perkins, *Introduction to High-Energy Physics*, Addison-Wesley, 1987.
- [26] P. A. M. Guichon, G. Q. Liu, A. W. Thomas, Virtual Compton scattering and generalized polarizabilities of the proton, *Nucl. Phys. A* 591 (1995) 606–638.
- [27] F. E. Low, Bremsstrahlung of very low-energy quanta in elementary particle collisions, *Phys. Rev.* 110 (1958) 974–977.

- [28] F. E. Low, Scattering of light of very low frequency by systems of spin 1/2, *Phys. Rev.* 96 (1954) 1428–1432.
- [29] M. Gell-Mann, M. L. Goldberger, Scattering of low-energy photons by particles of spin 1/2, *Phys. Rev.* 96 (1954) 1433–1438.
- [30] J. D. Jackson, *Classical Electrodynamics*, John Wiley & Sons, 1999.
- [31] P. A. M. Guichon, M. Vanderhaeghen, Virtual Compton scattering off the nucleon, *Prog. Part. Nucl. Phys.* 41 (1998) 125–190.
- [32] N. Degrande, Experimental study of the Virtual Compton Scattering Process at  $Q^2 = 1.0$  (GeV/c)<sup>2</sup>, Ph.D. thesis, Universiteit Gent (2001).
- [33] A. J. F. Siegert, Note on the interaction between nuclei and electromagnetic radiation, *Phys. Rev.* 52 (1937) 787–789.
- [34] D. Drechsel, G. Knochlein, A. Metz, S. Scherer, Generalized polarizabilities and the spin-averaged amplitude in virtual Compton scattering off the nucleon, *Phys. Rev. C* 55 (1997) 424–430.
- [35] D. Drechsel, G. Knochlein, A. Y. Korchin, A. Metz, S. Scherer, Structure analysis of the virtual Compton scattering amplitude at low energies, *Phys. Rev. C* 57 (1998) 941–952.
- [36] A. I. L'vov, S. Scherer, B. Pasquini, C. Unkmeir, D. Drechsel, Generalized dipole polarizabilities and the spatial structure of hadrons, *Phys. Rev. C* 64 (2001) 015203.
- [37] M. Vanderhaeghen, Double polarization observables in virtual Compton scattering, *Phys. Lett. B* 402 (1997) 243–250.
- [38] P. Kroll, M. Schurmann, P. A. M. Guichon, Virtual Compton scattering off protons at moderately large momentum transfer, *Nucl. Phys. A* 598 (1996) 435–461.
- [39] V. Bernard, N. Kaiser, A. Schmidt, U. G. Meissner, Consistent calculation of the nucleon electromagnetic polarizabilities in chiral perturbation theory beyond next- to-leading order, *Phys. Lett. B* 319 (1993) 269–275.
- [40] T. R. Hemmert, B. R. Holstein, G. Knochlein, S. Scherer, Virtual Compton scattering off the nucleon in chiral perturbation theory, *Phys. Rev. D* 55 (1997) 2630–2643.
- [41] T. R. Hemmert, B. R. Holstein, G. Knochlein, S. Scherer, Generalized polarizabilities and the chiral structure of the nucleon, *Phys. Rev. Lett.* 79 (1997) 22–25.
- [42] T. R. Hemmert, B. R. Holstein, G. Knochlein, D. Drechsel, Generalized polarizabilities of the nucleon in chiral effective theories, *Phys. Rev. D* 62 (2000) 014013.

- [43] C. W. Kao, M. Vanderhaeghen, Generalized spin polarizabilities of the nucleon in heavy baryon chiral perturbation theory at next-to-leading order, *Phys. Rev. Lett.* 89 (2002) 272002.
- [44] C.-W. Kao, B. Pasquini, M. Vanderhaeghen, New predictions for generalized spin polarizabilities from heavy baryon chiral perturbation theory, *Phys. Rev. D* 70 (2004) 114004.
- [45] V. Bernard, N. Kaiser, U.-G. Meissner, Chiral dynamics in nucleons and nuclei, *Int. J. Mod. Phys. E* 4 (1995) 193–346.
- [46] S. Scherer, Introduction to chiral perturbation theory, *Adv. Nucl. Phys.* 27 (2003) 277.
- [47] M. E. Peskin, D. V. Schroeder, *An Introduction to quantum field theory*, Addison-Wesley, 1995.
- [48] A. Metz, D. Drechsel, Generalized polarizabilities of the nucleon studied in the linear sigma model, *Z. Phys.* A356 (1996) 351–357.
- [49] A. Metz, D. Drechsel, Generalized polarizabilities of the nucleon studied in the linear sigma model. II, *Z. Phys.* A359 (1997) 165–172.
- [50] N. Isgur, G. Karl, P-Wave Baryons in the Quark Model, *Phys. Rev. D* 18 (1978) 4187.
- [51] G. Q. Liu, A. W. Thomas, P. A. M. Guichon, Virtual Compton scattering from the proton and the properties of nucleon excited states, *Austral. J. Phys.* 49 (1996) 905–918.
- [52] B. Pasquini, S. Scherer, D. Drechsel, Generalized polarizabilities of the proton in a constituent quark model revisited, *Phys. Rev. C* 63 (2001) 025205.
- [53] M. Vanderhaeghen, Virtual Compton scattering study below pion production threshold, *Phys. Lett. B* 368 (1996) 13–19.
- [54] A. Y. Korchin, O. Scholten, Nucleon polarizabilities in virtual Compton scattering, *Phys. Rev. C* 58 (1998) 1098–1100.
- [55] R. Berg, C. Lindner, Electron-proton Bremsstrahlung, *Nucl. Phys.* 26 (1961) 259–279.
- [56] D. Drechsel, G. Knochlein, A. Y. Korchin, A. Metz, S. Scherer, Low-energy and low-momentum representation of the virtual Compton scattering amplitude, *Phys. Rev. C* 58 (1998) 1751–1757.
- [57] B. Pasquini, M. Gorchtein, D. Drechsel, A. Metz, M. Vanderhaeghen, Dispersion relation formalism for virtual Compton scattering off the proton, *Eur. Phys. J. A* 11 (2001) 185–208.

- [58] D. Drechsel, O. Hanstein, S. S. Kamalov, L. Tiator, A unitary isobar model for pion photo- and electroproduction on the proton up to 1 GeV, Nucl. Phys. A645 (1999) 145–174.
- [59] N. d’Hose, et al., Double Polarization Virtual Compton Scattering in the threshold regime at MAMI, MAMI proposal (2001).
- [60] J. Roche, et al., The first determination of generalized polarizabilities of the proton by a virtual Compton scattering experiment, Phys. Rev. Lett. 85 (2000) 708–711.
- [61] N. d’Hose, Virtual Compton scattering at MAMI, Eur. Phys. J. A28 (2006) 117–127.
- [62] D. Lhuillier, Diffusion Compton Virtuelle a Basse Energie, Ph.D. thesis, Université de Caen (1997).
- [63] J. Roche, Diffusion Compton virtuelle à MAMI et mesure des polarisabilités généralisées du proton, Ph.D. thesis, Université Blaise Pascal (1998).
- [64] J. Friedrich, Messung der Virtuellen Comptonstreuung an MAMI zur Bestimmung Generalisierter Polarisierbarkeiten des Protons, Ph.D. thesis, Universität Mainz (2001).
- [65] G. Laveissière, et al., Measurement of the generalized polarizabilities of the proton in virtual Compton scattering at  $Q^2 = 0.92 \text{ GeV}^2$  and  $1.76 \text{ GeV}^2$ , Phys. Rev. Lett. 93 (2004) 122001.
- [66] E. J. Brash, A. Kozlov, S. Li, G. M. Huber, New empirical fits to the proton electromagnetic form factors, Phys. Rev. C65 (2002) 051001.
- [67] G. Laveissière, Electroproduction de photons et de pions sur le proton au quadriment de transfert  $Q^2 = 1.0 \text{ GeV}^2$ . Mesure des section efficaces et extraction de polarisabilités généralisées, Ph.D. thesis, Université Blaise Pascal (2001).
- [68] S. Jaminion, Diffusion Compton Virtuelle à Jefferson Lab (Expérience E(93050): Résultat Préliminaire des Section Efficaces ( $ep \rightarrow ep\gamma$ ) en vue d’Extraire les Polarisabilités Généralisées du Proton à  $Q^2 = 1.9 \text{ GeV}^2$ , Ph.D. thesis, Université Blaise Pascal (2000).
- [69] C. Jutier, Mesure de la Diffusion Compton Virtuelle en dessous de Création de Pion a Quadri-moment Transferé au carré  $Q^2 = 1.0 (\text{GeV}/c)^2$ , Ph.D. thesis, Université Blaise Pascal (2001).
- [70] P. Bourgeois, et al., Measurements of the generalized electric and magnetic polarizabilities of the proton at low  $Q^2$  using the VCS reaction, Phys. Rev. Lett. 97 (2006) 212001.
- [71] H. Fonvieille, Personal communication.

- [72] I. Bensafa, Mesure de l'asymétrie de spin de faisceau en diffusion Compton virtuelle polarisée sur le proton. Etude de spectre d'énergie du nucléon par le modèle de potentiel de type QCD, Ph.D. thesis, Université Blaise Pascal (2006).
- [73] S. S. Kamalov, S. N. Yang, Pion cloud and the  $Q^2$  dependence of  $\gamma^* N \leftrightarrow \Delta$  transition form factors, *Phys. Rev. Lett.* 83 (1999) 4494–4497.
- [74] I. K. Bensafa, Beam-helicity asymmetry in photon and pion electroproduction in the  $\Delta(1232)$  resonance region at  $Q^2 = 0.35 \text{ (GeV}/c)^2$ , *Eur. Phys. J. A* 32 (2007) 69–75.
- [75] H. Fonvieille, Analysis report SSA measurement, Internal Note, MAMI-A1 collaboration (2006).
- [76] H. Herminghaus, A. Feder, K. H. Kaiser, W. Manz, H. Von Der Schmitt, The Design of a Cascaded 800 MeV Normal Conducting CW Racetrack Microtron, *Nucl. Instrum. Meth.* 138 (1976) 1–12.
- [77] M. Steigerwals, Aufbau einer Quelle polarisierter Elektronen am Injektorlinac und Untersuchungen zur Spindynamik im MAMI, Ph.D. thesis, Universität Mainz (1998).
- [78] A. Jankowiak, The Mainz Microtron MAMI: Past and future, *Eur. Phys. J. A* 28S1 (2006) 149–160.
- [79] S. Širca, The axial form factor of the nucleon from coincident pion electro-production at low  $Q^2$ , Ph.D. thesis, University of Ljubljana (1999).
- [80] <http://wwa1.kph.uni-mainz.de/A1/>.
- [81] K. I. Blomqvist, et al., The three-spectrometer facility at the Mainz microtron MAMI, *Nucl. Instrum. Meth.* A403 (1998) 263–301.
- [82] T. Pospischil, Aufbau und Inbetriebnahme eines Protonen-Polarimeters an MAMI und Messung der Proton-Polarisation der Reaktion  $p(\vec{e}, e' \vec{p})\pi^0$  in paralleler Kinematik im Bereich der  $\Delta(1232)$ -Resonanz, Ph.D. thesis, Universität Mainz (2000).
- [83] P. Sauer, Entwicklung, Aufbau und Inbetriebnahme der vertikaler Driftkammern der Drei-Spektrometer-Anlage am Mainzer Mikrotron MAMI und Studium der Reaktion  $^{12}\text{C}(e, e' p') ^{11}\text{B}$  für mittlere und hohe Mukleonenimpulse im Kern, Ph.D. thesis, Universität Mainz (1995).
- [84] M. Korn, Entwicklung des Bahnrückverfolgungsverfahrens für die Drei-Spektrometer-Anlage und experimentelle Bestimmung der Abbildungseigenschaften der Spektrometer A und B mit Elastischer Elektronenstreuung, Ph.D. thesis, Universität Mainz (1995).
- [85] I. Ewald, Entwicklung und Erprobung einer langen, dünnen Flüssig-Wasserstoff-Targetzelle, Diploma thesis, Universität Mainz (1996).

- [86] G. Ban, et al., A Mott polarimeter for the search of time reversal violation in the decay of free neutrons, *Nucl. Instrum. Meth.* A565 (2006) 711–724.
- [87] D. Gustavson, et al., A Back Scattered Laser Polarimeter for  $e^+e^-$  Storage Rings, *Nucl. Instr. Meth.* 165 (1979) 177.
- [88] B. Wagner, et al., A Møller polarimeter for CW and pulsed intermediate-energy electron beams, *Nucl. Instrum. Meth.* A294 (1990) 541–548.
- [89] P. Bartsch, Design eines Møllerpolarimeters für die 3-Spektrometeranlage, Diploma thesis, Universität Mainz (1996).
- [90] P. Bartsch, Aufbau eines Møller-Polarimeters für die Drei-Spektrometer-Anlage und Messung der Helizitätsasymmetrie in der Reaktion  $p(\vec{e}, e'p)\pi^0$  im Bereich der  $\Delta$ -Resonanz, Ph.D. thesis, Universität Mainz (2001).
- [91] O. Strähle, Aufbau und betriebnahme des A1-Møllerpolarimeters, Diploma thesis, Universität Mainz (2000).
- [92] T. Pospischil, et al., The focal plane proton polarimeter for the 3-spectrometer setup at MAMI, *Nucl. Instrum. Meth.* A483 (2002) 713–725.
- [93] T. Pospischil, et al., The horizontal drift chambers for the focal plane proton polarimeter of the 3-spectrometer setup at MAMI, *Nucl. Instrum. Meth.* A483 (2002) 726–733.
- [94] E. Aprile-Giboni, et al., Proton Carbon Effective Analyzing Power Between 95 MeV and 570 MeV, *Nucl. Instrum. Meth.* 215 (1983) 147–157.
- [95] M. W. Mcnaughton, et al., The P C Analyzing Power Between 100 MeV and 750 MeV, *Nucl. Instrum. Meth.* A241 (1985) 435–440.
- [96] P. Janssens, et al., Monte Carlo simulation of virtual Compton scattering below pion threshold, *Nucl. Instr. Meth.* A566 (2006) 675–686.
- [97] G. Lafferty, T. Wyatt, Where to Stick Your Data Points: The Treatment of Measurements Within Wide Bins, *Nucl. Instrum. Meth.* A355 (1995) 541.
- [98] R. Hofstadter, Electron scattering and nuclear structure, *Rev. Mod. Phys.* 28 (1956) 214.
- [99] Y. S. Tsai, Pair Production and Brehmsstrahlung of Charged Leptons, *Rev. Mod. Phys.* 46 (1974) 815.
- [100] M. Vanderhaeghen, et al., QED radiative corrections to virtual Compton scattering, *Phys. Rev.* C62 (2000) 025501.
- [101] L. W. Mo, Y. S. Tsai, Radiative Corrections to Elastic and Inelastic  $ep$  and  $\mu p$  scattering, *Rev. Mod. Phys.* 41 (1969) 205.

- [102] J. Bartels, et al., Review of Particle Physics, *Eur. Phys. J.* 15 (2000) 166.
- [103] P. Janssens, Calibration of the optics of the spectrometers for the VCS90b setting, Internal Note, MAMI-A1 collaboration (2006).
- [104] L. Doria, Personal communication.
- [105] D. R. Giebink, Relativity and spin in one-, two- and three-body systems, *Phys. Rev.* C32 (1985) 502–515.
- [106] V. Dmitrasinovic, Wigner-Thomas spin precession in polarized coincidence electro-nuclear scattering, *Phys. Rev.* C47 (1993) 2195–2203.
- [107] V. Dmitrasinovic, Erratum: Wigner-Thomas spin precession in polarized coincidence elektro-nuclear scattering, *Phys. Rev.* C71 (2005) 059901.
- [108] H. Schmieden, Proton polarization in the  $p(\vec{e}, e' \vec{p})\pi^0$  reaction and the measurement of quadrupole components in the N to Delta transition, *Eur. Phys. J.* A1 (1998) 427–433.
- [109] L. J. Thomas, The Kinematics of an Electron with an Axis, *Phil. Mag.* 3 (1927) 1–22.
- [110] T. H. Cormet, C. E. Leiserson, R. L. Rivest, C. Stein, *Introduction to Algorithms*, MIT Press and McGraw-Hill, 2001.
- [111] C. Gianino, Experimental analysis of the Italian coffee pot ‘moka’, *Am. J. Phys.* 75 (2007) 43–47.
- [112] M. Vanderhaeghen, Personal communication.
- [113] B. Pasquini, Personal communication.

---

## Calibration of the spectrometers

---

For a high precision experiment as the one discussed in this thesis, a good calibration of the detectors is of major importance. In section 4.2.1 it is explained how the matrix elements of the optical transport in the spectrometer magnets are determined. These coefficients depend on the geometry of the magnets and they have to be determined only once for each different central momentum of the spectrometer. The reference frame of the focal plane coordinates, from which the optical transport starts, is fixed with respect to the wire chambers. The position of the wire chambers in the spectrometer is not fixed with enough accuracy and the offsets should be determined via a dedicated measurement as described in reference [103].

The magnetic field in the spectrometers is measured by NMR and Hall probes. And based on this measurement the central momentum is determined. To perform a more precise calibration, the distribution of the missing mass squared  $M_X^2$  is used: the central momenta of both spectrometers are modified to improve the reconstruction of  $M_X^2$ .

To estimate the position and the width of the distribution a combination of 2 Gaussians is adjusted to the experimental histogram. The position of the mean value and the amplitude of both Gaussians is the same, but the width is different. One Gaussian is used below, the other one above the position of the peak. The fitting function is only applied to the central region. The result is shown in figure A.1.a for the VCS90b beam time of December 2005. The FWHM of the distribution is  $541 \pm 1 \text{ MeV}^2/c^4$  and the peak is located at  $51.8 \pm 0.7 \text{ MeV}^2/c^4$ .

Once the maximum and width of the simulated  $M_X^2$  are known, the calibration of the central momenta of the spectrometers can be started. To perform the optimization of  $p_A$  and  $p_B$  the following procedure was used:

Starting from the initial values for the central momenta of spectrometer B (which is measured during the experiment), the maximum of the experimental  $M_X^2$ -distribution is set to  $51.8 \text{ MeV}^2/c^4$ , the maximum obtained for the simulated data, by modifying  $p_A$  (9 different values). For each value of  $p_A$  the same fit is applied to the the obtained  $M_X^2$ -histogram as in

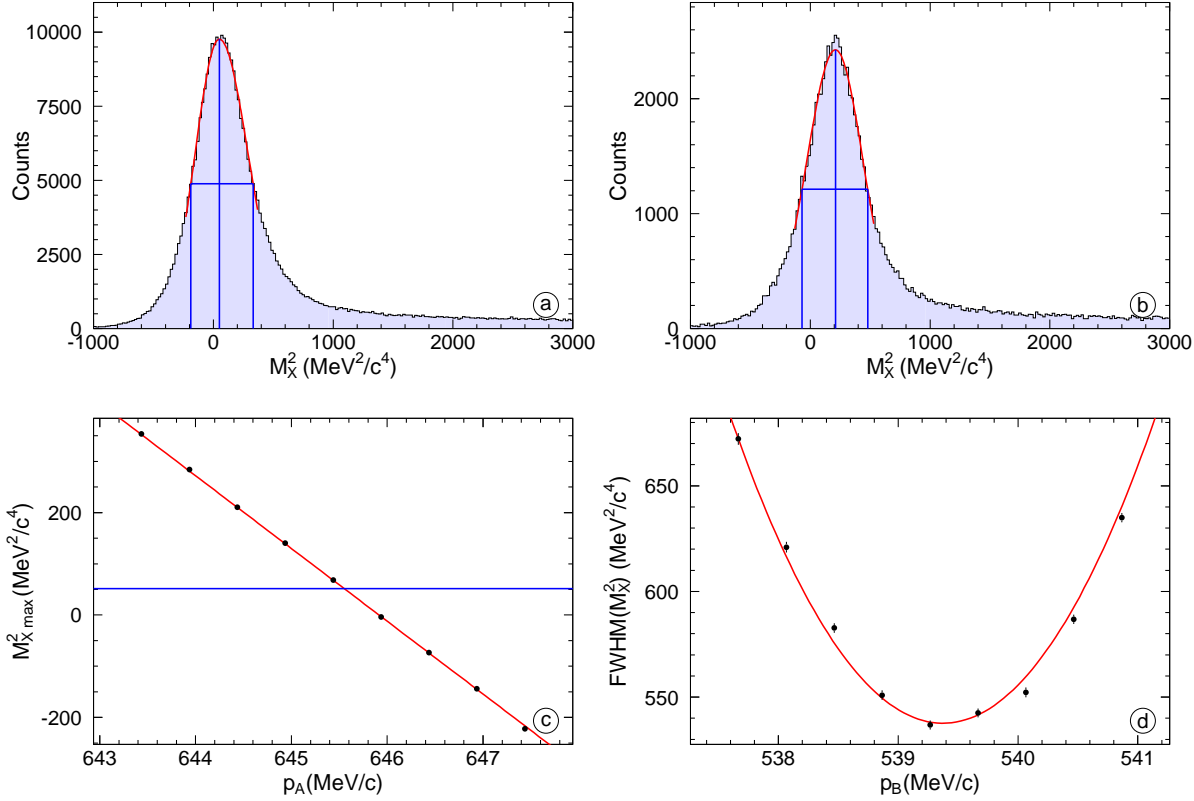


**Figure A.1:** a: Simulated  $M_X^2$ -distribution. b: Experimental  $M_X^2$ . c:  $M_{X \max}^2$  versus  $p_A$ . d:  $\text{FWHM}(M_X^2)$  versus  $p_B$ .

was done for the simulation (see figure A.1.b). A linear relation between  $p_A$  and the maximum of  $M_X^2$  is observed and a new value for  $p_A$  is found at the intersection with  $M_{X \max}^2 = 51.8 \text{ MeV}^2/c^4$  as shown in figure A.1.c.

Using the new value for  $p_A$   $\text{FWHM}(M_X^2)$  is determined for different values of  $p_B$ . Fitting a second order polynomial to  $\text{FWHM}(M_X^2)$  versus  $p_B$  a new value for  $p_B$  can be found which minimizes  $\text{FWHM}(M_X^2)$  for the given  $p_A$  (see figure A.1.d).

Now an iteration process is started: for the changed  $p_B$  a better  $p_A$  is obtained as explained above, ... After some iterations the procedure converges (for the VCS90b setting of December 2005) to

$$\begin{aligned} p_A &= 645.38 \pm 0.18 \text{ MeV}/c, \\ p_B &= 539.41 \mp 0.14 \text{ MeV}/c. \end{aligned} \tag{A.1}$$

The error on  $p_B$  is obtained directly from the fit shown in figure A.1.d, whereas  $\Delta p_A$  is obtained by optimizing  $p_A$  for  $p_B + \Delta p_B$  and  $p_B - \Delta p_B$ . Therefore the errors are anti-correlated.

---

## Reference frames and coordinates

---

In the experiment a lot of different reference frames are used. This appendix gives an overview of the reference frames and coordinate systems used in this work. All reference frames are denoted by e.g.  $\mathcal{R}_j^i$ . The corresponding axes are labeled in the same way: for this example the  $x$ -axis is indicated by  $x_j^i$  and the unit vector along the  $x$  axis by  $\hat{x}_j^i$ .

### B.1 Hall laboratory reference frame

The main reference frame of the A1 hall is the hall laboratory frame  $\mathcal{R}_h$ . The origin of the reference frame coincides with the central point in the target. This point is also the intersection of the rotation axis of the spectrometers with the horizontal plane  $(x_h, z_h)$  containing the centers of the acceptances of the spectrometers. The  $z_h$ -axis lies along the direction of the incoming beam and  $\hat{x}_h$  points towards spectrometer B. The orientation of  $\hat{y}_h$  is vertically down to form a right-handed reference frame.

### B.2 Spectrometer reference frame

To each of the spectrometers a reference frame is attached  $\mathcal{R}_{tg}^A$ ,  $\mathcal{R}_{tg}^B$  and  $\mathcal{R}_{tg}^C$ . In this frame the target coordinates are defined. The reference frame is attached to the spectrometer, thus its orientation with respect to  $\mathcal{R}_h$  depends on the position of the spectrometer. The origin of the spectrometer frame is the same point as the origin of the hall laboratory frame.

The horizontal plane through the center of the acceptance of the spectrometer is the  $(y_{tg}, z_{tg})$  plane<sup>1</sup>.  $\hat{z}_{tg}$  is perpendicular to the plane of the collimator and points inside the spectrometer.  $\hat{x}_{tg}$  points vertically down and this fixes the  $y_{tg}$ -axis.

---

<sup>1</sup>For spectrometer B the  $(y_{tg}^B, z_{tg}^B)$ -plane is only horizontal for in-plane settings of spectrometer B.

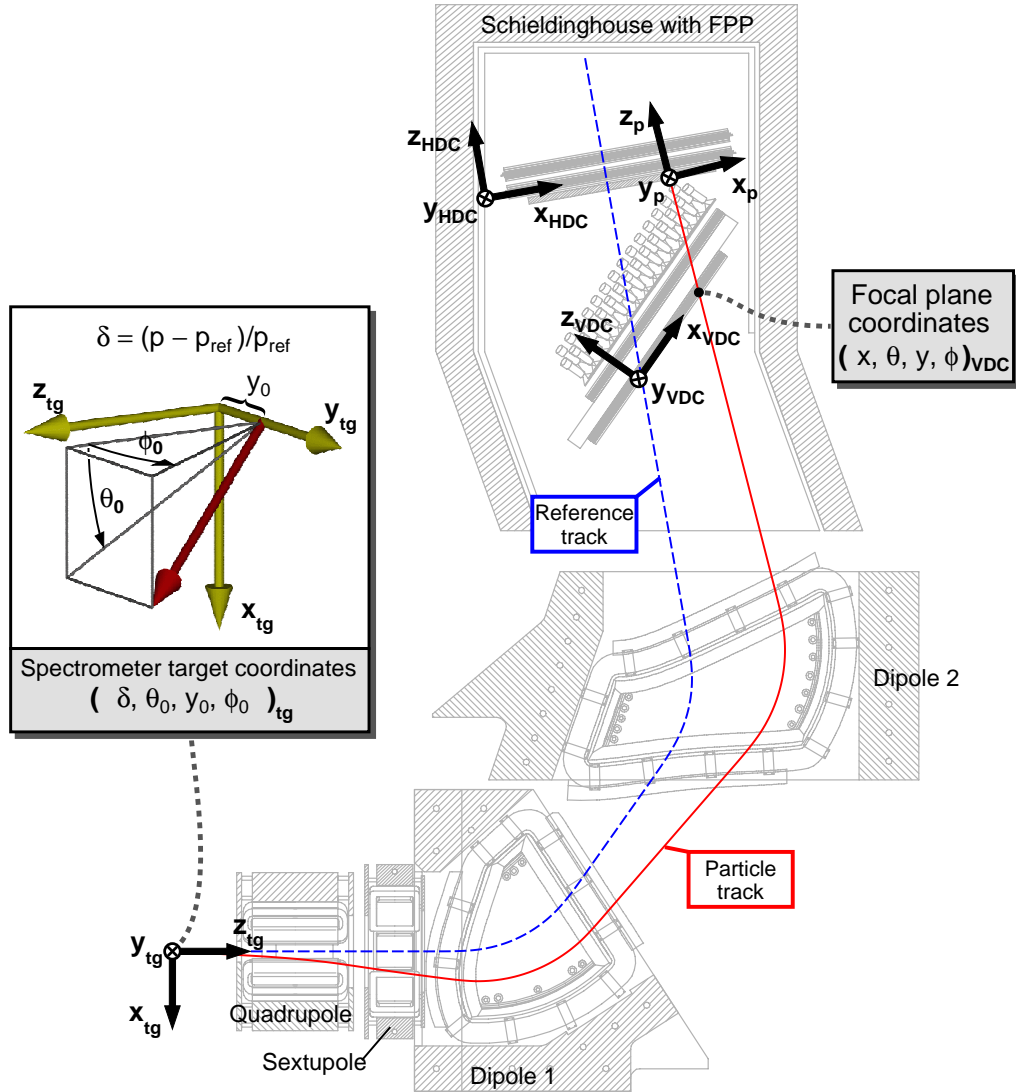


**Figure B.1:** Overview of the reference frames in spectrometer A. (Taken from [82].)

The spectrometer reconstructs four variables in the spectrometer frame:  $(\delta, \theta_0, y_0, \phi_0)_{tg}$ .  $\delta = (p - p_{ref})/p_{ref}$  is the relative momentum (where  $p$  is the momentum of the particle and  $p_{ref}$  the reference momentum of the spectrometer),  $\theta_0$  and  $\phi_0$  are the dispersive and non-dispersive angle, respectively, and  $y_0$  is the  $y$ -coordinate of the intersection of the particle track with the  $(x_{tg}, y_{tg})$ -plane. To refer to the e.g. dispersive angle of the particle in spectrometer A, the notation  $\theta_0^\Delta$  is used. The reference track for each of the spectrometers has  $(0,0,0,0)$  as target coordinates. The target coordinates and the spectrometer reference frame are illustrated in figure B.1.

### B.3 Focal plane reference frame

The focal plane reference frame  $\mathcal{R}_{\text{fp}}$  is the reference frame in which the track reconstruction is performed. The  $x_{\text{fp}}$ -axis lies in the focal plane in dispersive direction and  $\hat{z}_{\text{fp}}$  is perpendicular to the focal plane and points upwards (see figure B.1).

The focal plane coordinates  $(x, \theta, y, \phi)_{\text{fp}}$  are defined in such a way that the track of the particle in the focal plane as a function of  $z_{\text{fp}}$  is given by  $(x_{\text{fp}}, y_{\text{fp}}, z_{\text{fp}}) = (x + z_{\text{fp}} \tan \theta, y + z_{\text{fp}} \tan \phi, z_{\text{fp}})$ . Starting from the set  $(x, \theta, y, \phi)_{\text{fp}}$  the target variables are calculated using equation (4.1).

The VDC coordinates  $(x_1, s_1, x_2, s_2)_{\text{VDC}}$  are the coordinates of the intersection points of the particle track with each of the VDC wire planes.  $x_1$  corresponds to the first VDC,  $s_1$  to the second one, ... The wires of the first and third VDC are perpendicular to the dispersive direction and they measure the dispersive coordinates  $x_1$  and  $x_2$ . The wires of the other VDCs are rotated over  $40^\circ$ . The direction perpendicular to the wires in the plane of the VDC is called the  $s$ -direction, thus VDC 2 and 4 measure the intersection point in this direction:  $s_1$  and  $s_2$ . Based on  $(x_1, s_1, x_2, s_2)_{\text{VDC}}$  the focal plane coordinates are reconstructed.

### B.4 HDC reference frame

The  $(x_{\text{HDC}}, y_{\text{HDC}})$ -plane of the HDC reference frame  $\mathcal{R}_{\text{HDC}}$  coincides with the wires of the first HDC. Again  $x_{\text{HDC}}$  is the dispersive direction and  $z_{\text{HDC}}$  is perpendicular to the wires and points upwards (see figure B.1).

### B.5 Proton reference frame

The reference frame in which the polarization of the recoil proton is measured is called the proton reference frame and denoted by  $\mathcal{R}_p$ . The  $z_p$ -axis lies along the direction of the proton before the scattering on the carbon analyzer and the  $\hat{y}_p$  is parallel to  $y_{\text{HDC}}$ -axis. The reference frame  $\mathcal{R}_p$  is also drawn in figure B.1.

### B.6 Center-of-mass reference frames

Apart from the reference frames dependent on the experimental setup there are also reference frames determined by the kinematics of the VCS process. In the next subsections the choice of references frame in the center-of-mass of the proton and the photon is discussed.

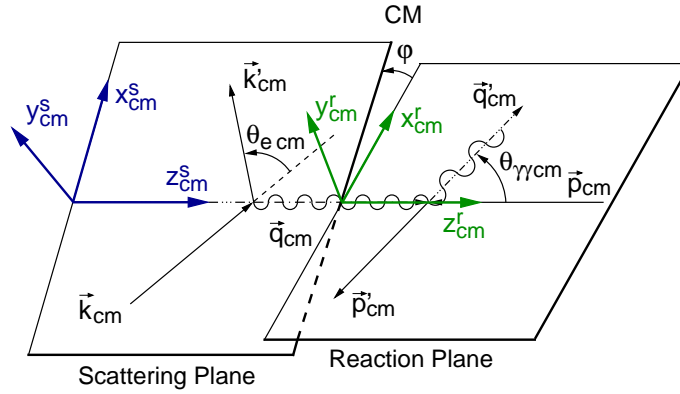


**Figure B.2:** The two center-of-mass reference frames.  $\mathcal{R}_{\text{cm}}^r$  is attached to the reaction plane and  $\mathcal{R}_{\text{cm}}^s$  is connected to the leptons.

### Choice of the center-of-mass reference frames

There are several possibilities for defining a reference frame in the center of mass for the VCS reaction. A first possibility is to attach the reference frame to the reaction plane. Such a reference frame was proposed by Guichon *et al.* [26] and [31]. One could also define the center-of-mass reference frame relative to the scattering plane. The reference frames attached to the reaction and scattering plane are denoted by  $\mathcal{R}_{\text{cm}}^r$  and  $\mathcal{R}_{\text{cm}}^s$  respectively (see figure B.2). The unit vectors of  $\mathcal{R}_{\text{cm}}^r$  are defined in equation (2.16) and  $\mathcal{R}_{\text{cm}}^s$  is defined by equation (7.6). The transformation from  $\mathcal{R}_{\text{cm}}^r$  to  $\mathcal{R}_{\text{cm}}^s$  is a rotation over  $\varphi$  around their common  $z_{\text{cm}}$ -axis.

The advantage of  $\mathcal{R}_{\text{cm}}^s$  is that for every possible scattering configuration the reference frame is uniquely defined, whereas for  $\vec{q}_{\text{cm}} \parallel \vec{q}'_{\text{cm}}$  the scattering plane is undefined and the choice of  $\mathcal{R}_{\text{cm}}^r$  is arbitrary. From this point of view  $\mathcal{R}_{\text{cm}}^s$  is preferred. However all formulas in section 2.6 are defined in reference frame  $\mathcal{R}_{\text{cm}}^r$ .

### Center-of-mass reference frame for theoretical calculations

In chapter 2 it is mentioned that one can calculate the polarizations of the BH+B process exactly based on the form factors of the proton. Two computer programs are available for this purpose: Vanderhaeghen *et al.* [37] and Pasquini *et al.* [57]. It is of major importance to know the reference frame in which these calculations have been performed. Both authors claim that this is the  $\mathcal{R}_{\text{cm}}^r$  frame ([112] and [113]). The result of the calculation of Pasquini is shown in figure B.3. It shows a negative  $\mathcal{P}_x$  for negative  $\theta_{\gamma\text{cm}}$ . The curve on this plot was calculated for  $\varphi = 0^\circ$  and  $\theta_{\gamma\text{cm}} < 0^\circ$  [113]. Also the program of Vanderhaeghen gives the same result for this particular definition of the kinematics ( $\varphi = 0^\circ$  and  $\theta_{\gamma\text{cm}} < 0^\circ$ ). However, for  $\varphi = 180^\circ$  and  $\theta_{\gamma\text{cm}} > 0^\circ$ , which is physically the same kinematical region, the sign of  $\mathcal{P}_x$  as calculated by the two programs differs, while the absolute value is the same: the code of Vanderhaeghen

yields a negative  $\mathcal{P}_x$ , but it is positive in the calculation of Pasquini (see figure B.4). The figure shows a sign flip of  $\mathcal{P}_x$  at  $\theta_{\gamma\gamma_{\text{cm}}} = 0^\circ$  and  $180^\circ$ . This sign flip is not present in the calculation of Vanderhaeghen, where  $\mathcal{P}_x$  is continuous. The experimentally observed  $x$ -component of  $\vec{\mathcal{P}}$  in  $\mathcal{R}_{\text{cm}}^r$  is positive<sup>2</sup>.

The confusion comes from the fact that negative values for  $\theta_{\gamma\gamma_{\text{cm}}}$  were used to present the results of previous experiments on one single plot (see e.g. 3.2). The points with  $\theta_{\gamma\gamma_{\text{cm}}} < 0$  correspond, according to the definition of Guichon, to  $\theta_{\gamma\gamma_{\text{cm}}} > 0$  and  $\varphi = 180^\circ$ .

In the framework of reference [26] the use of negative  $\theta_{\gamma\gamma_{\text{cm}}}$  values is not allowed. The definition of the reference frame  $\mathcal{R}_{\text{cm}}^r$  leads to the following momentum three vectors [26]:

$$\begin{aligned} \vec{q}_{\text{cm}} &= q_{\text{cm}} \begin{pmatrix} 0 \\ 0 \\ 1 \end{pmatrix}, & \vec{q}'_{\text{cm}} &= q'_{\text{cm}} \begin{pmatrix} \sin \theta_{\gamma\gamma_{\text{cm}}} \\ 0 \\ \cos \theta_{\gamma\gamma_{\text{cm}}} \end{pmatrix}, \\ \vec{k}_{\text{cm}} &= k_{\text{cm}} \begin{pmatrix} \sin \alpha \cos \varphi \\ \sin \alpha \sin \varphi \\ \cos \alpha \end{pmatrix}, & \vec{k}'_{\text{cm}} &= k'_{\text{cm}} \begin{pmatrix} \sin \alpha' \cos \varphi \\ \sin \alpha' \sin \varphi \\ \cos \alpha' \end{pmatrix}. \end{aligned} \quad (\text{B.1})$$

By definition of  $\mathcal{R}_{\text{cm}}^r$  is the  $x$ -component of the momentum of the outgoing photon positive. When negative values of  $\theta_{\gamma\gamma_{\text{cm}}}$  are used, the  $x$ -component of  $\vec{q}'_{\text{cm}}$  becomes negative according to equation (B.1) due to the  $\sin \theta_{\gamma\gamma_{\text{cm}}}$ . This is against the definition of  $\mathcal{R}_{\text{cm}}^r$ . Negative values for  $\theta_{\gamma\gamma_{\text{cm}}}$  correspond to another reference frame,  $\mathcal{R}_{\text{cm}}^{r'}$ , also attached to the reaction plane: it is rotated over  $180^\circ$  around the  $z$  axis with respect to  $\mathcal{R}_{\text{cm}}^r$ , since the  $x$  component of  $\vec{q}'_{\text{cm}}$  has the opposite sign. Both reference frames are presented in figure B.5 for  $\varphi = 0^\circ$  and  $180^\circ$ .

The difference between both calculations might be explained by a different choice of the reference frame. Suppose that the calculation of Vanderhaeghen is performed in the reference frame  $\mathcal{R}_{\text{cm}}^s$  in stead of  $\mathcal{R}_{\text{cm}}^r$ . For  $\varphi = 0^\circ$  both reference frames coincide, but for  $\varphi = 180^\circ$  the  $x$ - and  $y$ -axes are pointing in opposite directions. This would explain the sign difference for  $\varphi = 180^\circ$ .

When going to out-of-plane kinematics one can prove that both programs indeed use different reference frames. For the same values of  $\theta_{\gamma\gamma_{\text{cm}}}$  and  $\varphi$  different polarizations are obtained. But when the resulting polarization vector of the code of Pasquini for a given  $(\theta_{\gamma\gamma_{\text{cm}}}, \varphi)$  was rotated over  $\varphi$  around the  $z$ -axis the same result was obtained as when the code of Vanderhaeghen is executed with  $(\theta_{\gamma\gamma_{\text{cm}}}, 2\pi - \varphi)$ . This proves that one of the codes is defined in  $\mathcal{R}_{\text{cm}}^r$  and the other one  $\mathcal{R}_{\text{cm}}^s$ .

<sup>2</sup>In section 7.3.5 the polarizations are shown in the reference frame  $\mathcal{R}_{\text{cm}}^s$ . For in plane events with  $\varphi = 180^\circ$  the  $x$ - and  $y$ -axes point in the opposite direction of the axis of  $\mathcal{R}_{\text{cm}}^r$ .

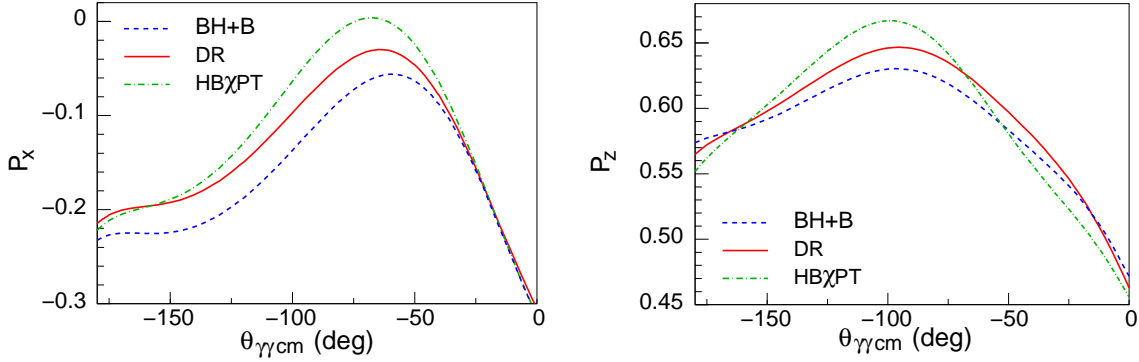


**Figure B.3:** Figure 37 of reference [18], showing the BH+B polarization (dashed line) and the effect of the GPs for  $q_{\text{cm}} = 600 \text{ MeV}/c$ ,  $q'_{\text{cm}} = 111.5 \text{ MeV}/c$ ,  $\varepsilon = 0.62$  and  $\varphi = 0^\circ$ . The effect of the GPs is calculated using the DR model of reference [57] (full line) and using HB $\chi$ PT [42] (dashed-dotted line).

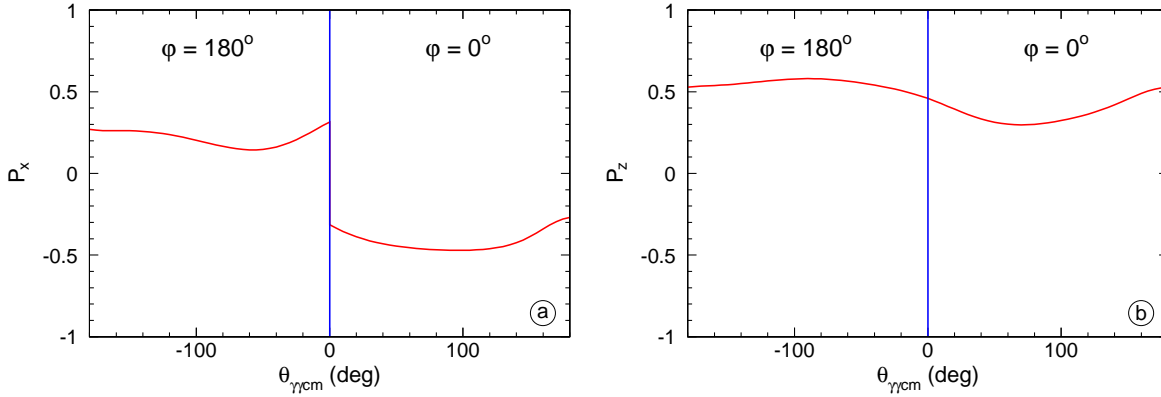


**Figure B.4:** The BH+B contribution to  $\mathcal{P}_x$  and  $\mathcal{P}_z$  for  $\varphi = 0^\circ$  and  $\varphi = 180^\circ$  calculated using [57]. A sign flip of  $\mathcal{P}_x$  is observed when going from negative to positive  $\theta_{\gamma\text{cm}}$ . This corresponds to the transition  $\varphi = 0^\circ \rightarrow 180^\circ$  for  $\theta_{\gamma\text{cm}} = 0^\circ$  and  $\theta_{\gamma\text{cm}} = 180^\circ$ .

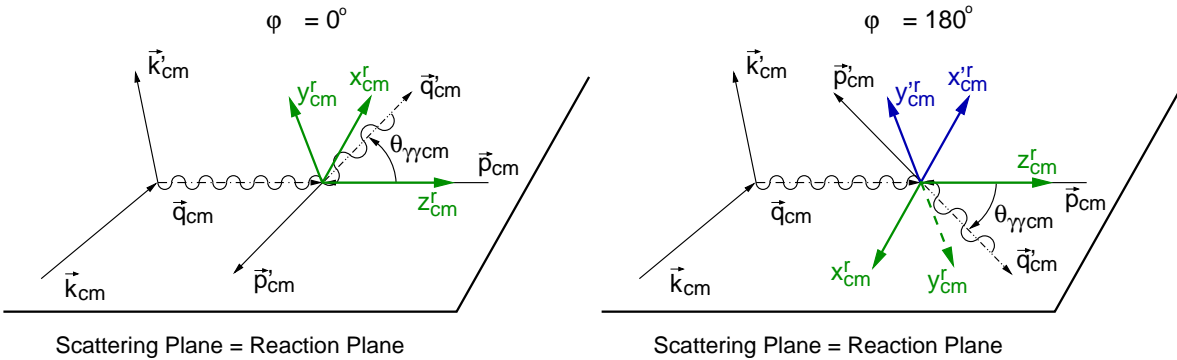


**Figure B.5:** Definition of the reference frames  $\mathcal{R}_{\text{cm}}^r$  and  $\mathcal{R}'_{\text{cm}}{}^r$ . For  $\varphi = 0^\circ$  or  $180^\circ$  the scattering and reaction plane coincide. The  $x$ - and  $y$ -axes of the reference frames point into opposite directions for  $\varphi = 180^\circ$ .

Another tests reveals that the code of Pasquini is performed in  $\mathcal{R}_{\text{cm}}^r$  and by consequence the calculations of Vanderhaeghen are performed in  $\mathcal{R}_{\text{cm}}^s$ . For  $\theta_{\gamma\gamma\text{cm}} = 0^\circ$  and  $\theta_{\gamma\gamma\text{cm}} = 180^\circ$   $\varphi$  is in principle not defined: from the physical point of view there is no difference between ( $\theta_{\gamma\gamma\text{cm}} = 180^\circ$ ,  $\varphi = 0^\circ$ ) and e.g. ( $\theta_{\gamma\gamma\text{cm}} = 180^\circ$ ,  $\varphi = 40^\circ$ ). For both combinations of angles the polarization should be the same. This is the case in Vanderhaeghen's code, but in the code of Pasquini the polarization vector seems to rotate with respect to the reference frame when  $\varphi = 0^\circ \rightarrow 360^\circ$  for  $\theta_{\gamma\gamma\text{cm}} = 180^\circ$ .

For  $\theta_{\gamma\gamma\text{cm}} = 0^\circ$  or  $\theta_{\gamma\gamma\text{cm}} = 180^\circ$  the scattering plane is not defined, since the real and virtual photon are moving along the same axis. In that case  $\mathcal{R}_{\text{cm}}^r$  is defined based on an arbitrary value of  $\varphi$ : when  $\varphi$  is varied from  $0^\circ$  to  $360^\circ$   $\mathcal{R}_{\text{cm}}^r$  rotates with respect to the scattering plane and also with respect to the polarization vector. The polarization vector seems to rotate, but actually it is the reference frame itself, which is rotating. The observation of a rotating polarization vector for  $\theta_{\gamma\gamma\text{cm}} = 180^\circ$  demonstrates that the calculation of Pasquini is performed in the reference frame  $\mathcal{R}_{\text{cm}}^r$ .

## B.7 Rotation from center-of-mass frame to the spectrometer frame

In a first step the spin of the proton is calculated in an intermediate reference frame in the laboratory system  $\mathcal{R}^s$  which is attached to the scattering plane (see figure B.6). Its orientation is only dependent on the momentum  $\vec{k}$  of the outgoing electron and the direction of the electron beam. The transformation of the coordinate system ( $\mathcal{R}^r \rightarrow \mathcal{R}^s$ ) is described by a rotation around the z-axis over  $\pi + \varphi$ . This transformation can be described by the matrix  $\mathbf{R}_z(\pi + \varphi)$ :

$$\begin{pmatrix} \mathcal{S}_x^s \\ \mathcal{S}_y^s \\ \mathcal{S}_z^s \end{pmatrix} = \mathbf{R}_z(\pi + \varphi) \begin{pmatrix} \mathcal{S}_x^r \\ \mathcal{S}_y^r \\ \mathcal{S}_z^r \end{pmatrix} = \begin{pmatrix} -\cos \varphi & \sin \varphi & 0 \\ -\sin \varphi & -\cos \varphi & 0 \\ 0 & 0 & 1 \end{pmatrix} \begin{pmatrix} \mathcal{S}_x^r \\ \mathcal{S}_y^r \\ \mathcal{S}_z^r \end{pmatrix}. \quad (\text{B.2})$$

Then a rotation to the laboratory frame ( $\mathcal{R}^s \rightarrow \mathcal{R}_h$ ) is applied (see figure B.7). The angles of the rotation are defined by  $\theta_\gamma$  and  $\varphi_\gamma$ , respectively the polar and azimuthal angle of the virtual photon in the hall laboratory frame:

$$\vec{S}_h = \mathbf{R}_z(-\varphi_\gamma) \mathbf{R}_y(-\theta_\gamma) \vec{S}^s. \quad (\text{B.3})$$

Finally, the transition from hall laboratory frame to spectrometer frame ( $\mathcal{R}_h \rightarrow \mathcal{R}_{\text{tg}}^A$ ) is given by

$$\vec{S}_{\text{tg}}^A = \mathbf{R}_x(-\theta_A) \mathbf{R}_z\left(\frac{\pi}{2}\right) \vec{S}_h. \quad (\text{B.4})$$

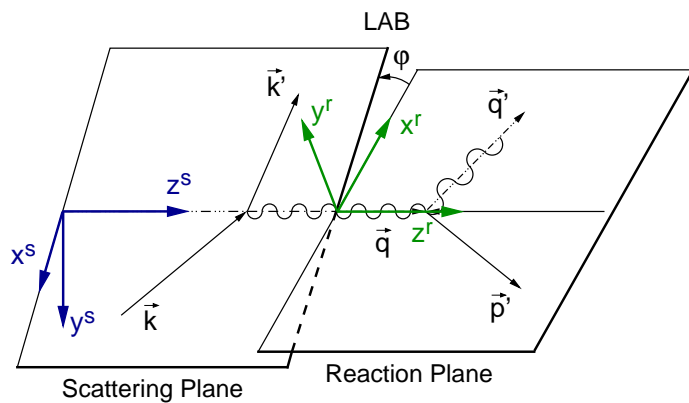


**Figure B.6:** The reaction plane reference frame  $\mathcal{R}^r$  (green) and the intermediate reference frame attached to the scattering plane  $\mathcal{R}^s$  (blue).

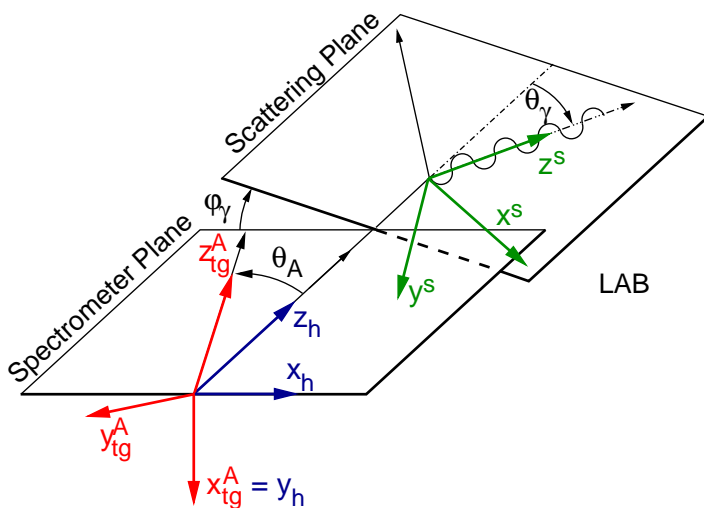


**Figure B.7:** The transformation from  $\mathcal{R}^s$  to the spectrometer frame  $\mathcal{R}^A_{tg}$  is defined by  $\theta_\gamma$ ,  $\phi_\gamma$  and  $\theta_A$ .  $\mathcal{R}_h$  is the hall laboratory frame.

---

## Tables

---

### C.1 Overview of the settings

The data for the determination of the double-spin asymmetry were collected during six periods in the years 2005 and 2006. To cover the interesting phase space two different settings were used, called VCS90 and VCS90b. In table C.1 an overview is given of the different periods.

Period	Setting	$p_{\text{ref}}^{\text{A}}$ (MeV/ $c$ )	$\theta^{\text{A}}$ (deg)	$p_{\text{ref}}^{\text{B}}$ (MeV/ $c$ )	$\theta^{\text{A}}$ (deg)	$E_{\text{b}}$ (MeV)
apr 2005	VCS90	619.49	34.10	546.40	50.60	854.49
jul 2005	VCS90	619.98	34.10	545.81	50.60	854.51
nov 2005	VCS90b	645.38	38.00	539.56	50.60	854.57
dec 2005	VCS90b	645.38	38.00	539.41	50.60	854.53
apr 2006	VCS90	620.25	34.10	545.33	50.60	854.49
jul 2006	VCS90b	646.27	38.00	538.75	50.60	854.49

**Table C.1:** Overview of the settings from the double polarized VCS experiment.

## C.2 Resolution effects in the simulation

	unit	spectrometer A	spectrometer B
$A_1$		0.867	0.879
FWHM <sub>1</sub>	mm	0.235	0.22
$A_2$		0.115	0.115
FWHM <sub>2</sub>	mm	0.6	0.66
$A_3$		0.016	0.0055
FWHM <sub>3</sub>	mm	8.9	19.
$A_4$		0.002	0.0005
FWHM <sub>4</sub>	mm	26.	26.5

**Table C.2:** The parameters for the simulation of the intrinsic resolution of the VDCs.  $A_i$  is the relative amplitude and FWHM <sub>$i$</sub>  is the width of Gaussian  $i$ .

Variable	Unit	Spectrometer A	Spectrometer B
$\delta$	rel. units	0.00064	0.00064
$\theta_0$	rad	0.003	0.003
$\phi_0$	rad	0.0028	0.0028
$y_0$	mm	8.0	2.4

**Table C.3:** The FWHM of the additional Gaussians sampled on the target coordinates.

### C.3 Cross section

#### Summary of the applied cuts

The cuts used for the calculation of the cross section are given by:

$$\begin{aligned}
 \left| (100 + \delta^A) \frac{665}{630} - 100 \right| &< 10 , \\
 |\delta^B| &< 7.5 , \\
 |T_{AB}| &< 3 \text{ ns} , \\
 -1000 \text{ MeV}^2/c^4 &< M_X^2 < 2000 \text{ MeV}^2/c^4 , \\
 -17.11 \text{ mm} &< z_v < 18.20 \text{ mm} , \\
 |\theta' - 90^\circ| &< 12^\circ , \\
 |\varepsilon - 0.645| &< 0.012 , \\
 |q_{\text{cm}} - 600 \text{ MeV}/c| &< 12 \text{ MeV}/c , \\
 |q'_{\text{cm}} - 90 \text{ MeV}/c| &< 15 \text{ MeV}/c , \\
 (z_v < 10 \text{ mm}) &|| (\phi_0^A < 4^\circ) .
 \end{aligned} \tag{C.1}$$

#### Experimental result

The cross section results without and with iterations are given in table C.4 and C.5.

Cross Sections VCS90b (in pb MeV <sup>-1</sup> sr <sup>-2</sup> )							
$\theta_{\gamma\gamma\text{cm}}$	$\varphi$	$d^5\sigma^{\text{BH+B}}$	$d^5\sigma_0$	$\theta_{\gamma\gamma\text{cm}}$	$\varphi$	$d^5\sigma^{\text{BH+B}}$	$d^5\sigma_0$
177.5°	180°	0.129	0.143 ± 0.002	122.5°	180°	0.151	0.142 ± 0.002
172.5°	180°	0.132	0.135 ± 0.002	117.5°	180°	0.147	0.141 ± 0.002
167.5°	180°	0.136	0.139 ± 0.002	112.5°	180°	0.142	0.135 ± 0.002
162.5°	180°	0.142	0.147 ± 0.002	107.5°	180°	0.137	0.129 ± 0.002
157.5°	180°	0.148	0.149 ± 0.002	102.5°	180°	0.132	0.121 ± 0.003
152.5°	180°	0.153	0.154 ± 0.002	97.5°	180°	0.126	0.120 ± 0.003
147.5°	180°	0.156	0.154 ± 0.002	92.5°	180°	0.122	0.110 ± 0.003
142.5°	180°	0.158	0.156 ± 0.002	87.5°	180°	0.117	0.103 ± 0.003
137.5°	180°	0.158	0.159 ± 0.002	82.5°	180°	0.113	0.104 ± 0.003
132.5°	180°	0.157	0.157 ± 0.002	77.5°	180°	0.109	0.099 ± 0.003
127.5°	180°	0.155	0.154 ± 0.002	72.5°	180°	0.106	0.099 ± 0.006
177.5°	0°	0.132	0.147 ± 0.003	172.5°	0°	0.141	0.165 ± 0.004

**Table C.4:** Overview of the cross section obtained without iterations.

Cross Sections VCS90b (in pb MeV <sup>-1</sup> sr <sup>-2</sup> )							
$\theta_{\gamma\gamma\text{cm}}$	$\varphi$	$d^5\sigma^{\text{BH+B}}$	$d^5\sigma_4$	$\theta_{\gamma\gamma\text{cm}}$	$\varphi$	$d^5\sigma^{\text{BH+B}}$	$d^5\sigma_4$
177.5°	180°	0.129	0.146 ± 0.002	122.5°	180°	0.151	0.142 ± 0.002
172.5°	180°	0.132	0.137 ± 0.002	117.5°	180°	0.147	0.140 ± 0.002
167.5°	180°	0.136	0.140 ± 0.002	112.5°	180°	0.142	0.135 ± 0.002
162.5°	180°	0.142	0.148 ± 0.002	107.5°	180°	0.137	0.128 ± 0.002
157.5°	180°	0.148	0.150 ± 0.002	102.5°	180°	0.132	0.120 ± 0.003
152.5°	180°	0.153	0.155 ± 0.002	97.5°	180°	0.126	0.119 ± 0.003
147.5°	180°	0.156	0.154 ± 0.002	92.5°	180°	0.122	0.109 ± 0.003
142.5°	180°	0.158	0.156 ± 0.002	87.5°	180°	0.117	0.102 ± 0.003
137.5°	180°	0.158	0.159 ± 0.002	82.5°	180°	0.113	0.103 ± 0.003
132.5°	180°	0.157	0.157 ± 0.002	77.5°	180°	0.109	0.098 ± 0.003
127.5°	180°	0.155	0.154 ± 0.002	72.5°	180°	0.106	0.099 ± 0.005
177.5°	0°	0.132	0.149 ± 0.003	172.5°	0°	0.141	0.167 ± 0.004

**Table C.5:** Overview of the cross section obtained after the iterations.

## C.4 Double-spin asymmetry

### Summary of the applied cuts

The cuts used for the selection of the VCS events are given by:

$$\begin{aligned}
 |T_{AB}| &< 1.5 \text{ ns} , \\
 -1000 \text{ MeV}^2/c^4 &< M_X^2 < 2000 \text{ MeV}^2/c^4 , \\
 -17.11 \text{ mm} &< z_v < 18.20 \text{ mm} , \\
 q'_{\text{cm}} &< 126 \text{ MeV}/c ,
 \end{aligned} \tag{C.2}$$

together with the cuts `ScintAProton` and `CherElectron2` (see section 6.1.3 and 6.1.4) to reduce the amount of background events.

For the polarimeter some other cuts have to be added:

$$\begin{aligned}
 \text{VDCOKA} &> 0 , \\
 \text{VDCOKB} &> 0 , \\
 0 &< \text{HDCOK} < 7 , \\
 \Delta\theta_{\text{fp}}^A &< 0.4 \text{ mrad} \\
 \Delta\phi_{\text{fp}}^A &< 2 \text{ mrad} , \\
 -185 \text{ mm} &< z_s < -55 \text{ mm} , \\
 \theta_{\text{fpp}} &> 12.66^\circ - 0.0238^\circ/\text{MeV } T_{\text{CC}} , \\
 t_d &< 250 \text{ ns} .
 \end{aligned} \tag{C.3}$$

and the cuts `SpinTraceCut` (see section 7.3.2) and `AnPowCut` (see section 7.1.6).

### Experimental result

The experimental result of the double-spin asymmetry is given in table C.6. The values for the BH+B contribution to the double-spin asymmetry are averaged over the complete experimental phase space for each bin in  $\theta_{\gamma\gamma\text{cm}}$ .

Double-spin asymmetry					
$\theta_{\gamma\gamma\text{cm}}$	$\varphi$	$\langle \mathcal{P}_x^{\text{BH+B}} \rangle$	$\mathcal{P}_x$	$\langle \mathcal{P}_y^{\text{BH+B}} \rangle$	$\mathcal{P}_y$
170°	180°	-0.31	$-0.26 \pm 0.05$	0.00	$0.00 \pm 0.07$
150°	180°	-0.28	$-0.28 \pm 0.04$	0.00	$-0.03 \pm 0.06$
130°	180°	-0.26	$-0.20 \pm 0.03$	-0.00	$0.02 \pm 0.04$
110°	180°	-0.25	$-0.18 \pm 0.04$	-0.00	$0.02 \pm 0.04$
90°	180°	-0.23	$-0.05 \pm 0.05$	-0.00	$-0.02 \pm 0.06$
70°	180°	-0.22	$-0.13 \pm 0.08$	-0.00	$-0.27 \pm 0.09$

**Table C.6:** Overview of the polarizations obtained in the experiment.